

# **Development and Investigation of an Efficient Electrolysis Process for the Conversion of Carbon Dioxide to Formate**

**Von der Fakultät Chemie der Universität Stuttgart  
zur Erlangung der Würde eines Doktors der Naturwissenschaften (Dr. rer. nat.)  
genehmigte Abhandlung**

**Vorgelegt von**

**Armin Löwe  
aus Kirchheim unter Teck**

**Hauptberichter: Prof. Dr.-Ing. Elias Klemm  
Mitberichter: Prof. Dr. rer. nat. Andreas Friedrich  
Prüfungsvorsitzender: Prof. Dr. rer. nat. Bernhard Hauer**

**Tag der mündlichen Prüfung: 01.03.2021**

**Institut für Technische Chemie der Universität Stuttgart**

**2021**







Supported by:



Federal Ministry  
for Economic Affairs  
and Energy

on the basis of a decision  
by the German Bundestag

Die Verantwortung für den Inhalt dieser Veröffentlichung liegt beim Autor.

The author is responsible for the content of this publication.



---

## **Erklärung über die Eigenständigkeit der Dissertation**

Ich versichere, dass ich die vorliegende Arbeit mit dem Titel

„Development and Investigation of an Efficient Electrolysis Process for the Conversion of Carbon Dioxide to Formate“

selbständig verfasst und keine anderen als die angegebenen Quellen und Hilfsmittel benutzt habe; aus fremden Quellen entnommene Passagen und Gedanken sind als solche kenntlich gemacht.

## **Declaration of Authorship**

I hereby certify that the dissertation entitled

„Development and Investigation of an Efficient Electrolysis Process for the Conversion of Carbon Dioxide to Formate“

is entirely my own work except where otherwise indicated. Passages and ideas from other sources have been clearly marked.

Stuttgart, September 11<sup>th</sup>, 2020

---

Place, date

---

Signature - Armin Löwe





---

## **Acknowledgment**

My greatest gratitude goes to Prof. Dr.-Ing. Elias Klemm for providing me the opportunity to work on this exceptional interesting topic that I hope will accompany my future career. Special thanks also for allowing me to pursue own ideas, providing a great working environment, imparting knowledge and for the detailed corrections on the present work.

I want to extend my gratitude also to Dennis Kopljar who introduced me to this, at that time, completely unknown topic. Also, to Fabian Bienen. Thanks to the both of you for the large number of fruitful discussions, helpful tips, for assisting with preparations and, Dennis, your great work I could start from.

Thanks a lot to the whole institute, but most importantly to the electrochemical reaction engineering group, for the great teamwork, wonderful discussions no matter day or night, awesome working environment and a lot of fun.

Furthermore I want to thank all colleagues for the conducted measurements. Heike Fingerle for trying so hard to measure our unwilling samples. Barbara Gehring, Dennis Beierlein and Jan Florenski for measuring all those TGA samples and Efi Hadjixenophontos for taking the TEM images. To all colleagues, i'd like to thank you for the wonderful time at this institute!



You live your life by a code, an ethos. Every man does. It's your shoreline. It's what guides you home.

And trust me, you're always trying to get home.

- *Act of Valor*, 2012



Dedicated to my parents.



# Contents

<b>1</b>	<b>Abstract</b>	<b>1</b>
<b>2</b>	<b>Zusammenfassung</b>	<b>5</b>
<b>3</b>	<b>Introduction</b>	<b>9</b>
<b>4</b>	<b>Theoretical Background</b>	<b>13</b>
4.1	Electrochemical basics . . . . .	13
4.1.1	The electrical double layer . . . . .	14
4.1.2	Cell voltage and electrode potentials . . . . .	16
4.1.3	Kinetic aspects . . . . .	18
4.1.4	Quantitative relations . . . . .	24
4.1.5	Important aspects of electrochemical cells . . . . .	25
4.2	Carbon dioxide reduction reaction . . . . .	27
4.2.1	Fundamentals . . . . .	27
4.2.2	Equilibrium potentials . . . . .	29
4.2.3	Electrocatalytic conversion of carbon dioxide . . . . .	31
4.2.4	Influence of operating conditions . . . . .	37
4.3	Gas diffusion electrodes . . . . .	43
4.3.1	Wetting behavior . . . . .	46
4.3.2	Mass transport in gas diffusion electrodes . . . . .	49
4.3.3	Equivalent circuit model of porous electrodes . . . . .	50
4.4	Process concepts for carbon dioxide electrolysis . . . . .	53
4.4.1	Aspects to consider for alkaline reaction conditions . . . . .	53
4.4.2	Coupling with downstream bipolar membrane electrodialysis . . . . .	54

4.4.3	Alternative anode reactions . . . . .	56
<b>5</b>	<b>Motivation and Objectives</b>	<b>59</b>
<b>6</b>	<b>Experimental Section</b>	<b>63</b>
6.1	Preparation methods . . . . .	63
6.1.1	Homogeneous precipitation of supported metal oxides . . . . .	63
6.1.2	Oxidative pretreatment of the Vulcan XC 72 support . . . . .	65
6.1.3	Synthesis of supported palladium nanoparticles . . . . .	65
6.1.4	Preparation of gas diffusion electrodes . . . . .	65
6.2	Experimental setup . . . . .	67
6.2.1	Details for the semi-batch mode of operation . . . . .	68
6.2.2	Details for the continuous mode of operation . . . . .	68
6.2.3	Used and developed electrochemical cells . . . . .	70
6.3	Analytical methods . . . . .	75
6.3.1	Quantification of gaseous products . . . . .	75
6.3.2	Quantification of dissolved products . . . . .	75
6.3.3	Catalyst and electrode characterization . . . . .	76
6.4	Electroanalytical methods . . . . .	79
6.4.1	Determination of electrode activity and wetting . . . . .	79
6.4.2	Determination of faradaic and energetic efficiencies . . . . .	82
6.4.3	Estimations on the catalyst's oxidation state . . . . .	84
6.5	Data evaluation . . . . .	85
6.5.1	Analysis of semi-batch operation . . . . .	85
6.5.2	Analysis of continuous operation . . . . .	87
6.5.3	Double layer capacitance and activity evaluation . . . . .	88
6.6	Fundamental investigations on new process concepts . . . . .	89
6.6.1	Bipolar membrane electrodialysis for downstream processing . . . . .	89
6.6.2	Selective alcohol oxidation as alternative anode reaction . . . . .	93
<b>7</b>	<b>Results and Discussion</b>	<b>97</b>
7.1	Reproducibility . . . . .	99
7.1.1	Reproducibility of galvanostatic experiments . . . . .	99
7.1.2	Reproducibility of polarization curves and double layer capacitance . . . . .	102



---

7.2	Investigations on the catalyst . . . . .	105
7.2.1	Type of catalyst . . . . .	105
7.2.2	Synthesis parameters for tin oxide based catalysts . . . . .	110
7.2.3	Tin oxide loading . . . . .	111
7.3	Investigations on process conditions . . . . .	117
7.3.1	The effect of temperature . . . . .	117
7.3.2	Effects of the electrolyte . . . . .	125
7.3.3	Requirements for reactant and electrolyte purity . . . . .	137
7.4	Further optimization of the electrode's matrix . . . . .	143
7.4.1	Influence of preparation parameters . . . . .	143
7.4.2	Fine tuning the electrode's hydrophobicity . . . . .	143
7.5	Merging single parameter optimizations . . . . .	147
7.6	Temporal behavior . . . . .	149
7.6.1	Long-term stability . . . . .	149
7.6.2	Transient behavior . . . . .	154
7.7	Scale-up . . . . .	161
7.7.1	Scale-up of the catalyst synthesis . . . . .	161
7.7.2	Scale-up of the electrode preparation . . . . .	161
7.7.3	Scale-up of the electrochemical cell . . . . .	163
7.8	Process concepts . . . . .	171
7.8.1	Coupling carbon dioxide electrolysis with bipolar membrane electrodialysis . . . . .	171
7.8.2	Coupling carbon dioxide reduction with selective alcohol oxidation . . . . .	179
<b>8</b>	<b>Conclusion and Outlook</b>	<b>183</b>
8.1	Conclusion . . . . .	183
8.2	Outlook . . . . .	187
<b>9</b>	<b>Appendix</b>	<b>211</b>
9.1	Carbon dioxide reduction reaction - Standard potential calculation . . . . .	213
9.2	Preparation methods - Additional derivations . . . . .	215
9.2.1	Preparation of the supported catalyst . . . . .	215
9.2.2	Preparation of gas diffusion electrodes . . . . .	216
9.3	Electroanalytical methods - Supporting explanations . . . . .	217
9.4	Investigations on the catalyst . . . . .	220

## Contents

---

9.4.1	Type of catalyst . . . . .	220
9.4.2	Tin oxide loading - Estimations on the quantity of metallic tin . . . . .	222
9.5	Investigations on process conditions . . . . .	223
9.5.1	The effect of temperature . . . . .	223
9.5.2	Concentration effects . . . . .	224
9.5.3	Electrolyte purity . . . . .	225
9.6	Temporal behavior - Long-term stability . . . . .	227
9.7	Process concepts . . . . .	228
9.7.1	Operating carbon dioxide electrolysis in the recycled product mixture . . . . .	228
9.7.2	Coupling carbon dioxide reduction with selective alcohol oxidation . . . . .	229

## Listings

**Table 1:** List of abbreviations.

Abbreviation	Description
AB	acetylene black
ABS	acrylonitrile butadiene styrene
ACS	American Chemical Society
AEM	anion exchange membrane
AOR	alcohol oxidation reaction
AsB	angle selective backscattered electron
ATR-IR	attenuated total reflection infrared spectroscopy
ATR-SEIRAS	attenuated total reflectance surface-enhanced infrared absorption spectroscopy
BPED	bipolar membrane electrodialysis
BPM	bipolar membrane
CB	carbon black
$C_{DL}$	double layer capacitance
CE	counter electrode
CEq	chemical equation
CEM	cation exchange membrane
CI	current interrupt
CL	catalytic layer
CO	carbon monoxide
CO <sub>2</sub> EL	CO <sub>2</sub> electrolysis
CO <sub>2</sub> RR	CO <sub>2</sub> reduction reaction
CV	cyclic voltammetry
DC	direct current
DD	double-distilled
DFAFC	direct formic acid fuel cell
DFFC	direct formate fuel cell

---

Abbreviation	Description
DFT	density functional theory
DI	deionized
DLR	German Aerospace Center, Stuttgart, Germany (dt. Deutsches Zentrum für Luft- und Raumfahrt)
EC	electrical connection
ECE	energetic cathode efficiency
ECSA	electrochemical active surface area
EDL	electrical double layer
EE	energy efficiency
EIS	electrochemical impedance spectroscopy
FA	formic acid
CA	carbonic acid
FE	faradaic efficiency
FID	flame ionization detector
GC	gas chromatography
GDE	gas diffusion electrode
GDL	gas diffusion layer
GHG	green house gas
GLS	gas-liquid separator
GWP	global warming potential
HER	hydrogen evolution reaction
HPLC	high performance liquid chromatography
ICP-OES	inductively coupled plasma optical emission spectroscopy
IHP	inner Helmholtz plane
ITC	Institute of Technical Chemistry, University of Stuttgart, Germany
KESD	polyethylene[polystyrenesulfonic acid-co-divinylbenzene]
LSV	linear sweep voltammetry
MFC	mass flow controller
MFM	mass flow meter

---

---

Abbreviation	Description
MOR	methanol oxidation reaction
MPI	Max Planck institute, Stuttgart, Germany
NBR	nitrile butadiene rubber
OC	outer connection
OCP	open circuit potential
OER	oxygen evolution reaction
OHP	outer Helmholtz plane
ORR	oxygen reduction reaction
p.a.	proanalysis
PEEK	polyether ether ketone
PEM	polymer electrolyte membrane
ph. Eur.	European Pharmacopoeia (fr. Pharmacopoeia Europaea)
PMMA	poly(methyl methacrylate)
PTFE	poly(tetrafluoroethylene)
RDE	rotating disk electrode
RE	reference electrode
RID	refractive index detector
SDS	sodium dodecyl sulfate
SEM	scanning electron microscopy
SHE	standard hydrogen electrode
TCD	thermal conductivity detector
TEM	transmission electron microscopy
TGA	thermogravimetric analysis
VBA	Excel's visual basic for applications
VX	Vulcan XC 72
WE	working electrode
XAS	X-ray absorption spectroscopy
XES	X-ray emission spectroscopy
XRD	X-ray diffraction

---

**Table 2:** List of symbols.

Symbol	Description	Unit
$\alpha$	activity coefficient	-
$\alpha_s$	symmetry factor	-
$\Delta_f H^\theta$	standard formation enthalpy	$\text{kJ mol}^{-1}$
$\Delta_R G^\theta$	standard Gibb's free energy	$\text{kJ mol}^{-1}$
$\Delta_R H^\theta$	standard reaction enthalpy	$\text{kJ mol}^{-1}$
$\Delta_R S^\theta$	standard reaction entropy	$\text{J mol}^{-1} \text{K}$
$S^\theta$	standard entropy	$\text{J mol}^{-1} \text{K}$
$\eta$	overpotential	V
$\kappa$	electrical conductivity	$\text{S m}^{-1}$
$\lambda$	wavelength	m
$\rho$	density	$\text{g m}^{-3}$
$\rho_r$	resistivity	$\Omega \text{ m}$
$\sigma$	loading	$\text{g m}^{-2}$
$\Phi$	volume fraction	-
$\varphi$	electric potential	V
$\varphi_H$	Helmoltz layer potential	V
$\varphi_p$	porosity	-
$A$	area	$\text{m}^2$
$c$	concentration	M
$C$	capacitance	$\text{F m}_{\text{geo}}^{-2}$
$C_g$	conversion factor	-
$D$	diffusion coefficient	$\text{m}^2 \text{s}^{-1}$
$d$	distance	m
$\bar{d}$	mean diameter	m
$E$	electrical energy	W s
$ECE$	energetic cathode efficiency	%
$EE$	energetic efficiency	%

Symbol	Description	Unit
$FE$	faradaic efficiency	%
$f$	CO <sub>2</sub> excess factor	-
$f_{\text{mixture}}$	mixing factor	-
$I$	current	A
$j$	current density	A m <sup>-2</sup>
$k$	reaction rate constant	s <sup>-1</sup>
$k_m$	mass transfer coefficient	s <sup>-1</sup>
$l$	length	m
$m$	mass	g
$M$	molar mass	g mol <sup>-1</sup>
$n$	molar amount of substance	mol
$p$	pressure	Pa
$P$	electric power	W
$q$	electric charge	C
$R$	resistance	Ω
$r$	reaction rate	mol s <sup>-1</sup>
$S$	solubility	mol L
$T$	temperature	°C
$t$	time	s
$V$	voltage	V
$V_f$	volume	L
$\dot{V}_F$	volumetric flow rate of converted CO <sub>2</sub> according to Faraday's law	L s <sup>-1</sup>
$\dot{V}_f$	volumetric flow rate	L s <sup>-1</sup>
$V_m$	molar volume	L mol <sup>-1</sup>
$\nu$	stoichiometric factor	-
$w$	mass fraction	-
$z$	number of transferred electrons	-

**Table 3:** List of indices.

Index	Description
$\Omega$	ohmic
A	anode
A spec.	area specific
ad	adsorbed
AM	anode to membrane
AR	anode to reference electrode
aq	solved in water
C	cathode
CB	carbon black
CM	cathode to membrane
CR	cathode to reference electrode
CT	charge transfer
diff	diffusion
DL	double layer
eff	effective
el	electrolyte
F	Faraday
FA	formic acid



---

Index	Description
g	gaseous
geo	geometrical
GSE	galvanostatic electrolysis
intr	intrusion
IR	<i>IR</i> compensated
lim	limiting
M	membrane
max	maximum
Me	metal
min	minimum
mix	mixed
ox	oxidation/oxidized/oxidized form
p	particle
prec	precursor
red	reduction/reduced form
res	residue
ZC	zero charge

---

**Table 4:** List of constants.

---

Constant	Value	Unit	Description
<i>F</i>	96485.3	A s mol <sup>-1</sup>	Faraday constant
<i>R</i>	8.314	JK <sup>-1</sup> mol	Gas constant

---



# 1 | Abstract

To date, the very basis of the vast majority of chemical products, fuels and energy is fossil based. Especially chemical industry is often bound to such resources due to a lack of alternatives or for economical reasons. In order to be able to move from fossil fuel consumption towards a more sustainable, carbon neutral supply new processes need to be established. This includes not only replacing carbon dioxide (CO<sub>2</sub>) emitting ones, but also developing such processes that use this green house gas as carbon resource.

Besides thermocatalytically activated conversion processes, the electrochemical reduction of CO<sub>2</sub> to value-added products recently gained a lot of interest. The basic idea is to convert CO<sub>2</sub> in highly concentrated exhaust gas streams with renewable electric power. Depending on the applied catalyst different products including formate/formic acid, oxalic acid, methane, light alcohols, carbon monoxide or synthesis gas are reported. All these products represent platform chemicals for numerous upstream processes.

The present work focuses on the development of an energy efficient electrolysis process that converts CO<sub>2</sub> into formate salts or formic acid at high current density. In contrast to the huge amount of research that focuses on catalyst development, systematic variations of reaction conditions like temperature, gas feed purity or electrolyte composition are far less reported. They were investigated with the aim of enhancing the energetic efficiency of formate formation. The thereby used gas diffusion electrode (GDE) is also a unique type of electrode that is barely reported for CO<sub>2</sub> reduction reaction (CO<sub>2</sub>RR) to formate, which was further optimized to reach, to date, unreported current densities of up to  $-1500 \text{ mA cm}^{-2}$ . The focus was thereby not only set to maximize said current densities but also to allow for industrial relevant lifetimes. The obtained insights were then used to scale up the cell from  $1 \text{ cm}^2$  to  $10 \text{ cm}^2$  and finally to  $70 \text{ cm}^2$  of geometrical electrode surface.

Regarding the reaction conditions, an unexpected dependency of the limiting current density on temperature was found. In contrast to literature, which consistently suggests lower operating temperatures to enhance CO<sub>2</sub> solubility, an optimum performance at 50 °C was observed. This value can be explained by the contrary development of CO<sub>2</sub> solubility and diffusivity with temperature leading to a maximum

in mass transport at said temperature. Experimental data and calculations from a simple model support this explanation. On top of that, the used type of GDE shows a limitation in product mass transport for certain conditions that, to the best of the author's knowledge, has not been reported yet. One of the view notable influences of the used electrolyte on CO<sub>2</sub>RR was attributed to the applied cation. Alkali metal ions with a large ionic radius increased the electrode's activity significantly and allowed for a longer lifetime in the straightforward order of Na<sup>+</sup> < K<sup>+</sup> < Rb<sup>+</sup> < Cs<sup>+</sup>. However, due to relatively high material costs for salts other than sodium based ones, cation recovery needs to be established in a final process. Highly concentrated mixtures of formate and bicarbonate salts were found to be unsuitable, mainly due to a strong product mass transport limitation and excessive CO<sub>2</sub> gas formation inside the GDE. Both aspects cause a strong shift of selectivity in favor of hydrogen formation. On the other hand, the type of anion or other specifications like pH (7 to 14) and salt concentration (0.1 M to 2 M) showed no notable influence.

Instead of using a typical multi-layered GDE design with a more distinct spatial separation of gas and liquid phase, a homogeneous single-layer design was used. A bimodal pore structure of specific hydrophobicity allows for an efficient CO<sub>2</sub> transport through open macropores towards a large number of liquid filled pores. The latter are formed by carbon agglomerates bearing the electrocatalyst, which was investigated regarding the type of metal/metal oxide, loading and synthesis method. Tin oxide was confirmed to be the material of highest energetic efficiency, even though there are more active or selective alternatives. Due to the potentiostatic character of tin oxide and a loading dependent deactivation, a tin loading of 0.5 mg cm<sub>geo</sub><sup>-2</sup> was found to be best suited for long-term operation, while a higher loading of 7.5 mg cm<sub>geo</sub><sup>-2</sup> allows for the highest activity in short-term operation. Deactivation effects were investigated even though the causes could not be identified or quantified with absolute certainty. During short-term operation the optimized cathode side can be operated with as little as -620 mV of *IR* compensated overpotential at a current density of -200 mA cm<sup>-2</sup>. This represents a top value compared to literature (up to August 2019).

Partly exchanging the poly-(tetrafluoroethylene) (PTFE) binder with Nafion significantly increased the limiting current density. It is suspected that a local increase in hydrophilicity results in an extended amount of wetted agglomerates while the highly hydrophobic gas transport pores remain open. A GDE matrix composition of 15:20:65 Nafion:PTFE:Acetylene Black was found to be optimal. Combining this matrix with an increased electrode loading of 2 mg cm<sub>geo</sub><sup>-2</sup> and the best performing electrolyte ([CsCl] = 2 M, pH = 10) yielded a current density of -1500 mA cm<sup>-2</sup> at 79 % of formate selectivity and -900 mV of *IR* compensated overpotential.

---

During long-term operation, long diffusion pathways for the formed product, reduction of the electrocatalytically active species and a mechanical degradation of the GDE were found to limit the time on stream. Target-oriented adjustments in the electrode's composition prolonged the lifetime from 24 h to 250 h. Furthermore, an observed shift from CO<sub>2</sub> reduction to hydrogen formation is caused by reduction of the electrocatalytically active tin oxide to metallic tin. Here, the selectivity was partly recovered by periodically applying a slight oxidative polarization.

The gained insights were used to perform an energy efficient scale-up of the cell with completely revised geometry and components. A filter press type cell with minimized electrode distance, effective electric contacting and oxygen bubble removal was designed and fabricated. It reaches a total cell voltage of 2.7 V to 3.0 V at a current density of 200 mA cm<sup>-2</sup> and a total current of 14 A (active electrode area = 70 cm<sup>2</sup>). This corresponds to an energy efficiency of 26 % to 23 % and again represents a top value compared to literature (up to August 2019).

Finally, new process concepts are examined on a basic level. First, a bipolar membrane electro dialysis (BPED) cell is investigated for potential coupling with CO<sub>2</sub> electrolysis (CO<sub>2</sub>EL). Such process can be used for downstream protonation of formed formate, product purification and concentration, as well as for metal hydroxide regeneration. Results will demonstrate its general functionality but, until now, dialysis is limited to low formic acid concentrations of 0.5 M to 1 M. Trying to assess higher concentrations than that results in high diffusion losses of uncharged formic acid through adjoining membranes. Second, selective alcohol oxidation is evaluated for its potential to replace the hitherto used oxygen evolution reaction (OER). Using a nickel mesh anode yielded an anodic formate formation with 86 % selectivity at -200 mA cm<sup>-2</sup>.



## 2 | Zusammenfassung

Bis heute basiert der Großteil der Produktion von chemischen Produkten, Kraftstoffen und Wärme auf fossilen Rohstoffen. Speziell die chemische Industrie ist dabei oft, aufgrund mangelnder Alternativen oder aus ökonomischen Gründen, auf solch fossile Rohstoffe angewiesen. Um in der Lage zu sein auf eine nachhaltigere, kohlenstoffneutrale Produktion umschwenken zu können, müssen neue Prozesse etabliert werden. Dies beinhaltet nicht nur den Ersatz von Kohlendioxid ( $\text{CO}_2$ ) emittierenden Prozessen, sondern auch die Entwicklung von solchen, die  $\text{CO}_2$  als Kohlenstoffquelle nutzen.

Neben thermokatalytisch aktivierten Umwandlungsprozessen hat die elektrochemische Reduktion von  $\text{CO}_2$  zu höherwertigen Produkten kürzlich deutlich an Interesse gewonnen. Die grundlegende Idee ist,  $\text{CO}_2$  aus hochkonzentrierten Abgasströmen mittels Strom aus erneuerbaren Energien umzusetzen. Abhängig vom verwendeten Katalysator sind dabei unterschiedliche Produkte zugänglich, wie zum Beispiel Formiat/Ameisensäure, Oxalsäure, Methan, kurzkettige Alkohole, Kohlenmonoxid oder Synthesegas. All diese Produkte stellen Plattformchemikalien für zahlreiche weiterführende Prozesse dar.

Die vorliegende Arbeit befasst sich mit der Entwicklung eines energieeffizienten Elektrolyseprozesses, der  $\text{CO}_2$  zu Formiatsalzen, bzw. ferner Ameisensäure, bei hohen Stromdichten umwandelt. Im Gegensatz zu den zahlreichen Forschungsarbeiten, die sich mit der Entwicklung neuer Katalysatoren beschäftigen, sind systematische Untersuchungen von Reaktionsbedingungen, wie Temperatur,  $\text{CO}_2$ -Reinheit oder Elektrolytzusammensetzung, deutlich weniger beschrieben. Solche Reaktionsbedingungen wurden mit dem Ziel untersucht, die Energieeffizienz der Formiat/Ameisensäureproduktion zu steigern. Die dabei verwendeten Gasdiffusionselektroden (GDEs) bilden einen einzigartigen Typ Elektrode, der bisher für die  $\text{CO}_2$  Reduktionsreaktion ( $\text{CO}_2\text{RR}$ ) zu Formiat kaum berichtet und im Laufe dieser Arbeit weiter optimiert wurde. Damit wurden bisher unveröffentlichte Stromdichten von bis zu  $-1500 \text{ mA cm}^{-2}$  erreicht. Der Fokus der Entwicklung wurde dabei nicht nur auf die Maximierung der Stromdichte gelegt, sondern auch darauf industriell relevante Standzeiten zu erreichen. Die gewonnenen Erkenntnisse wurde dann verwendet, um die Elektrolysezelle schrittweise von  $1 \text{ cm}^2$  auf  $70 \text{ cm}^2$  an geometrischer Kathodenoberfläche hochzuskalieren.

Im Hinblick auf die untersuchten Reaktionsbedingungen wurde eine unerwartet starke Abhängigkeit der limitierenden Stromdichte von der Temperatur beobachtet. Im Gegensatz zur Literatur, welche konsistent möglichst geringe Temperaturen empfiehlt um die CO<sub>2</sub> Löslichkeit zu erhöhen, wurde eine optimale Temperatur von 50 °C bestimmt. Dieser Wert kann durch die entgegengesetzten Abhängigkeiten der CO<sub>2</sub> Löslichkeit und des CO<sub>2</sub> Diffusionskoeffizienten von der Temperatur erklärt werden, was zu einem Maximum an CO<sub>2</sub> Massentransport bei der genannten Temperatur führt. Experimentelle Daten und Berechnungen aus einem einfachen Modell unterstützen diese Erklärung. Zudem zeigt der verwendete Typ GDE für bestimmte Reaktionsbedingungen eine Produkt-Massentransportlimitierung welche, nach dem besten Wissen des Autors, für diese Reaktion bisher noch nicht beschrieben wurde. Einer der wenigen merklichen Einflüsse des Elektrolyten auf die CO<sub>2</sub>RR bezieht sich auf die Wahl des Kations. Alkali-metallionen mit großem Ionenradius erhöhten die Elektrodenaktivität signifikant und erlaubten deutlich längere Standzeiten in der Reihenfolge Na<sup>+</sup> < K<sup>+</sup> < Rb<sup>+</sup> < Cs<sup>+</sup>. Allerdings müsste durch die in analoger Reihenfolge ebenso ansteigenden Materialkosten eine Kationenrückgewinnung im finalen Prozess stattfinden. Hochkonzentrierte Mischungen von Formiat- und Bicarbonatsalzen wurden als ungeeignet bewertet, da sie zu einer starken Produktdiffusionslimitierung und übermäßiger CO<sub>2</sub>-Gasbildung innerhalb der GDE führen. Beide Aspekte bewirken eine Verschiebung der Selektivität hin zu einer verstärkten Wasserstoffbildung. Hingegen zeigten andere Arten von Anionen, sowie Unterschiede im pH Wert (7 - 14) oder der Salzkonzentration (0.1 M - 2 M) keinen nennenswerten Einfluss.

Im Gegensatz zu den typischerweise verwendeten, mehrschichtigen GDEs, welche eine deutlichere räumliche Trennung von Gas- und Flüssigphase zeigen, wurden in der vorliegenden Arbeit homogene, einschichtige GDEs verwendet. Eine bimodale Porenstruktur mit spezifischer Hydrophobizität ermöglicht dabei eine starke Verzahnung von Gastransport- und flüssigkeitsgefüllten Poren. Letztere werden durch Kohlenstoffagglomerate geformt die den Elektrokatalysator tragen. Dieser wurde hinsichtlich des verwendeten Metalls/Metalloxids, der Beladung und seiner Synthesemethode untersucht. Zinnoxid wurde als der Elektrokatalysator mit der höchsten energetischen Effizienz bestätigt, obwohl es entweder aktivere oder selektivere Alternativen gäbe. Aufgrund des potentioselektiven Charakters von Zinnoxid und einer beladungsabhängigen Deaktivierung ergab sich eine Zinnbeladung von 0.5 mg cm<sub>geo</sub><sup>-2</sup> als bestgeeignet für den Langzeitbetrieb. Hingegen zeigte eine Zinnbeladung von 7.5 mg cm<sub>geo</sub><sup>-2</sup> die höchste Aktivität im Kurzzeitbetrieb von nur 30 min. Auftretende Deaktivierungseffekte wurden untersucht, wobei die zugrundeliegenden Effekte nicht mit absoluter Sicherheit identifiziert oder gar quantifiziert werden konnten. Im Kurzzeitbetrieb kann die optimierte GDE mit nur -620 mV an *IR*-kompensiertem Überpotential bei einer Stromdichte von -200 mA cm<sup>-2</sup> betrieben werden, was einem im Vergleich zur vorhandenen Literatur (Stand August 2019) Spitzenwert entspricht.



---

Ein teilweiser Austausch des verwendeten Polytetrafluorethylen (PTFE) Bindemittels durch Nafion ergab eine deutliche Steigerung der limitierenden Stromdichte. Es wird vermutet, dass eine Erhöhung der lokalen Hydrophilie die Anzahl benetzter Agglomerate steigert, ohne dabei die nötigen CO<sub>2</sub> Transportporen zu fluten. Eine Matrixzusammensetzung von 15:20:65 an Nafion:PTFE:Acetylene Black wurde dabei als optimal befunden. Die Kombination dieser optimierten Matrix mit einer erhöhten Beladung von 2 mg cm<sub>geo</sub><sup>-2</sup> und der Verwendung des besten Elektrolyts ([CsCl] = 2 M, pH = 10) ermöglichte eine Stromdichte von -1500 mA cm<sup>-2</sup> bei 79 % Formiat Selektivität und nur -900 mV an *IR*-kompensiertem Überpotential.

Im Langzeitbetrieb wurden die langen Diffusionswege für das Produkt Formiat, eine Reduktion des aktiven Metalloxides und eine mechanische Degradation der GDE als limitierende Faktoren für die maximale Betriebsdauer festgestellt. Eine Anpassungen der Elektrodenzusammensetzung verlängerte die Betriebsdauer dabei von 24 h auf 250 h. Weiter wurde festgestellt, dass die Reduktion des Metalloxides für eine Verschiebung des Produktspektrums weg von CO<sub>2</sub>RR Produkten hin zur Wasserstoffbildung verantwortlich ist. Hier konnte die Selektivität durch Regeneration des Katalysators mittels periodischer Rückoxidation über geringe anodische Polarisierung teilweise wieder hergestellt werden.

Die während dieser Arbeit gewonnen Erkenntnisse wurden schließlich dazu verwendet, die verwendete Elektrolysezelle unter Berücksichtigung der maximalen Energieeffizienz hochzuskalieren. Eine komplett überarbeitete Geometrie im Filter-Press-Stil mit optimierten Komponenten erlaubt eine deutliche Minimierung des Elektrodenabstands, die effiziente elektrische Kontaktierung, sowie eine verbesserte Sauerstoffabfuhr. Die Zelle erreicht dabei Zellspannungen zwischen 2.7 V und 3 V bei einer Stromdichte von 200 mA cm<sup>-2</sup> und einem Gesamtstrom von 14 A (geometrische Elektrodenfläche = 70 cm<sup>2</sup>). Dies bedeutet eine Energieeffizienz zwischen 26 % und 23 % und entspricht im Vergleich zur bisherigen Literatur (Stand August 2019) ebenso einem Spitzenwert.

Letztlich wurden neue Prozesskonzepte als Proof-of-Concept Studien untersucht. Dazu zählt zum einen eine mögliche Kopplung von CO<sub>2</sub>-Elektrolyse und Bipolarmembran Elektrodialyse. Solch ein nachgeschalteter Dialyseprozess kann dazu verwendet werden in der Elektrolyse gebildetes Formiat zu protonieren, Produktströme aufzureinigen und anzureichern, sowie verbrauchtes Alkalimetallhydroxid zurückzugewinnen. Die generelle Funktion der Bipolarmembran Elektrodialyse wurde bestätigt, ist aber noch durch die zur Verfügung stehenden Membranen und die damit verbundene hohe Diffusionsrate der Ameisensäure auf geringe Ameisensäurekonzentrationen von 0.5 M bis 1 M begrenzt. Zum anderen wurde die selektive Alkoholoxidation als Anodenreaktion bzw. als Ersatz für die bisher verwendete Sauerstoffbildungsreaktion untersucht. Unter Verwendung eines Nickelkatalysators wurde anodenseitig die Bildung von Formiat mit einer Selektivität von 86 % bei einer Stromstärke von 200 mA cm<sup>-2</sup> beobachtet.



## 3 | Introduction

Within the last hundred years consumption of fossil-based resources rose in an exponential manner. To date, chemical industry, electricity production and the transportation sector are the biggest consumers.<sup>[1]</sup> The related emission of CO<sub>2</sub> is thereby well known to be a major cause of climate change, induced by excessive green house gas (GHG) emission. Even though CO<sub>2</sub> has the lowest global warming potential (GWP) of all GHGs defined in the Kyoto protocol, its sheer mass of emission makes it the major cause.<sup>[2]</sup> Compared to the year 1990, atmospheric CO<sub>2</sub> concentration in 2018 has already risen by around 16 % to 407 ppm.<sup>[3]</sup> As a consequence, average global temperature increased by around 0.5 °C compared to 1990 and by around 1 °C compared to 1950 with effects already being noticeable.<sup>[4]</sup>

For the last decades, awareness for the excessive emission of green house gases like CO<sub>2</sub> strongly rose, not only among scientists but also in the public and among business stakeholders. Interest for and emphasis on products being produced sustainably increased along with that. However, in light of the current fossil-based industry, it becomes obvious that new sustainable and competitive pathways need to be developed. A carbon neutral economy should not only be addressed by reducing the amount of CO<sub>2</sub> emissions but also by utilizing this GHG as a feedstock to produce value-added substances.

At the same time, renewable energy sources have a continuously rising share in the electricity production.<sup>[5]</sup> However, their fluctuating nature leads to periods of excess and deficit, which limits their share for a stable power supply. Thus, renewable energies require large-scale storage solutions. A promising and intensively studied pathway addressing both, CO<sub>2</sub> conversion and energy storage, is the electrochemical reduction of CO<sub>2</sub> using excess electricity. The obtained products can be stored and used for time-delayed power recovery e.g. in fuel cells.<sup>[6]</sup> Different products including formic acid, alcohols and light aliphatic hydrocarbons are reported that can suit this purpose.

Among multiple products that are accessible by electrochemical reduction of CO<sub>2</sub>, CO (or synthesis gas) and formic acid have been shown to be producible with industrial relevant selectivity, energy efficiency, current density and long-term stability.<sup>[7]</sup> Both products are produced by a two-electron transfer process, which explains their easy accessibility. While CO or synthesis gas are of specific interest for

synthetic fuel production via the Fischer-Tropsch process, applications for formic acid are of broader range. Besides its use in non-chemical industries such as dyeing, textile and leather processing,<sup>[8]</sup> it could be used as fuel<sup>[6]</sup> or feedstock for further upgrading<sup>[9]</sup>.

Formic acid and formate are both described as fuels utilized in a direct formic acid or direct formate fuel cell (DFAFC or DFFC). However, some major issues within such devices prevail. In DFAFC CO is a hardly suppressed side product which deactivates the noble metal catalyst. Also, the high volumetric energy density of concentrated formic acid comes along with the downside of a strong corrosivity. In DFFC, corrosivity of the fuel and CO evolution are widely eliminated but the low energy density of an aqueous formate solution limits its application to stationary ones.<sup>[6]</sup> More promising would be a downstream upgrading step to higher hydrocarbons. Formatotrophic microbes have been shown to be able to convert formic acid into a variety of different fuels, chemicals or even long chain molecules. To name a few examples ethanol, isobutene, propane, acetone, fatty acids or proteins are reported.<sup>[9-11]</sup>

For applications in chemical industry, formic acid can be used as save and transportable source of carbon monoxide and/or hydrogen e.g. for carbonylation,<sup>[12]</sup> hydrogenation<sup>[13]</sup> or hydrocarboxylation<sup>[14]</sup> reactions. Also, formic acid can be decomposed to either hydrogen or CO, depending on the catalyst and reaction conditions used.<sup>[15, 16]</sup> This fact makes it a safe and transportable precursor for decentralized hydrogen, synthesis gas or CO production.

Electrochemical reduction of CO<sub>2</sub> to various products has recently experienced a boost in attention. Most of the investigations are focusing on the catalyst itself with all kinds of concepts, including metal/metal oxide or alloy based systems, organometallic or single-site and structured catalysts.<sup>[17, 18]</sup> Even though some catalyst systems have been shown to exhibit high activity and/or selectivity, their limited stability or material costs often exclude them from industrial applications.<sup>[17]</sup> The high overpotential necessary for CO<sub>2</sub>RR at sufficiently high current densities remains challenging with energy efficiencies barely exceeding 30 %. So far, simple nano-structuring of earth abundant metals like tin seems the best option for industrialization.<sup>[17]</sup>

Another major subject of investigation is the transfer to electrode systems that allows access to industrial relevant current densities. Gas diffusion electrodes (GDEs) must be mentioned as the by far most common system for this task. Their optimization is of highly complex nature and requires controlling the electrode's composition, while considering multiple aspects of reaction conditions. With such optimized electrodes, results can then be transferred into continuous mode of operation and into scaled-up electrolyzers.<sup>[17-19]</sup>

---



## 4 | Theoretical Background

Within this chapter important basics of electrochemistry, CO<sub>2</sub> reduction reaction (CO<sub>2</sub>RR) and gas diffusion electrodes (GDEs) are discussed. The electrochemical background includes basic concepts of electrified solid/liquid interfaces and respective descriptions of thermodynamics, kinetics and quantitative relationships. In contrast to these long-known fundamentals, CO<sub>2</sub>RR with application of GDEs is a rather novel field of research. Literature results regarding important parameters like electrode composition or reaction conditions are therefore summarized. Finally, a short outlook into a conceivable process concept and alternative anode reactions are provided.

### 4.1 Electrochemical basics

Electrochemical reactions in general can be divided into two main classes. One are those in a galvanic element, being spontaneous redox reactions to provide electrical energy. Most known examples here are batteries and fuel cells. The second class are reactions of redox active compounds, which consume electric power and produce substances of higher energy content. Excluding batteries, the respective electrochemical cell is then called an electrolyzer. Characteristic for both classes is the local separation of reduction and oxidation reaction, as well as of electron and mass transport, enabling the storage or supply of electric power. The present work focuses on the second class to store electrical energy in form of formate/formic acid. Therefore, no detailed discussion of galvanic elements shall be given here.

During electrolysis endergonic redox reactions are forced to proceed by an external direct current (DC). As for this fact, the standard Gibb's free energy ( $\Delta_R G^\theta$ ) is positive and the standard cell voltage is defined as being negative. For most applications such an electrochemical cell is composed of two parts, an anode and a cathode side, often divided by a separator (see figure 4.1). Electrons are conducted through an outer circuit from the anode, where the oxidation reaction takes place (positively polarized), to the cathode side, where the reduction reaction takes place (negatively polarized). A separator in between allows charge balancing while keeping anolyte and catholyte apart to avoid contamination or

re-oxidizing and re-reduction of formed products. In general, three different types of separators are available. While anion exchange membranes (AEMs) and cation exchange membranes (CEMs) are selective to the respective ion, diaphragms allow an unspecific transport.<sup>[20]</sup>

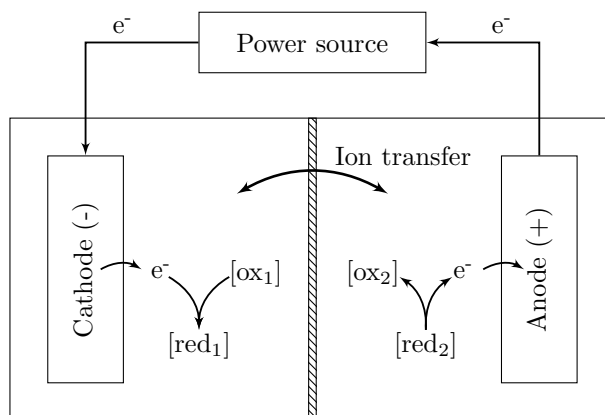
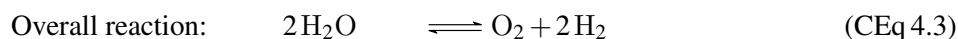
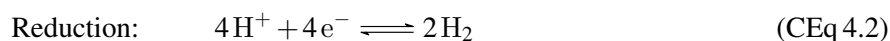
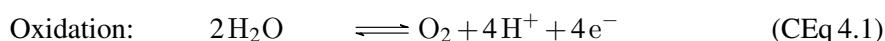


**Figure 4.1:** Schematic illustration of an electrolysis cell.

One of the seemingly easiest examples is electrolytic water splitting under acidic conditions. The overall reaction, represented by the chemical equation (CEq), (CEq 4.3) is separated into an anodic oxidation (CEq 4.1) and a cathodic reduction (CEq 4.2). At the positively polarized anode water is split into molecular oxygen, protons and electrons. While the produced oxygen remains in or can be released from the anode compartment, electrons are transferred through the outer electrical circuit to the negatively polarized cathode. Produced protons can move through the CEM or diaphragm and are reduced to hydrogen. Reaction (CEq 4.3) has a  $\Delta_R G^\theta$  of  $-237.13 \text{ kJ mol}^{-1}$ , which corresponds to a standard cell voltage of  $-1.23 \text{ V}$ .<sup>[20]</sup>



### 4.1.1 The electrical double layer

Whenever an electronic conductor comes into contact with an ionic conductor redox reactions take place, forming a potential difference at the phase boundary. This applies to the two electrodes of an electrochemical cell, which are both in contact with the ion conducting electrolyte. These two solid-liquid interfaces are of special importance as they represent the location where the electrochemical conversion takes place. Considering a metal electrode in contact with an electrolyte the isotropic character of the bulk liquid phase is interrupted, inducing an orientation of solvent dipoles and charged species by inter-



actions with the solid phase. This orientation of dipoles and charges results in an electrification of the electrolyte close to the phase boundary. In addition, the mobile electrons in the solid metal phase react to this electrification by moving towards the boundary. The formed parallel layers of ions in the solid phase and counter ions in the liquid phase are the origin of the term electrical double layer (EDL).<sup>[21]</sup> This separation of charges results in a measurable potential difference  $\varphi$ . During electrolysis the potential difference is enforced by the outer circuit electronics, controlling the excess charge in the solid phase.

An illustration of this electrified interface and the corresponding course of electric potential is given in figure 4.2. Since the solid electrode is usually highly conductive it cannot sustain an electric field inside itself. Any excess charge is therefore residing with maximum distance to other electrons at the surface. The first liquid phase mono-layer in contact with the charged electrode surface is mainly consisting of solvent dipole molecules, while the second mono-layer is occupied by solvated ions of opposite charge. The latter is called outer Helmholtz plane (OHP). In this simplest model, introduced by and named after H. v. Helmholtz, the amount of charge in the OHP is equal to the excess charge of the solid electrode and the absolute value of potential decreases linearly to zero (model a) in figure 4.2). This structure of two parallel planes of opposite charge can be seen as a classical plate capacitor. The Helmholtz model, however, was not able to explain the observed dependence of capacitance upon the electrode potential. L. Gouy and G. Chapman came up with a model that was based on the idea that charge carriers, in contrast to the fixed electrode surface charges, exist in a diffusive layer (model b) in figure 4.2). Ions in the vicinity of an electrode are not only influenced by electrostatic forces but also by thermal movements. Due to the decreasing influence of the electrode, counter charge concentration is the highest close to the phase boundary, dropping exponentially with increasing distance from the charged electrode surface. A simplification made in this theory was a point-charge assumption, allowing counter charges to approach the electrode surface arbitrary close. O. Stern dropped this approximation by defining a minimum distance from the electrode (model c) in figure 4.2). Basically, the Stern theory combines Helmholtz's and Gouy-Chapmann's ideas with some charges being fixed in a parallel mono-layer, similar to the OHP, and other being located in a diffusive layer. Thus, the absolute value of potential shows a linear disclaim turning into an exponential course.<sup>[21-23]</sup>

Although solvent molecules occupy the electrode, ions of contrary and equal charge may adsorb on the surface. The layer formed by the centers of these ions is called inner Helmholtz plane (IHP) and influences the potential difference depending on the type of ion adsorbed (model d) in figure 4.2). Electrode surface, IHP and OHP are also known as triple layer. However, not all ions are able to adsorb on the electrode. In order to allow for this process Gibb's free energy of adsorption has to be negative. First, solvent molecules have to be removed from the electrode's surface to free up space. Second, solvent

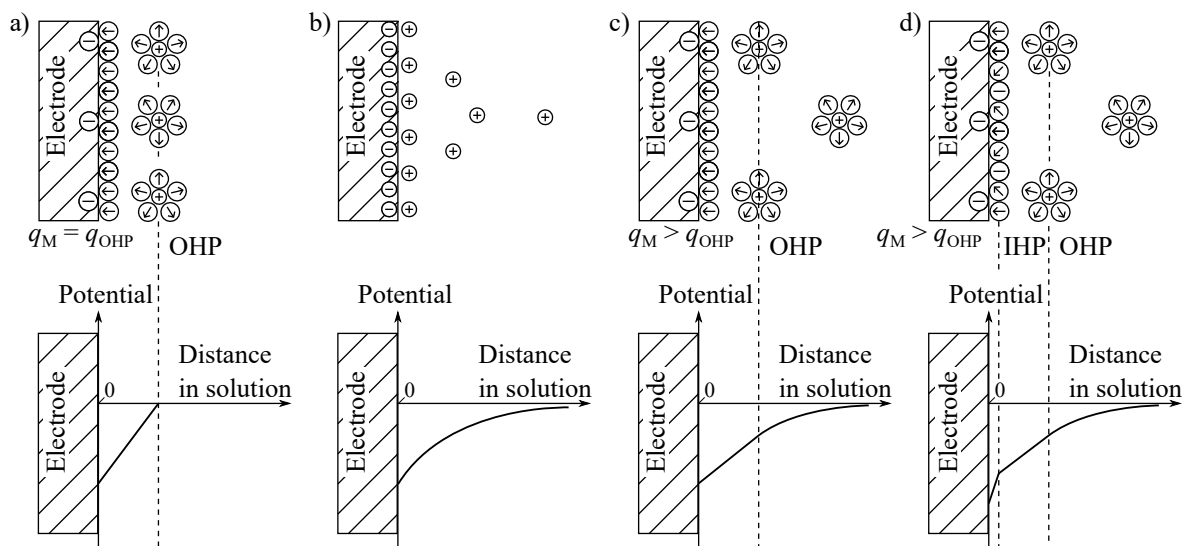


**Figure 4.2:** Illustration of different electrical double layer models and respective course of electric potential on a negatively polarized electrode.

a) Helmholtz model: a rigid plane model with equal charge amounts within the electrode ( $q_M$ ) and outer Helmholtz plane ( $q_{OHP}$ ) resulting a linear change in potential.

b) Gouy-Chapmann model: counter ions are represented by point-charges in a diffusive layer.

c) Stern Model: an extension of the rigid Helmholtz model by a diffusive layer.

d) Extension of the Stern model by adsorbed negative ions increasing the metal charge density.

Figure adapted from Bockris and Reddy.<sup>[21]</sup>

molecules in the ion hydration shell need to be stripped off before adsorption can take place. While changes in water-electrode interactions are positive, changes in ion-electrode interactions are negative. Ion-water interactions are therefore typically decisive whether the total change in Gibb's free energy of adsorption is negative or positive. Especially for weakly hydrated ions like iodide or cesium negative values can be obtained, allowing for adsorption.<sup>[21, 22]</sup>

#### 4.1.2 Cell voltage and electrode potentials

In order to force an endergonic electrochemical reaction to occur, a certain minimum voltage is necessary. Both half-cell reactions contribute to this voltage with their respective equilibrium potential  $\varphi^0$ , which depends on temperature, pressure and concentration of substances. When measured under standard conditions, meaning a temperature of 25 °C, reactant and product activities equal to 1 mol L<sup>-1</sup> as well as a partial pressure of 101.3 kPa, it is called the standard electrode potential  $\varphi^\theta$ . The cells standard voltage  $V^\theta$  and equilibrium voltage  $V^0$  is then given by:

$$V^\theta = \varphi_{\text{cathode}}^\theta - \varphi_{\text{anode}}^\theta \quad (4.1.1)$$

$$V^0 = \varphi_{\text{cathode}}^0 - \varphi_{\text{anode}}^0 \quad (4.1.2)$$

$V^\theta$  results from plain thermodynamics and can be calculated from the reaction's  $\Delta_R G^\theta$  as follows [20]:

$$V^\theta = -\frac{\Delta_R G^\theta}{zF} \quad (4.1.3)$$

Whereat  $z$  is the number of electrons transferred and  $F$  the Faraday constant ( $F = 96\,485.3 \text{ A s mol}^{-1}$ ). Individual electrode potentials cannot be measured, thus, comparing half-cell reactions requires a reference potential. Often the redox couple  $\text{H}^+/\text{H}_2$ , the so called standard hydrogen electrode (SHE), is used for this purpose with its defined  $\varphi^\theta$  of 0 V. Hence, recording half-cell potentials is typically done in a three electrode configuration illustrated in figure 4.3. The current is passed from working electrode (WE) to counter electrode (CE), while the voltage is measured between WE and reference electrode (RE). A high ohmic resistance prevents the flow of current between WE and RE.

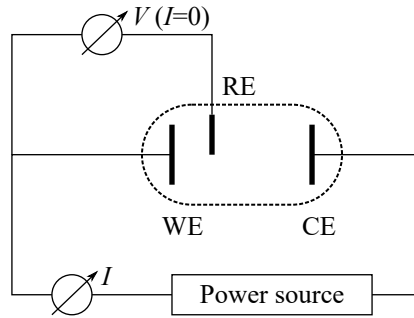


**Figure 4.3:** Electrode arrangement and points of measurement in a three electrode configuration. Figure adapted from V. Schmidt.[20]

The electrode potential is a state function only depending on temperature, concentration and pressure. In terms of differing temperatures the equilibrium potential is given by:[20]

$$\varphi^0(T) = \varphi^\theta + \left( \frac{d\varphi^0}{dT} \right)_{P,c} \cdot (T - T^\theta) \quad (4.1.4)$$

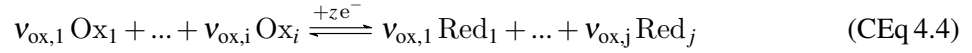
with:

$$\left( \frac{d\varphi^0}{dT} \right)_{P,c} = \frac{\Delta_R S}{zF} \quad (4.1.5)$$

Describing the dependency of reactant and product concentrations on the electrode potential is possible with the Nernst equation:[20]

$$\varphi^0 = \varphi^\theta + \frac{RT}{zF} \cdot \ln \frac{\prod_{k=1}^i \alpha_{\text{ox}, k}^{v_{\text{ox}, k}}}{\prod_{m=1}^j \alpha_{\text{red}, m}^{v_{\text{red}, m}}} \quad (4.1.6)$$

With  $\alpha$  being the activities of the components reacting according to the general redox reaction:



The present work focuses on the CO<sub>2</sub> electroreduction around ambient pressure, meaning a maximum of 20 mbar relative pressure. For this reason the influence of pressure on the electrode potential is neglected here since a  $\Delta p$  of 20 mbar (maximum over pressure obtained in all experiments) equals to a  $\Delta\phi^0$  of only 0.2 mV.

### 4.1.3 Kinetic aspects

The so far discussed electrode potentials and cell voltages exclusively consider thermodynamics, meaning all participating reactions are in equilibrium. Whenever a current is applied to this system certain reactions are accelerated and equilibria are disturbed. At the electrode-electrolyte interface electronic conductance turns into ionic conductance to close the electrical circuit. This charge transfer across the phase boundary causes chemical transformations resulting the electrolysis products, either directly or by subsequent chemical steps.

#### 4.1.3.1 Different types of overpotential

Whenever a current is passed through the cell, measured electrode potentials, respectively cell voltage, will differ from the calculated equilibrium potential/voltage. This difference is called overpotential or overvoltage  $\eta$ .

$$\eta_{\text{half-cell}}(j) = \phi_{\text{measured}}(j) - \phi^0 \quad (4.1.7)$$

$$\eta_{\text{cell}}(j) = V_{\text{measured}}(j) - V^0 \quad (4.1.8)$$

Overpotential arises from multiple causes, which can be divided into three categories: activation, concentration and ohmic overpotentials. Activation overpotentials relate to limitations in the fundamental steps of a reaction like ad- or desorption and surface reaction rates. Concentration overpotentials refer to all mass transport related resistances. This includes depletion of reactants or accumulation of products at the active site, caused by high reaction rates and/or slow diffusion rates. They also arise from bubble formation which reduces the active electrode surface area or liquid cross section area for ion transport.

Last, ohmic overpotentials are originating from the finite conductivity of electrodes, electrolytes, membrane or outer circuit.<sup>[20, 24, 25]</sup> The measured electrode potential can therefore be expressed as:

$$\varphi(j) = \varphi^0 + \eta_{\text{activation}}(j) + \eta_{\text{concentration}}(j) + \eta_{\text{ohmic}}(j) \quad (4.1.9)$$

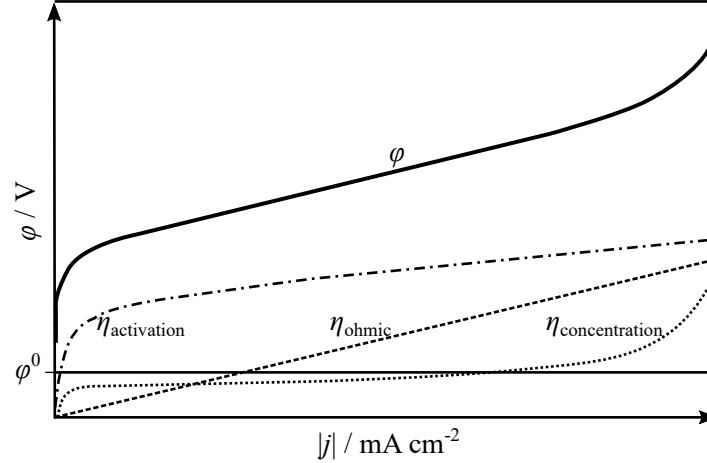


**Figure 4.4:** Contributions of activation, concentration and ohmic overpotential to the electrode potential as function of current density. Figure adapted from Endrodi et al.<sup>[26]</sup>

Basically, the different contributions, activation, concentration and ohmic overpotential relate to, catalyst, electrode and cell design, respectively. As indicated in equation 4.1.9 all three types of overpotential are a function of the current density passed through the cell, giving individual contributions to the electrode potential as illustrated in figure 4.4.

Ohmic overpotentials ideally correlate in a linear manner with current density according to Ohm's law ( $V = IR$ ). The outer circuit and metal electrodes themselves usually show very high electronic conductivity and do not contribute significantly to voltage losses. On the other hand, ionic charge transport through the electrolyte and membrane, as well as electrical conductivity through electrodes with large amounts of insulating binders is comparatively low. Ohmic losses therefore strongly depend on the cell design and electrolyte, namely the electrode-electrode distance and electrode/electrolyte conductivity. Nevertheless, to be still able to compare different electrode systems investigated in individual cells, the ohmic overpotential is usually measured and the electrode potential is compensated ( $IR$ -drop compensation). For some applications electrochemical impedance spectroscopy (EIS) is a powerful technique to determine this ohmic resistance but its implementation and evaluation is rather complex.

Another, much easier way, is the current interrupt (CI) method, depicted in figure 4.5. The equivalent circuit, known as Randle's equivalent circuit, contains a charge transfer resistance parallel to a capacitor representing the chemical reaction and EDL, respectively. Additionally, two ohmic resistors in series

represent the electron and ion conducting phase. During electrolysis the applied current  $I_0$  is periodically turned off and the decay in voltage is analyzed. All ohmic losses instantaneously vanish and the voltage drops from  $V_0$  to  $V_1$ . The non-ohmic charge transfer resistance  $R_{CT}$  however, is still influenced by the parallel double layer capacitor  $C_{DL}$ . Hence, it gives a discharge curve with finite voltage decay, indicated in the top diagram of figure 4.5 between  $t_0$  and  $t_1$ . The total off-time  $t_1 - t_0$  is thereby in a range of 100  $\mu\text{s}$  and the total ohmic resistance  $R_{\Omega}$  is given by:<sup>[24, 27]</sup>

$$R_{\Omega} = \frac{V_0 - V_1}{I_0} \quad (4.1.10)$$

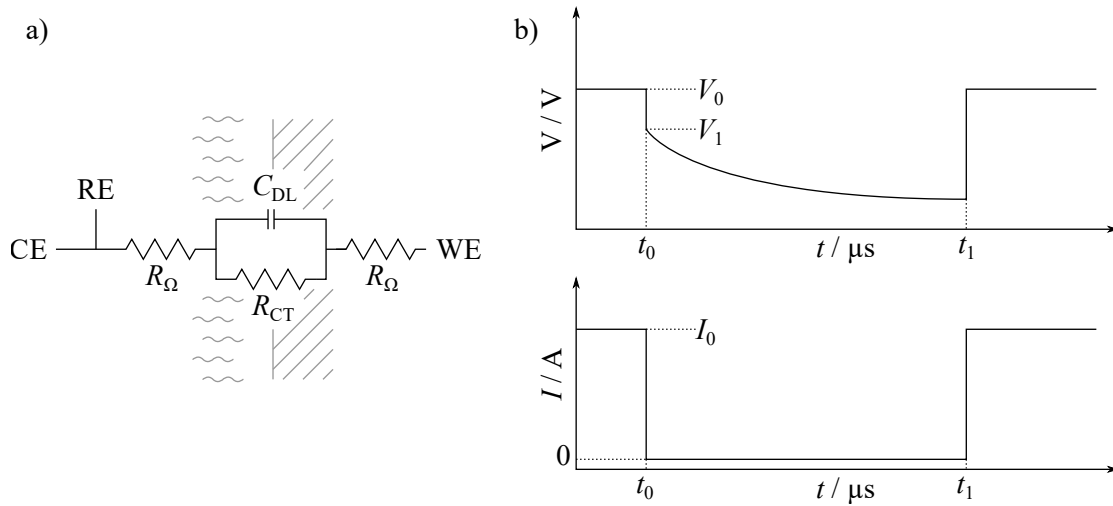


**Figure 4.5:** a) Randle's equivalent circuit with b) idealized course of voltage and current after current interruption. CE: counter electrode; RE: reference electrode; WE: working electrode. Figure adapted from van der Merwe et al.<sup>[24]</sup>

Concentration or diffusion overpotentials exist whenever an electrochemical reaction is occurring. By consuming or producing substances, concentrations close to the active site differ from the bulk phase, influencing the electrode potential. When the rate of the electrochemical reaction (given by current density) exceeds the rate of the mass transport towards or away from the electrode's surface, concentration overpotential rises exponentially. In other words, diffusion of reactants, products or charge carriers becomes the rate determining step and a further increase in the applied voltage does not yield higher currents.<sup>[25, 28]</sup> This, however, does only apply to simple reaction systems. In more complex systems like the reduction of  $\text{CO}_2$  in aqueous solutions, other reducible substances (e.g. water) can accept electrons leading to an indeed increasing current but yielding other products such as hydrogen.

The exponential correlation between activation overpotential and current density is discussed in the next section.

### 4.1.3.2 The Butler-Volmer equation

As indicated in figure 4.4, activation overpotentials are dominating at low current densities. In analogy to the Arrhenius equation describing the temperature dependence of reaction rates, J. Butler and M. Volmer introduced a description for the influence of electrode potential on current density. Figure 4.6 represents the Gibb's free energy as a function of the reaction coordinate. By applying an electric potential the energy state of electrons inside the solid phase ( $e^-(ox)$ ) is raised by  $zF\Delta\phi$ , while the one of the reduced charge carrier species in the liquid phase ( $e^-(red)$ ) is not influenced. Thus, the energy state of the activated complex is raised by  $\alpha_s zF\Delta\phi$ .  $\alpha_s$  is determining the symmetry of the activation barrier and is therefore also called symmetry factor ( $0 < \alpha_s < 1$ ). Note that the following discussion refers solely to the cathode (forward reaction in figure 4.6 is a reduction), at which both oxidation (ox) and reduction (red) can possibly occur due to reversibility.<sup>[21, 28]</sup>

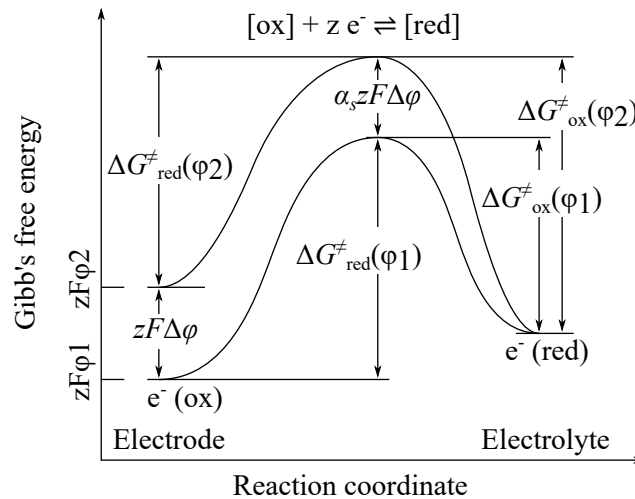


**Figure 4.6:** Gibb's free energy for the transition of an electron from a negatively polarized electrode to a charge carrier in the electrolyte. Figure adapted from Hamann and Vielstich.<sup>[28]</sup>

In general, the rate of a first-order chemical reaction is given by a rate constant  $k$  and the reactant concentration  $c$ :

$$r = k \cdot c \quad (4.1.11)$$

The rate constant of a reaction is thereby influenced by the Gibb's energy of activation ( $\Delta G^{\ddagger}$ ) according to the Arrhenius equation:

$$k = k^0 \cdot \exp \left[ -\frac{\Delta G^{\ddagger}}{RT} \right] \quad (4.1.12)$$

The rate of reduction reaction is therefore given by:

$$r_{\text{red}} = k_{\text{red}} \cdot c(\text{ox}) = k_{\text{red}}^0 \cdot c(\text{ox}) \cdot \exp \left[ -\frac{\Delta G_{\text{red}}^\ddagger(\varphi_1)}{RT} \right] \quad (4.1.13)$$

With  $c(\text{ox})$  being the reactant concentration. When applying an electrode potential  $\Delta\varphi$  the electron's Gibb's free energy is raised from  $zF\varphi_1$  to  $zF\varphi_2$ . Together with  $j_{\text{red}} = -zFr_{\text{red}}$ , partial current density of the forward reaction or reduction  $j_{\text{red}}$  can be described as:

$$j_{\text{red}}(\varphi_2) = -zFk_{\text{red}}^0 \cdot c(\text{ox}) \cdot \exp \left[ -\frac{\Delta G_{\text{red}}^\ddagger(\varphi_2)}{RT} \right] \quad (4.1.14)$$

Taking figure 4.6 into account,  $\Delta G_{\text{red}}^\ddagger(\varphi_2)$  can be rewritten as:

$$j_{\text{red}}(\varphi_2) = -zFk_{\text{red}}^0 \cdot c(\text{ox}) \cdot \exp \left[ -\frac{\Delta G_{\text{red}}^\ddagger(\varphi_1) + (1 - \alpha_s)zF\Delta\varphi}{RT} \right] \quad (4.1.15)$$

with  $\Delta\varphi = \varphi_2 - \varphi_1$ . Setting  $\varphi_1$  as the potential equal to the reference electrode, the term  $-\Delta G_{\text{red}}^\ddagger(\varphi_1)/RT$  becomes constant and can be included into a derived rate constant  $k_{\text{red}}^{0'}$ .  $\varphi_2$  then corresponds to the measured electrode potential  $\varphi$ .

$$j_{\text{red}}(\varphi) = -zFk_{\text{red}}^{0'} \cdot c(\text{ox}) \cdot \exp \left[ -\frac{(1 - \alpha_s)zF}{RT} \cdot \varphi \right] \quad (4.1.16)$$

In the same way, the partial current density of the backward reaction or oxidation can be expressed by:

$$j_{\text{ox}}(\varphi) = zFk_{\text{ox}}^{0'} \cdot c(\text{red}) \cdot \exp \left[ \frac{\alpha_s zF}{RT} \cdot \varphi \right] \quad (4.1.17)$$

Equations 4.1.16 and 4.1.17 describe the partial current densities of reduction and oxidation reaction, depending on the electrode potential  $\varphi$ . At an open circuit condition all components are in equilibrium and both reactions are equally fast. The respective current density is called exchange current density  $j_0 = j_{\text{ox}}(\varphi^0) = |j_{\text{red}}(\varphi^0)|$ . Applying Nernst's equation (equation 4.1.6) and the definition of overpotential according to equation 4.1.7, both partial current densities can be expressed as:



$$j_{\text{red}}(\eta) = -j_0 \cdot \exp\left[-\frac{(1-\alpha_s)zF}{RT} \cdot \eta\right] \quad (4.1.18)$$

$$j_{\text{ox}}(\eta) = j_0 \cdot \exp\left[\frac{\alpha_s zF}{RT} \cdot \eta\right] \quad (4.1.19)$$

with:

$$j_0 = zFk_{\text{red}}^0 \cdot c(\text{ox}) \cdot \exp\left[-\frac{\Delta G_{\text{red}}^\ddagger(\varphi^0)}{RT}\right] \quad (4.1.20)$$

$$j_0 = zFk_{\text{ox}}^0 \cdot c(\text{red}) \cdot \exp\left[-\frac{\Delta G_{\text{ox}}^\ddagger(\varphi^0)}{RT}\right] \quad (4.1.21)$$

Finally, adding up both partial current densities results in the Butler-Volmer equation:<sup>[21, 28]</sup>

$$j(\eta) = j_{\text{ox}}(\eta) + j_{\text{red}}(\eta) = j_0 \cdot \left\{ \exp\left[\frac{\alpha_s zF}{RT} \cdot \eta\right] - \exp\left[-\frac{(1-\alpha_s)zF}{RT} \cdot \eta\right] \right\} \quad (4.1.22)$$

Obviously, the  $j(\eta)$  function depends on the exchange current density and symmetry factor  $\alpha_s$ . Especially  $j_0$  depends directly on the electrode's activity, determining  $\Delta G_{\text{red}}^\ddagger(\varphi_1)$ . Figure 4.7 illustrates the Butler-Volmer equation with some arbitrary values for  $j_0$  and  $\alpha_s$ .  $j_0 = 10 \cdot 10^{-4} \text{ A cm}^{-2}$  corresponds to relatively active reaction system like the  $\text{H}^+/\text{H}_2$  couple at metal electrodes.  $j_0 = 10 \cdot 10^{-6} \text{ A cm}^{-2}$ , on the other hand, corresponds to a moderately active system like the  $\text{CO}_2/\text{HCOO}^-$  couple on a tin oxide electrode.<sup>[28, 29]</sup> As mentioned,  $\alpha_s$  describes the symmetry of the curve. At  $\alpha_s = 1/2$  equal absolute values of negative or positive overpotential result in the same absolute value of current. With differing  $\alpha_s$  reduction or oxidation are accelerated differently.<sup>[21]</sup>

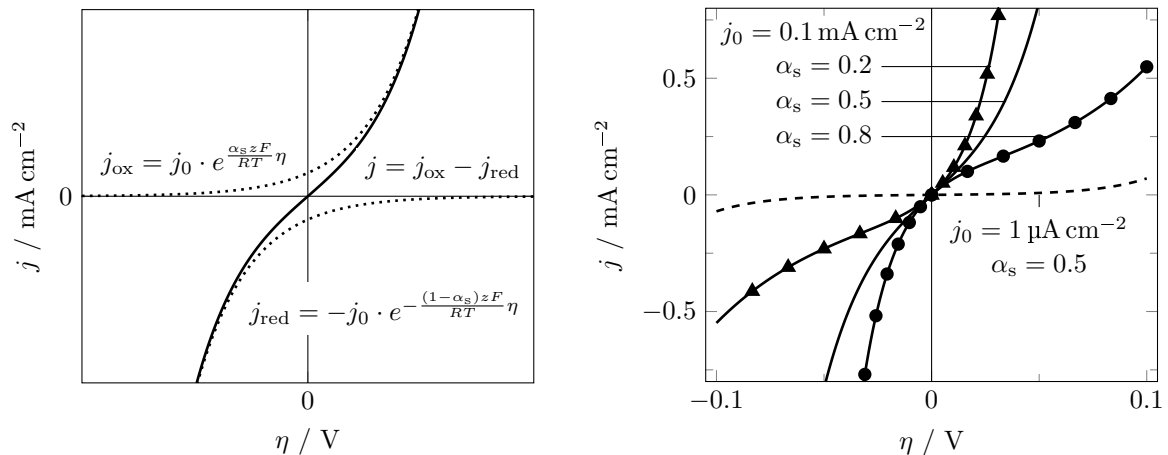


**Figure 4.7:** The dependence of current density on overpotential according to Butler-Volmer.<sup>[21, 28]</sup>  
a) Contribution of reductive and oxidative current density to the observed one ( $\alpha_s = 0.5$ ).  
b) Effect of different values for  $\alpha_s$  and  $j_0$ .

#### 4.1.4 Quantitative relations

Quantitative relations between the introduced electric charge and converted substance are an absolute fundamental in electrolysis and were first described by Faraday in 1834.<sup>[30]</sup> Faraday described the deposited molar amount of substance  $n_F$  as being proportional to the passed electric charge  $q$  and reversed proportional to the substance valance. Mathematically speaking this can be expressed as:

$$n_F \sim \frac{q}{z} \quad (4.1.23)$$

The proportionality constant  $F$  is named after Faraday and the so-called Faraday's first law reads as follows:

$$q = z \cdot F \cdot n_F \quad (4.1.24)$$

With

$$q = I \cdot t \quad (4.1.25)$$

the molar amount of substance can be expressed as:

$$n_F = \frac{I \cdot t}{z \cdot F} \quad (4.1.26)$$

$n_F$  therefore represents the maximum amount of product to be formed. However, electrolysis is rarely completely selective. In electrochemical processes it is common to express this selectivity as faradaic efficiency ( $FE$ ) towards product  $i$ , defined as:

$$FE_i = \frac{n_i}{n_F} \cdot 100\% = \frac{n_i \cdot z \cdot F}{I \cdot t} \cdot 100\% \quad (4.1.27)$$

This value includes side reactions and short circuit currents. The latter is especially important in industrial scaled electrolyzers with a high total current. Short circuit currents strongly depend on the reactor design, while the extent of side reactions is mostly based on catalyst, electrode design and reaction conditions. With the  $FE$  to the desired product  $i$  and the equilibrium voltage of the overall reaction (equation 4.1.2) an energy efficiency ( $EE$ ) of the electrolysis can now be calculated.

$$EE_i = \frac{V_{\text{cell}}^0}{V_{\text{cell}}} \cdot FE_i \quad (4.1.28)$$

For most electrochemical investigations cathode potential is measured against a reference electrode instead of the cell voltage. In order to still be able to compare the performance of reported systems, the energetic cathode efficiency (*ECE*) is introduced and defined as:

$$ECE_i = \frac{\varphi_{C, \text{vs SHE}}^0}{\varphi_{C, \text{vs SHE, IR}}} \cdot FE_i \quad (4.1.29)$$

Note that the *ECE* does not represent a real energetic efficiency, since ohmic overpotentials and the counter reaction are not considered in this value. Also, the *ECE* depends on the reference electrode chosen for obtaining  $\varphi^0$  and  $\varphi$ . It does, however, allow a comparison of the cathode's performance. A high energetic efficiency is only achieved by a combination of high selectivity and low overpotentials. Both strongly depend on the chosen catalyst, type of electrode and applied reaction conditions. The cell design in turn influences mainly the ohmic overpotentials.

The total power consumption  $P$  of an electrolyzer is simply calculated by the product of cell voltage and current passed.

$$P = V_{\text{cell}} \cdot I \quad (4.1.30)$$

Multiplied by time gives the electrical energy  $E$ :

$$E = P \cdot t \quad (4.1.31)$$

In order to be able to compare different types of electrodes, the measured current is typically normalized to the geometrical surface area  $A_{\text{geo}}$  of the electrode and given as current density.

$$j = \frac{I}{A_{\text{geo}}} \quad (4.1.32)$$

#### 4.1.5 Important aspects of electrochemical cells

The term electrochemical cell describes any type of reactor in which redox reactions are conducted using or generating electric power. Depending on the type of application different basic designs are common. Fundamental research on a nanometer scale like the investigation of catalyst systems usually requires to work with low amounts of material and thus small reactor volumes. The latter is especially important when chemical analysis of produced or consumed substances is targeted. Usually, non-industrial electrodes like glassy carbon supports with deposited electrocatalytically active components are employed,

which need to be operated at low current densities to avoid mass transport limitation. The resulting low amounts of product or little changes in reactant concentration are challenging to detect if the cell volume is too large. For these reasons, H-type cells or low-volume vessels incorporating special electrodes like rotating (ring) disk or dropping mercury electrodes are applied.

For industrial applications an energy efficient production is targeted. Multiple designs are therefore known, which need to be selected depending on aspects e.g. regarding electrode structure, type of electrolyte, operating temperature or mass transport. A main issue to be considered is the reduction of power consumption while maintaining high currents. This implies the reduction of voltage losses caused by different, already discussed, effects. Reaction overpotentials due to moderately active electrodes, mass transport limitations and ohmic resistances are thereby to recall. Optimizing the electrochemical cell therefore needs to address all these issues, while also considering aspects of manufacturing, material costs and long-term stability.

The ability to scale up a cell either by geometrical expansion or by numbering-up is also of great importance. Increasing the active electrode area by multiplying single cells is called stacking. While different ways to connect multiple cells are known, putting them in series is probably the most common way. Here, the anode of one cell is electrically connected to the cathode of the next cell either by a bipolar plate or by external wiring. Such a stack incorporating thin plates of electrodes and electrolyte flow fields is illustrated in figure 4.8.

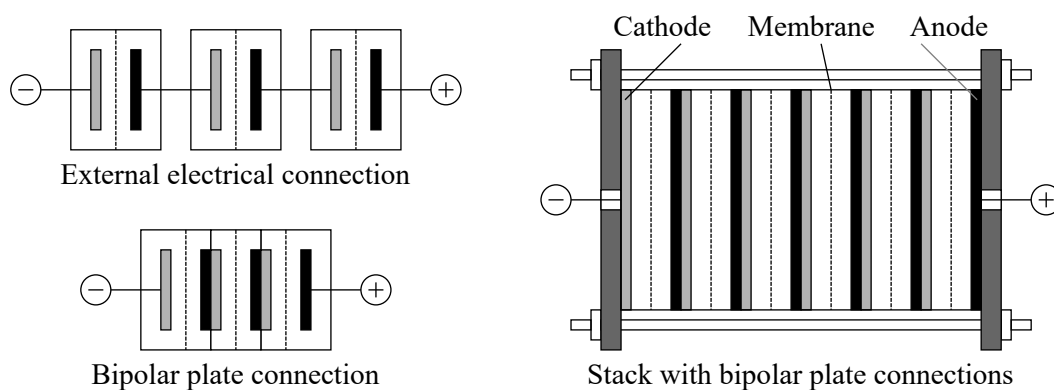


**Figure 4.8:** Schematic illustration of multiple cells being stacked in a filter press. Figure adapted from V. Schmidt.<sup>[20]</sup>

## 4.2 Carbon dioxide reduction reaction

The chemical conversion of CO<sub>2</sub> is a long known and studied topic with multiple possible pathways and products. Basically, these pathways can be divided into two groups of reactions. First, reactions where the oxidation state of the carbon atom, +IV, is maintained, for example during production of urea, salicylic acid, polycarbonates or other inorganic carbonates.<sup>[7, 31]</sup> These reactions require comparatively low amounts of energy and sometimes not even a catalytic process. The second group of reactions contains pathways in which the final product has a lower oxidation state than +IV. Examples would be oxalic acid (+III), formic acid or CO (+II), methanol (-II) and methane (-IV). These reactions require much larger amounts of energy, but their general demand is also higher. Production of such substances can be done thermocatalytically like in the methanol synthesis process or in the Sabatier reaction.<sup>[7]</sup> While these reactions require quite harsh reaction conditions, electrochemical reduction allows a conversion at ambient pressure and temperature. CO<sub>2</sub> electrolysis (CO<sub>2</sub>EL) has been studied intensively for the past five decades including a variety of different products.<sup>[32]</sup> The following sections focus on different aspects of the electrochemical conversion of CO<sub>2</sub> like thermodynamics, catalysts, mechanisms and reaction conditions.

### 4.2.1 Fundamentals

Depending on the catalyst and electrolyte used, CO<sub>2</sub> can be converted into several products. The most common ones are listed in equations (CEq 4.5) - (CEq 4.7). Besides the well investigated pathways to formate/formic acid, CO and methane, higher hydrocarbons with a brought range of products like alkenes<sup>[33, 34]</sup>, alcohols<sup>[35, 36]</sup>, aldehydes and ketones<sup>[37]</sup> are also known. When using aprotic solvents a direct coupling of two CO<sub>2</sub> radical anions forming oxalate is also possible.<sup>[38]</sup> Except for oxalate formation a source of protons is of course necessary. This, however, leads to the problem that these protons themselves can be reduced to hydrogen in a reaction called hydrogen evolution reaction (HER) (CEq 4.8). This undesired product represents one of the main side reactions in CO<sub>2</sub>RR. Its formation has to be suppressed by applying the right catalyst, electrode and reaction conditions.

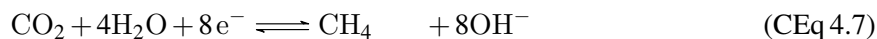
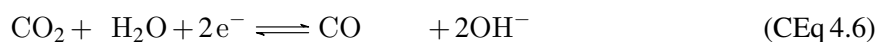
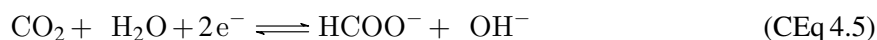
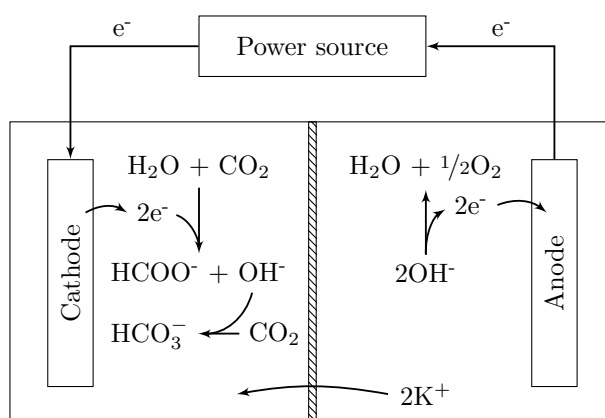
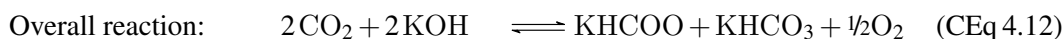
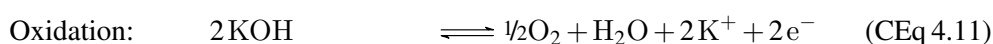
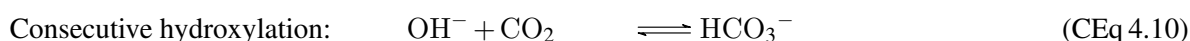
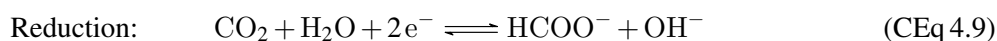


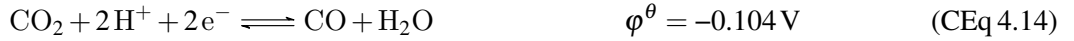
Figure 4.9 shows a schematic illustration of an alkaline electrolysis cell converting  $\text{CO}_2$  and a metal hydroxide to the respective metal formate, bicarbonate and oxygen. Reaction (CEq 4.9) proceeds on the cathode, forming formate and hydroxide ions. Another  $\text{CO}_2$  molecule can then react with the formed hydroxide ion in a consecutive hydroxylation to bicarbonate. On the anode, hydroxide ions are oxidized to oxygen leaving behind water and the cation of the metal hydroxide (CEq 4.11). These cations are transferred through the membrane to maintain charge neutrality, leading to the overall reaction (CEq 4.12).



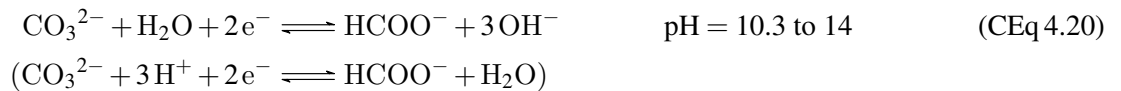
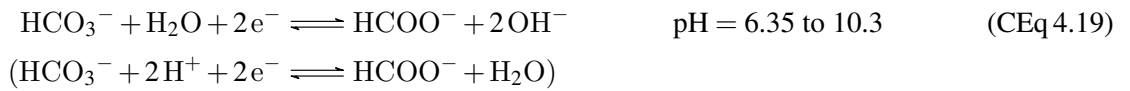
**Figure 4.9:** Schematic illustration of an electrolysis cell converting  $\text{CO}_2$  and potassium hydroxide into the respective formate/bicarbonate salt mixture and oxygen.

### 4.2.2 Equilibrium potentials

Using equation 4.1.1 and 4.1.3, the standard electrode potential for the CO<sub>2</sub>RR to the most common C<sub>1</sub>-products can be calculated. For a detailed calculation and thermodynamic literature values of standard formation enthalpy and entropy see appendix section 9.1, p. 213. The following values are given vs SHE at pH = 0,  $T = 25^\circ\text{C}$  and  $p = 101.3\text{kPa}$ .



When formulating the reaction equation for the reduction of CO<sub>2</sub> to formate/formic acid, there are multiple possibilities depending on the present species, which again depend on pH and respective  $pK_a$  values. Between a pH of 0 and 3.77 ( $pK_{a, \text{formic acid}}$ ) formic acid is the main product while at higher pH formate is formed. On the other hand, the thermodynamically stable form of CO<sub>2</sub> within a pH range of 6.35 ( $pK_{a, \text{carbonic acid}}$ ) to 10.3 ( $pK_{a, \text{bicarbonate}}$ ) is bicarbonate. Above that range carbonate is the main form. This leads to the following reaction equations. For an easier discussion later on, all of them are also represented in their proton utilizing form.



Transforming equation 4.1.6 with the definition of the pH ( $\text{pH} = -\log(\alpha_{\text{H}^+})$ ) and with the convention that under standard conditions all other activities are equal to 1, leads to the following general  $\varphi^0(\text{pH})$  relation.

$$\varphi^0 = \varphi^\theta - 0.059\text{ V} \cdot \frac{V_{\text{H}^+}}{z} \cdot \text{pH} \quad (4.2.1)$$

It is obvious that the slope of this function depends on the  $v_{H^+}/z$  ratio, which is different for reactions (CEq 4.17) to (CEq 4.20). Based on this ratio and the  $pK_a$  values for formic acid, carbonic acid and bicarbonate the  $\varphi^0(\text{pH})$  function can be plotted in a so called Pourbaix diagram (see figure 4.10). While the slope of the  $\text{CO}_2$ ,  $\text{HCO}_3^-$ ,  $\text{CO}_3^{2-}/\text{HCOOH}$ ,  $\text{HCOO}^-$  equilibrium potential differs for different pH ranges, it is constant for the  $\text{CO}_2$  ( $\text{HCO}_3^-$ ,  $\text{CO}_3^{2-}$ )/ $\text{CO}$ ;  $\text{CO}_2$  ( $\text{HCO}_3^-$ ,  $\text{CO}_3^{2-}$ )/ $\text{CH}_4$  and  $\text{H}^+/\text{H}_2$  couples with a slope of  $-0.059 \text{ V}$ . These courses of the equilibrium potential over pH are well known from literature.<sup>[39–41]</sup> However, bicarbonate and carbonate salts itself cannot be converted electrochemically to formate/formic acid.<sup>[42]</sup> Instead, physically solved  $\text{CO}_2$  is the active species.<sup>[42]</sup> This consideration leads to the fact that chemical equation (CEq 4.18) applies to a pH range of 3.77 to 14. The resulting equilibrium potential is given by the upper solid line in figure 4.10 ( $\text{CO}_2/\text{HCOOH}$ ,  $\text{HCOO}^-$ ). Calculated equilibrium potentials show that at high pH values  $\text{CO}_2\text{RR}$  to formate is favored against production of  $\text{CO}$  and hydrogen.

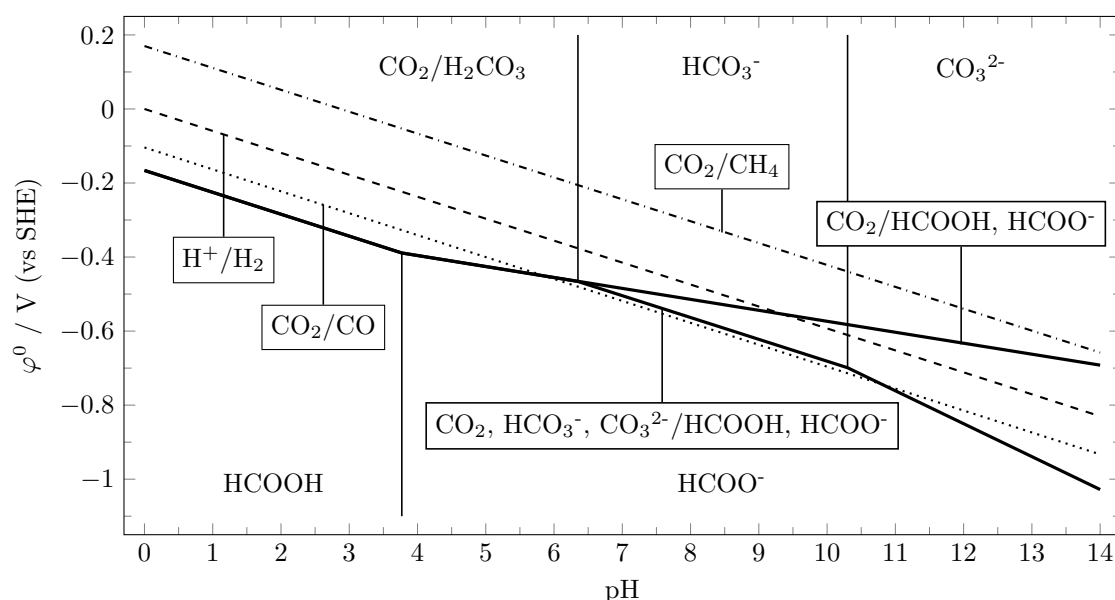


**Figure 4.10:** Pourbaix diagram for hydrogen evolution and various  $\text{CO}_2$  reduction reaction products. The lower solid line represents the equilibrium potential for the  $\text{CO}_2$ /bicarbonate/carbonate - formic acid/formate redox couple, when the thermodynamically stable species are considered. The upper solid line considers  $\text{CO}_2$  as reactant over the whole pH range.

The present work focuses mainly on the reduction reaction of  $\text{CO}_2\text{EL}$ . However, a counter reaction is always necessary for electron donation. In most studies oxygen evolution reaction (OER) serves as counter reaction. Mainly due to its simple handling. Figure 4.11 shows the equilibrium cell voltage for  $\text{CO}_2\text{RR}$  to formate/formic acid and OER as function of pH. Usually, electrolyzers work at the same pH value for both half-cells due to the ability of proton/cation exchange through the membrane. Thermody-



namically speaking this makes a pH of 14 the best working point with a minimum potential difference of  $V_{\min}^0 = -1.095 \text{ V}$ .

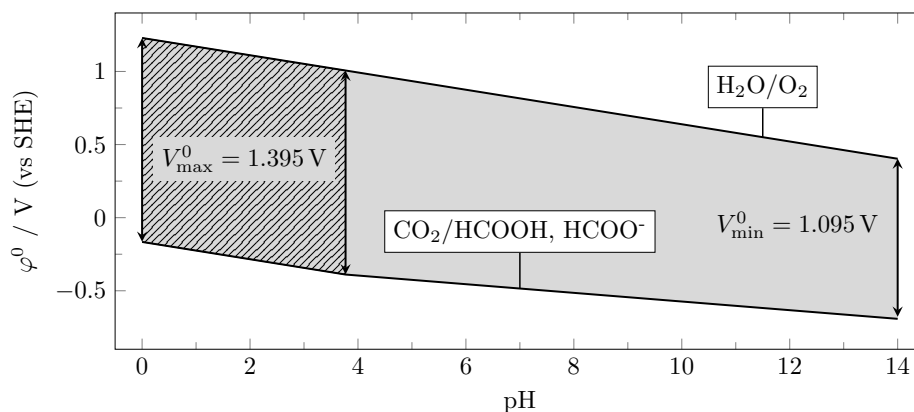


**Figure 4.11:** Pourbaix diagram for  $\text{CO}_2$  reduction to formic acid/formate and oxygen evolution reaction. The difference between both represents the standard cell voltage.

### 4.2.3 Electrocatalytic conversion of carbon dioxide

Carbon dioxide with its linear geometry is a very stable molecule ( $\Delta G_f = -394 \text{ kJ mol}^{-1}$ )<sup>[43]</sup>. This fact requires a relatively high energy input, or energy rich co-reactants, to convert it. Schwarz and Dodson reported the first electron transfer step, forming the  $\text{CO}_2$  radical anion, to occur at  $-2.24 \text{ V (vs. SHE)}$ , which is  $-2.07 \text{ V}$  to  $-1.55 \text{ V}$  larger than the equilibrium potential.<sup>[44]</sup> The need for an effective catalyst is obvious. It is not only needed because of the high activation energy but also to achieve a high selectivity since the equilibrium potentials of various  $\text{CO}_2\text{RRs}$  and HER are similar. A catalyst with low overpotential for the desired product and high overpotential for all undesired reactions is necessary. In light of this, it becomes intelligible that the vast majority of current studies on electrochemical  $\text{CO}_2$  conversion focuses on the development of highly active and selective catalyst systems. Metal, metal oxide and alloy based systems are the most intensively studied ones.<sup>[45–47]</sup> Metal chalcogenide,<sup>[47]</sup> homogeneous<sup>[48]</sup> and metal-free<sup>[49]</sup> catalyst systems, however, are also well known. In the present work solely metal and metal oxide catalysts were used and the following discussion exclusively addresses these systems.

#### 4.2.3.1 Metal/metal oxide catalysts

Metal/metal oxide based catalysts can be divided into four major groups, depending on the main product. Metals that form mainly formate/formic acid (Sn, Pb, Hg, In, Cd, Bi), metals that form mainly CO (Au, Ag, Zn) and metals that form high amounts of hydrocarbons (Cu).<sup>[32, 39]</sup> The last group of metals is not active for  $\text{CO}_2\text{RR}$  and produces mainly hydrogen (Pt, Ni, Fe).<sup>[32]</sup> Within the first group, tin oxide is

the most investigated metal oxide, mainly due to its high performance, low price and non-toxicity.<sup>[50]</sup> However, *FE* and *ECE* of the respective catalyst can vary significantly, depending on the type of metal, its oxidation state, particle size, morphology or the presence of co-catalysts.<sup>[17]</sup> Figure 4.12 gives a slight overview over the enormous amount of literature, illustrating the achieved *FE* and *ECE* or *EE* over the applied current density.

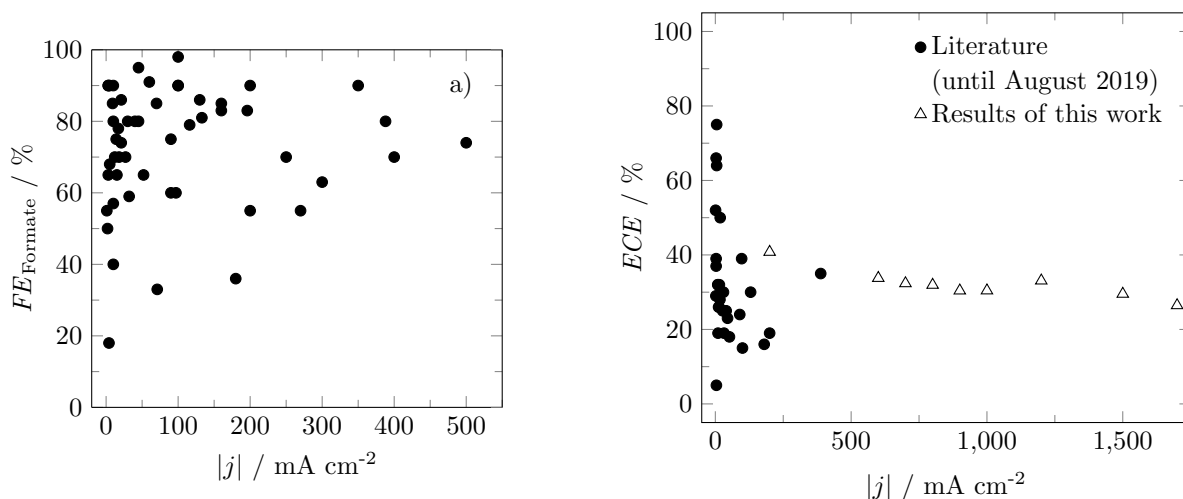


**Figure 4.12:** Summary of a) faradaic efficiencies to formate,<sup>[19, 29, 41, 51–79]</sup> and b) energetic cathode efficiencies<sup>[29, 41, 51–75]</sup> and energy efficiencies<sup>[19, 51, 76–79]</sup> reported in literature (up to August 2019) over the respective current density. Only formate selective metal, metal oxide and metal alloy based catalyst systems of the elements Sn, Pb, In, Bi and Cu are represented.

The oxidation state of the catalyst is probably the most important factor determining selectivity and activity. For tin based systems the presence of surface oxide species is mandatory. Metallic tin shows no significant activity towards  $\text{CO}_2\text{RR}$ . In fact it even is a moderate catalyst for HER.<sup>[58, 80]</sup> Surface tin oxide forms easily when exposed to air, but can be reduced during cathodic operation.<sup>[58, 81]</sup> Whenever the native oxide layer is removed, either by acidic or electrochemical etching, HER partial current density strongly increases.<sup>[58]</sup> Figure 4.13 shows the thermodynamically stable regions for tin and tin oxides. From a pure thermodynamic point of view tin based catalysts should not be able to convert  $\text{CO}_2$ . The onset potential for reduction of  $\text{CO}_2$  to formate is around  $-1 \text{ V}$  vs SHE with a typical window of operation between  $-1.3 \text{ V}$  to  $-1.6 \text{ V}$  vs SHE.<sup>[59]</sup> At these potentials tin should exist in its metallic form. Fortunately, the reduction of tin(II)-(IV) oxide is kinetically hindered.<sup>[82]</sup> In-operando spectroscopic methods like Raman and X-ray absorption spectroscopy (XAS) revealed that a metastable oxidized state is maintained even at much more negative potentials than suggested by thermodynamics.<sup>[81, 82]</sup> Depending on the production method of the catalyst, a tin(II) mixed oxide/hydroxide is formed on the surface with a core of metallic tin or tin(IV) oxide.<sup>[82, 83]</sup>

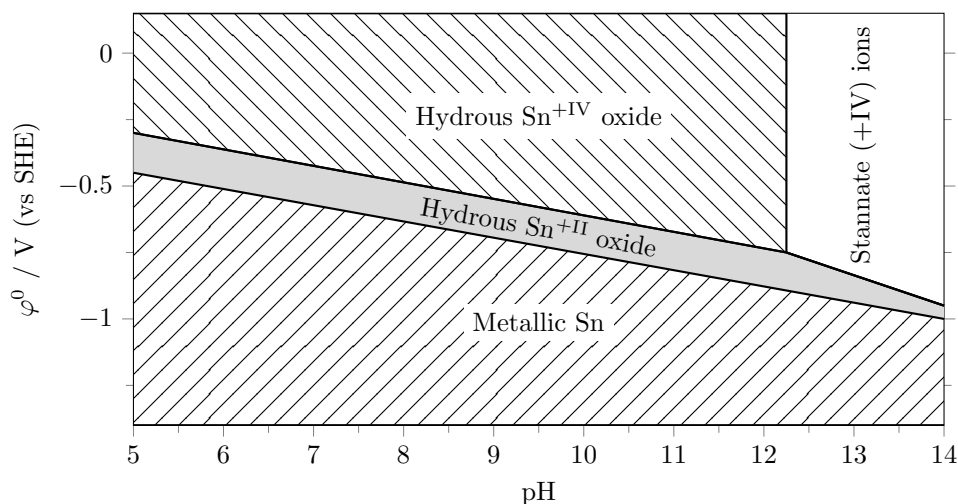


**Figure 4.13:** Pourbaix diagram of tin. Figure adapted from Dutta et al.<sup>[81]</sup>

These findings, however, cannot be simply transferred to other metals. While indium shows a similar behavior for anodized or etched surfaces as tin, lead and bismuth show a higher selectivity when fully reduced.<sup>[80]</sup> In general, it is also hard to state a ranking for different metal catalysts, as their performance depends on too many factors. While some groups report activity and selectivity in the order of  $\text{Pb} > \text{Sn}$  and  $\text{Pb} > \text{Sn}$ , respectively,<sup>[62, 66]</sup> others report it in the order of  $\text{Sn} > \text{Pb}$  and  $\text{Sn} > \text{Pb}$ ,<sup>[84]</sup>  $\text{Pb} > \text{Sn}$  and  $\text{Sn} > \text{Pb}$ <sup>[85]</sup> or  $\text{Sn} > \text{Pb}$  and  $\text{Pb} > \text{Sn}$ .<sup>[39]</sup>

$\text{CO}_2\text{RR}$  is known to be a surface sensitive reaction, meaning that activity and selectivity of a catalyst depend on its particle size and morphology. For example, Zhang et al. prepared tin(IV) oxide particles of different particle sizes ranging from 3 nm to 200 nm in diameter, supported on carbon black. As a key message the authors reported a maximum in formate  $FE$  at a particle size of  $\bar{d}_p = 5$  nm. Their suggested explanation, despite not being proven, is that the binding energy between key intermediates and the active site shows an optimum for 5 nm particles.<sup>[74]</sup> Another explanation for such an optimum might be derived from DFT studies for the conversion of  $\text{CO}_2$  to  $\text{CO}$ , whereat edge sites of Au nanoparticles favor  $\text{CO}_2\text{RR}$  and corner sites favor HER.<sup>[86]</sup>

Apart from adjusting the size of spherical nanoparticles, much effort is invested in creating defined morphologies. Examples are simple rod-,<sup>[87]</sup> coralline-<sup>[88]</sup> or urchin-like<sup>[89]</sup> structures, as well as dendritic<sup>[90]</sup> structures and sheets forming hierarchical mesoporous systems<sup>[91]</sup>. The motivation for structuring catalysts is versatile. One aspect is the higher amount of active sites per geometrical electrode surface or per catalyst mass. Compared to polycrystalline metal foils, structured catalysts obtain a much larger surface area and more unsaturated atoms.<sup>[92]</sup> Another aspect is mass transport. Besides the intrinsic activity of an active site its accessibility by the reactant is a crucial point, which can be addressed by a special electrode design. For example Li et al. demonstrated a superior performance of

thin sheets, consisting of highly porous tin oxide, compared to planar metal foils and even some GDEs. They attributed the higher activity to an increased active surface area and enhanced CO<sub>2</sub> mass transfer.<sup>[91]</sup> Last, non-oriented primary particles create numerous grain boundaries within the catalyst particle, which hinder an efficient electron transport. In contrast to that, straight rod- or wire-like structures can provide undisturbed electron transport.<sup>[93]</sup> However, highly structured materials again come with their own disadvantages. Synthesis often requires templates and hydrothermal conditions. The resulting particles are typically in a range of 100 nm to 2 μm.<sup>[88, 91, 94, 95]</sup> This can complicate an efficient introduction in electrode systems like GDEs or lead to low mass activity. Using GDEs the particle size reduction to a target size of 5 nm achieves a comparable or even better performance than the mentioned special structured materials.<sup>[19]</sup>

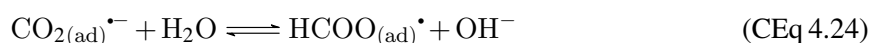
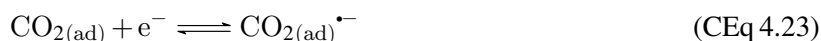
#### 4.2.3.2 Catalyst deactivation

Chemical or physical changes to the catalyst with negative impact on performance, in general referred to as catalyst deactivation, have been reported repeatedly by different groups. Various mechanisms for deactivation are known, e.g. induced either by unsuitable cathodic polarization or other interfering substances. Highly negative potentials may change the catalysts oxidation state, e.g. from tin(II) to tin(0), which is just moderately active for CO<sub>2</sub>RR as previously mentioned.<sup>[81]</sup> Anawati et al. reported a minimum in cathode deactivation at -1.6 V vs SHE. Less negative potentials increased the oxide layer thickness, while significantly more negative potentials lead to the formation of KSn. The colloidal intermetallic compound formed between catalyst and electrolyte was found to be responsible for material loss and cathode deactivation.<sup>[96]</sup> This transition is reported to occur on a time-scale of several hours and might be an explanation for material loss reported by multiple groups, especially at higher current densities.<sup>[53, 63, 97]</sup> Other present substances like heavy metal impurities are also well known to contribute to a cathode deactivation. Impurities in the electrolyte can be deposited during cathodic polarization and interfere with the CO<sub>2</sub>RR catalyst either by poisoning the active site itself, or by providing HER active sites.<sup>[39]</sup> Hori et al. showed that pre-electrolyzing the electrolyte can prevent deactivation of a copper based catalyst effectively by removing heavy metals from the electrolyte.<sup>[98]</sup> Last, the reactant CO<sub>2</sub> itself can lead to deactivation. Reports state a black deposit, which was analyzed to be mostly graphitic, blocking active sites. Different recovering techniques like deep cathodic polarization or anodic polarization turned out to be able to remove these deposits either by mechanic stripping with high amounts of hydrogen being produced or by anodic oxidation.

### 4.2.3.3 Reaction mechanisms

Carbon dioxide electroreduction can lead to a broad variety of products with different reaction pathways competing. The extent at which each pathway is undergone depends mainly on the catalysts, leading to the four different groups of metals described in section 4.2.3.1. The following description of proposed reaction mechanisms will focus on formate production with some remarks about CO and hydrocarbon formation.

Each overall reaction pathway consists of multiple elemental steps. The formate producing pathway can be summarized as follows:



Equation (CEq 4.21) and (CEq 4.22) refer to an initial equilibrium, which is connected to the CO<sub>2</sub>/carbonic acid/bicarbonate/carbonate equilibrium resulting in the required adsorbed CO<sub>2</sub>.<sup>[42, 99]</sup> This adsorbed species is then activated by a single electron transfer yielding the CO<sub>2</sub> radical anion. Analysis of different electrode-electrolyte systems showed similar characteristics in obtained polarization curves indicating that all reaction pathways share the same rate determining step. The only shared pathway for all CO<sub>2</sub>RR products is the single electron transfer of equation (CEq 4.23) (see figure 4.14). Subsequent protonation of the CO<sub>2</sub> radical anion and a second single electron transfer leads to formate which desorbs from the active site.<sup>[99]</sup>

One major difference which determines the main selectivity of a catalyst arises from equation (CEq 4.24). CO<sub>2</sub> orientation towards the electrode's surface during protonation is a crucial parameter. Feaster et al. calculated binding energies for two cases with either a \*COOH or \*OCOH adsorption orientation by density functional theory (DFT) and correlated their results with observed partial current densities of CO or formate. Volcano plots for both cases were thereby obtained which fit very well to experimental data. CO selective metals like gold and silver are on top of the volcano shaped function  $j_{\text{CO}}(*\text{COOH}$  binding energy), while other metals bind this intermediate either too strong (platinum) or too weak (tin). When using the binding energy of the \*OCOH intermediate as descriptor, tin is on top of the  $j_{\text{HCOO}^-}(*\text{OCOH}$

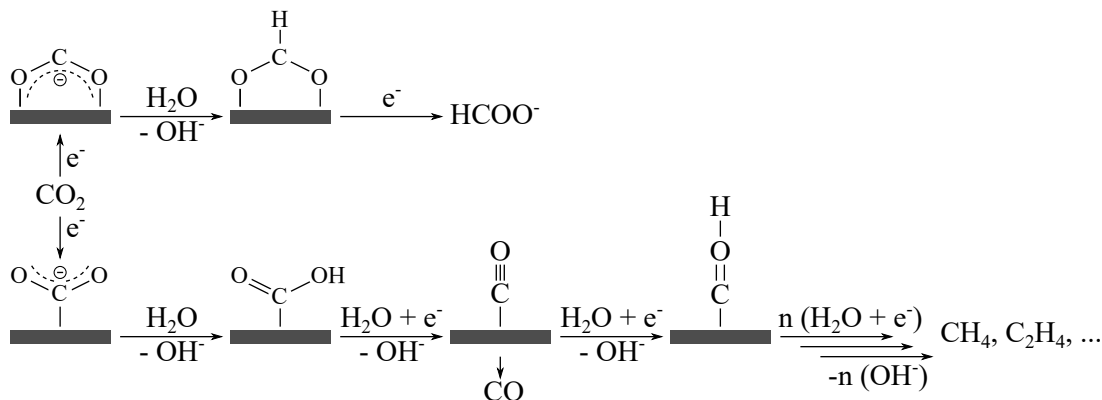


**Figure 4.14:** Mechanisms of different CO<sub>2</sub> reduction reaction pathways leading to the three major groups of products, namely formate, CO and hydrocarbons. Figure adapted from Zhu et al.<sup>[47]</sup> with contents of Feaster et al.<sup>[100]</sup>.

binding energy) plot. These results suggest that CO selective metals tend to bind the CO<sub>2</sub> radical anion at the carbon atom, while formate selective metals bind it via the oxygen atoms.<sup>[100]</sup>

Coordination of CO<sub>2</sub> towards a tin surface via the oxygen atoms is in good accordance with other investigations stating that under electrolysis conditions a surface carbonate species is formed.<sup>[83]</sup> As mentioned in section 4.2.3.1 multiple groups reported the importance of an oxide surface layer which contains a mixture of surface oxides and hydroxides.<sup>[58, 80, 81, 101]</sup> Without these oxygen species CO<sub>2</sub> cannot adsorb in the necessary orientation. Instead, protons can adsorb more easily to the metallic surface, hence shifting the selectivity towards hydrogen.<sup>[101]</sup>

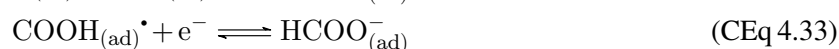
Another pathway that is based on \*COO adsorption is the formation of hydrocarbons. This way is based on the fact that CO does not desorb easily from a copper surface as it is the case for e.g. silver based electrodes.<sup>[102]</sup> Adsorbed CO is thereby further reduced in multiple single electron transfer and protonation reactions.<sup>[99]</sup>

The first hydrogen atom addition can proceed by two different ways. First, by the previously described addition of a proton from free or adsorbed water to the CO<sub>2</sub> radical anion. This reaction is proposed to occur on most solid metal catalysts (equation (CEq 4.24)). Second, it can proceed via insertion into a metal hydride as follows:



The major difference for both reactions is the activation step. Within the first described mechanism CO<sub>2</sub> itself needs to be activated by an initial single electron transfer, which requires a comparatively large amount of energy.<sup>[39]</sup> The second described mechanism is only known for palladium based nanoparticle catalysts operated at low overpotential (at least for heterogeneous catalyst systems). Instead of CO<sub>2</sub>

activation water is used to form a metal hydride in an initial step, which consecutively reacts with CO<sub>2</sub>. In addition, specially designed homogeneous catalyst were also reported to be able to promote this mechanism. It allows a significant reduction of the overall activation barrier and related overpotential.<sup>[99, 103]</sup> Thus, the reaction mechanism changes to:



#### 4.2.4 Influence of operating conditions

In recent years several studies have been published focusing on different operating conditions like type and concentration of electrolyte, pH or temperature. All these parameters will be described in the following subsections. The main problem when trying to assess optimum reaction conditions is that presented studies are barely comparable due to the high complexity of such electrolysis systems. However, the large number of publications allows the identification of trends and starting points for the herein investigated system.

##### 4.2.4.1 Effects of the electrolyte

In every electrochemical cell the electrolyte, which can exist in liquid or solid state, is responsible for ion transport between both current bearing electrodes. In polymer electrolyte membrane (PEM) electrolyzers for example the electrolyte consist of a solid CEM sandwiched between the two electrodes. This concept is especially applicable for producing gaseous products like CO or CH<sub>4</sub>, which can be extracted by a humidified CO<sub>2</sub> feed. For alkaline CO<sub>2</sub>RR a liquid electrolyte between cathode and membrane is usually applied to remove the produced formate salt. In general this liquid electrolyte consists of a solvent with a conductive salt and should fulfill the following requirements.<sup>[20]</sup>

- Chemically and electrochemically stable within the used potential range.
- High solubility for reactants and products.
- High mobility of reactants and products to facilitate fast mass transport.

- Stabilization of reaction intermediates.
- Low resistivity to avoid ohmic losses.
- High heat conductivity to remove or supply heat locally.
- Low vapor pressure to avoid dilution of the CO<sub>2</sub> feed, bubble formation and uncontrolled recondensation.

Even though the cathodic stability of water is rather moderate (HER competing with CO<sub>2</sub>RR) and the solubility of CO<sub>2</sub> is very low ( $S_{\text{CO}_2, 20^\circ\text{C}} = 35 \text{ mmol L}^{-1}$ )<sup>[38]</sup>, the lack of alternatives leads to water as the most widely used solvent.

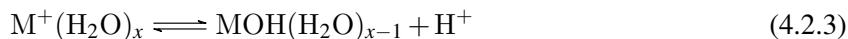
The type of cation in the electrolyte is known to influence the CO<sub>2</sub>RR significantly. While the observations of different research groups are quite consistent with larger cations increasing the electrode's activity and selectivity, the given explanations are more diverse. Even though the presented effects are reported for silver or gold based electrodes they are believed to also apply to tin based systems since the adsorption of CO<sub>2</sub> is not affected and the rate determining step is equal.<sup>[104]</sup> Thorson et al. attributed the measured trend in activity of  $\text{Li}^+ < \text{Na}^+ < \text{K}^+ < \text{Rb}^+ < \text{Cs}^+$  to basically two effects, which are both based on cation adsorption on the electrode surface. First, small cations in general show a higher hydration power, meaning more water molecules are contained within the hydration shell. This leads to a lower cation adsorption on the negatively charged cathode. Adsorbed cations, however, can stabilize reaction intermediates like the CO<sub>2</sub> radical anion. Accordingly, large cations show a better stabilization. Second, adsorbed cations have an influence on the potential of the outer Helmholtz layer,  $\varphi_{\text{OHP}}$ . Due to a higher propensity for larger cations to adsorb on the electrode,  $\varphi_{\text{OHP}}$  becomes less negative.<sup>[104]</sup> This difference in turn results in a decrease in adsorbed H<sup>+</sup> according to equation 4.2.2.<sup>[105]</sup> Since H<sup>+</sup> is involved in the rate determining step of the HER (RDS:  $\text{H}^+ + \text{e}^- \rightleftharpoons \text{H}^*$ )<sup>[106]</sup> a lower concentration of H<sup>+</sup> means a more negative equilibrium potential. Thus, the partial current density of hydrogen at a given electrode potential is smaller for larger cations.

$$[\text{H}^+]_{\text{Electrode}} = [\text{H}^+]_{\text{Bulk}} \cdot \exp \left[ -\frac{\varphi_{\text{OHP}} \cdot F}{RT} \right] \quad (4.2.2)$$

In contrast to these explanations, Mills et al. calculated the adsorption equilibrium potentials for alkali metal cations on transition metals via DFT. Their results showed that cation adsorption is unfavored at typical electrode potentials in CO<sub>2</sub>RR of  $-1.2 \text{ V}$  to  $-1.6 \text{ V}$  (vs SHE) and requires even higher potentials in the range of  $-2.1 \text{ V}$  to  $-2.6 \text{ V}$  (vs SHE). Furthermore, the steric effect of larger cations has been investigated using a modified Poisson-Boltzmann theory and was found to be negligible.<sup>[107]</sup> Singh et al. concluded from these findings that neither cation adsorption nor steric effects provide sufficient



justification and that another effect has to exist. The authors used a multiphysics model to investigate the effect of cation hydrolysis.<sup>[108]</sup> Metal ions in aqueous solution form a hydration shell which can undergo an acid-base reaction according to:



This reaction creates a potential buffer system but for bulk phase cations the  $pK_a$  value is rather high, e.g. 13.6 for  $Li^+$  and 14.7 for  $Cs^+$ . Thus, for medium alkaline electrolytes cation hydrolysis is negligible. This changes significantly when the cation approaches the strongly negative polarized electrode. Due to stronger electrostatic interactions, hydrolysis proceeds much faster and the  $pK_a$  value drops especially for larger cations, e.g. to 11.6 for  $Li^+$  and to 4.3 for  $Cs^+$ . Therefore, larger cations provide a greater buffer capacity and prevent the formation of bicarbonates or carbonates close to the electrode. The larger amount of available  $CO_2$  reduces the reaction's overpotential and increases the electrode's activity.<sup>[108]</sup> These theoretical findings were recently confirmed by in-situ attenuated total reflectance surface-enhanced infrared absorption spectroscopy (ATR-SEIRAS), although to a lesser extent than predicted.<sup>[109]</sup>

In contrast to the straight forward size dependence of alkaline metal cations, the effect of anions is more complex due to their greater variety and more versatile chemical characters. Depending on the type of anion, effects on pH and pH buffer capacity, strength of adsorption or  $CO_2$  buffer capacity have to be considered. In general bicarbonate is the most widely used anion, mainly due to its ability to buffer pH and  $CO_2$  concentration. During  $CO_2RR$  in neutral to alkaline electrolytes hydroxide ions are produced in stoichiometric quantities (see (CEq 4.9)), which leads to a higher local pH, depending on the current density. The carbonic acid/bicarbonate/carbonate system can compensate for this increase to a certain extent which allows higher concentrations of solvated  $CO_2$  at the active site, compared to non-buffered systems.<sup>[38]</sup> Note that bicarbonate or carbonate ions themselves cannot be reduced and have to be protonated and dehydrated to  $CO_2$  first in order to be available for conversion.<sup>[42, 110]</sup> The pH dependency of the  $FE_{CO_2RR \text{ products}} : FE_{H_2}$  ratio is known to have a maximum in neutral to slightly alkaline media with acidic values favoring HER by excessive proton availability and highly alkaline conditions shifting the carbonic acid equilibrium away from free  $CO_2$ .<sup>[51, 78, 111, 112]</sup> This, however, strongly depends on the type of electrode and current density as both have a large influence on the local pH.<sup>[111]</sup>

Different research groups reported the electrolyte's pH value to be one of the most crucial parameters in  $CO_2RR$ , especially when working in an H-type cell with long reactant diffusion pathways. The pH dependency is thereby reported to arise from the related  $CO_2$ /carbonic acid/bicarbonate/carbonate equilibrium instead of protons being involved in the rate determining step.<sup>[41, 113, 114]</sup> However,  $CO_2RR$

results in the production of one or more hydroxide ions, depending on the product formed. Especially at high current densities this gives a much higher local pH compared to the bulk. Burdyny and Smith predicted the local pH to quickly rise with increasing current density and to show similar values at  $-200 \text{ mA cm}^{-2}$ , regardless of the bulk electrolyte. Accordingly, the initial large difference in solvated  $\text{CO}_2$  vanishes with increasing reaction rates.<sup>[111]</sup>

Besides bicarbonate, hydroxide, sulfate, fluoride, chloride, bromide and iodide salts are repeatedly reported. Halides have been investigated especially on copper and silver electrodes and are reported to improve production rates of methane, higher hydrocarbons<sup>[115–117]</sup> and  $\text{CO}$ <sup>[118]</sup> in the order  $\text{F}^- < \text{Cl}^- < \text{Br}^- < \text{I}^-$ . The increasing adsorption strength of  $\text{F}^-$  to  $\text{I}^-$  is assumed to be the decisive factor. Large anions like  $\text{Br}^-$  help to stabilize the adsorbed  $\text{CO}_2$  molecule during the geometry changing first single electron transfer step by donating electron density to the positively polarized carbon atom. Furthermore, it is suggested that the adsorption of halides suppresses the adsorption of protons and thus increases the HER overpotential. Hence, a stronger halide adsorption favors  $\text{CO}_2\text{RR}$  over HER.<sup>[117, 118]</sup> The ranking for activity and selectivity between hydroxide, sulfate, bicarbonate and halides in contrast is not consistent in literature and should be investigated for each electrolysis system separately.<sup>[71, 112, 119, 120]</sup>

In order to minimize ohmic overpotentials and raise energetic efficiency, electrolyte concentrations should generally be adjusted to a maximum in ionic conductivity. This is usually the case for salt concentrations in the order of magnitude of 5 M.<sup>[20]</sup> At lower concentrations fewer ions have to move faster to carry the necessary amount of charge which in turn requires a stronger potential gradient throughout the liquid.<sup>[22]</sup> Higher concentrations, on the other hand, can lead to the formation of neutral conglomerates which do not contribute to conductivity.<sup>[20]</sup> Comparing results presented in literature it can be concluded that higher concentrations are beneficial for the partial current density towards the respective  $\text{CO}_2\text{RR}$  product.<sup>[114, 120–122]</sup> However, for most publications this gain in current density is attributed to lower ohmic resistances. Even when working with  $IR$  corrected electrode potentials it is challenging to devote any benefit exclusively to concentration. Secondary effects arising from the electrolyte's properties have to be considered. For example potassium bicarbonate concentration also influences the amount of solvated  $\text{CO}_2$  available.<sup>[123]</sup> At high concentrations, diffusion coefficients and  $\text{CO}_2$  solubility are also affected.<sup>[124, 125]</sup> Furthermore, ion specific adsorption influences the stabilization of reaction intermediates and/or alters the parasitic proton adsorption within the EDL. Hence, ion concentration is as well important for stabilizing/destabilizing effects.<sup>[38]</sup> Some of the described effects are beneficial while others can reduce the reaction's efficiency and electrolyte concentration should be optimized for each electrolysis system under realistic reaction conditions.

#### 4.2.4.2 The influence of temperature

Even though temperature is not the primary driving force for electrochemical reactions it remains an important parameter. Apart from high temperatures applications e.g. in solid oxide electrolyzers ( $T > 800^\circ\text{C}$ ) many cells are operated under elevated temperature to reduce the overall power consumption. PEM electrolyzers for example are typically operated between  $50^\circ\text{C}$  to  $80^\circ\text{C}$  in order to increase reaction kinetics and mass transport, and to reduce ohmic losses.<sup>[126]</sup>

In general this is common knowledge in electrochemistry. However, investigations for  $\text{CO}_2\text{RR}$  with a systematic variation from room temperature are rather scarce.<sup>[112, 127, 128]</sup> Reported results for electrode activity are absolutely consistent. All studies show an expected rise in current density with increasing temperature as the kinetics of all competing reactions are accelerated.<sup>[17]</sup> Selectivity behavior, on the other hand, is more complex and strongly depending on the investigated system. While M. Azuma suggested a temperature of  $0^\circ\text{C}$  using plane metal foils in an H-type cell with  $\text{CO}_2$  saturated electrolytes,<sup>[127]</sup> Kim *et al.* reported an optimum at  $20^\circ\text{C}$  on a tin foil in a continuous flow-through system.<sup>[112]</sup> While those two investigations focused exclusively on the temperatures influence on the catalyst, the group of McIlwain used a silver based GDE in continuous mode. Here, the authors reported an optimum  $FE$  at  $35^\circ\text{C}$ .<sup>[128]</sup> Besides the differences in optimum temperature, the explanations of all authors are similar. An increasing temperature leads to a decrease in  $\text{CO}_2$  solubility, shifting selectivity towards HER due to an aggravated mass transport. However, suggested low operating temperatures would be adverse for the energetic efficiency since ohmic and concentration overpotentials are generally higher at reduced temperatures. One goal of GDE optimization should therefore be to shift the peak  $FE$  to higher temperatures.

What seems to be forgotten in the given explanation is that besides the solubility of  $\text{CO}_2$ , diffusion coefficients also depend on temperature in reverse order as shown in figure 4.15. Both values, solubility and diffusion coefficient, determine the  $\text{CO}_2$  mass transport, which in the end determines the electrode's performance. Note that in figure 4.15 solubility is given for aqueous 2 M sodium chloride solutions, while diffusion coefficients are reported in pure water due to a lack of literature data. However, the difference between pure water and saline solutions at  $20^\circ\text{C}$  is reported to be as little as  $0.4 \cdot 10^{-5} \text{ cm}^2 \text{ s}^{-1}$ .<sup>[125]</sup> This difference is below the discrepancy between the two given references of around  $0.6 \cdot 10^{-5} \text{ cm}^2 \text{ s}^{-1}$  and can be neglected.

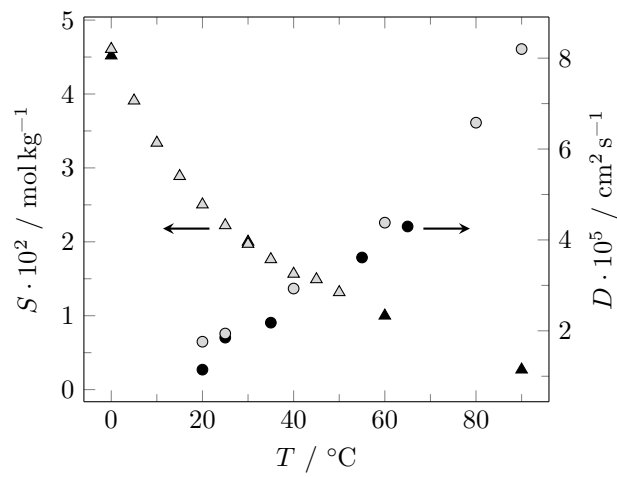


**Figure 4.15:** Influence of temperature on the  $\text{CO}_2$  solubility  $S$  in 2 M aqueous sodium chloride solution (filled triangles,<sup>[124]</sup> open triangles<sup>[129]</sup>) and on the  $\text{CO}_2$  diffusion coefficient  $D$  in water (filled circles,<sup>[130]</sup> open circles<sup>[131]</sup>).

### 4.3 Gas diffusion electrodes

As mentioned, CO<sub>2</sub> solubility in water is very low ( $S_{\text{CO}_2, 20^\circ\text{C}} = 35 \text{ mmol L}^{-1}$ )<sup>[38]</sup> and further decreasing at elevated temperatures.<sup>[124]</sup> This leads to severe mass transport limitation and limits the maximum current density at planar electrodes like metal foils to a few mA cm<sup>-2</sup>. Assuming a stagnant boundary layer of 50 μm<sup>[111]</sup> at the electrode and a temperature of 50 °C,  $j_{\text{lim}}$  can be estimated by:<sup>[50]</sup>

$$\begin{aligned}
 j &= -zF \cdot k_{\text{m, CO}_2} \cdot c_{\text{CO}_2} = -zF \cdot \frac{D_{\text{CO}_2}}{l_{\text{diff}}} \cdot c_{\text{CO}_2} & (4.3.1) \\
 &= -2 \cdot 96485 \text{ C mol}^{-1} \cdot \frac{3.2 \cdot 10^{-9} \text{ m}^2 \text{ s}^{-1}}{5 \cdot 10^{-5} \text{ m}} \cdot 13.2 \text{ mol m}^{-3} \\
 &\approx -164 \text{ kA m}^{-2} = -16.4 \text{ mA cm}^{-2}
 \end{aligned}$$

With  $k_{\text{m, CO}_2}$  being the mass transfer coefficient, calculated by dividing the CO<sub>2</sub> diffusion coefficient  $D_{\text{CO}_2}$ <sup>[132]</sup> by the diffusion length  $l_{\text{diff}}$ <sup>[111]</sup>, and  $c_{\text{CO}_2}$  being the CO<sub>2</sub> concentration in brine at 50 °C<sup>[124]</sup>. Forcing a higher absolute value of current density than -16 mA cm<sup>-2</sup> through the cell only gives rise to hydrogen production since water is the only reducible species remaining at the active site. However, for an industrial application current densities of at least 200 mA cm<sup>-2</sup> are considered essential.<sup>[111, 128]</sup> While high-pressure electrolyzers are known to supply enough CO<sub>2</sub> to reach such current densities, their large-scale application is challenging and expensive.<sup>[133]</sup>

Porous electrodes like GDEs in turn can intensify CO<sub>2</sub> transport at ambient pressure by providing a huge internal surface area with enlarged gas-liquid contact area and enhanced CO<sub>2</sub> mass transfer. Such electrodes are already applied in industrial processes for both energy transformation and chemical synthesis. Examples are water electrolyzers and hydrogen fuel cells or the application of oxygen reduction reaction (ORR) as energy efficient cathode reaction in the chloralkali process.

Inside a GDE a thin film of liquid electrolyte covers catalytic active sites which results in short CO<sub>2</sub> diffusion pathways of a few tens to hundred nm.<sup>[111, 134]</sup> The huge increase in current density when using GDEs compared to planar electrodes was demonstrated to be at a factor of around 100.<sup>[6]</sup> GDEs generally need to provide an optimum compromise between gas, current, heat and ion transport while maintaining a sufficient mechanical stability and high surface area. For industrial applications also processability, long-term stability, toxicity and costs are important. Two basic designs for GDEs can be differentiated from literature, illustrated in figure 4.17, a) + b). The much more frequently used design in CO<sub>2</sub>RR incorporates a highly hydrophobic gas diffusion layer (GDL) for gas transport and a more or less flooded

catalytic layer (CL) as reaction zone (see figure 4.17, a)). This CL bears the catalytic active component bound by an ionomer/polymer. Nafion and poly-(tetrafluoroethylene) (PTFE) are usually used as such binders. While Nafion is more hydrophilic, thus enhancing electrode wetting, catalyst usage and proton transfer, hydrophobic PTFE prevents flooding and creates open gas transport pores.<sup>[68]</sup> This GDL/CL design typically reaches current densities ranging from  $-10 \text{ mA cm}^{-2}$  to  $-200 \text{ mA cm}^{-2}$ , with the highest reported value at  $-388 \text{ mA cm}^{-2}$ .<sup>[51, 53, 55, 57, 67]</sup>

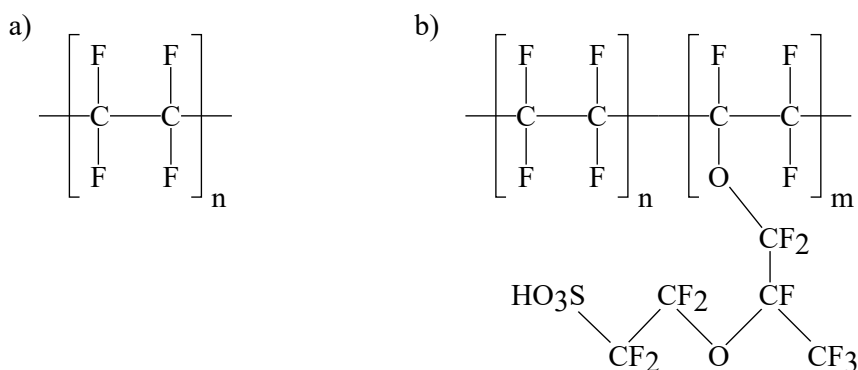


**Figure 4.16:** Chemical structure of a) poly-(tetrafluoroethylene) and b) Nafion.<sup>[135]</sup>

The second GDE design is better-known from alkaline fuel cells<sup>[136]</sup> or oxygen-depolarized cathodes in the chloralkali process.<sup>[137]</sup> It consists of a single layer, containing a homogeneous mixture of the binding ionomer/polymer and carbon black loaded with the active component. Large hydrophobic gas transport pores are thereby located close to smaller pores, which are filled with electrolyte by electrocapillary forces (also called electrocapillarity). Thus, the more or less two-dimensional interface between electrolyte and gas phase in the GDL/CL design is extended deeper into the electrode, creating a larger reaction zone. Such designed GDEs can be produced fairly easy by dry-rolling or dry-pressing a mixture of carbon support, catalyst and binding agent onto a supporting metal mesh, which also acts as current collector.<sup>[138]</sup> Integrating the current collector into the GDE's matrix allows for an efficient electrical contact between cathode and outer contact and a good current distribution (see part b) in figure 4.17). For the ease of preparation, however, homogeneous single-layer GDEs described in the present work were mainly tested without an integrated current collector. Instead, they were electrically contacted by a loose stainless steel mesh and spring contact with a carbon paper acting as mechanical separator (see part c) in figure 4.17).

The reaction zone inside a GDE is often referred to as "three-phase boundary". This, more historically related term, implies the reaction to take place at an interface between solid, liquid and gas phase. Such an interface is restricted to single points or lines within a three dimensional structure, thus providing an extremely small reaction zone. Instead CO<sub>2</sub>RR is supposed to occur on a liquid-solid two-phase boundary with short distances to a gas-liquid two-phase boundary. Indications for a such structured re-

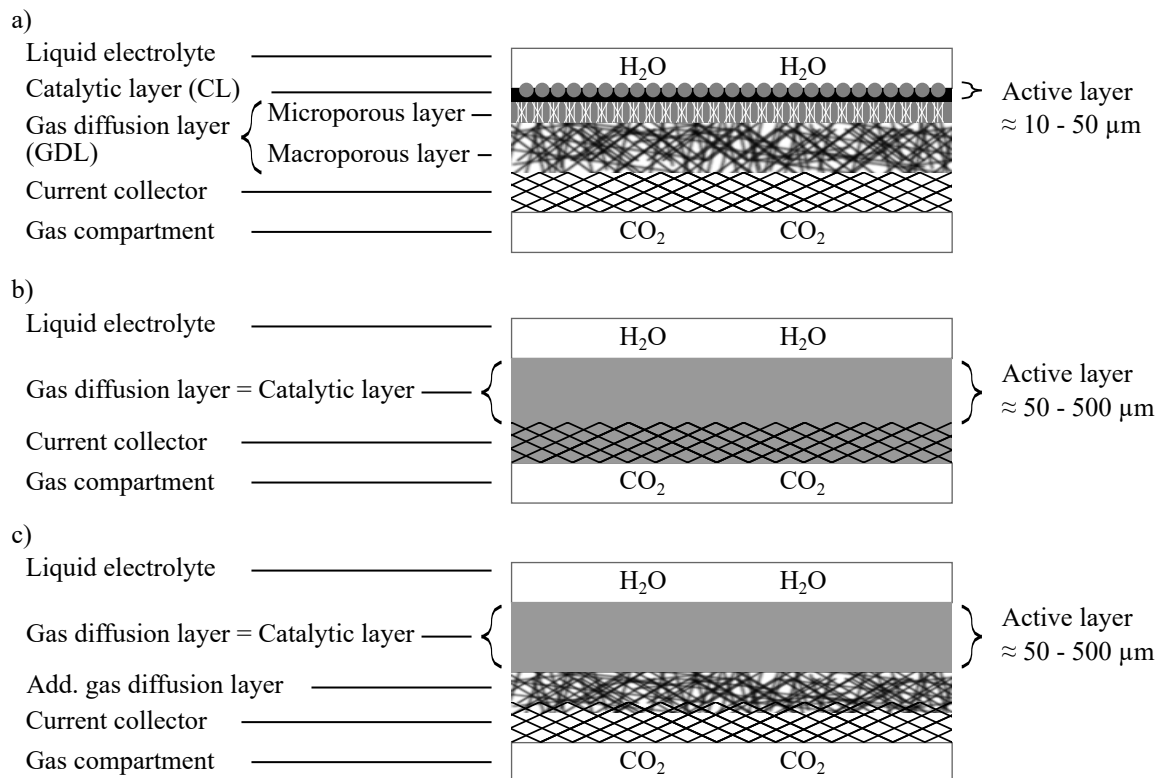


**Figure 4.17:** Schematic illustration of different types of gas diffusion electrodes.

- GDL/CL design with a catalytic layer (CL) bound to a gas diffusion layer (GDL) with a current collector as backbone for enhanced mechanical stability and electric contacting.
- Single-layer design with integrated current collector for enhanced mechanical stability and effective electric contacting.
- Single-layer design as it was used in the present work. The current collector is not permanently integrated but connected by a carbon paper, which acts as mechanical separator and additional gas diffusion layer.

action zone is given by multiple observations. First, most metals form a highly hydrophilic surface when operated at high degrees of polarization, which results in a readily wetting. It is hard to assume that the liquid film covering the metal is interrupted to free up space for gaseous  $\text{CO}_2$ . Second,  $\text{CO}_2\text{RR}$  is strongly accelerated when deploying micro- and mesoporous carbon materials whose pores are completely filled with electrolyte by strong capillary forces. Last, also within a completely flooded CL reduction proceeds where  $\text{CO}_2$  can only be transported by diffusion through the liquid.<sup>[111]</sup> Hence, the term three-phase boundary should only be used as a synonym.

### 4.3.1 Wetting behavior

The properties of described homogeneous single-layer GDEs can be modified significantly by varying type and amount of carbon black, binder or catalyst. Carbon black powders for example can exhibit strongly differing surface areas, pore sizes or hydrophobicity.<sup>[136]</sup> Binding agents, on the other hand, primarily influence the electrode's hydrophobicity and macropore structure. Performance optimization therefore requires considering both components with an ideal ratio of open  $\text{CO}_2$  transport pores and electrolyte filled regions in intense contact. In previous work at the Institute of Technical Chemistry, University of Stuttgart, Germany (ITC), a mixture of 65 wt-% acetylene black (AB) mixed with 35 wt-% PTFE was found to result in a highly efficient  $\text{CO}_2$  mass transport providing appropriate pore sizes and hydrophobicity.<sup>[138]</sup>

Carbon black in general consists of primary nanoparticles coalesced and intergrown to aggregates. These aggregates interconnect inside the GDE to agglomerates by weak intermolecular forces. Aggregates and agglomerates contain mainly mesopores.<sup>[139, 140]</sup> During the GDE preparation process large  $\text{CO}_2$  transport pores are introduced by mixing the carbon black with PTFE particles followed by a ther-

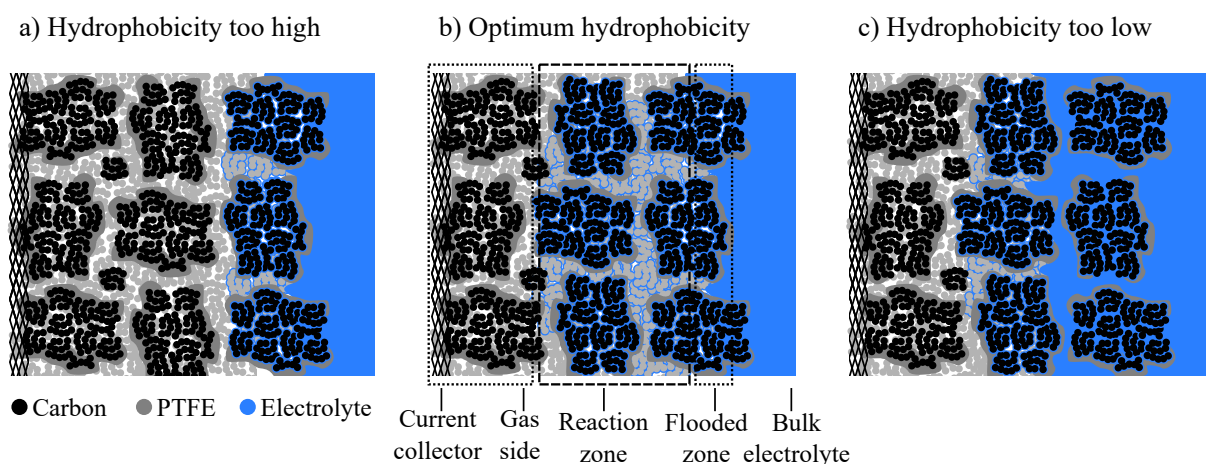


**Figure 4.18:** Schematic representation of the used homogeneous single-layer gas diffusion electrodes with different scenarios for electrode wetting.



mal treatment, during which the PTFE melts, leaving highly hydrophobic macropores. This composition results in the necessary bimodal pore structure.<sup>[138]</sup> When an electric potential is applied mesopores are being filled with electrolyte by capillary forces. Agglomerates are assumed to be filled with and covered by a thin film of electrolyte. CO<sub>2</sub> is converted inside and around these wetted agglomerates bearing the active component.<sup>[134]</sup> The described morphology is visualized in figure 4.18 for different scenarios of wetting. Scenario a) represents an insufficient intrusion of electrolyte. The electrochemical active surface area (ECSA) is rather small, resulting in a low activity and low maximum current density with regard to the geometrical electrode area. Scenario c) represents the opposite extreme case. Too many areas of the GDE are flooded with electrolyte, including macropores. Even though the ECSA is strongly extended, CO<sub>2</sub> transport to a large number of active sites is limited due to elongated diffusion pathways. Only with an optimum wetting as illustrated in scenario b), where macropores remain open, efficient CO<sub>2</sub> mass transport is ensured while maintaining a large ECSA. Note that the existence or extent of the flooded zone in scenario b) is neither confirmed nor refuted yet and is part of ongoing research. An indication for its existence is given by the fact that CO<sub>2</sub> breakthrough is stopped shortly after applying a moderate current density. Hence, the presumably formed flooded zone is sealing the bulk electrolyte towards the gas side.

Before any electric potential is applied, a solid-liquid contact is barely given due to the highly hydrophobic character of both PTFE and AB.<sup>[141]</sup> Only under polarization electrolyte starts to penetrate into the porous structure. This effect is known by the term electrocapillarity, which describes the influence of electric potential on the surface tension. In general, the surface tension is governed by the chemical nature of electrolyte and electrode. When their properties are altered by the application of an electric potential, surface tension is also influenced. An idealized electrocapillary curve is given in figure 4.19 with  $\phi_{ZC}$  being the potential of zero charge. With increasing the absolute value of electrode potential, surface tension is lowered and electrolyte allowed to enter the GDE.<sup>[21, 23]</sup> For carbon based electrodes with small amounts of oxygenated surface groups  $\phi_{ZC}$  is in the range of 0 V (vs. SHE).<sup>[142]</sup> The electrode potential  $\phi$ , on the other hand, depends mainly on the catalysts activity. CO<sub>2</sub>RR usually requires relatively high absolute values of potential, which also means a strong reduction in surface tension. Consequently, the electrode itself needs to possess a highly hydrophobic structure in order to avoid flooding.

Even though electrolyte intrusion depth is expected to depend on the electrode potential in a power function-like manner (see figure 4.19), Lundblad and Björnbom showed that this correlation is indeed rather linear. The authors explained this behavior of PTFE bound carbon electrodes by the opposing effect of electrocapillary and electroosmosis. The latter describes the flux of water being dragged against

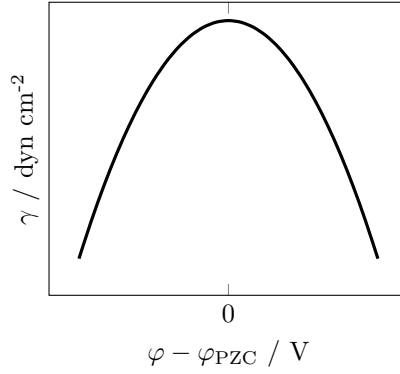


**Figure 4.19:** Idealized electrocapillary curve with surface tension as function of the electrode potential, normalized to the potential of zero charge. Figure adapted from Bard and Faulkner.<sup>[23]</sup>

the direction of electrolyte intrusion by ion migration under current flow. Besides the influence of electrode potential, it was shown that the current density related to the electrode potential has a comparatively small influence on electrolyte intrusion depth and that intrusion continuous over time. The independent investigation of electrode potential and current density was thereby achieved by a potentiostatic-galvanostatic experimental design, using ORR as charge transfer reaction. Altering the oxygen concentration allows for the variation of current density at a fixed electrode potential or of electrode potential for a fixed current density.<sup>[142]</sup>

Determination of the wetted electrode area or ECSA can be done by different methods but is not trivial in complex structures like GDEs. Lead underpotential deposition, hydrogen adsorption, CO stripping or double layer capacitance analysis are all well-known electrochemical methods for obtaining the ECSA.<sup>[27, 143, 144]</sup> However, the main problem thereby is that the electrochemical active surface is not necessarily active for CO<sub>2</sub> reduction. Considering a flooded zone, as illustrated in figure 4.18, c), where reactant mass transport is insufficient, this area is included in the ECSA but cannot contribute to CO<sub>2</sub> reduction. The geometrical intrusion depth, on the other hand, can be assessed by cross section scanning electron microscopy (SEM) imaging coupled with element selective methods like X-ray emission spectroscopy (XES) which can detect residual components of the electrolyte.<sup>[142]</sup>

Within the present work double layer capacitance ( $C_{DL}$ ) was used to assess a measure of the wetted surface area. As described in section 4.1.1, p. 14, the EDL formed at the solid-liquid interface can be seen as a classical capacitor. Its capacitance  $C$ , related to the geometrical surface area, is thereby given as:

$$C_{DL} = \frac{dq}{d\phi} \cdot \frac{1}{A_{geo}} = \frac{I_{DL} \cdot dt}{d\phi} \cdot \frac{1}{A_{geo}} = j_{DL} \cdot \frac{dt}{d\phi} \quad (4.3.2)$$

$$j_{DL} = C_{DL} \cdot \frac{d\phi}{dt} \quad (4.3.3)$$

The double layer charging current density  $j_{DL}$  is therefore proportional to the variation of potential with time  $d\phi/dt$ , also known as the scan rate. Recording cyclic voltammograms in a non-faradaic range where only the double layer capacitor is charged and discharged enables measuring the  $C_{DL}$ . Plotting observed current densities over the scan rate at which they were measured results in a linear correlation with  $C_{DL}$  as slope. An illustration of this method is given in the appendix (see figure 9.4, p. 219). Note that this method provides absolute values of capacitance. In order to obtain the ECSA, surface specific capacitance  $C_{DL, A\ spec.}$  of the electrode-electrolyte couple has to be known:

$$ECSA = \frac{C_{DL}}{C_{DL, A\ spec.}} \quad (4.3.4)$$

### 4.3.2 Mass transport in gas diffusion electrodes

As previously described, mass transport is a fundamental property determining an electrode's activity, especially for reactions with low reactant solubility like CO<sub>2</sub>RR. This does not only apply to reactant transport towards the active site but also to the transport of products away from it into the bulk phase. Referring to the GDE schema in figure 4.18, p. 46, different transport mechanisms are described in the following.

First, CO<sub>2</sub> needs to be transported from the gas bulk phase to the gas-liquid interface by convection and/or diffusion. The influence of convection is only considerable when the gas volume consumed is larger than the produced one, which is the case in CO<sub>2</sub>RR. Especially for formate selective reduction two CO<sub>2</sub> molecules are consumed per extent of reaction while producing almost exclusively solved products. This consumption results in a decrease in pressure along the gas side of the GDE, thus creating a convective CO<sub>2</sub> transport towards the liquid phase. This effect is lowered for high amounts of gaseous side products being formed or at elevated temperatures where solvent evaporation becomes significant. In such case, mass transport by diffusion due to a CO<sub>2</sub> concentration gradient comes into account.

After dissolution in the electrolyte, CO<sub>2</sub> is transported to the active site solely by diffusion. First, film diffusion towards the surface of wetted agglomerates has to be overcome, followed by pore diffusion into these agglomerates where the electrochemical conversion takes place. After reduction to formate a negatively charged species is obtained. This adds ionic drift under an electric field (sometimes referred to as migration or, even though incorrect, as electromigration) to diffusion and convection as sources of ionic mass transport. The force onto ionic molecules per unit charge is thereby given by the electric field, which in turn is obtained by dividing the potential difference between both electrode surfaces by their distance. Together with the substance specific mobility the drift velocity is determined. Inside the GDE,

migration and diffusion are both strongly contributing to mass transport due to a high concentration gradient. In the bulk electrolyte, on the other hand, concentration differences are much lower, especially when forced convection comes into play by stirring or a turbulent liquid flow. Here, migration and convection are the dominating type of mass transport.<sup>[22, 23, 25, 145]</sup>

Diffusion of solved CO<sub>2</sub> towards the active surface is commonly seen as the rate limiting step in CO<sub>2</sub>RR.<sup>[39]</sup> A quantitative description of the diffusion flux is given by Fick's law:

$$J = -D_{\text{CO}_2} \cdot \frac{dc_{\text{CO}_2}}{dx} \quad (4.3.5)$$

with  $dc_{\text{CO}_2}/dx$  being the concentration gradient along the direction of movement and  $D_{\text{CO}_2}$  the diffusion coefficient. The latter is a function of substance motion, which in turn depends on parameters like temperature, solvent viscosity and molecule size.<sup>[22]</sup>

### 4.3.3 Equivalent circuit model of porous electrodes

Besides the mentioned influence of electrolyte concentration on the energetic efficiency and intrinsic activity, conductivity can indirectly influence the electrode's selectivity. Especially for highly wetted GDEs like the ones described in the present work with an intrusion depth of up to 800 μm (see section 7.6.1, p. 149), different contributions to the total resistance should be mentioned. Considering a simple model of porous electrodes shown in figure 4.20, electricity follows the way of lowest total resistance between point A and B. The two extreme cases of path 1 and path 2 shall be discussed here. It is assumed that the concentration of solved CO<sub>2</sub> is only high close to the gas-liquid interface due to its consumption along the pore. Note that this model considers the reaction zone inside a porous electrode as being completely flooded (compare to figure 4.18, p. 46) and active sites being homogeneously spread over the whole electrode.

$$\text{Path 1: } R_{\text{total}} = R_{\text{CB}, 1} + R_{\text{CT}, \text{CO}_2\text{RR}} + R_{\text{el}, 1} + R_{\text{el}, 2} + R_{\text{el}, 3}$$

$$\text{Path 2: } R_{\text{total}} = R_{\text{CB}, 1} + R_{\text{CB}, 2} + R_{\text{CB}, 3} + R_{\text{CT}, \text{HER}} + R_{\text{el}, 3}$$

For path 1 this means that charges can be transferred into liquid phase at a low charge transfer resistance ( $R_{\text{CT}, \text{CO}_2\text{RR}}$ ) due to the large concentration of solved CO<sub>2</sub>. After that, electrolyte resistance ( $R_{\text{el}}$ ) has to be overcome in order to reach point B. At path 2 electricity takes the way of, presumably lower, carbon resistance ( $R_{\text{CB}}$ ) to the geometrical electrode surface. At this point CO<sub>2</sub> availability is low and charge transfer into liquid phase can only proceed when hydrogen is formed at a high overpotential.

Thus, a high charge transfer resistance ( $R_{CT, HER}$ ) has to be overcome. With increasing extent of wetting or electrolyte intrusion depth ( $l_{intr.}$ ) electrolyte resistance increases, gradually giving rise to electrons following path 2 instead of 1. Hence, the selectivity shifts from CO<sub>2</sub>RR products to hydrogen. In order to avoid this shift, electrolyte resistance should be low and the charge transfer resistance for hydrogen production high.

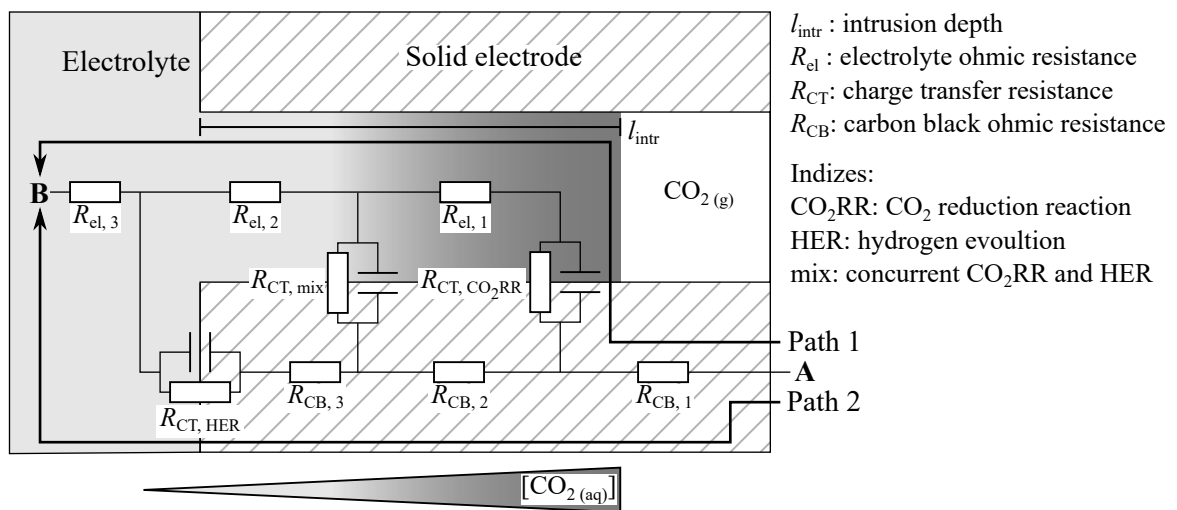


**Figure 4.20:** Equivalent circuit model of porous electrodes, illustrating different pathways for electricity from outer circuit (A) into the bulk electrolyte (B). Figure adapted from V. Schmidt.<sup>[20]</sup>

## 4.4 Process concepts for carbon dioxide electrolysis

For an industrial process it is obviously of high importance to not only optimize the reduction and oxidation reaction but also to envisage products of highest possible market value or of specific need. In the present work, alkaline CO<sub>2</sub>RR is investigated, coupled with OER as oxidation reaction. According to equation (CEq 4.12) in section 4.2.1, p. 28, this system yields a mixture of potassium formate and potassium bicarbonate at the cathode, as well as oxygen on the anode. Depending on the application, different problems may occur from this. Formate is known to be an energy storage molecule, which can be used in a direct formate fuel cell (DFFC). However, its power output is limited when large amounts of bicarbonate are present.<sup>[6]</sup> Other applications require formic acid instead of formate salts, which calls for an additional downstream protonation step.<sup>[11]</sup> Nevertheless, alkaline CO<sub>2</sub>RR has some undeniable advantages discussed in the following section. In order to maintain the beneficial effect of alkaline conditions but still yield pure formic acid as product, a potential coupling of alkaline CO<sub>2</sub>EL with bipolar membrane electrodialysis will be presented. Last, some alternative oxidation reactions are presented that could replace the energy intensive OER.

### 4.4.1 Aspects to consider for alkaline reaction conditions

The reduction of CO<sub>2</sub> can be performed over a wide range of pH with advantages and disadvantages of alkaline over acidic conditions listed below.

Advantages	Disadvantages
a) Suppression of HER through low proton concentration.	a) Production of near stoichiometric amounts of bicarbonate salts.
b) Higher catalyst stability.	b) Two mole of potassium hydroxide consumed per mole formate.
c) Cheaper anode and electrolyzer materials.	
d) Avoids further acidification of the catholyte due to the acidic character of produced formic acid.	

The main reason the majority of researchers work under alkaline conditions is the efficient suppression of HER. Due to the reduced proton concentration, the equilibrium potential of the H<sup>+</sup>/H<sub>2</sub> couple decreases by as much as -826 mV, while the one of CO<sub>2</sub>/formate only drops by -526 mV when increasing the pH from 0 to 14. This increases the difference in onset potential in favor of CO<sub>2</sub>RR. Also, tin

oxide as active species is a lot more stable under alkaline than under acidic conditions according to the Pourbaix diagram (see figure 4.2.3.1, p. 31). The problem of instability in acidic media also applies to the anode catalyst and materials used for the electrolyzer. Under alkaline pH cheap components from nickel or stainless steel can be used. At low pH, on the other hand, only precious metals like platinum or iridium are applicable as anode catalyst, while other cell components like bipolar plates require special corrosion protection.<sup>[146]</sup> Last, when working below the  $pK_a$  of formic acid (3.77), the acidic character of the product formed will further decrease the pH, possibly contributing to an increased hydrogen production.

However, alkaline CO<sub>2</sub>RR also suffers from some fundamental disadvantages. While under acidic conditions ( $pH < pK_a$ ) formic acid is obtained with no significant amount of bicarbonate (reaction (CEq 4.35)), alkaline conditions yield the known mixture of formate and bicarbonate (reaction (CEq 4.36)). Hence, a downstream purification process would be required. Also, reaction (CEq 4.36) consumes two mole of potassium hydroxide which, without regeneration, is an economic showstopper.



#### 4.4.2 Coupling with downstream bipolar membrane electro dialysis

One possibility to use alkaline CO<sub>2</sub>EL and still obtain formic acid as final product is the coupling with downstream protonation of produced formate salts. The bipolar membrane electro dialysis (BPED) is known to be such a process, protonating salts of organic acids like acetic, gluconic, citric, lactic or formic acid, while also producing the respective metal hydroxide.<sup>[147]</sup>

A bipolar membrane (BPM) is a laminate comprising an AEM and CEM with a catalytically active species like graphene oxide in between. When applying a voltage, water is dissociated inside the BPM. Obtained protons and hydroxide ions are then transferred in the direction of cathode and anode, respectively. Different membrane arrangements forming a two or three compartment dialysis cell exist, schematically shown in figure 4.21. Each of the two has its own advantages and disadvantages regarding cell voltage, formic acid cross-over or maximum product concentration.<sup>[147–149]</sup>

The two compartment configuration is generally considered to be more efficient as each electrolyte chamber and membrane contributes to the total cell voltage, mainly by ohmic resistances. However, in this configuration the feed itself is acidified making it unusable for coupling with CO<sub>2</sub>EL as it will be



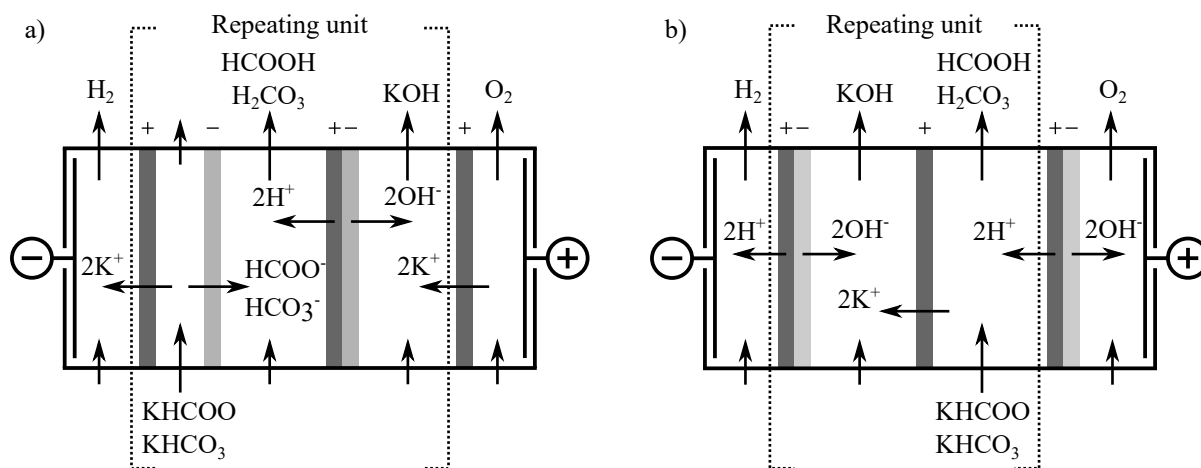


**Figure 4.21:** a) Three and b) two compartment configuration of bipolar membrane electrodes for formic acid and potassium hydroxide production from potassium formate. Figure adapted from Jamie-Ferrer et al.<sup>[148, 149]</sup>

discussed in section 7.8.1, p. 171. Using a three compartment cell, formate and bicarbonate salts are depleted from the input stream with cations and anions leaving through the CEM and AEM, respectively. Anions are then protonated to form the respective acid while potassium cations are combined with hydroxide anions. Both configurations are terminated by a reduction and an oxidation reaction. Both reactions contribute to the overall cell voltage which makes stacking of multiple repeating units essential for efficient dialysis.

Even though this seems a promising method to produce formic acid, so far, it is investigated to a very limited extent. From literature only the protonation of pure formate solutions is known. However, it could also help to purify the electrolysis product stream from the large amounts of bicarbonate. Protonation of bicarbonate yields unstable carbonic acid, which decomposes to water and  $\text{CO}_2$ . After a simple gas-liquid separation, pure formic acid solution can be obtained. Of course this presumes no addition of supporting electrolytes, e.g. potassium chloride. Instead, a recycled mixture of formate and/or bicarbonate needs to be applied.

A very fundamental problem of electrochemically generated products trapped in liquid phase such as formate/formic acid is their concentration. They are typically obtained in concentrations well below 1 M (< 5 wt-%). Compared to that, regarding formic acid as product, the merchantable concentration is 22.5 M (85 wt-%), making a downstream distillation step necessary. According to calculations of the project partner Plinke GmbH, KBR, distillation of a 1 M aqueous formic acid solution would require  $43\,638 \text{ kWh } t_{\text{FA}}^{-1}$  of energy input, which currently corresponds to around  $1462 \text{ € } t_{\text{FA}}^{-1}$  (assuming  $0.055 \text{ € kWh}^{-1}$  heating costs and  $0.01 \text{ € kWh}^{-1}$  cooling costs).<sup>[150]</sup> Considering a 85 wt-% formic acid market value of  $600 \text{ € } t_{\text{FA}}^{-1}$ <sup>[151]</sup>, any discussion for economic efficiency is superfluous in this scenario. Hence, a concentration step between electrolysis and distillation is necessary. In general, BPED can also

be used for this purpose. By recirculating the obtained formic acid product stream in the BPED cell, its concentration can be increased. In section 7.8.1, p. 171, it will be shown that a concentration of around 6 M to 7 M is necessary to minimize the total energy consumption of BPED and distillation.

Ferrer et al. already demonstrated the production of up to 7 M formic acid from 2 M sodium formate solutions in a three compartment BPED cell.<sup>[147]</sup> They reported an acid current efficiency of around 75 % at a product concentration of 7 M and identified the losses as being caused by diffusion of uncharged formic acid through the AEM and BPM. The rate of diffusion thereby strongly depends on the used membrane, but also on the applied current density, salt concentrations in neighboring compartments and on the temperature.<sup>[147, 148]</sup>

### 4.4.3 Alternative anode reactions

In order to reduce the power consumption of an electrolyzer, both cathode and anode reaction are to be optimized. In light of this, OER shows some fundamental issues. It brings in a quite high standard potential of 1.23 V (vs. RHE) and, even when using highly efficient iridium or nickel/iron based catalysts, an additional overpotential of around 0.35 V.<sup>[146]</sup> The obtained product oxygen may not be of sufficient value to justify this high energy input. Other oxidation reactions and oxidation products should therefore be considered and are already reported. A few examples shall be given here. Lister and Dufek reported the coupling of CO<sub>2</sub>RR with chlorine production.<sup>[152]</sup> However, considering the well established chloralkali process the need for this product is questionable. Also, the standard electrode potential of the Cl<sub>2</sub>/Cl<sup>-</sup> redox couple ( $\varphi^\theta = 1.36\text{ V vs SHE}$ ) is even higher than the one for OER. The oxidation of processed biomass is another possible reaction. Here, alcohols can be used energetically to minimize the electrical energy consumption by total<sup>[153]</sup> or partial oxidation<sup>[154, 155]</sup> of the reactant (alcohol oxidation reaction (AOR)). The partial oxidation also allows for the synthesis of products like acetate, lactate or glycolate, which can be obtained with high selectivity.<sup>[154]</sup> The main benefit is a much smaller equilibrium voltage for CO<sub>2</sub>RR-AOR than for CO<sub>2</sub>RR-OER (see figure 4.22) but anode materials often suffer from poisoning or carbonation.<sup>[156]</sup> In contrast to the oxidation of water during OER, partial oxidation to hydrogen peroxide has also been reported<sup>[157]</sup> even though the product's stability is rather low. Here the direct application e.g. for disinfection without the need for storage would be advantageous.

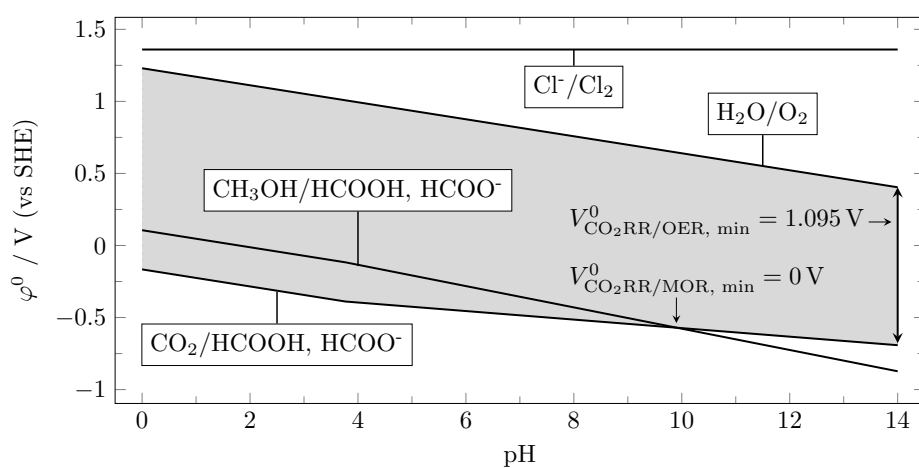


**Figure 4.22:** Pourbaix diagram of different oxidation reactions with resulting equilibrium cell voltages when coupled with CO<sub>2</sub> reduction reaction to formic acid/formate. OER: oxygen evolution reaction; MOR: methanol oxidation reaction.



## 5 | Motivation and Objectives

The electrochemical production of formate or formic acid from CO<sub>2</sub> is a promising way to store excess energy from renewable energy sources and to produce a value-added substance. Besides the massive amount of publications focusing on exploration of new, highly active catalyst systems, investigations focusing on a systematic variation of reaction conditions are far less reported. Reaction conditions, as well as electrode and cell design are important aspects with an at least similar optimization potential than the electrocatalyst. Important steps towards an industrial application have also been shabbily treated so far. Long-term stability applies not only to the catalyst itself but also to the electrode bearing the catalyst and needs to be extended to several hundreds or thousands of hours. The scalability of the electrode system is at least as important. This includes the catalyst synthesis, electrode fabrication, performance during electrolysis and the complete housing of the electrochemical cell.

Recent work of D. Kopljar at the Institute of Technical Chemistry, University of Stuttgart, Germany (ITC) demonstrated a superior performance of specially designed gas diffusion electrodes (GDEs) regarding activity and selectivity at high current densities.<sup>[138]</sup> However, multiple questions regarding reaction conditions, catalyst or electrode preparation and composition, long-term stability, scale-up and general process concepts remained open. These questions were investigated in the present work, which consequently separates into said aspects.

Scattered literature reports on the examination of reaction conditions like temperature, type and concentration of electrolyte, feed purity are existent but are often inconsistent, mostly since they are based on different electrode systems. Here, a large potential for increasing the energetic efficiency by reducing ohmic losses is given, provided that the chosen electrode is able to work under elevated temperature and electrolyte concentration. Also, type, concentration, pH and purity of the electrolyte are reported to have a significant influence on activity and selectivity, which should be investigated also for the system under investigation.

Electrode composition including type and dispersion of the electrocatalytically active species mainly determines activation and concentration overpotentials. So far, some of the materials and processing

parameters used during previous investigations are based on historical specifications that have not been investigated in a systematic manner. Fine-tuning certain specifications of the GDE like the type of catalyst, electrode loading and composition of the binder still bears a large potential for investigations and optimizations.

Last, some fundamental problems regarding the process concept need to be tackled. Although alkaline CO<sub>2</sub> reduction provides indisputable benefits, formic acid as product is of greater interest. Proof-of-concept studies focusing on downstream processing and exchange of the anode reaction are therefore to be performed to evaluate their general feasibility.

Summarizing the tasks for the present work: an energy efficient and long-term stable system has to be developed based on a recently introduced GDE design. Scalability and system integration are thereby also of great importance with regard to industrialization.







## 6 | Experimental Section

The following sections give a detailed description of preparation methods, experimental setup, analytical and electrochemical measuring routines, as well as data evaluation. Electrode preparation methods include the oxidative pretreatment of Vulcan XC 72 (VX), loading of the active component on the carbon black and finally the GDE fabrication itself. Description of the experimental setup includes the developed electrochemical cells and established peripheral equipment for fluid management, electric power control and analytics. A list of the used chemicals with respective purity and supplier is given in the appendix (see table 9.1 and 9.2, p. 211 and 212).

Note that given electrode loadings always refer to the mass of metal in its metallic form, even though active species are mainly present as oxide prior to or during electrolysis. The reason for this convention is that the homogeneous precipitation method, described later on, does not always quantitatively result a specific oxide form. This would lead to miscalculated loading values and an error in weighing during the gas diffusion electrode (GDE) preparation.

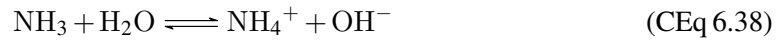
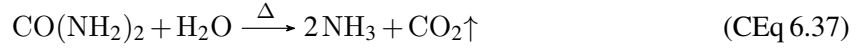
### 6.1 Preparation methods

#### 6.1.1 Homogeneous precipitation of supported metal oxides

Except for supported palladium nanoparticles, described in section 6.1.3, all catalytic active components reported in the present work were prepared by a homogeneous precipitation method first described by Song and Kang.<sup>[158]</sup> D. Kopljar transferred their method to the loading of carbon black with tin oxide, resulting in highly dispersed nanoparticles with narrow size distribution.<sup>[19, 158]</sup> Now, this method was further developed to match requirements for scalability and processability.

The basic principle is a homogeneous metal oxide precipitation induced by urea decomposition. In contrast to other precipitating agents like aqueous hydroxide solutions, urea hydrolysis raises the pH very homogeneously over the whole reaction vessel, rather than locally at the point of addition. Temperature

induced urea hydrolysis follows the chemical equation (CEq) (CEq 6.37), accompanied by the formation of hydroxide ions (CEq 6.38). These hydroxide ions in turn catalyze the hydrolysis of the tin precursor (CEq 6.39). During further electrode processing, formed tin(II) oxide is completely oxidized to tin(IV) oxide (CEq 6.40), as confirmed by X-ray diffraction (XRD) analysis (see appendix section 9.4, p. 220).



The standard catalyst, resulting in an electrode loading of  $\sigma_{\text{Sn}} = 1 \text{ mg cm}_{\text{geo}}^{-2}$  of tin on acetylene black (AB) ( $w_{\text{Sn on AB}} = 2.6 \text{ wt}\%$ ), was prepared as follows. AB (4.53 g) was suspended in 100 mL double-distilled water, containing 10 mM of sodium dodecyl sulfate (SDS), by vigorous stirring overnight. The SDS surfactant was added to enhance the wetting of AB and ensure an intense solid/liquid contact during synthesis. In order to completely break down the hydrophobic agglomerates, the suspension was subsequently sonicated for 1 h. The volume  $V_f$  of the used reaction vessel was thereby around double the size as liquid phase required. After addition of 0.225 g of  $\text{SnCl}_2 \cdot 2\text{H}_2\text{O}$  ( $c = 0.01 \text{ M}$ ) and 3 g of urea ( $c = 0.5 \text{ M}$ ), hydrolysis was performed by heating to  $90^\circ\text{C}$  under reflux for 4 h. The slurry was cooled down to room temperature naturally, filtered, the supported catalyst carefully washed with 500 mL double-distilled water and dried at  $100^\circ\text{C}$  over night. The masses for metal precursor (prec), carbon black (CB) and urea depend on the desired metal (Me) loading  $\sigma_{\text{Me}}$  and the solvent volume (batch size). They were calculated by the following equations. Urea concentration was always kept at the optimum value for smallest possible nanoparticles (0.5 M), as reported by Song and Kang.<sup>[158]</sup>

$$m_{\text{prec}} = c_{\text{prec}} \cdot M_{\text{prec}} \cdot V_{f, \text{solvent}} \quad (6.1.1)$$

$$m_{\text{CB}} = \frac{38 \text{ mg cm}_{\text{geo}}^{-2} \cdot V_{f, \text{solvent}} \cdot c_{\text{prec}} \cdot M_{\text{Me}}}{\sigma_{\text{Me}}} \quad (6.1.2)$$

$$m_{\text{urea}} = c_{\text{urea}} \cdot V_{f, \text{solvent}} \cdot M_{\text{urea}} \quad (6.1.3)$$

A detailed derivation of the given equations is presented in the appendix (see section 9.2, p. 215). The described precipitation method was further investigated by varying the tin precursor type and concentration, as well as by varying hydrolysis temperature and solvent. For XRD analyses of the precipitated

metal oxides it was necessary to precipitate them in absence of the support. As supported catalyst the high amount of carbon did not allow for sufficiently intensive reflexes.

### 6.1.2 Oxidative pretreatment of the Vulcan XC 72 support

In order to allow for an easier electrolyte intrusion at low degrees of polarization VX was treated with nitric acid. Introduction of oxygenated species to the carbon surface increases the hydrophilicity and intensifies electrode wetting. VX ( $m = 11.89$  g) was suspended in nitric acid ( $c = 7.2$  M,  $V_{f, \text{solvent}} = 250$  mL) and stirred at room temperature for 30 min. The suspension was heated to  $60$  °C and stirred for another 30 min. After cooling down to room temperature naturally, the suspension was filtered and washed thoroughly with deionized water. Finally the modified carbon was dried at  $100$  °C over night.

### 6.1.3 Synthesis of supported palladium nanoparticles

In contrast to most metal oxide catalysts, palladium needs to be present in its metallic form to achieve a high activity for  $\text{CO}_2$  reduction reaction ( $\text{CO}_2\text{RR}$ ). The standard urea precipitation method, described in section 6.1.1, however, does not supply reductive conditions and is therefore unsuitable. Also, since the Pd-GDE is supposed to be operated under little absolute values of cathode potentials the typically used AB/poly-(tetrafluoroethylene) (PTFE) matrix is not suitable. Its extreme hydrophobicity would not allow for a sufficient wetting and hence electrochemically active surface area. Instead, oxidatively pretreated VX was found to be more suitable and was loaded with palladium.

The palladium nanoparticle synthesis is inspired by the method described by H. Nguyen, using ethylene glycol as both solvent and reduction agent.<sup>[159]</sup> For an anticipated metal loading of  $\sigma_{\text{Pd}} = 1$  mg  $\text{cm}_{\text{geo}}^{-2}$  ( $w_{\text{Pd on VX}} = 2.6$  wt-%), 7 g of the pretreated VX were suspended in 500 mL of ethylene glycol. After strong magnetic stirring over night, 0.183 g of  $\text{Pd}(\text{NO}_3)_2 \cdot 2\text{H}_2\text{O}$  dissolved in 80 mL of water were added. The mixture was sonicated for 1 h and subsequently heated to  $90$  °C for 3 h under reflux. After cooling down to room temperature naturally, the loaded CB was filtered and thoroughly washed with water. Finally, it was dried at  $100$  °C over night.

### 6.1.4 Preparation of gas diffusion electrodes

Homogeneous single-layer GDEs were prepared by mixing the catalyst loaded CB ( $m_{\text{Me}_x\text{O}_y+\text{CB}}$ ) with a powdered polymeric binder in a knife-mill, followed by a dry-pressing and a heating step. The amounts of material needed for a single electrode were calculated as follows. If not stated otherwise each electrode contained 38 mg of pure CB per square centimeter of geometrical surface area and a binder:CB ratio of

35:65. Typically, PTFE was used as binder, which could partly be replaced by a Nafion powder to alter the electrode's hydrophobicity. Obtained electrodes usually showed a height of around 800  $\mu\text{m}$ . For a detailed derivation of the following equations see the appendix (section 9.2, p. 215).

$$m_{\text{Me}_x\text{O}_y+\text{CB}} = A_{\text{geo}} \cdot 38 \text{ mg cm}_{\text{geo}}^{-2} + \frac{1}{v_x} \cdot \frac{\sigma_{\text{Me}} \cdot A_{\text{geo}}}{M_{\text{Me}}} \cdot M_{\text{Me}_x\text{O}_y} \quad (6.1.4)$$

$$m_{\text{binder}} = A_{\text{geo}} \cdot 38 \text{ mg cm}_{\text{geo}}^{-2} \cdot \frac{w_{\text{binder}}}{w_{\text{CB}}} \quad (6.1.5)$$

$v_x$  represents the stoichiometric factor of the metal in the metal oxide. The calculated masses were multiplied with a factor  $f_{\text{mixture}}$  in a way that the mass of the mixture was around 4 g, which corresponds to the filling quantity of the knife-mill.

$$m_{\text{GDE}} = m_{\text{Me}_x\text{O}_y+\text{CB}} + m_{\text{binder}} \quad (6.1.6)$$

$$m_{\text{mixture}} = f_{\text{mixture}} \cdot m_{\text{GDE}} \quad (6.1.7)$$

Mixing was performed in a stepwise manner by setting the knife-mill to full speed for 10 s followed by a 20 s break, allowing the fine powder to settle down again. These steps were repeated for a total of three times. For electrodes with a geometrical surface area of 7  $\text{cm}^2$  to 28  $\text{cm}^2$  the amount of mixed material as calculated from equations 6.1.4 to 6.1.6 was placed in a cylindrical steel mask with corresponding area. The mixture was pressed in a hydraulic press with a pressure of 10  $\text{kN cm}^{-2}$  for 3 min. Finally, the extremely fragile electrode was sintered in a muffle furnace under nitrogen atmosphere at 340  $^{\circ}\text{C}$  (heating rate = 3.5  $\text{K/min}$ ) for 10 min. This method was varied in terms of pressing power and time, as well as for the temperature and duration of thermal treatment.

Electrodes of larger area (110  $\text{cm}^2$ ) were prepared by the project partner German Aerospace Center, Stuttgart, Germany (DLR). They exclusively contained PTFE powder of 520  $\mu\text{m}^{[160]}$  in participle size to ensure a sufficient mechanical stability. A rectangular frame (with height, width and length of 1 cm, 12 cm and 25 cm) was placed on a fine, flat nickel mesh of around 20 cm times 30 cm. The frame was completely filled with the catalyst loaded CB and PTFE mixture. Any excess material was removed by a doctor blade. The light powder mixture was manually precompressed in order to be able to remove the solid frame. The precompressed electrode was then transferred into a roller with a roll gap of 600  $\mu\text{m}$ . Electrodes were rolled in a single pass with a speed of around 2  $\text{cm s}^{-1}$  and a force of 1 kN. Finally, the electrode was sintered under nitrogen with the same temperature program as for the previously described 7  $\text{cm}^2$  to 28  $\text{cm}^2$  large electrodes and cut into shape (around 9 cm times 12 cm).

## 6.2 Experimental setup

Figure 6.1 gives an overview of the complete setup planned and constructed for the present work. It was designed to fit the needs of a semi-batch and continuous mode of operation for all three electrochemical cells, described later on.

For that purpose two CO<sub>2</sub> mass flow controllers (MFCs) (C-1 and C-2) were available, covering a dosing range of 5 mL min<sup>-1</sup> to 500 mL min<sup>-1</sup>. This corresponds to a range in current of about 0.2 A to 20 A (see table 6.5, p. 81). Another 250 mL min<sup>-1</sup> nitrogen MFC (C-3) was available for flushing or dilution of the gas feed. Depending on the necessary volumetric gas flow rate, two different tubing sizes were available. In order to minimize the dead volume, 1/8" pipes and tubes were used for flow rates smaller than 50 mL min<sup>-1</sup>. On the other hand, when flow rates higher than 50 mL min<sup>-1</sup> were necessary, 1/4" pipes and tubes were used to avoid a critical back pressure that damages the GDE. For the same reason, an outlet gas by-pass (V-17) was used to pass only around 5 mL min<sup>-1</sup> through one of the GCs. After passing a gas-liquid separator (GLS), outlet gas flow quantification was done by a 3 mL min<sup>-1</sup> to 500 mL min<sup>-1</sup> mass flow meter (MFM) (R-3). The gas composition was then analyzed using gas chromatography (GC), either in a conventional gas chromatograph (7890A, Agilent Technologies) or in a micro gas chromatograph ( $\mu$ -GC, G3581A, Agilent Technologies). Pressure monitoring (I-9) only serves for malfunction analysis.

In order to control the liquid phase bulk temperature during electrolysis both electrolytes were circulated through heat exchange loops placed inside a thermostat. Circulation was thereby done by means of two peristaltic pumps (P-2 and P-3) with a volumetric flow range of 10 mL min<sup>-1</sup> to 100 mL min<sup>-1</sup> and temperature recording at R-4 and R-5.

Electric power was supplied by a Gamry Reference 3000 potentiostat, which delivered a maximum current of  $\pm 3$  A at up to  $\pm 16$  V. A reference 30k booster was available for higher currents, which could supply a maximum of  $\pm 30$  A, with an asymmetric compliance voltage limit of +20 V and -2.5 V. Thus, during operation at a current higher than 3 A, electrolysis was performed in a two electrode configuration with the anode serving as working electrode.

Gas management, meaning the feed dosing and outlet gas flow recording, was done by a custom-made Excel visual basic for applications (VBA) script with FlowDDE as data exchange server. Recording of electrolyte temperature and cell voltage (if not recorded by the potentiostat), as well as controlling of the circulation pumps was done by custom-made Python scripts. Actual values therefore are provided by a current/voltage and two thermocouple bricklets (non-stackable sensor/actuator modules) connected

to a master and two direct current (DC) bricks (stackable microcontroller modules for sensing and controlling) (Tinkerforge GmbH).<sup>[161]</sup> Controlling of the potentiostat was done via the Gamry Framework software. The conventional GC and the  $\mu$ -GC were controlled by Agilent's Chemstation and OpenLab software, respectively.

### 6.2.1 Details for the semi-batch mode of operation

For short times of electrolysis all used cells could be operated in semi-batch mode, meaning the electrolytes were added batch-wise while  $\text{CO}_2$  was fed continuously. Pumps P-4 and P-5 were thereby disconnected. Electrolyte volume of both half-cells including the external heat exchange system is given in table 6.1. While the catholyte was varied, 5 M potassium hydroxide was used as anolyte. During standard operation time of 45 min for galvanostatic electrolysis three GC measurements were performed. While gas analysis was done online, a sample of the catholyte was taken and measured by offline high performance liquid chromatography (HPLC) after electrolysis.

### 6.2.2 Details for the continuous mode of operation

The setup illustrated in figure 6.1 represents the continuous mode of operation. For the exact supply of fresh electrolyte to each of the two half-cells, a multi-channel peristaltic pump (P-4.1 and P-4.3, model reglo digital, Ismatec) was used. The volumetric flow in each channel could be controlled individually within a range of  $0.1 \text{ mL min}^{-1}$  to  $30 \text{ mL min}^{-1}$ . Since the used flow rates (see table 6.4 and 6.5, p. 80 and 81) were too low to effectively control the liquid phase temperature, circulation through the heat exchange loops was also enabled. While the catholyte was varied for investigation, 1 M potassium hydroxide was used as anolyte (if not stated otherwise). In this mode of operation liquid products were analyzed by online HPLC. The reference electrode used in the  $1 \text{ cm}^2$  standard GDE test cell could not be installed leak-proof and hence the cathode side remained open. Therefore, a portion of the catholyte (about 50 % of the feed flow rate) was pumped (P-4.2) through the HPLC's sample loop. The remaining catholyte was pulled off by another peristaltic pump, here referred to as excess removal pump (P-5) (see figure 6.2, p. 72). Condensed water vapor was removed from the gas flow by separation in a GLS and the outlet gas phase was analyzed by the online  $\mu$ -GC.

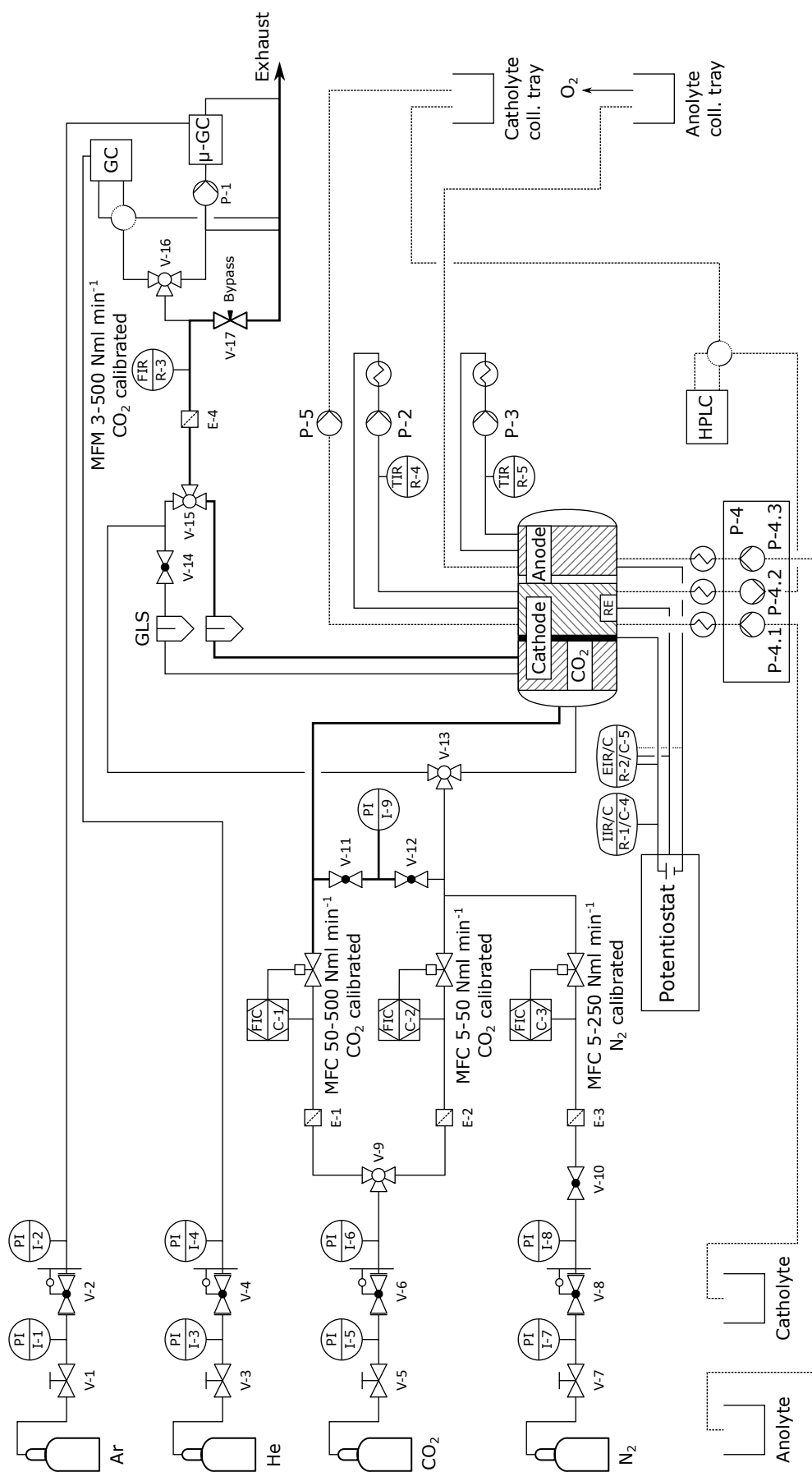


**Figure 6.1:** Piping and instrumentation diagram of the whole setup installed for the present work. 1/8" tubing (thin lines) was used when working with the 1 cm<sup>2</sup> standard GDE test cell and 1/4" tubing (bold lines) was used for both scaled-up cells. P-4, P-5 and the online high performance liquid chromatograph (HPLC) were only connected during continuous mode of operation.

### 6.2.3 Used and developed electrochemical cells

Within the present work three custom-made electrochemical cells were designed and fabricated in-house. Two of them were based on a similar model developed by the project partner DLR, namely the standard GDE test cell with an active cathode area of  $1\text{ cm}^2$  (see figure 6.2), as well as the first scaled-up model with  $10\text{ cm}^2$  (see figure 6.3). For both cells the main housing parts were milled from poly-(methyl methacrylate) (PMMA) blocks while other parts like cathode masks or anode and membrane holders were 3D printed using fused deposition modelling (FDM) with acrylonitrile butadiene styrene (ABS) filament (Prusa Research). The mostly transparent structure allows visual observation and easy constructional adaptation to any occurring problem.

Both cells represent a bridging technology between typical electrochemical cells made for evaluating catalysts and industrial cells with maximum energy efficiency. Small batch cells housing simple planar or rotating disk electrodes (RDEs) are reasonable for assessing intrinsic catalytic activities at low amounts of material. However, these kinds of cells do not address aspects like heat and mass transport, local discrepancies in electrolyte properties or electrode degeneration at industrial relevant current densities. Fully optimized flow-through cells, on the other hand, require much more effort for catalyst and electrode preparation, cell assembly or implementation of reference electrodes.

The standard GDE test cell was used to assess and optimize electrode, electrolyte or process condition related effects with little amounts of electrode material necessary. The obtained findings were then used to apply optimized reaction conditions and electrode compositions to the first scaled-up cell to investigate effects originating from geometrical differences. Both cells are housing circular GDEs with the current collector and GDL being pressed against the GDE through a spring contact. For the  $1\text{ cm}^2$  standard GDE test cell a Hg/HgO (1 M KOH) reference electrode was used. In the  $10\text{ cm}^2$  cell, however, a silver wire was applied as pseudo reference electrode, which was in turn referenced against the regular Hg/HgO reference electrode in the respective electrolyte at operating temperature.

Based on knowledge created from monitoring product selectivity and differentiating multiple contributions to the cell voltage, a second stage scale-up cell was developed. It exhibits a fundamental change in geometry by applying a filter press design, shown in figure 6.4. Reduction of the cathode-anode distance and of ohmic resistances within the electric contacting of the cathode were thereby key factors. First, a specially designed and 3D printed catholyte flow field allowed for a mechanically stable GDE support while ensuring uniform flow distribution<sup>[78]</sup> at a cathode-anode distance of just 4 mm. Second, the cathode's current collector was integrated into the GDE by rolling the prepared mixture of binder and



carbon black onto a nickel mesh. This results in an intensive contact and reduces electronic resistances. Last, the anode was integrated into a thin silicon sealing. Hence, the gap between membrane and anode was minimized and trapping of oxygen bubbles was reduced. In contrast to the other two designs, an equally sized cathode, membrane and anode was used to comply with even larger industrial electrolyzers. Due to the compact design no reference electrode was incorporated.

All cells host a fine nickel mesh as anode for oxygen evolution reaction (OER) as counter reaction. For the 1 cm<sup>2</sup> and 10 cm<sup>2</sup> cell a larger anode compared to the cathode was chosen to avoid any possible limitations originating from the OER. If not stated otherwise electrolytes were prepared from American Chemical Society (ACS) grade salts and in-house prepared double-distilled (DD) water. If the electrolyte's pH had to be altered it was adjusted with solid metal hydroxide with matching cation. An overview of important characteristics of all three cells is given in table 6.1.

**Table 6.1:** Overview of important characteristics for all three electrochemical cells developed within the present work.

A: geometrical surface area;  $d_{CM}$ ,  $d_{AM}$ : cathode to membrane and anode to membrane distance.

Indices: A: anode; M: membrane; C: cathode; el: electrolyte.

Values for electrolyte volume  $V_{f,el,C}$  and  $V_{f,el,A}$  include the reactor, as well as the external heat exchange system.

Cell	$A_{GDE}$	$A_A$	$A_{GDE}/A_M$	$d_{CM}$	$d_{AM}$	$V_{f,el,C}$	$V_{f,el,A}$	Electrode configuration
	/ cm <sup>2</sup>		-	/ mm		/ mL		
Standard GDE test cell	1	2	0.08	26	10	20	40	Two and/or three (Hg/HgO (1M KOH))
First stage scale-up	10	20	0.25	19	2-8	100	150	Two and/or three (pseudo Ag)
Second stage scale-up	70	70	1	4	<1	35	≈ 5	Two

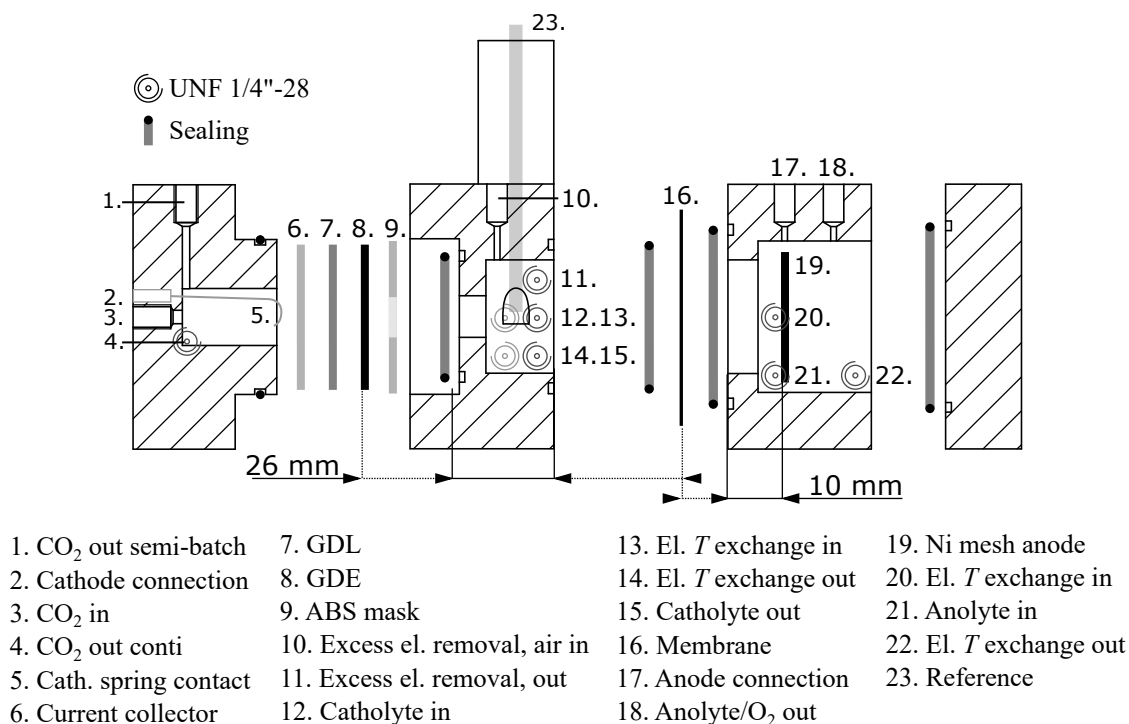


**Figure 6.2:** Exploded view of the developed standard gas diffusion electrode test cell, which is based on a similar cell from German Aerospace Center, Stuttgart, Germany. The cell houses a **gas diffusion electrode (GDE) of 7 cm<sup>2</sup> with an active electrode area of 1 cm<sup>2</sup>** and exhibits a cathode-anode distance of 36 mm. Electrical contact to the GDE is given by a stainless steel spring contact pushing against the current collector and gas diffusion layer (GDL). During semi-batch mode of operation ports 4, 11, 12, 15 and 20 were blocked. For continuous long-term measurements port 1 is closed and CO<sub>2</sub> removed at the bottom of the gas compartment in order to withdraw condensed water. Port 10, 11: excess electrolyte removal. During electrolysis catholyte is continuously withdrawn at port 15 and pumped through the online HPLC with  $\dot{V}_{f, \text{HPLC}} < \dot{V}_{f, \text{el. C, in}}$  to avoid draining, potentially caused by fluctuations in the respective flow rate. The remaining excess catholyte is withdrawn periodically when liquid level reaches the outlet 11, where a pump continuously pulls air through port 10. As for this effort it was possible to employ a non-leak-proof reference electrode.

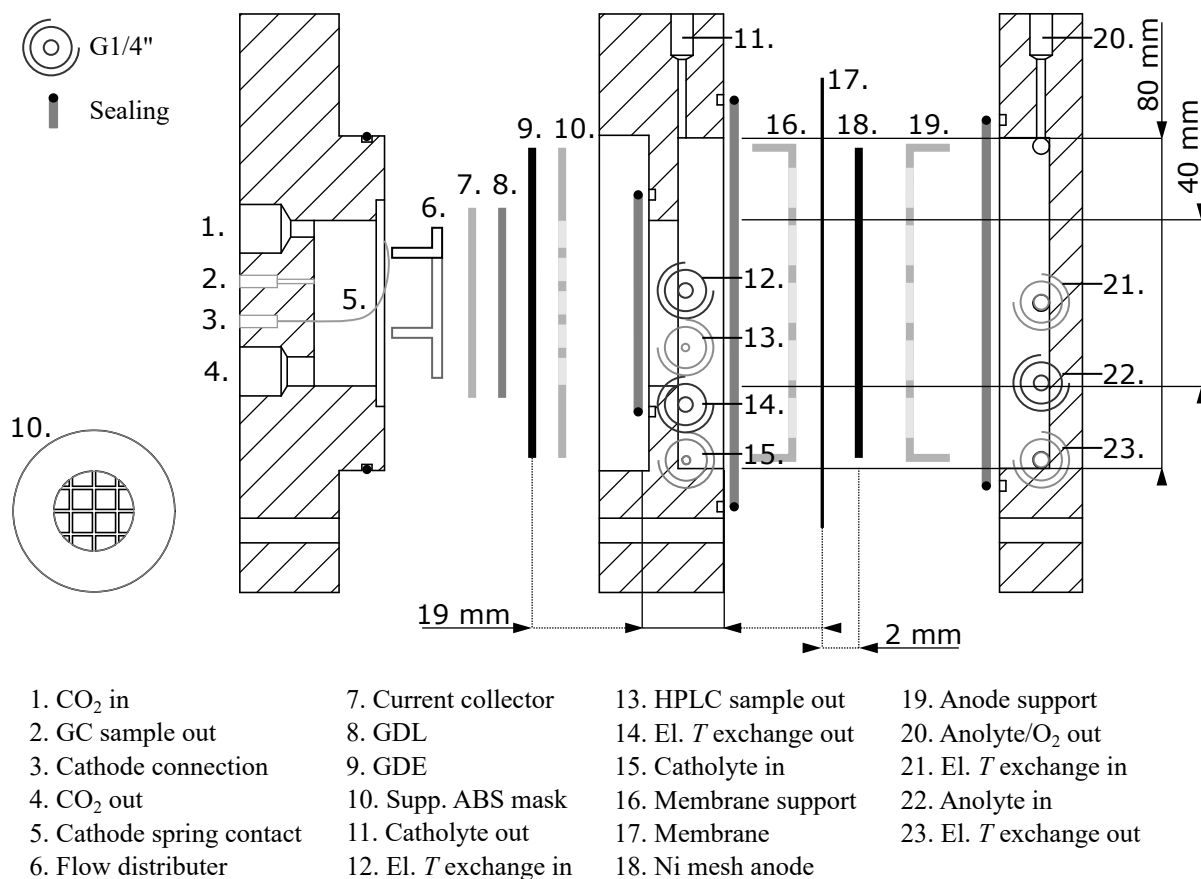


**Figure 6.3:** Exploded view of the developed first stage scale-up cell. The cell houses a **gas diffusion electrode (GDE) of 28 cm<sup>2</sup> with an active electrode area of 10 cm<sup>2</sup>** and exhibits a cathode-anode distance of 21 mm. Electrical contact to the GDE is given by a stainless steel spring contact pushing against the current collector and gas diffusion layer (GDL). In contrast to the small cell, a 3D printed supporting mask, 10, was used to stabilize the fragile GDE. During semi-batch mode of operation ports 13, 15 and 22 were closed.

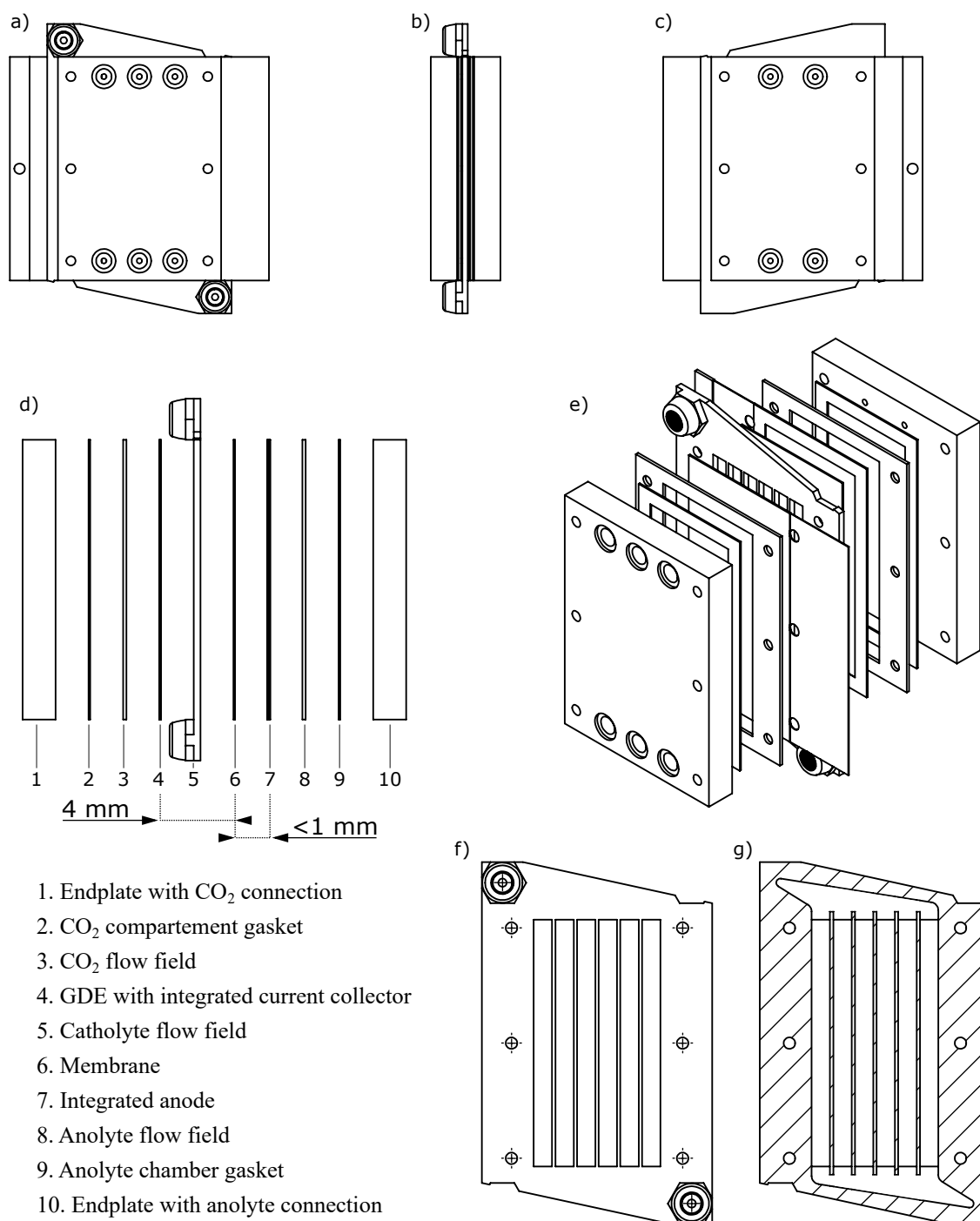


**Figure 6.4:** Detail and exploded view of the developed second stage scale-up cell. A filter-press design is applied, housing a **gas diffusion electrode (GDE) of 110 cm<sup>2</sup> with an active electrode area of 70 cm<sup>2</sup>** and a cathode-anode distance of 4 mm. Cathode, membrane and nickel mesh anode are equally sized.

a) to c) Cathode, side and anode view of the assembled cell.

d) and e) Exploded view showing the different components.

f) and g) Top and cross section view of the 3D printed catholyte flow field.

## 6.3 Analytical methods

### 6.3.1 Quantification of gaseous products

The gas phase composition at the gas outlet, containing hydrogen, CO, methane, unreacted CO<sub>2</sub> and nitrogen, if added, was analyzed using online GC. A conventional GC (7890A series, Agilent Technologies) and a  $\mu$ -GC (G3581A, Agilent Technologies) was used for semi-batch and continuous mode of operation, respectively. In both cases the gas outlet stream was passed continuously through the instrument's sample loop. While for the 1 cm<sup>2</sup> cell the whole gas outlet stream was passed, a bypass system had to be installed for the 10 cm<sup>2</sup> and 70 cm<sup>2</sup> cell. This bypass limited the flow through the sample loop to around 5 mL min<sup>-1</sup> to avoid critical back pressures. Important instrument settings are listed in table 6.2.

**Table 6.2:** Instrumental parameters of the conventional GC (7890A) and  $\mu$ -GC (G3581A) used within the present work.

Parameter	GC 7890A	$\mu$ -GC G3581A
Column	PLOT Q 30 m x 530 $\mu$ m x 40 $\mu$ m Molsieve 2 m x 3.18 mm x 2 mm	CP-Cox 1 m
Detectors	TCD, FID	TCD
Carrier gas	He	Ar
Carrier gas pressure / kPa	527	200
Injector temperature / °C	150	110
Column temperature program	Keep at 50 °C for 10 min, heat to 150 °C with 20 °C min <sup>-1</sup>	120 °C
Detector temperature	200	110
Split	4:1	-
Analysis time	15 min	3 min

### 6.3.2 Quantification of dissolved products

Products dissolved in the electrolyte like formate and bicarbonate were analyzed using HPLC (1260 Infinity II, Agilent Technologies) with a refractive index detector (RID). For semi-batch experiments samples were taken after electrolysis and measured twice in offline mode. During electrolysis water is dragged from the anode to cathode side by migrating cations and their hydration shell. Therefore,

catholyte volume changes and its determination after electrolysis is crucial to calculate the amount of formate formed. Catholyte volume was determined by pumping the liquid into a measuring cylinder by means of the peristaltic circulation pump. For measurements in continuous mode of operation a portion of the catholyte output flow (around 50 % of the input flow rate) was pumped through a sample loop for online analysis. Instrument settings were identical for offline and online mode, listed below.

**Table 6.3:** Instrumental parameters of the HPLC (1260 Infinity II) used within the present work for both offline and online analysis.

Parameter	1260 Infinity II
Column	Nucleogel Sugar 810H, 30 cm, Macherey Nagel
Detector	RID
Eluent	5 mM H <sub>2</sub> SO <sub>4</sub> in water
Eluent flow	0.6 mL min <sup>-1</sup>
Injection volume	5 μL to 40 μL
Column temperature	50 °C
Detector temperature	55 °C

### 6.3.3 Catalyst and electrode characterization

Catalyst and electrode characterization was done by thermogravimetric analysis (TGA), XRD, transmission electron microscopy (TEM) and scanning electron microscopy (SEM).

Metal loading of the carbon support ( $\sigma_{\text{Me}}$ ) was evaluated via TGA (Setsys TG 16/18, Setaram Inc.) by B. Gering, D. Beierlein and J. Florenski. After catalyst preparation described in section 6.1.1, p. 63, a sample was heated to 1000 °C in synthetic air atmosphere with a heating rate of 5 °C min<sup>-1</sup>. The obtained remaining mass fraction  $w_{\text{res}}$  was assumed to consist solely of the most stable oxide form of the respective metal, like tin(IV) oxide in case of tin based catalysts. The amount of noncombustible components in the carbon support was found to be below the detection limits of the instrument and was neglected.

$$\sigma_{\text{Me}} = \frac{V_x \cdot m_{\text{Me}_x\text{O}_y+\text{CB, GDE}} \cdot w_{\text{res}} \cdot \frac{M_{\text{Me}}}{M_{\text{Me}_x\text{O}_y}}}{A_{\text{geo}}} \quad (6.3.1)$$

Investigation of the active component was performed by XRD. Due to the large amount of carbon contained in the supported catalyst, analysis had to be performed on the active material itself. Precipitation was done according to the description in section 6.1.1, p. 63, without the carbon support.

Diffraction patterns were recorded with a D8 Advance (Bruker corp.) and a Cu-K $\alpha$  X-ray radiator operated at  $\lambda = 1.5$  nm,  $V = 40$  kV and  $I = 40$  mA.

SEM imaging was performed at the DLR by Mrs. Plock using a Zeiss ULTRA plus microscope equipped with an angle selective backscattered electron (AsB) detector. TEM images were obtained at the Max Planck Institute, Stuttgart, Germany (MPI) by Mrs. Hadjixenophontos using a Philips CM200 FEG at 200 kV.





## 6.4 Electroanalytical methods

The following sections describe the electrochemical analysis routines that were used to determine key performance indicators. This applies mainly to electrode activity, selectivity, energetic cathode efficiency (*ECE*) or energy efficiency (*EE*) and double layer capacitance ( $C_{DL}$ ). Key parameters of the different routines described in the next sections are summarized in tables 6.4 and 6.5. For each routine a new GDE was used. For additional explanations of the different measurement routines see the appendix (section 9.3, p. 217).

### 6.4.1 Determination of electrode activity and wetting

The activity of an electrode is determined by several factors which will be discussed in chapter 7. To give a quick preview, such factors are the catalyst, binding agent, wetting behavior, type and concentration of the electrolyte or temperature. The problem when trying to assess the electrode's activity is the strong interconnection of mentioned factors. While the bulk electrolyte composition and temperature can easily be adjusted, they can strongly differ near the reaction zone. Even more important or problematic is the extent of wetting, which depends on the applied potential (assuming using the same electrolyte, temperature and electrode). In light of this fact, comparison of electrode activities is done in two different ways.

The first way is by simply comparing the cathode potential at a certain time and current density during the performed galvanostatic electrolysis, described in section 6.4.2. This way was chosen as it is crucial for the final process to control the current instead of the voltage to prevent the GDE from deactivation and to avoid a selectivity shift by mass transport limitation. However, the problem with this method is that if an electrode shows a higher activity than another, a less negative potential is applied, which again results in a lower driving force for electrowetting. Thus, less catalyst is contacted by the electrolyte.

The second way is to perform linear sweep voltammetry (LSV) scans after a potentiostatic preconditioning routine. The preconditioning routine is necessary to wet the electrode and to make the active sites accessible to the electrolyte. Without this preconditioning no noteworthy current would be measurable during the LSV. In contrast to the first method, electrode wetting is controlled by the set potential. As shown in table 6.4, preconditioning consists of two consecutive potentiostatic electrolysis steps. During the first one, a strong driving force for electrowetting is applied by setting a cathode potential of  $\varphi_{C, IR} = -1.66$  V for 2 min. Electrolyte is thereby quickly pulled into the GDE and seals it to stop the crossover of  $CO_2$  into the cathode chamber. Without this first step the initial bubbling through of  $CO_2$  led to strong

**Table 6.4:** Overview of the experimental routine used for determining electrode activity and degree of wetting in semi-batch mode of operation.

Key performance indicator	Experiment sequence	$t$	$\dot{V}_{f, \text{CO}_2}$ / mL min <sup>-1</sup>	Settings
Activity and wetting (semi-batch)	Preflushing	5 min	10	-
	Potentiostatic preconditioning	2 min	15	$\varphi_{\text{C, IR}} = -1.66 \text{ V (vs. SHE)}$ $j_{\text{max}} = -800 \text{ mA cm}^{-2}$
	Potentiostatic preconditioning	30 min	15	$\varphi_{\text{C, IR}} = -1.36 \text{ V (vs. SHE)}$
	Linear sweep voltammetry	-	15	$d\varphi_{\text{C, IR}}/dt = 50 \text{ mV s}^{-1}$ $\varphi_{\text{C, IR, start/end}} = -0.36 \text{ V (vs. SHE)}$ $\varphi_{\text{C, IR, end}} = -1.66 \text{ V (vs. SHE)}$
	<i>Cyclic voltammetry (optional)</i>	-	5	$d\varphi_{\text{C, IR}}/dt = 100 \text{ mV s}^{-1}$ $\varphi_{\text{C, IR, start/end}} = -1.26 \text{ V (vs. SHE)}$ $\varphi_{\text{C, IR, return}} = 1.14 \text{ V (vs. SHE)}$ 5 cycles
	Open circuit potential	20 min	5	-
	Cyclic voltammetry (non-faradaic)	-	5	$d\varphi_{\text{C}}/dt = 20 \text{ mV s}^{-1}$ to $100 \text{ mV s}^{-1}$ $\varphi_{\text{C, start/end}} = 0.1 \text{ V (vs. OCP)}$ $\varphi_{\text{C, return}} = 0.5 \text{ V (vs. OCP)}$ 5 cycles

**Table 6.5:** Overview of the experimental routines used for determining product distribution, energetic efficiencies and degree of wetting in semi-batch or continuous mode of operation. CO<sub>2</sub> volumetric flow rate required for reduction (not including bicarbonate formation) according to Faraday's law:  $\dot{V}_F = (j_{\text{GSE}} A_{\text{geo}} V_m) / (zF)$ , with excess factor  $f = 4$ .

Key performance indicator	Experiment sequence	$t$	$\dot{V}_{\text{F, CO}_2}$ / mL min <sup>-1</sup>	Settings
	Preflushing	5 min	10	-
	Galvanodynamic preconditioning	100 s	$\dot{V}_F \cdot f / 2$	$dj/dt = j_{\text{GSE}} / 100 \text{ s}$
	Galvanostatic electrolysis	(40 min) 45 min	$\dot{V}_F \cdot f$	$j_{\text{GSE}} = -200 \text{ mA cm}^{-2}$ to $-1700 \text{ mA cm}^{-2}$
<i>FE, ECE</i> and/or <i>EE</i> <i>wetting</i> (optional) (semi-batch)	<i>Open circuit potential</i> (optional)	20 min	5	-
	<i>Cyclic voltammetry</i> (non-faradaic, optional)	-	5	$d\varphi_{\text{C, IR}}/dt = 20 \text{ to } 100 \text{ mV s}^{-1}$ $\varphi_{\text{C, start/end}} = 0.1 \text{ V (vs. OCP)}$ $\varphi_{\text{C, return}} = 0.5 \text{ V (vs. OCP)}$ 5 cycles
	<i>Cyclic voltammetry</i> (optional)	-	5	$d\varphi_{\text{C, IR}}/dt = 100 \text{ mV s}^{-1}$ $\varphi_{\text{C, IR, start/end}} = -1.26 \text{ V (vs. SHE)}$ $\varphi_{\text{C, IR, return}} = 1.14 \text{ V (vs. SHE)}$ 5 cycles
-----				
	Preflushing	5 min	10	-
	Galvanodynamic preconditioning	100 s	$\dot{V}_F \cdot f / 2$	$dj/dt = j_{\text{GSE}} / 100 \text{ s}$
<i>FE, ECE</i> and <i>EE</i> (continuous)	Galvanostatic electrolysis	24 h to 250 h	$\dot{V}_F \cdot f$	$j_{\text{GSE}} = -200 \text{ mA cm}^{-2}$ to $-400 \text{ mA cm}^{-2}$ , $\dot{V}_{\text{F, el}}$ see equation 6.4.1
	<i>Cyclic voltammetry</i> (optional)	-	5	$d\varphi_{\text{C, IR}}/dt = 100 \text{ mV s}^{-1}$ $\varphi_{\text{C, IR, start/end}} = -1.26 \text{ V (vs. SHE)}$ $\varphi_{\text{C, IR, return}} = 1.14 \text{ V (vs. SHE)}$ 5 cycles

fluctuations in the geometrical surface area in contact with electrolyte, which in turn lead to a low reproducibility. Maximum current density was set to  $-800 \text{ mA cm}^{-2}$  to avoid mechanical degradation by excessive hydrogen gas production. The second preconditioning step was performed immediately after the first one at a lower cathode potential of  $\varphi_{\text{C, IR}} = -1.36 \text{ V}$  for 30 min to ensure a decent wetting without deactivation effects. These values were found empirically and showed a reasonable compromise between maintaining gas tightness for moderately active electrodes/conditions and avoiding deactivation for highly active electrodes/conditions. Problematic effects of deactivation and insufficient current density are illustrated in the appendix (see figure 9.1, p. 217). Finally, polarization curves were recorded with a scan rate of  $d\varphi_{\text{C, IR}}/dt = 50 \text{ mV s}^{-1}$  in a potential range of  $-0.36 \text{ V}$  (vs. SHE) to  $-1.66 \text{ V}$  (vs. SHE) by means of LSV.

However, it is important to mention that simply applying the same cathode potential does not guarantee a consistent wetting throughout different experiments. Especially when electrochemically active components like the carbon black support or the catalyst itself are altered. For this reason and in order to optimize the GDE's composition,  $C_{\text{DL}}$  was measured as described in section 4.3.1, p. 46. Non-faradaic cyclic voltammograms were therefore recorded after a 20 min break of open circuit, using different scan rates  $d\varphi_{\text{C}}/dt$  between  $20 \text{ mV s}^{-1}$  and  $100 \text{ mV s}^{-1}$ . Recording of the cyclic voltammetry (CV) curves (voltammograms) was started at  $+0.1 \text{ V}$  (vs. OCP) and returned at  $+0.5 \text{ V}$  (vs. OCP). To record undisturbed CVs that show a parallel course, it is important to let the open circuit potential (OCP) stabilize and get to a potential more positive than  $-0.3 \text{ V}$  (vs. SHE) beforehand (see appendix figure 9.3, p. 219). This was achieved within the 20 min open circuit break between electrolysis and  $C_{\text{DL}}$  analysis. The problem with this procedure is that in the meantime the electrolyte can withdraw from the pore structure, distorting the result. Attempts to shorten this downtime by short-circuiting cathode and anode, setting a slightly positive polarization to the cathode, vary the CV scan range or flushing with  $\text{N}_2$  were not successful. Note that the measured  $C_{\text{DL}}$  is the product of electrochemical active surface area (ECSA) and area specific capacitance. The latter is not known and strongly depends on the material. Thus, special attention is required when comparing  $C_{\text{DL}}$  values of different electrodes.

## 6.4.2 Determination of faradaic and energetic efficiencies

### 6.4.2.1 Assessing the complete product distribution

The standard procedure for determining the product distribution and energetic efficiencies (*ECE* and *EE*) in semi-batch mode was to apply a certain current density for 45 min and to analyze the formed products as described in section 6.3. Reproducibility, especially at higher absolute values of current density,

was increased by adding a galvanodynamic preconditioning step prior to galvanostatic electrolysis. This preconditioning allows to steadily increase the current density instead of directly applying the full current to a completely non-wetted GDE with very low ECSA. At absolute values of current density higher than  $500 \text{ mA cm}^{-2}$  hydrogen formation increases non-linear with time, making three GC measurements necessary. The first one was taken 6 min into the galvanostatic electrolysis step. From that point on measurements were taken every 15 min. The concentration of dissolved formate was analyzed by offline HPLC after electrolysis.

During long-term measurements in continuous mode of operation electrolytes were both fed at a volumetric flow rate of  $1 \text{ mL min}^{-1}$ . This value corresponds to a current of 200 mA. For higher absolute values of current density and/or geometrical electrode area electrolyte flow rate was adjusted as follows:

$$\dot{V}_{f, \text{el}} = \frac{|j_{\text{GSE}}| \cdot A_{\text{geo}}}{200 \text{ mA}} \cdot 1 \text{ mL min}^{-1} \quad (6.4.1)$$

For both semi-batch and continuous mode of operation, volumetric  $\text{CO}_2$  feed flow rate was calculated based on Faraday's law and an excess factor  $f$  of 4. This value takes into account that besides the amount of  $\text{CO}_2$  being reduced, stoichiometric amounts are converted to bicarbonate. These two moles per one molar extent of reaction were doubled to ensure a sufficient excess. Flow rates were consequently set to:

$$\dot{V}_{f, \text{CO}_2} = \frac{|j_{\text{GSE}}| \cdot A_{\text{geo}} \cdot V_{\text{m}}}{zF} \cdot f \quad (6.4.2)$$

Voltages were either recorded against the counter or the Hg/HgO (1 M KOH) reference electrode with or without  $IR$  compensation enabled. Faradaic and energetic efficiencies were calculated as described in section 6.5.

#### 6.4.2.2 Fast hydrogen selectivity screening

For the investigation of mass transport related limitations a large number of experiments (144 different conditions - 180 runs) would have been necessary. However, since only the hydrogen faradaic efficiency ( $FE$ ) is used to determine the degree of mass transport limitation, a complete product distribution analysis is not necessary. A fast analysis routine for gaseous products during stepped galvanostatic electrolysis was therefore established. Current density was ramped up and held at certain values for 15 min according to the sequence shown in figure 6.5. Shortly before the end of each step hydrogen  $FE$  was analyzed by a single GC measurement. The volumetric  $\text{CO}_2$  feed flow rate was automatically adjusted for each step, calculated by equation 6.4.2, with  $z = 2$ ,  $f = 4$  and  $A_{\text{geo}} = 1 \text{ cm}^2$ .

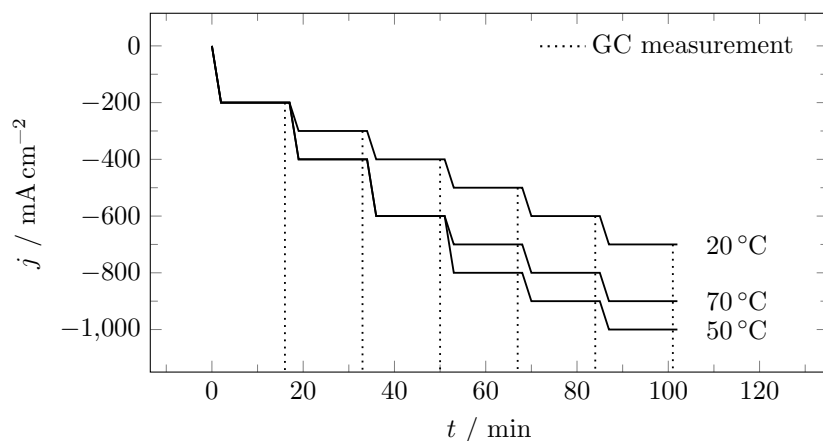


**Figure 6.5:** Current density profile during fast hydrogen selectivity screening. Each galvanostatic step  $i$  was held for 15 min and ramped with  $dj/dt = (j_i - j_{i-1})/60$  s.

### 6.4.3 Estimations on the catalyst's oxidation state

A rough estimation about the catalysts oxidation state can be given by means of recording cyclic voltammograms and measuring the charge passed for the oxidation of metallic tin. The CV measurements were started at a reductive potential of  $-1.26$  V (vs. SHE) and swept in anodic direction (up to  $+1.14$  V (vs. SHE)). When metallic tin is present, an oxidation peak can be observed at around  $-0.55$  V (vs. SHE) (see appendix figure 9.14, p. 227). With a given scan rate, integration of this peak returns the tin oxidation charge  $q_{\text{Sn ox}}$ , which is a measure of the available amount of tin. Integration was done via the Gamry Analyst software between  $-0.65$  V (vs. SHE) and  $-0.4$  V (vs. SHE) using the third recorded cycle. This method is of course very limited in its quantitative accuracy e.g. due to unknown oxidation and reduction kinetics, overlapping oxidation processes and possible side reactions but the obtained values seem reasonable.

## 6.5 Data evaluation

All data recorded during standardized experiments listed in tables 6.4 and 6.5 were evaluated by VBA scripts to ensure consistent and accurate analysis.

### 6.5.1 Analysis of semi-batch operation

During galvanostatic electrolysis GC chromatograms, volumetric flow rate of the outlet gas stream, as well as the compensated and uncompensated cathode and/or cell voltage were recorded.

GC chromatograms were integrated by the software Chemstation with appropriate integration parameters and imported to the Excel evaluation file. The different peak areas were thereby assigned to the respective component by the measured retention time obtained from either the flame ionization detector (FID) ( $\text{CH}_4$ ) or thermal conductivity detector (TCD) ( $\text{H}_2$ ,  $\text{CO}$  and  $\text{CO}_2$ ) signal. Together with the stored calibration data the volume fraction  $\Phi_i$  of every component  $i$  in the outlet gas stream was calculated.

For the absolute amount of gaseous products formed, the recorded volumetric flow rate data are imported and linked to the evaluated GC data. The exact time of the corresponding online GC sample injection was found and assigned to the respective volume fractions  $\Phi_i$ . More precisely, the script searched for short but strong flow rate fluctuations, which were caused by a sharp pressure peak as the GC's injection valves switched. They were identified by calculating the difference between two successive data points and comparing it to a certain threshold. Depending on the number  $n$  of performed GC measurements a polynomial trend line of  $n$ -th order was then applied to every measured component, resulting in  $\Phi_i(t)$  functions. They describe the trend of volume fractions over the full time of electrolysis. Since the used MFM was calibrated for pure  $\text{CO}_2$ , each measured flow rate ( $\dot{V}_{f, \text{meas}}$ ) data point was corrected using the determined  $\Phi_i(t)$  functions and the manufacturer's specific conversion factors  $C_{g, i}$ <sup>[162]</sup>:

$$\dot{V}_f(t) = \dot{V}_{f, \text{meas}} \cdot \frac{C_{g, \text{mix}}(t)}{C_{g, \text{CO}_2}} \quad (6.5.1)$$

with:

$$C_{g, \text{mix}}(t) = \frac{C_{g, \text{H}_2}}{\Phi_{\text{H}_2}(t)} + \frac{C_{g, \text{CO}}}{\Phi_{\text{CO}}(t)} + \frac{C_{g, \text{CH}_4}}{\Phi_{\text{CH}_4}(t)} + \frac{C_{g, \text{CO}_2}}{\Phi_{\text{CO}_2}(t)} \quad (6.5.2)$$

With the corrected volumetric flow rate  $\dot{V}_f(t)$  and the volume fraction of the respective component, absolute masses of each component produced in between two recorded flow rates (step size:  $t_{\text{step}} = 2$  s to 10 s) were calculated using the density  $\rho$ .<sup>[162]</sup>

$$m_i(\text{per step}) = \dot{V}_f(t) \cdot \Phi_i(t) \cdot \rho_i \cdot t_{\text{step}} \quad (6.5.3)$$

Adding up all calculated masses and converting them into the molar amount of substance  $n$  with their molar mass  $M$  leads to the total amount of product  $i$ .

$$n_i = \frac{\sum m_i(\text{per step})}{M_i} \quad (6.5.4)$$

With these values the final step was to convert the molar amount of substance  $i$  into its  $FE$ , using Faraday's law:

$$FE_i = \frac{n_i}{n_F} = n_i \cdot \frac{zF}{It} \quad (6.5.5)$$

The dissolved main product formate was analyzed after electrolysis by offline HPLC. The recorded chromatogram was as well analyzed by the software Chemstation with appropriate integration parameters and imported to the Excel evaluation file. Comparing measured area values with the stored calibration data leads to the molar concentration of formate, which is then converted to the produced molar amount of substance by multiplying with the determined catholyte volume (see section 6.3.2, p. 75). Applying equation 6.5.5 then gives the formate  $FE$ .

If operated in two electrode configuration, compensated and uncompensated cell voltages were recorded. Raw data were imported to the evaluation file and essential values found by the script. Depending on the measured voltage, the real or  $IR$  compensated  $EE$  was calculated by:

$$EE_{i(\text{IR})} = \frac{V_{\text{cell}}^\theta}{V_{\text{cell}(\text{IR})}} \cdot FE_i \quad (6.5.6)$$

Note that the  $EE$  always consists of contributions of cathode and anode. In order to be able to connect selectivity and activity of the GDE itself in a single value, the  $ECE$  was introduced. It was obtained from measuring the cathode potential against a reference electrode and applying the following equation. Note that this value depends on the reference potential, only allowing limited conclusions.

$$ECE_i = \frac{\varphi_{\text{C, vs SHE}}^0}{\varphi_{\text{C, vs SHE, IR}}} \cdot FE_i \quad (6.5.7)$$



### 6.5.2 Analysis of continuous operation

Similar to the semi-batch experiments, GC chromatograms, outlet gas volumetric flow rate, as well as the compensated and uncompensated cathode and/or cell voltage were recorded. Gas and liquid phase analysis was performed once every hour. In contrast to short-term experiments, product distribution was evaluated for each measurement instead of being averaged.

Gaseous products were evaluated by converting the measured volumetric flow rate according to its composition by:

$$\dot{V}_f = \dot{V}_{f, \text{meas}} \cdot \frac{C_{g, \text{mix}}}{C_{g, \text{CO}_2}} \quad (6.5.8)$$

with:

$$C_{g, \text{mix}} = \frac{C_{g, \text{H}_2}}{\Phi_{\text{H}_2}} + \frac{C_{g, \text{CO}}}{\Phi_{\text{CO}}} + \frac{C_{g, \text{CH}_4}}{\Phi_{\text{CH}_4}} + \frac{C_{g, \text{CO}_2}}{\Phi_{\text{CO}_2}} \quad (6.5.9)$$

Using the measured volume fraction and density of component  $i$  gives the molar amount of substance flow according to:

$$\dot{n}_i = \frac{\dot{V}_f \cdot \Phi_i \cdot \rho_i}{M_i} \quad (6.5.10)$$

which in turn can be transformed into the respective  $FE$ :

$$FE_i = \frac{\dot{n}_i}{\dot{n}_F} = n_i \cdot \frac{zF}{I} \quad (6.5.11)$$

Liquid product analysis was calculated from obtained formate concentrations  $c_{\text{Formate}}$  and the set volumetric catholyte flow rate  $\dot{V}_{f, \text{el, C}}$ :

$$FE_{\text{Formate}} = \frac{\dot{n}_{\text{Formate}}}{\dot{n}_F} = c_{\text{Formate}} \cdot \dot{V}_{f, \text{el, C}} \cdot \frac{zF}{I} \quad (6.5.12)$$

$ECE$  and  $EE$  were then calculated by equation 6.5.7 and 6.5.6.

### 6.5.3 Double layer capacitance and activity evaluation

According to equation 4.3.3, p. 48, the wetted electrode can be seen as classical capacitor with a certain capacitance. This  $C_{DL}$  is accessible by recording CVs in a range where no chemical conversion takes place (non-faradaic range). Obtained double layer charging current density and used scan rate correlate in a linear manner with the slope representing the  $C_{DL}$ .

$$j_{DL} = C_{g, DL} \cdot \frac{d\phi_C}{dt} \quad (6.5.13)$$

Evaluation was performed by plotting the charging current at the center of both voltage limits and applying a linear regression. An exemplary plot of measured CVs is represented in the appendix (see figure 9.4, p. 219).

In terms of activity determination onset potentials were obtained from recorded polarization curves (LSV measurements) by applying a baseline correction and a current density threshold of  $-1 \text{ mA cm}^{-2}$ . The baseline was obtained within a certainly non-faradaic range close to the  $\text{CO}_2\text{RR}$  active range (visible by a linear course) and subtracted from the polarization curve. The first data point ( $\phi_{C, IR}$  step size = 5 mV) of the corrected polarization curve to exceed the threshold was identified as onset potential. Other than that activity at higher current densities was determined by comparing obtained polarization curves without further calculations.

## 6.6 Fundamental investigations on new process concepts

### 6.6.1 Bipolar membrane electro dialysis for downstream processing

As a proof of concept, the general feasibility of using bipolar membrane electro dialysis (BPED) to protonate the formate/bicarbonate mixture obtained from alkaline CO<sub>2</sub> electrolysis (CO<sub>2</sub>EL) in a downstream process was investigated. From literature (see section 4.4.2, p. 54) it is known that high concentrations of organic acids can be obtained from their salts while simultaneously generating metal hydroxides. To develop and fabricate a BPED cell, proof its general functionality and investigate the protonation of formate/bicarbonate mixtures were the objectives of this part.

First, a suitable cell had to be developed, which was initially planned to be coupled with the first scaled-up cell (10 cm<sup>2</sup>). Hence, the total current of both cells had to be identical in order to protonate the same amount of anions as formed during electrolysis (formate, bicarbonate or hydroxide). With CO<sub>2</sub>EL being operated at 200 mA cm<sup>-2</sup> on a 10 cm<sup>2</sup> electrode a current of 2 A is obtained. From the bipolar membrane (BPM)'s manufacturer it is known that the used membrane (FBM, Fumatech BWT GmbH) should be handled at current densities below 100 mA cm<sup>-2</sup>. To avoid any possibility of destruction of the membrane from higher current densities due to a potentially non-uniform current distribution a value of 50 mA cm<sup>-2</sup> was chosen for electro dialysis. This requires an active area of 40 cm<sup>2</sup>. In order to keep the formate/bicarbonate cycle separated from the formic acid cycle (see figure 7.45, p. 172) and to allow for independent concentrations within them, a three-compartment configuration was chosen (see figure 4.21, p. 55).

In the easiest form, meaning a single repeating unit, a three-compartment electrolysis cell actually consists of five different compartments as two additional ones are always required for the terminal electrochemical reactions. In the cell developed herein, all of these compartments are formed by a 3D printed ABS flow field between two nitrile butadiene rubber (NBR) gaskets and are separated against each other by a certain membrane. Figure 6.6 gives an overview of the arrangement of flow fields, gaskets and membranes. Both terminal compartments (C1 and C5) contained a fine nickel mesh electrode for water reduction (in C1) and oxidation (in C5). All membranes were polyether ether ketone (PEEK) reinforced and provided by Fumatech BWT GmbH. FKB-PK-130, FAB-PK-130 and FBM-PK were used as cation exchange membrane (CEM), anion exchange membrane (AEM) and BPM, respectively.

Investigations on the process of generating formic acid from a formate/bicarbonate salt mixture have been conducted in the setup shown in figure 6.7. Compartment C2 to C4 were thereby operated in

single-pass mode and fed with different model electrolytes of various concentrations (E-C2 to E-C4). Within compartments C1 and C5 a 1 M potassium hydroxide solution was cycled. All electrolytes were pumped through the cell by peristaltic pumps at  $10 \text{ mL min}^{-1}$ . Both outlet streams of compartments C1 and C5 were passed through GLSs to remove formed hydrogen and oxygen. The GLS of C1 was thereby constantly flushed with nitrogen to avoid high volume fractions of hydrogen for safety reasons.

Electrolyte storage tanks, except for the product collecting ones, were placed in a cryostat for temperature control. They were kept at temperatures between room temperature and  $-6^\circ\text{C}$ . The cell itself could not be cooled or heated. Therefore, electrolyte temperature was monitored at the cell inlet (R-1 to R-3) and outlet (R-4 to R-6) of compartments C2, C3 and C4. Additionally, an inline pH-sensor (R-7) could be placed at one of the outlets of these three compartments.

A Gamry Reference 3000 potentiostat was used for electric power supply, with the cell being operated in two electrode configuration. Prior to galvanostatic operation, a galvanodynamic preconditioning was applied to gently start-up the cell. This preconditioning consisted of a controlled linear increase in current density from  $0 \text{ mA cm}^{-2}$  to  $50 \text{ mA cm}^{-2}$  within 100 s. Directly after this start-up galvanostatic dialysis was performed for 45 min with a current of 2 A.

While pH and temperature were recorded continuously, samples of the used electrolytes of compartments C2, C3 and C4 were taken within the last minute of galvanostatic operation from the outlet stream. They were analyzed with HPLC according to the method described in table 6.3.

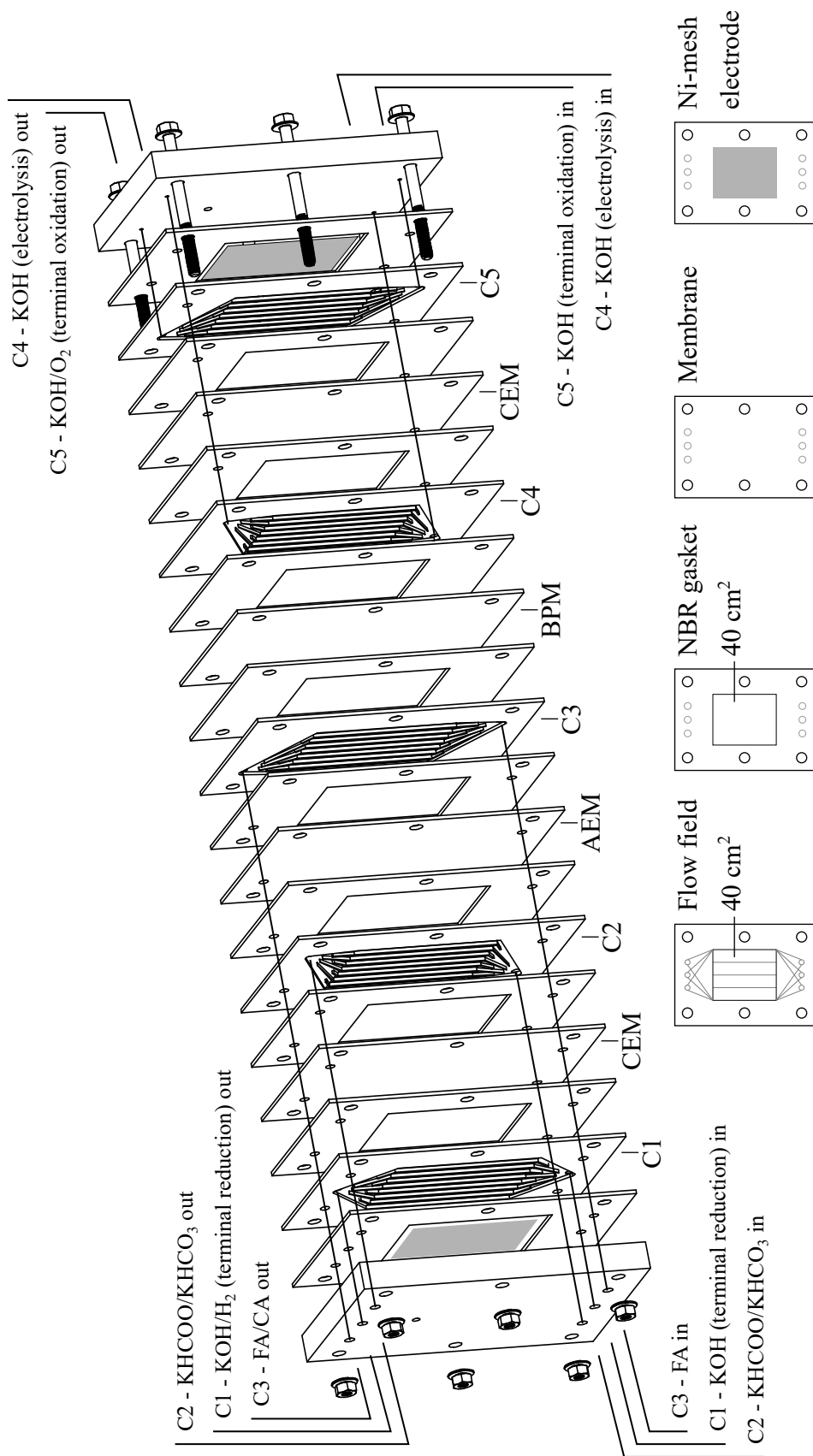


**Figure 6.6:** Exploded view of the developed bipolar membrane electrolysis cell. Flow fields are 3D printed from acrylonitrile butadiene styrene filament and sealed with nitrile butadiene rubber (NBR) gaskets. Used cation exchange membranes (CEMs), the anion exchange membrane (AEM) and the bipolar membrane (BPM) were provided by Fumatech BWT GmbH. FA: formic acid; CA: carbonic acid.

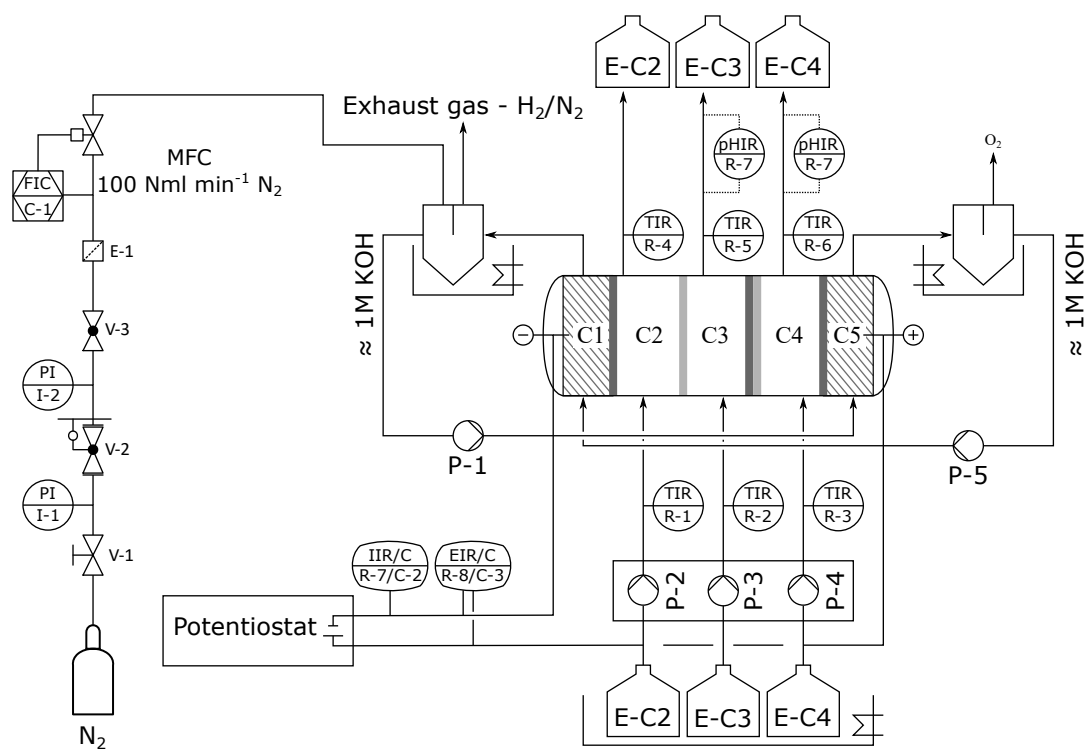


**Figure 6.7:** Piping and instrumentation diagram of the setup used to investigate the protonation of formate/bicarbonate mixtures in the bipolar membrane electrodesysis cell of figure 6.6.

### 6.6.2 Selective alcohol oxidation as alternative anode reaction

As described in section 4.4.3, p. 56, alcohol oxidation reaction (AOR) is described in literature as alternative anode reaction to OER. Typically, the used alcohol is totally oxidized to reduce the electrolyzers power consumption as far as possible. Within the present work, selective alcohol oxidation is aspired to produce the respective organic acid salt, while simultaneously lowering the power consumption. Again, as a proof of concept study, different metals with moderate activity towards the total oxidation have been investigated regarding their activity and selectivity towards organic acid salt formation. Nickel, iron, cobalt and copper were used as electrocatalysts to oxidize methanol, ethanol, n-propanol and i-propanol in aqueous solution with different concentrations of potassium hydroxide added.

All experiments were performed at a temperature of 50 °C, which was again ensured by external heat exchange loops in a thermostat with peristaltic pumps for liquid circulation. While the anolyte was varied during investigations, 1 M potassium hydroxide was used as catholyte. Anolyte and catholyte had a volume of 40 mL and 30 mL, respectively and were separated by a Nafion membrane.

First, the oxidation half-cell reaction was investigated by screening the activity of mentioned metals in terms of CV measurements. Experiments were conducted in a batch-type cell, shown in figure 6.8 with the electrochemically active metal applied as meshes of similar mesh size and wire thickness (see table 9.2, p. 212). A fine platinum mesh and a Hg/HgO (1 M KOH) were used as counter and reference electrode, respectively. Both, working and counter electrode had a geometrical area of 3 cm<sup>2</sup> and were used without any further pretreatment. Cyclic voltammograms were recorded between 0.14 V (vs. SHE) to 0.74 V (vs. SHE) with a scan rate of 50 mV s<sup>-1</sup>. Five cycles were recorded, of which the last one was used for activity evaluation.

Based on the found activities, nickel was chosen as best option to investigate the product distributions obtained with different alcohols. Galvanostatic electrolysis was therefore performed for 35 min at 200 mA cm<sup>-2</sup> in a three electrode configuration with *IR* compensation enabled. Gaseous products were flushed out of the anode half-cell by a constant stream of nitrogen being fed at 5 mL min<sup>-1</sup>. The gas outlet was thereby connected to a MFM and  $\mu$ -GC to determine the *FEs* of gaseous products (CO<sub>2</sub>, CO and O<sub>2</sub>). Liquid products such as aldehydes, ketones or carboxylic acids were analyzed via HPLC. *FEs* were calculated according to the description given in section 6.5.1, p. 85. Specific conductivity of the used electrolytes was analyzed using a Hamilton Conducell 4USF conductivity sensor.

Last, CO<sub>2</sub>RR was coupled with methanol oxidation reaction (MOR) on a nickel mesh to demonstrate the general feasibility. As illustrated in figure 6.9, the standard GDE test cell was used for this purpose

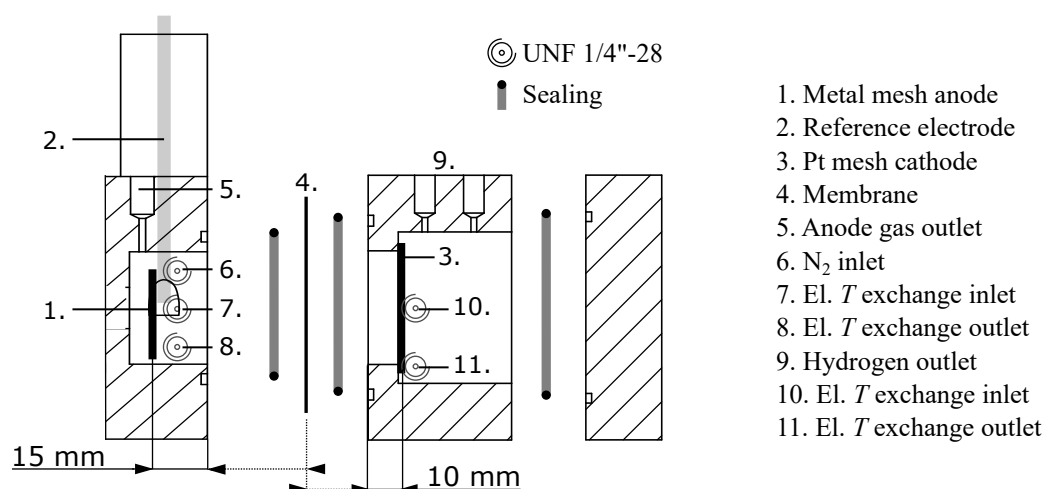


**Figure 6.8:** Exploded view of the cell used for investigating the selective alcohol oxidation.

with a standard GDE ( $A_{\text{geo}} = 1 \text{ cm}^2$ ) as cathode and nickel mesh ( $A_{\text{geo}} = 3 \text{ cm}^2$ ) as anode. Galvanostatic electrolysis was performed for 45 min at  $200 \text{ mA cm}^{-2}$  in two electrode configuration with  $IR$  compensation enabled. A 2 M potassium chloride solution ( $\text{pH} = 10$ ) was used as catholyte, while 1 M potassium hydroxide was used as anolyte either pure or with 1 M of methanol added.

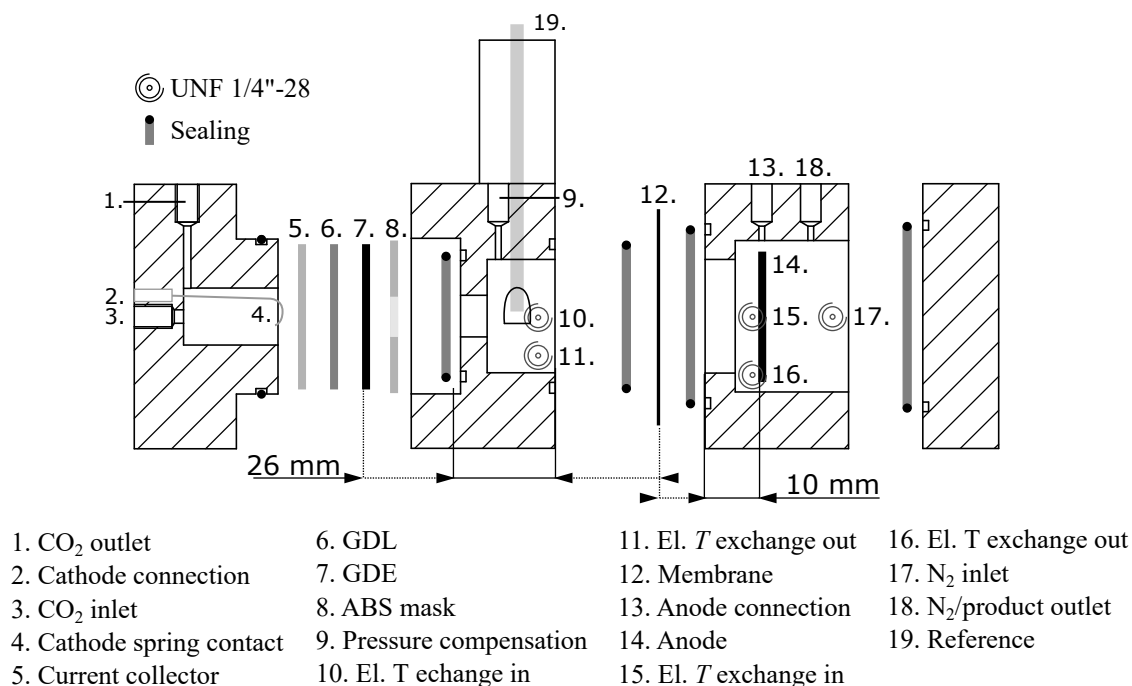


**Figure 6.9:** Exploded view of the cell used for coupling  $\text{CO}_2$  reduction reaction and alcohol oxidation reaction.







## 7 | Results and Discussion

Results presented and discussed in this chapter are based on the fundamental preliminary work of A. Inan<sup>[163]</sup> and D. Kopljar<sup>[138]</sup> at the Institute of Technical Chemistry, University of Stuttgart, Germany (ITC). This accounts for both, the used gas diffusion electrodes (GDEs) and the 1 cm<sup>2</sup> standard GDE test cell in which they were tested. In the present work, the homogeneous catalyst precipitation and electrode preparation method introduced by Inan and Kopljar were further developed. Furthermore, reaction conditions and GDEs composition were optimized and attempted to be transferred into continuous mode of operation and into scaled-up electrolyzers. Last, overall process concepts like coupling CO<sub>2</sub> electrolysis (CO<sub>2</sub>EL) with bipolar membrane electro dialysis (BPED) and selective alcohol oxidation were investigated on a fundamental basis.

First some general annotations. If not stated otherwise the GDE's composition is as follows: poly-(tetrafluoroethylene) (PTFE) powder with a particle size of 4 μm<sup>[160]</sup> (35 wt-%) and acetylene black (AB) (65 wt-%) form the GDE's matrix. The total mass per area was set to 55 mg cm<sub>geo</sub><sup>-2</sup>. Tin oxide is thereby deposited on the carbon support with a final tin loading of  $\sigma_{Sn} = 1 \text{ mg cm}_{geo}^{-2}$ . The active electrode area is 1 cm<sup>2</sup>. Electrodes with these specifications will be referred to as standard GDE. Equally, the term standard GDE matrix only refers to the standard ratio PTFE:AB of 35:65. In some cases the used GDE is specified by the abbreviation xMe/CB, meaning an electrode loading of x mg cm<sub>geo</sub><sup>-2</sup> of metal Me on the carbon black (CB) support with a standard matrix composition. Though cell voltages in electrolysis are defined as being negative, they will be presented by positive values for an easier understanding of the correlation between given electrode potentials and cell voltages.



## 7.1 Reproducibility

In order to give an idea of the general reproducibility of standard experiments like the determination of product distribution during galvanostatic electrolysis, polarization curves and double layer capacitance ( $C_{DL}$ ), reproducibility was analyzed. The following sections focus on quantifying and increasing the reproducibility of such experiments by adjusting the measurement protocol. Each experiment is done with a new GDE. Given values for reproducibility thus comprise the GDE preparation and the experimental routine as summarized in table 6.4 and 6.5, p. 80 and p. 81. A distinction will be made within and between different batches of catalyst synthesis.

### 7.1.1 Reproducibility of galvanostatic experiments

Reproducibility of measured faradaic efficiencies ( $FEs$ ) and cathode potentials was evaluated for galvanostatic experiments with moderate ( $j = -200 \text{ mA cm}^{-2}$ ) and high ( $j = -1000 \text{ mA cm}^{-2}$ ) current densities. Table 7.1 shows measured values and standard deviations of  $FEs$  for the three main products and for the cathode potential at a current density of  $-200 \text{ mA cm}^{-2}$  obtained within and between different batches of catalyst synthesis. 2 M potassium bicarbonate ( $\text{pH} = 10$ ) was used as catholyte. Electrolysis was performed with two GC measurements and no electrode preconditioning prior to galvanostatic control. Under these conditions a high reproducibility is achieved within and between different batches of catalyst synthesis. Gaseous products and cathode potential show a standard deviation below 1 % (of their absolute value) and of 20 mV, respectively. Standard deviation for formate measured via high performance liquid chromatography (HPLC) is noticeably larger, mainly due to greater inaccuracies in electrolyte volume determination (see section 6.3.2, p. 75). This error propagates for the energetic cathode efficiency ( $ECE$ ), resulting in standard deviations of around 1 %.

**Table 7.1:** Faradaic efficiencies, compensated cathode potentials and energetic cathode efficiencies with their standard deviation within and between different batches of catalyst synthesis at moderate current density.

Operating conditions: semi-batch;  $j = -200 \text{ mA cm}^{-2}$ ,  $t = 45 \text{ min}$ ,  $T = 50 \text{ }^\circ\text{C}$ ,  $[\text{KHCO}_3] = 2 \text{ M}$ ,  $\text{pH} = 10$ ; two GC measurements, two HPLC measurements from a single sample; standard GDE.

Batch number	$FE / \%$			$FE_{\text{total}}$ / %	$\varphi_{C, IR}$ / V (vs. SHE)	$ECE$ %	Runs
	$\text{H}_2$	CO	Formate				
1	$2.7 \pm 0.2$	$10.8 \pm 0.3$	$85.7 \pm 2.0$	$99.2 \pm 2.3$	$-1.29 \pm 0.02$	$38 \pm 1.1$	4
2	$3.5 \pm 0.7$	$9.9 \pm 0.2$	$87.2 \pm 1.8$	$100.6 \pm 2.2$	$-1.30 \pm 0.02$	$38 \pm 1.0$	3
avg.	$3.0 \pm 0.7$	$10.4 \pm 0.7$	$86.3 \pm 2.0$	$99.8 \pm 2.3$	$-1.29 \pm 0.02$	$38 \pm 1.1$	7

The described operating conditions give reliable values for moderate current densities but result in large standard deviations at significantly higher current densities, especially for hydrogen production (see condition a) in table 7.2). For this reason, different operating parameters were modified to enhance reproducibility. Since prior to operation the GDE is barely in contact with the electrolyte (a layer of gas is visible between the GDE and electrolyte), applying the full current of galvanostatic operation right away without any preconditioning can be harmful. At the beginning of electrolysis electrode wetting is low, corresponding to a small electrochemical active surface area (ECSA). This results in very high local current densities ( $j_{\text{local}} = I/ECSA$ ) for which  $\text{CO}_2$  transport is not fast enough. The consequently high hydrogen production rate may damage the electrode's structure. Applying a galvanodynamic preconditioning with a scan rate of  $dj/dt = -10 \text{ mA cm}^{-2} \text{ s}^{-1}$  prior to galvanostatic electrolysis lowered the mean hydrogen production and increased reproducibility by 23 % and 55 %, respectively (condition b)). Using potassium chloride as electrolyte again reduced the hydrogen *FE* by about 21 % but had just a minor impact on reproducibility (condition c)). A specific reason for the better performance was not confirmed but it might be attributed to electrolyte decomposition (see figure 7.22, p. 137). Especially at high current densities, the recorded flow of the outlet gas stream tended to show an exponential increase with time instead of a roughly linear behavior at low current densities. Therefore, having just two GC measurements and a subsequent linear fit for the hydrogen and CO volume fraction (see section 6.5, p. 85) is not suitable. Shortening the GC measurement time interval and having three measurements instead of just two clearly decreased standard deviation to only 0.1 % to 0.2 % for gaseous products (condition d)).

Table 7.3 summarizes the standard deviations measured under condition d) for different batches of catalyst synthesis. Results still show a good reproducibility within each batch but large deviations occur between individual batches of catalyst synthesis. A definite reason therefore was not found. Taken transmission electron microscopy (TEM) images showed no significant differences but analysis of tin oxide nanoparticles on carbon black is difficult due to the necessary large magnification and corresponding high intensity of the electron beam. Tin loading was confirmed to be consistent with  $(1.02 \pm 0.01) \text{ mg cm}_{\text{geo}}^{-2}$ .

For these reasons, systematic variations of process conditions or GDE compositions reported in the present work were always performed with a single batch of catalyst synthesis. If not stated otherwise, average standard deviations listed in table 7.1 and 7.3 can be assumed.

**Table 7.2:** Faradaic efficiencies, compensated cathode potentials and energetic cathode efficiencies with their standard deviation for different adjustments in the measurement protocol at high current density. General operating conditions: semi-batch,  $j = -1000 \text{ mA cm}^{-2}$ ,  $t = 45 \text{ min}$ ,  $T = 50 \text{ }^\circ\text{C}$ ; two HPLC measurements from a single sample; standard GDE.

Operating conditions	$FE / \%$			$FE_{\text{total}} / \%$	$\varphi_{\text{C, IR}} / \text{V (vs. SHE)}$	$ECE / \%$	Runs
	$\text{H}_2$	CO	Formate				
a)	$14.4 \pm 5.6$	$5.4 \pm 0.9$	$72.2 \pm 4.7$	$92.0 \pm 4.5$	$-1.55 \pm 0.01$	$28 \pm 1.7$	4
b)	$11.1 \pm 2.5$	$5.0 \pm 0.7$	$74.7 \pm 2.8$	$90.7 \pm 2.3$	$-1.53 \pm 0.01$	$28 \pm 1.1$	3
c)	$8.8 \pm 2.2$	$8.5 \pm 0.3$	$80.4 \pm 2.6$	$97.7 \pm 1.0$	$-1.55 \pm 0.04$	$30 \pm 1.2$	3
d)	$8.0 \pm 0.1$	$7.9 \pm 0.2$	$80.8 \pm 1.5$	$96.7 \pm 1.3$	$-1.55 \pm 0.02$	$30 \pm 0.7$	3
a):	The set current density is directly applied without any preconditioning of the gas diffusion electrode. Electrolyte: 2 M $\text{KHCO}_3$ , pH = 10. Gas phase analysis: two GC measurements.						
b):	Condition a) but with galvanodynamic preconditioning of the electrode with $dj/dt = -10 \text{ mA cm}^{-2} \text{ s}^{-1}$ .						
c):	Condition b) but with the $\text{KHCO}_3$ electrolyte being replaced by 2 M KCl, pH = 10.						
d):	Condition c) but with three GC measurements with shortened analysis time interval.						

**Table 7.3:** Faradaic efficiencies, compensated cathode potentials and energetic cathode efficiencies with their standard deviation/error within and between different batches of catalyst synthesis at high current density.

Operating conditions: semi-batch;  $j = -1000 \text{ mA cm}^{-2}$ ,  $t = 45 \text{ min}$ ,  $T = 50 \text{ }^\circ\text{C}$ ,  $[\text{KCl}] = 2 \text{ M}$ , pH = 10; three GC measurements, two HPLC measurements from a single sample; standard GDE.

Batch number	$FE / \%$			$FE_{\text{total}} / \%$	$\varphi_{\text{C, IR}} / \text{V (vs. SHE)}$	$ECE / \%$	Runs
	$\text{H}_2$	CO	Formate				
1	$8.0 \pm 0.1$	$7.9 \pm 0.2$	$80.8 \pm 1.5$	$96.7 \pm 1.3$	$-1.55 \pm 0.02$	$30 \pm 0.7$	3
2	$18.0 \pm 0.3$	$7.1 \pm 0.6$	$76.5 \pm 0.7$	$101.6 \pm 1.6$	$-1.62 \pm 0.06$	$27 \pm 1.0$	2
3	$19.8 \pm 1.3$	$7.4 \pm 0.4$	$71.7 \pm 1.6$	$98.9 \pm 1.6$	$-1.62 \pm 0.06$	$25 \pm 1.1$	5
avg.	$15.9 \pm 5.6$	$7.5 \pm 0.5$	$75.4 \pm 4.4$	$98.8 \pm 2.3$	$-1.60 \pm 0.04$	$27 \pm 1.7$	10

### 7.1.2 Reproducibility of polarization curves and double layer capacitance

Recorded polarization curves were as well tested for their reproducibility within and between different batches of catalyst synthesis. Results in figure 7.1 and table 7.4 show similar trends as for galvanostatic measurements. Within each batch of catalyst synthesis standard deviations are much smaller compared to deviation between different batches. From the polarization curves it can be assumed that measured deviations arise from mass transport related disparities like catalyst dispersion and amount of active sites. This is indicated by the much larger deviations at high current densities (mass transport governed region) compared to low current densities. Whenever  $\text{CO}_2$  mass transport is not sufficient, cathode potential needs to become more negative since the production of hydrogen takes place at a higher overpotential than  $\text{CO}_2$  reduction. Differences in the chemical nature of the electrocatalyst like oxidation state seem to be less likely as measured onset potentials are comparable (see table 7.4).

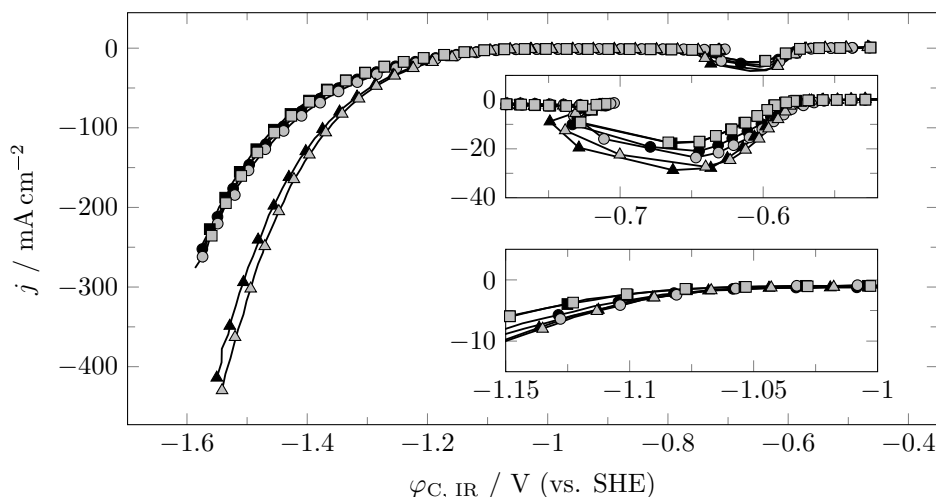


**Figure 7.1:** Polarization curves of the standard gas diffusion electrode prepared from different batches of catalyst synthesis. Circles, squares and triangles represent different batches, respectively. Open and filled marks represent results obtained from different electrodes but the same batch. Operating conditions: semi-batch;  $T = 35\text{ }^\circ\text{C}$ ,  $[\text{KHCO}_3] = 2\text{ M}$ ,  $\text{pH} = 10$ ; standard GDE.

A comparison of measured current densities at a certain cathode potential allows a quantification of standard deviations from recorded polarization curves. Again minor differences are obtained within each catalyst batch, while between different syntheses deviation can be as large as  $\pm 76\text{ mA cm}^{-2}$ . Hence, comparing different operating conditions requires investigation within a single batch of catalyst synthesis. Measured  $C_{\text{DL}}$  values (see table 7.5), on the other hand, show a much lower standard deviation between different batches. This strengthens the assumption that large discrepancies in obtained current



density result from catalyst related effects. Differences in other properties like porosity or hydrophobicity would result larger deviations in electrode wetting and hence in measured  $C_{DL}$ .

**Table 7.4:** Current densities obtained at certain compensated cathode potentials and respective error within and between different batches of catalyst synthesis. Values for current density are obtained from figure 7.1.

Operating conditions: semi-batch;  $T = 35\text{ }^{\circ}\text{C}$ ,  $[\text{KHCO}_3] = 2\text{ M}$ ,  $\text{pH} = 10$ ; standard GDE.

Batch number	$\varphi_{C, IR} / \text{V (vs. SHE)}$			$\varphi_{C, onset} / \text{V (vs. SHE)}$	Runs
	-1.2	-1.35	-1.5		
$j / \text{mA cm}^{-2}$					
1	$-15 \pm 1$	$-53 \pm 2$	$-153 \pm 3$	$-1.077 \pm 0.006$	2
2	$-19 \pm 1$	$-86 \pm 3$	$-295 \pm 15$	$-1.079 \pm 0.005$	2
3	$-12 \pm 1$	$-45 \pm 1$	$-146 \pm 4$	$-1.091 \pm 0.005$	2
avg.	$-15 \pm 3$	$-61 \pm 20$	$-198 \pm 76$	$-1.082 \pm 0.008$	6

**Table 7.5:** Measured double layer capacitance and respective standard deviation/error within and between different batches of catalyst synthesis.

Operating conditions: semi-batch;  $T = 35\text{ }^{\circ}\text{C}$ ,  $[\text{KHCO}_3] = 2\text{ M}$ ,  $\text{pH} = 10$ ; standard GDE .

Batch number	$C_{DL} / \text{mF cm}_{\text{geo}}^{-2}$	Runs
1	$2.4 \pm 0.2$	2
2	$2.7 \pm 0.1$	2
3	$2.2 \pm 0.1$	2
avg.	$2.4 \pm 0.3$	6



## 7.2 Investigations on the catalyst

An important factor when optimizing an electrochemical system for maximum energetic efficiency is the used catalyst. It allows to significantly reduce reaction overpotentials and control the reaction's selectivity. Due to the strong interplay between electrode activity, cathode potential, catalyst oxidation state, electrode wetting and selectivity it is important to test potential catalyst systems under industrial relevant operating conditions. Known formate selective metals have been deposited on the AB support via a homogeneous precipitation method. They were tested for their performance at current densities of  $j = -200 \text{ mA cm}^{-2}$  and  $-600 \text{ mA cm}^{-2}$  and cathode potentials between  $\varphi_{\text{C, IR}} = -0.34 \text{ V}$  (vs. SHE) and  $-1.64 \text{ V}$  (vs. SHE). Palladium based catalysts recently also gained some interest in research. They show great potential for significant reduction of the overpotential but also issues with low stability. In contrast to metals or metal oxides, which activate  $\text{CO}_2$ , palladium nanoparticles can activate water to form a palladium hydride surface, which then in turn can react with  $\text{CO}_2$ . However, such palladium hydrides are only stable within a small potential window.<sup>[164]</sup> Also, they tend to suffer from CO poisoning.<sup>[103]</sup> To evaluate their potential, attempts to incorporate and test palladium based catalysts into the described type of GDE were carried out.

Of all investigated elements tin will be shown to exhibit the best compromise between activity, selectivity and stability and hence is then further investigated. Synthesis parameters of the homogeneous tin oxide precipitation that have not been described by Song and Kang<sup>[158]</sup> were checked for any significance. Also, the GDE's metal loading is an important parameter and its effect was investigated.

### 7.2.1 Type of catalyst

Comparing literature results shows that there is no consistent efficiency ranking for different catalyst materials. For example, Pander et al. reported the order of activity and formate  $FE$  as being  $\text{Pb} < \text{In} \approx \text{Sn}$ ,<sup>[80]</sup> while Mahmood et al. reported an order of  $\text{In} \approx \text{Sn} < \text{Pb}$  for activity and  $\text{Sn} < \text{In} < \text{Pb}$  for  $FE$ .<sup>[66]</sup> Causes for such differing rankings might be differences in oxidation state,<sup>[165]</sup> particle size<sup>[74]</sup>, morphology<sup>[93]</sup>, type of electrode<sup>[6]</sup> or set potential<sup>[165]</sup> since all these parameters strongly effect activity and selectivity. For this reason, some of the most reported metals/metal oxides were loaded on AB via homogeneous precipitation and tested for their activity and selectivity. Requirements for the chosen materials were a known selectivity towards formate and the accessibility by the used precipitation method. X-ray diffractograms of the unsupported but equally treated catalysts are given in the appendix (see figure 9.5, p. 220). They revealed the presence of  $\text{SnO}_2$  and  $\text{In}_2\text{O}_3$  for the tin and indium based catalyst, respectively, prior

to electrolysis. The lead based catalyst mainly showed reflexes of  $\text{Pb}_2\text{O}_3$  but also significant amounts of  $\text{Pb}_3\text{O}_4$  and  $\text{Pb}_3\text{O}_2\text{Cl}_2$ .

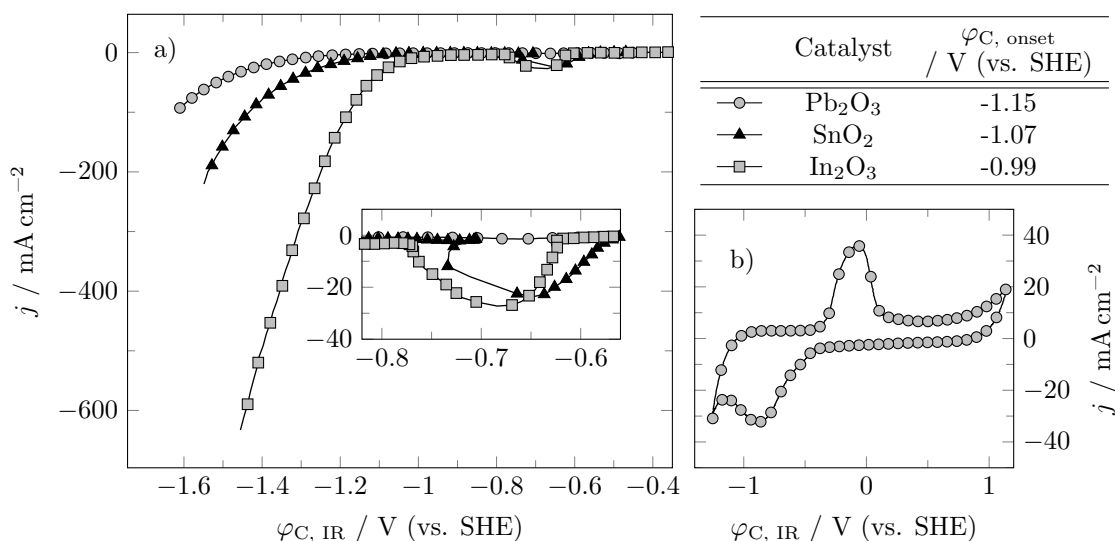


**Figure 7.2:** a) Polarization curves for different metals/metal oxides, supported on acetylene black.  
 b) Cyclic voltammogram of the lead based catalyst to show the position of lead oxide reduction when possible.  
 Electrode loadings were adjusted to match the molar amount of substance of the standard gas diffusion electrode (see table 7.6).  
 Operating conditions: semi-batch;  $T = 35^\circ\text{C}$ ,  $[\text{KHCO}_3] = 2\text{ M}$ ,  $\text{pH} = 10$ ; standard GDE matrix.

Measured onset potentials (see figure 7.2 a)) show another order of activity than expected from literature, namely  $\text{Pb} < \text{Sn} < \text{In}$ . It is important to know that according to Pander et al. the surface of lead is active for  $\text{CO}_2\text{RR}$  in the reduced state, while the surfaces of tin and indium are active in an oxidic state.<sup>[80]</sup> The lead oxide derived catalyst shows no reductive peak attributed to the reduction of oxidic species. Such reduction peak is only observable after previous oxidation within cyclic voltammetry (CV) measurements (see figure 7.2 b)). Indium and tin oxide catalysts, on the other hand, show a reduction peak at around  $-0.65\text{ V}$  (vs. SHE). These peaks suggest that tin and indium are present in a partially oxidized state while lead is fully reduced to its metallic state. Thus, under negative polarization, all mentioned elements are present in their  $\text{CO}_2\text{RR}$  active form. The observed activity ranking should therefore be seen as characteristic for the used catalyst preparation method.

Regarding formate *FE* at a moderate current density ( $j = -200\text{ mA cm}^{-2}$ ), an order of  $\text{In} < \text{Sn} < \text{Pb}$  was observed (see table 7.6). A detailed explanation cannot be given, since correlating selectivities with certain active sites requires surface sensitive characterization methods operating under negative polarization. Pander et al used in-situ ATR-IR spectroscopy for this purpose and reported a metastable surface carbonate ( $\text{MeOCOO}^-$ ) on tin and indium catalysts while for lead based ones  $\text{CO}_2$  is bound directly to the metal atom ( $\text{MeCOO}^-$ ). In contrast to the present work the authors reported the order of

formate selectivity to be  $\text{Pb} \approx \text{In} < \text{Sn}$ , again illustrating the strong dependence of selectivity on the exact electrode and catalyst design.<sup>[80]</sup>

At a higher absolute value of current density ( $j = -600 \text{ mA cm}^{-2}$ ) the observed order changes to  $\text{Pb} < \text{In} < \text{Sn}$ . Especially for the less active lead catalyst, hydrogen evolution strongly increases. Due to the low activity a deep cathodic potential is necessary to reach the enforced current density. At such highly negative potentials ( $\varphi_{\text{C, IR}} = -2.3 \text{ V}$  (vs. SHE)) the CB support itself produces significant amounts of hydrogen.

Note that the sum of all *FEs* of the indium based catalyst does only add up to 91 % to 95 %. From literature it could be expected that alcohols were also formed.<sup>[166]</sup> However, neither HPLC, nor gas chromatography (GC) analysis revealed the existence of any alcohols.

Even though tin does neither show the best activity nor the highest selectivity, it still exhibits good values for both. The *ECE* represents a measure that considers these two aspects. Comparing these values, tin clearly shows the highest efficiency independent of the current density.

**Table 7.6:** Faradaic efficiencies, compensated cathode potentials and energetic cathode efficiencies of different metal/metal oxide catalysts at different current densities.

For the lead based catalyst electrode loading was adjusted to match the molar amount of substance of the tin and indium based one.

Operating conditions: semi-batch;  $t = 45 \text{ min}$ ,  $T = 35 \text{ }^\circ\text{C}$ ,  $[\text{KHCO}_3] = 2 \text{ M}$ ,  $\text{pH} = 10$ ; standard GDE matrix.

Catalyst	$\sigma_{\text{Me}}$ / $\text{mg cm}_{\text{geo}}^{-2}$	$j$ / $\text{mA cm}^{-2}$	<i>FE</i> / %			$\varphi_{\text{C, IR}}$ / V (vs. SHE)	<i>ECE</i> / %
			H <sub>2</sub>	CO	Formate		
In <sub>2</sub> O <sub>3</sub>	1		24	7	60	-1.30	26
SnO <sub>2</sub>	1	-200	2	5	93	-1.39	38
Pb <sub>2</sub> O <sub>3</sub>	1.75		2	2	96	-1.75	31
In <sub>2</sub> O <sub>3</sub>	1		23	7	64	-1.62	23
SnO <sub>2</sub>	1	-600	20	5	75	-1.44	30
Pb <sub>2</sub> O <sub>3</sub>	1.75		50	1	49	-2.30	12

In recent years palladium based catalysts gained a lot of interest in CO<sub>2</sub>RR to formate, mainly due to a much higher activity compared to the recently described metal/metal oxide based catalysts ( $\eta_{\text{Pd}} \approx -200 \text{ mV}$  vs.  $\eta_{\text{Me}_x\text{O}_y} \approx -700 \text{ mV}$  at  $j = -10 \text{ mA cm}^{-2}$ ).<sup>[103]</sup> This major difference arises from a fundamental difference in the reaction mechanism further described in section 4.2.3.3, p. 35. Hence, palladium based catalysts were incorporated into the used GDE matrix and tested for their performance under potentiostatic control. Controlling the potential instead of current density is important since selectivity of palladium is reported to strongly depend on the applied electrode potential.<sup>[164]</sup> However, this potential also determines the surface tension and hence the degree of wetting. Reported cathode

potentials of around  $-700$  mV (vs. SHE) were expected and proven to be too small to achieve a sufficient wetting of the standard GDE matrix. Therefore, the GDE's matrix was changed to oxidatively pretreated Vulcan XC 72 (VX) with PTFE as binder. VX is a more hydrophilic carbon black than AB. It was pretreated with nitric acid to further increase hydrophilicity, allowing for an easier electrolyte intrusion at low absolute values of electrode potential.<sup>[138]</sup> Palladium was deposited on this carbon support with two different loadings. The corresponding polarization curves in figure 7.3 show a much higher activity with a trend consistent to the electrode's palladium loading. Compared to the standard tin oxide catalyst,  $\text{CO}_2$  reduction starts at much less negative potentials, just as expected from literature. Note that the obtained polarization curves were not recorded as usual by preconditioning the GDE followed by a LSV measurement. Instead they were recorded by performing potentiostatic electrolysis at each step for 15 min. In this case no preconditioning is necessary which would require a certain potential appropriate for both, the tin oxide and the palladium based catalyst. Such a potential was not found as palladium tends to deactivate with more negative electrode potentials.

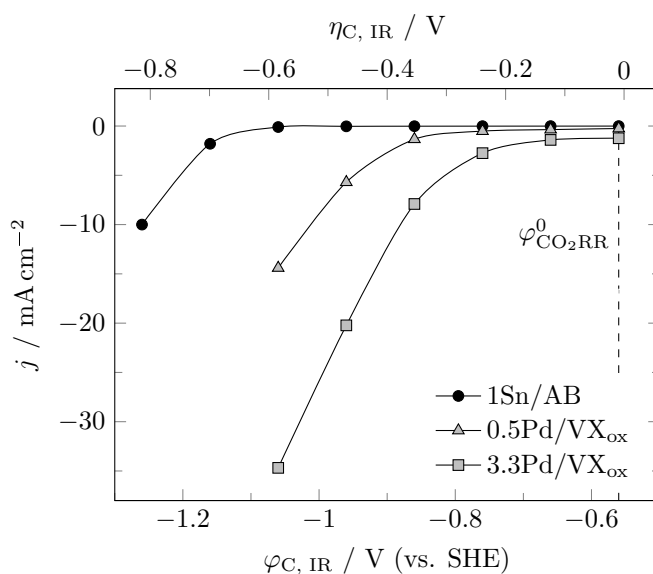


**Figure 7.3:** Polarization curves for two palladium based gas diffusion electrodes with different loadings on a pre-oxidized Vulcan XC 72 support, compared to the standard gas diffusion electrode. In contrast to typically shown polarization curves obtained after a preconditioning routine, results shown here were recorded by a stepwise increase in potential without any preconditioning. At each value potentiostatic electrolysis was performed for 15 min. Current density at the end of each step is plotted.

$$\eta_{C, IR} = \eta_{\text{activation}} + \eta_{\text{concentration}}$$

Operating conditions: semi-batch;  $T = 50^\circ\text{C}$ ,  $[\text{KCl}] = 2 \text{ M}$ ,  $\text{pH} = 10$ ; PTFE:CB ratio = 35:65.

As mentioned, palladium based catalysts show a strong dependence on the applied potential. Product distribution was therefore recorded for certain potentials at which a sufficient current density has been achieved. Electrode 0.5Pd/VX<sub>ox</sub> showed a similar trend as reported by Gao et al. with formate as main product at less negative potentials and a shift to CO with more negative ones.<sup>[167]</sup> The reason behind this

shift was reported to be a transition in the palladium phase. At less negative potentials surface hydrogen coverage is high, facilitating the formation of a palladium hydride, which reduces CO<sub>2</sub> to formate via a CO<sub>2</sub> insertion mechanism. At more negative potentials, however, a pure palladium phase is formed at which CO<sub>2</sub> can only be converted via direct activation, mainly resulting CO. Hydrogen evolution already starts at  $-0.6$  V of overpotential. However, due to the fact that CO selectivity continues to increase up to an overpotential of  $-0.7$  V with  $j = -32 \text{ mA cm}^{-2}$ , CO<sub>2</sub> availability seems to be sufficient at  $\eta_{\text{C, IR}} = -0.6$  V. Consequently, hydrogen evolution is catalyst related and does not primarily result from mass transport limitation. For the higher loaded electrode 3.3Pd/VX<sub>ox</sub>, a completely different behavior is obtained. Here CO is the main product over the whole range with hydrogen rising at higher current densities, probably due to a deploying mass transport limitation. A confirmed explanation for this major difference cannot be given at this point. It is known that the formation of palladium hydride can only proceed at a sufficient rate for small nanoparticles, i.e. their size influences CO<sub>2</sub>RR rates.<sup>[103, 164, 168]</sup> Even though this might have an influence, TEM analysis revealed that the particles of 3.3Pd/VX<sub>ox</sub> ( $(13 \pm 3)$  nm) are just slightly larger than those of 0.5Pd/VX<sub>ox</sub> ( $(10 \pm 3)$  nm). All in all, the moderate selectivity towards formate significantly lowers the *ECE*. Even though the onset potential could be lowered by as much as 400 mV, *ECE* of the palladium catalyst does not outperform the tin oxide reference catalyst at current densities larger than  $10 \text{ mA cm}^{-2}$ .

However, it has to be mentioned that the applied synthesis method does not result in an ideal catalyst. TEM imaging revealed the existing of relatively large particles, compared to the tin oxide catalyst obtained from homogeneous precipitation. Also, particle distribution and particle size distribution are very poor. This applies to both metal loadings shown in the appendix (see figure 9.6, p. 221).

A main problem when using palladium based catalysts is that their selectivity has to be carefully controlled since CO also tends to poison active sites.<sup>[103, 169]</sup> Even though this deactivation is reversible,<sup>[103]</sup> electrode life times of thousands of hours would be required in order to justify the utilization of a noble metal like palladium. Especially when abundant metals like tin can operate at a comparable *ECE*, this effort has rather low chances of success and further investigations on palladium were discontinued.

**Table 7.7:** Double layer capacitances, current densities, faradaic efficiencies and energetic cathode efficiencies obtained at certain overpotentials for palladium based catalysts in comparison to the standard gas diffusion electrode.

$$\eta_{C, IR} = \eta_{\text{activation}} + \eta_{\text{concentration}}$$

Operating conditions: semi-batch;  $t = 30$  min,  $T = 50$  °C,  $[KCl] = 2$  M,  $pH = 10$ ; PTFE content = 35 wt-%.

Electrode	$\varphi_{C, IR}$ / V (vs. SHE)	$\eta_{C, IR}$ / V	$C_{DL}$ / $\text{mF cm}_{\text{geo}}^{-2}$	$j$ / $\text{mA cm}^{-2}$	$FE$ / %			$ECE$ / %
					H <sub>2</sub>	CO	Formate	
0.5Pd/VX <sub>ox</sub>	-0.96	-0.37	11.9	-7	0	18	82	49
	-1.06	-0.47	15.5	-13	0	28	72	39
	-1.16	-0.57	16.3	-25	20	55	25	12
	-1.26	-0.67	21.9	-32	32	63	4	2
	-1.36	-0.77	25.4	-57	48	50	2	1
3.3Pd/VX <sub>ox</sub>	-0.86	-0.27	15.9	-4	0	87	13	9
	-0.96	-0.37	24.5	-7	0	94	6	4
	-1.06	-0.47	26.7	-39	21	64	15	8
1Sn/AB	-1.06	-0.47	0.5	-2.7	0	8	92	50
	-1.16	-0.57	0.7	-16.1	0	11	88	44
	-1.26	-0.67	1.1	-47.8	6	8	86	39
	-1.36	-0.77	1.5	-148	2	5	93	39

## 7.2.2 Synthesis parameters for tin oxide based catalysts

The homogeneous precipitation of tin oxide was varied for the parameters listed below. Addition of the surfactant sodium dodecyl sulfate (SDS) helps to suspend the highly hydrophobic AB aggregates in the solvent and to ensure accessibility of the tin precursor into the pores. Complete removal of the surfactant during filtration was confirmed by attenuated total reflection infrared spectroscopy (ATR-IR) and measuring the  $C_{DL}$ . Type and concentration of precursor, solvent and temperature might effect the precipitation process and lead to different particle sizes, reported to show differing activities.<sup>[74]</sup> However, none of the below listed parameters showed any difference in activity or selectivity higher than the standard deviation for different batches of catalyst synthesis.

- Surfactant addition:  $[SDS] = 0$  mM to 10 mM.
- Type of tin precursor:  $\text{SnCl}_2 \cdot 2\text{H}_2\text{O}$ ,  $\text{SnCl}_4 \cdot 5\text{H}_2\text{O}$ ,  $\text{SnCl}_4$ .
- Precursor concentration:  $[\text{SnCl}_2 \cdot 2\text{H}_2\text{O}] = 1$  mM to 10 mM
- Type of solvent: water, water/glycol 1:1.
- Precipitation temperature: 90 °C to 150 °C (water/glycol 1:1 was used as solvent for  $T > 100$  °C).



Addition of SDS is still recommendable as it facilitates the suspension of AB and simplifies the handling of the slurry during synthesis. A detailed physico-chemical characterization of the supported tin oxide nanoparticles and the final GDE was already given by D. Kopljar<sup>[138]</sup> and is not part of the present work. In order to give a brief idea for the size of carbon agglomerates and tin oxide particles scanning electron microscopy (SEM) and TEM images for AB loaded with 2.6 wt-% of tin (corresponds to an electrode loading of  $1 \text{ mg cm}_{\text{geo}}^{-2}$ ) are shown in figure 7.4. Carbon agglomerates range between 100 nm and 200 nm in diameter with irregular shaped particles. In contrast to the less energy intensive SEM imaging, TEM images suffer severely from particle movement at strong magnifications. Hence, size evaluation is not as accurate but tin particles are estimated to be around 3 nm in diameter.

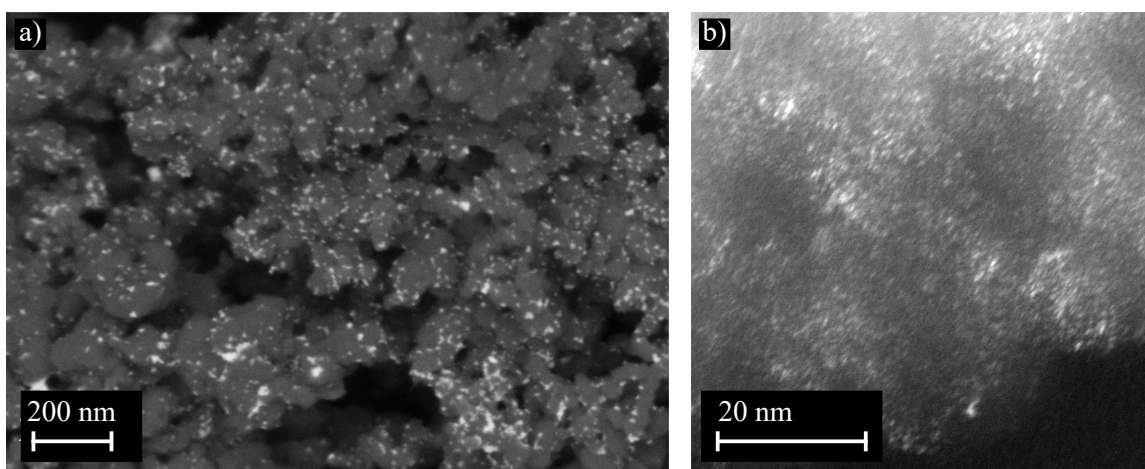


**Figure 7.4:** a) Scanning and b) transmission electron microscopy images of tin oxide (white) loaded acetylene black (grey).  $w_{\text{Sn}} = 2.6 \text{ wt-\%}$ .

### 7.2.3 Tin oxide loading

Typically, minimizing the amount of metal necessary for a certain activity is a high priority goal in catalyst development. This applies especially when precious metals have to be used. For  $\text{CO}_2\text{RR}$  to formate, however, tin is a rather abundant element. Assuming a reasonable lifetime of the GDE this allows to move the focus in catalyst development to other points of interest like optimizing the *ECE*. Figure 7.5 compares the activity of different tin loadings during potentiostatic preconditioning and subsequent LSV.

Unsurprisingly, initial activity rises with increasing electrode loading (see figure 7.5 a) at  $t = 3 \text{ min}$ ). However, a strong deactivation is visible over time for  $\sigma_{\text{Sn}} > 5 \text{ mg cm}_{\text{geo}}^{-2}$ , which is more pronounced in the potentiostatic preconditioning but also observable in the dynamic measurement of the polarization curve (see figure 7.5 b)). In the latter, a loading of  $7.5 \text{ mg cm}_{\text{geo}}^{-2}$  already shows a course that is slightly differing from the typical exponential behavior. At an even higher loading of  $10 \text{ mg cm}_{\text{geo}}^{-2}$  activity clearly

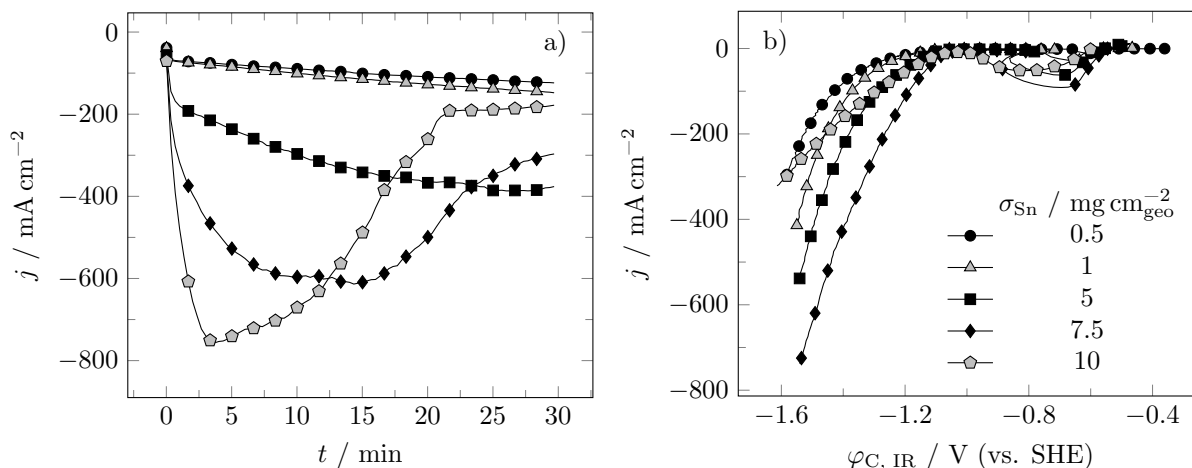


**Figure 7.5:** a) Course of current density during the second potentiostatic preconditioning step ( $\varphi_{C, IR} = -1.36$  V (vs. SHE), see table 6.4, p. 80) for different electrode loadings between  $0.5 \text{ mg cm}_{\text{geo}}^{-2}$  and  $10 \text{ mg cm}_{\text{geo}}^{-2}$ .

b) Polarization curves obtained immediately after potentiostatic preconditioning.

The legend applies to both figures.

Operating conditions: semi-batch;  $T = 35$  °C,  $[\text{KHCO}_3] = 2$  M,  $\text{pH} = 10$ ; standard GDE matrix.

decreases again over the whole range of current density. Three main effects might be relevant for this observation.

- Electrode flooding due to a lowered hydrophobicity of the carbon support by a high coverage with more polar tin oxide.
- Destructing of the GDE's structure by excessive hydrogen production at high current densities.
- Catalyst related effects due to lower metal-support interactions or smaller particle-particle distances:
  - Reduction of the active oxide species to metallic tin.
  - Catalyst leaching.
  - Particle agglomeration.

The first hypothesis, electrode flooding, is refuted by the measured  $C_{DL}$  values either for different loadings after preconditioning, or over time during 30 min of potentiostatic electrolysis (see figure 7.6 a) and b), respectively). Keeping in mind that capacitance is shown instead of ECSA and that the specific capacitance of tin oxide is significantly higher than the one of AB<sup>[170, 171]</sup>, the differences in electrode wetting after electrolysis are not as pronounced to explain such a huge difference in deactivation behavior. Also, when having a look at the course of potential over time for a loading of  $\sigma_{Sn} = 10 \text{ mg cm}_{\text{geo}}^{-2}$ , deactivation already starts at moderate  $C_{DL}$  values were lower loaded electrodes show no sign of deactivation.

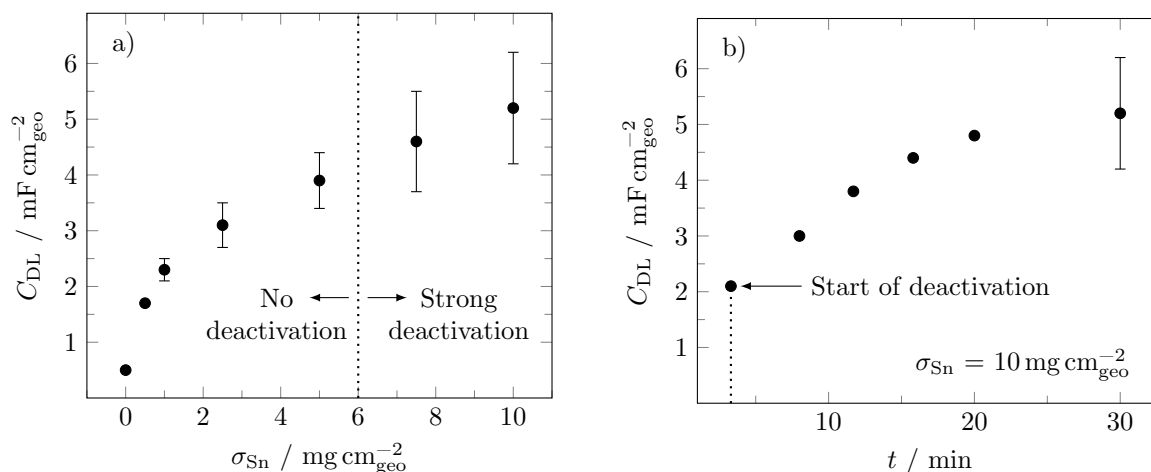


**Figure 7.6:** a) Double layer capacitance of gas diffusion electrodes with electrode loadings between  $0.5 \text{ mg cm}_{\text{geo}}^{-2}$  to  $10 \text{ mg cm}_{\text{geo}}^{-2}$  after both potentiostatic preconditioning steps (see table 6.4, p. 80). b) Time dependent double layer capacitance for a loading of  $10 \text{ mg cm}_{\text{geo}}^{-2}$ . Each value was measured with a fresh gas diffusion electrode. Operating conditions: semi-batch;  $T = 35^\circ\text{C}$ ,  $[\text{KHCO}_3] = 2 \text{ M}$ ,  $\text{pH} = 10$ ; standard GDE matrix.

The second hypothesis, structure deterioration by excessive hydrogen evolution, is reputed by galvanostatic electrolysis at moderate current density ( $j = -200 \text{ mA cm}^{-2}$ ). Figure 7.7 shows a similar trend as for potentiostatic electrolysis with a clear deactivation at a loading of  $10 \text{ mg cm}_{\text{geo}}^{-2}$ . However, no significant increase in hydrogen  $FE$  ( $<3\%$ ) was found compared to the other loadings.

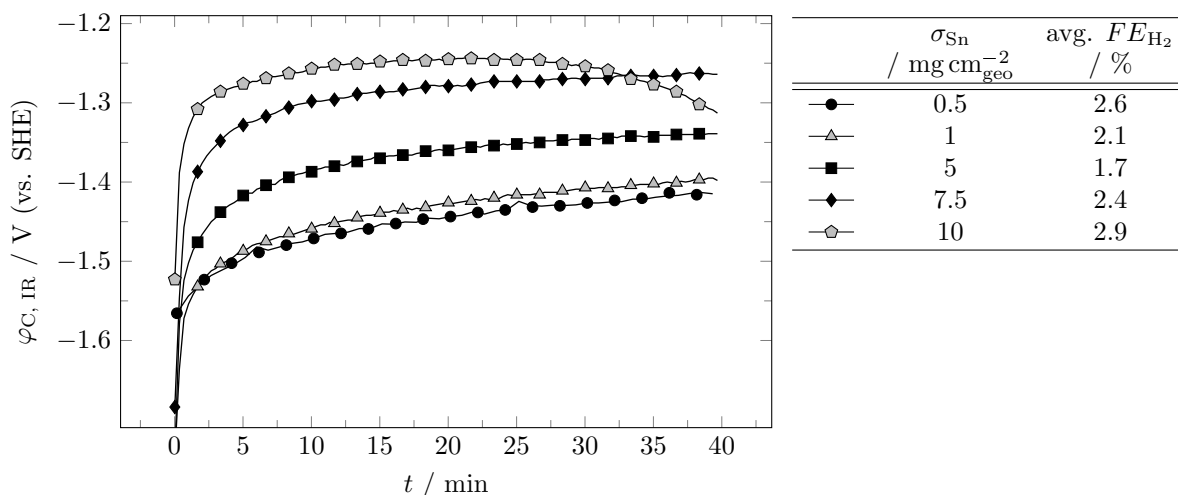


**Figure 7.7:** Course of cathode potential over time and average hydrogen faradaic efficiency at a current density of  $-200 \text{ mA cm}^{-2}$  for different electrode loadings. Operating conditions: semi-batch;  $T = 35^\circ\text{C}$ ,  $[\text{KHCO}_3] = 2 \text{ M}$ ,  $\text{pH} = 10$ ; standard GDE matrix.

These results suggest that the third hypothesis - catalyst related effects - is responsible for the observed deactivation. Hence, different possible deactivation mechanisms were investigated. According to Dutta et al. tin oxide is gradually reduced to metallic tin, starting at a cathode potential of  $-1 \text{ V (vs. SHE)}$ . CV measurements after 30 min of potentiostatic preconditioning at  $-1.26 \text{ V}$ ,  $-1.36 \text{ V}$

or  $-1.46$  V (vs. SHE), indeed revealed an increase in the charge passed for metallic tin oxidation when increasing the loading from  $1 \text{ mg cm}_{\text{geo}}^{-2}$  to  $10 \text{ mg cm}_{\text{geo}}^{-2}$  (see appendix figure 9.7, p. 222). However, comparing the tin oxidation charge for a given potential during preconditioning, a loading of  $10 \text{ mg cm}_{\text{geo}}^{-2}$  results in a roughly ten times larger value than a loading of  $1 \text{ mg cm}_{\text{geo}}^{-2}$  ( $q_{\text{Sn ox, } 10 \text{ mg cm}_{\text{geo}}^{-2}} = 48 \text{ mC}$ ,  $114 \text{ mC}$  and  $205 \text{ mC}$ , compared to  $q_{\text{Sn ox, } 1 \text{ mg cm}_{\text{geo}}^{-2}} = 5 \text{ mC}$ ,  $12 \text{ mC}$  and  $20 \text{ mC}$  at  $-1.26$  V,  $-1.36$  V and  $-1.46$  V (vs. SHE), respectively). Even though this analysis method is not supposed to be very accurate and cannot distinguish between surface and bulk material, it suggests that there is no major difference in oxidation state between different loadings.

Different groups reported an unspecified loss of active material during electrolysis.<sup>[53, 63, 97]</sup> In order to check for the possibility of catalysts leaching, the catholyte's tin content after 40 min of galvanostatic electrolysis was analyzed by inductively coupled plasma optical emission spectroscopy (ICP-OES). Despite a large error of measurement induced by the overpowering amount of potassium salt in the catholyte sample an undeniable quantity of tin was found. Raising the current density from  $-200 \text{ mA cm}^{-2}$  to  $-800 \text{ mA cm}^{-2}$  increased the mass of tin in the electrolyte from  $0.06 \text{ mg}$  to  $0.11 \text{ mg}$ . Considering the used metal loading of  $10 \text{ mg cm}_{\text{geo}}^{-2}$  and that presumably 15 % to 25 % of the electrode is wetted, this would imply a leaching of 2 % to 7 %. Due to the large uncertainties of both ICP-OES analysis and ECSA determination exact values might differ. All in all, leaching seems to contribute to deactivation but further quantitative statements cannot be given.

One last explanation would be the agglomeration of tin oxide nanoparticles. A larger number of particles in closer proximity to each other tend to agglomerate more easily than fewer particles with larger distances. This option, however, could not be verified due to the very limited magnification and sharpness of taken TEM images.

Similar results were obtained in continuous mode of galvanostatic electrolysis over 24 h of time on stream, with higher loadings resulting in a faster deactivation, even though temperature and electrolyte composition are different. Figure 7.8 shows the performance of electrodes loaded with  $0.25 \text{ mg cm}_{\text{geo}}^{-2}$  to  $2.5 \text{ mg cm}_{\text{geo}}^{-2}$ . Again, initial activity is much larger for higher loaded electrodes, which directly correlates with the amount of CO being produced. This correlation arises from the potentiostatic character of tin-based catalysts with less negative potentials favoring CO formation.<sup>[58, 61, 90]</sup> The increasing amount of CO with increasing electrode loading is supposed to be another reason for deactivation. For a loading of  $2.5 \text{ mg cm}_{\text{geo}}^{-2}$ , CO FE rises quickly to about 20 % with additional 5 % of hydrogen. Thus, CO<sub>2</sub> partial pressure is reduced by 25 %, lowering the amount of solved reactant accordingly and inducing mass transport limitations. Once this limitation sets in, more hydrogen needs to be produced to keep up the enforced current, which in turn lowers CO<sub>2</sub> availability further. The higher rate of hydrogen evolution

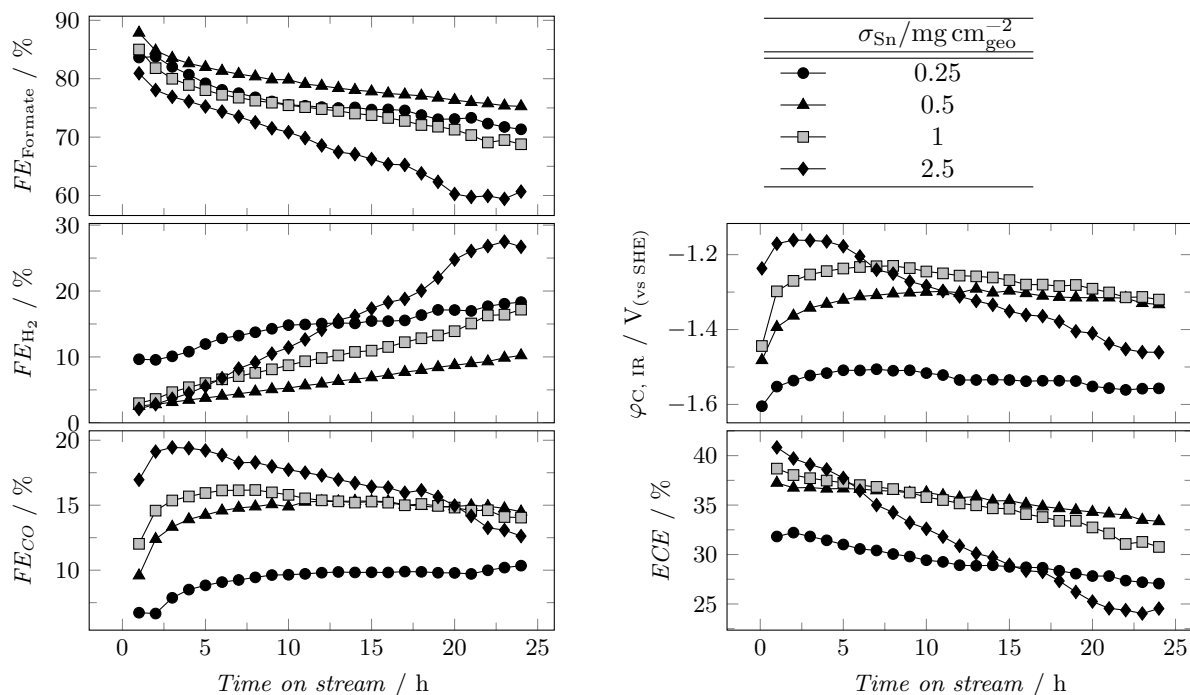


**Figure 7.8:** Long-term performance analysis for different electrode loadings.

Operating conditions: continuous;  $j = -200 \text{ mA cm}^{-2}$ ,  $T = 50 \text{ }^\circ\text{C}$ ,  $[\text{KCl}] = 1 \text{ M}$ ,  $\text{pH} = 10$ ; standard GDE matrix.

reaction (HER) also requires a more negative electrode potential, which presumably leads to an increased reduction of tin oxide to metallic tin.<sup>[81]</sup> Tin metal itself exhibits an increased activity for HER, which raises the hydrogen production rate and feed dilution even further.<sup>[165]</sup> A vicious circle arises and the decline in formate production accelerates.

When the electrode loading is too low mass transport limitation sets in due to a higher absolute value of current density required per active site. Results show that this is the case for a loading of  $0.25 \text{ mg cm}_{\text{geo}}^{-2}$  where hydrogen is at a high level already at the first point of measurement. Consequently, a tin loading of  $0.5 \text{ mg cm}_{\text{geo}}^{-2}$  was found to be optimal for long-term operation.



## 7.3 Investigations on process conditions

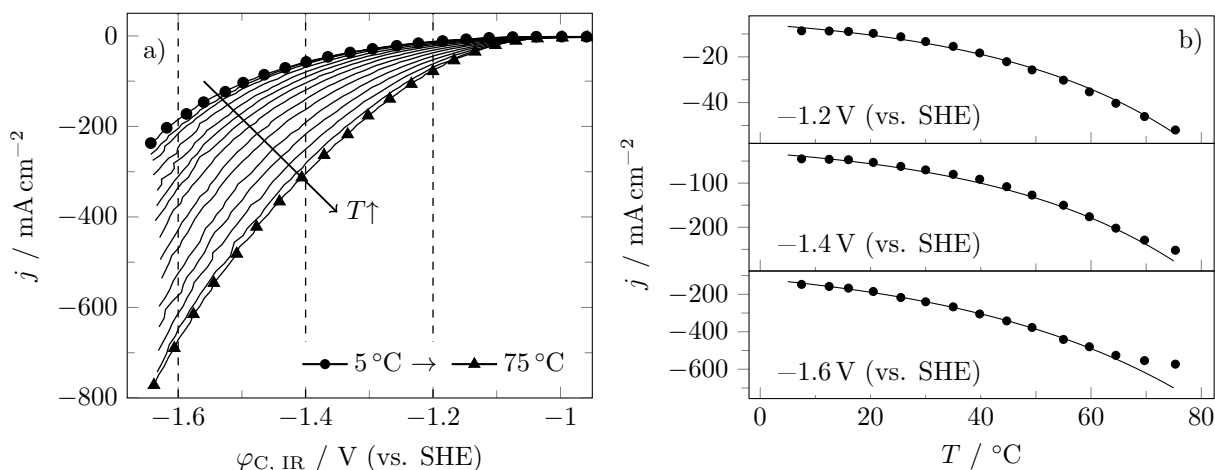
The investigation of optimum process conditions is a wide and manifold field. Not only physical parameters like temperature or differential pressure (not investigated here due to the electrode's low mechanical stability) are of special importance but also chemical parameters like type, concentration or purity of the electrolyte and CO<sub>2</sub> feed. Again all mentioned parameters will be demonstrated to have a strong interconnection influencing both ohmic and reaction related overpotentials.

### 7.3.1 The effect of temperature

Among different reaction parameters temperature is one of the most important ones. It affects primarily reaction kinetics and slightly the equilibrium potential as described in section 4.2.4.2, p. 41. Higher temperatures are also of great importance to reduce overpotentials throughout the cell. E.g. polymer electrolyte membrane (PEM) electrolyzers are typically operated at temperatures of 50 °C to 80 °C, mainly for the benefit of enhanced electrode kinetics, mass transport and ionic conductivity.<sup>[126]</sup> However, running a complex system like a GDE, especially at higher current densities, requires additional considerations of reactant and product mass transport (including concentration gradients and diffusion coefficients), as well as electrode wetting (including viscosity and surface tension) and solvent evaporation. This section describes the influence of temperature on the performance of standard GDEs for short-term (low electrolyte intrusion depth) and long-term operation (high electrolyte intrusion depth).

The following results were obtained after 30 min to 45 min of electrolysis, which corresponds to an electrolyte intrusion depth of around 70 μm (determined by SEM/X-ray emission spectroscopy (XES) element mapping, see appendix figure 9.8, p. 223). Figure 7.9 a) depicts polarization curves obtained for different temperatures between 5 °C to 75 °C, which reveal a pronounced influence of temperature. Note that these curves were obtained with the same electrode, which was first preconditioned by potentiostatic electrolysis at 35 °C as described in section 6.4.1, p. 79. In this way differences in electrode wetting can be neglected. Evidence for this assumption is given by measuring the electrode's  $C_{DL}$  before the first and after the last linear sweep voltammetry (LSV) scan, resulting in similar values ( $C_{DL, \text{before}} = 1.54 \text{ mF cm}_{\text{geo}}^{-2}$  and  $C_{DL, \text{after}} = 1.46 \text{ mF cm}_{\text{geo}}^{-2}$ ). Also, LSV scans themselves do not enhance the electrode's activity. Four consecutive LSV scans at the same operating conditions even showed a small decrease in activity (see appendix figure 9.2, p. 218). Between every LSV scan a 5 min open circuit break was applied to allow the next temperature to stabilize.

Electrode activity clearly increases over the whole investigated temperature range, which is in good accordance with literature.<sup>[112, 127, 128]</sup> With increasing temperature diffusion coefficients<sup>[130, 131]</sup> (see



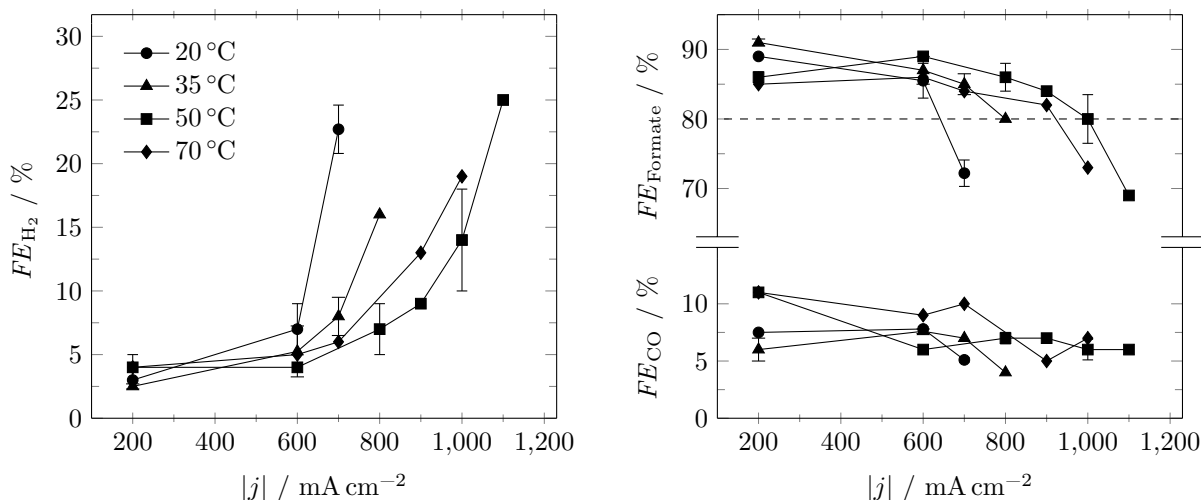
**Figure 7.9:** a) Polarization curves obtained at different temperatures from a single electrode preconditioned at 35 °C. b) Course of current density as function of temperature for different cathode potentials. Solid lines represent an exponential fit (not considering diverging points at elevated temperatures). Operating conditions: semi-batch; [KCl] = 2 M, pH = 10; standard GDE.

figure 4.15, p. 42) and electrode kinetics are enhanced exponentially (see equation 4.1.22, p. 23), thus lowering the concentration and activation overpotential, respectively. At low absolute values of cathode potentials, meaning low current densities and a microkinetic control, this transfers directly to an exponentially increasing current density with temperature (see figure 7.9 b)). However, for higher absolute values of cathode potentials (-1.6 V, meaning a significantly higher current density) mass transport becomes rate determining. This leads to a deviation from the exponential increase with an inflection point and flattening of current density over temperature. Note that such a curve could also be obtained when CO<sub>2</sub> mass transport stays constant, simply by reaching a limiting current density. Proof that CO<sub>2</sub> mass transport limitation is indeed influenced by temperature and responsible for the observed flattening was found by analyzing the product distribution under galvanostatic control. Figure 7.10 depicts *FEs* of the three major products. By defining a minimum formate *FE* of 80 % a limiting current density can be determined for each temperature with -600 mA cm<sup>-2</sup>, -800 mA cm<sup>-2</sup>, -1000 mA cm<sup>-2</sup> and -900 mA cm<sup>-2</sup> for 20 °C, 35 °C, 50 °C and 70 °C, respectively. Hence, a temperature of 50 °C was found to be optimal.

On the other hand, hydrogen *FE* is a good indicator for mass transport limitation (see figure 7.10 a)). The power supply unit enforces the set current density through the cell. As soon as CO<sub>2</sub> is depleting, water remains the only reducible species, giving rise to the HER. Increasing the temperature from 20 °C to 50 °C clearly shifts the steep rise in hydrogen production to higher absolute values of current density. A further increase to 70 °C, however, again reverses this trend.

At a moderate current density of -200 mA cm<sup>-2</sup> temperature has no relevant influence on HER, but slightly on the CO:formate ratio. As a general trend, higher temperatures correspond to an increased CO





**Figure 7.10:** Average faradaic efficiencies for the three main products over current density at different temperatures.

The legend applies to both figures.

Operating conditions: semi-batch;  $t = 45 \text{ min}$ ,  $[\text{KHCO}_3] = 2 \text{ M}$ ,  $\text{pH} = 10$ ; standard GDE.

formation. Again this can be explained by the potentiostatic character of tin oxide. Consequently, the obtained formate  $FE$  is the highest at 35 °C ( $\varphi_{\text{C, IR, } t=45 \text{ min}} = -1.34 \text{ V}$  (vs. SHE)) with 91 % and the lowest at 70 °C ( $\varphi_{\text{C, IR, } t=45 \text{ min}} = -1.23 \text{ V}$  (vs. SHE)) with 85 %.

A deeper investigation of temperature dependent mass transport limitation requires consideration of the following aspects:

- Wetted electrode surface or ECSA, which determines the local current density ( $j_{\text{local}} = I/\text{ECSA}$ ).
- Reactant mass transport depending on  $\text{CO}_2$  solubility and diffusion coefficient.
- Product mass transport into the bulk phase electrolyte, depending on the formate diffusion coefficient.

When using GDEs, electrode wetting is amongst the most important parameters. It determines the amount of available active sites, local current density and diffusion pathways for reactants and products. As described in section 4.3.1, p. 46, electrode wetting depends on the applied potential. This would imply a larger degree of wetting and with that a possible flooding at low temperatures, as more negative cathode potentials are necessary for a certain current density. However, temperature also indirectly affects electrowetting by reducing viscosity and surface tension of the electrolyte (see figure 7.11).  $C_{\text{DL}}$  analysis after potentiostatic electrolysis revealed an increasing degree of wetting with rising temperature. In contrast to that, galvanostatic electrolysis leads to relatively stable values for  $C_{\text{DL}}$ . Here, the contrary effects of less negative electrode potentials and easier electrowetting at higher temperatures seem to compensate each other. Thus, differences in electrode wetting can be neglected for the discussion of mass transport limitation and corresponding product distribution.

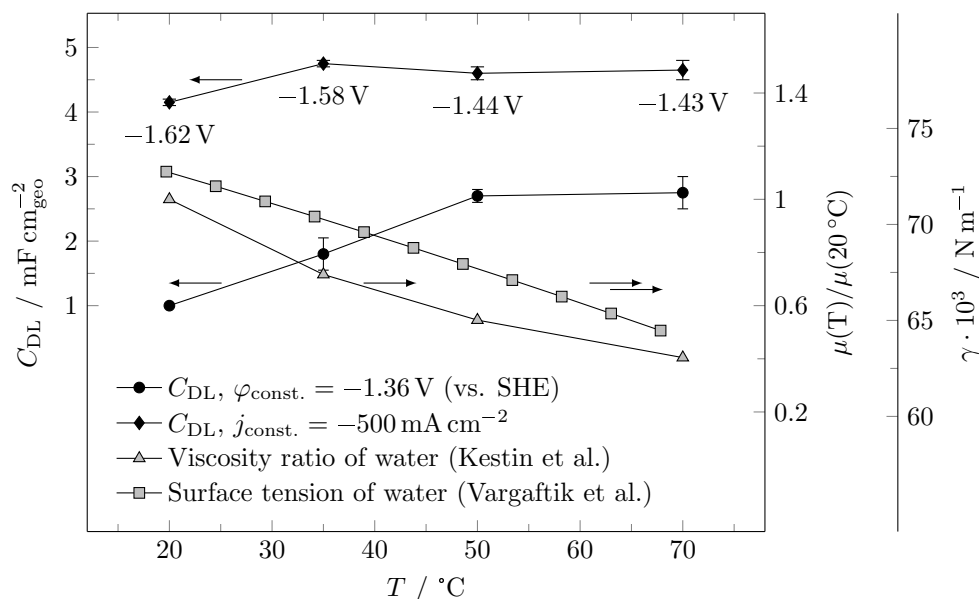


**Figure 7.11:** Double layer capacitance obtained after potentiostatic and galvanostatic electrolysis, compared to the relative viscosity<sup>[172]</sup> and surface tension<sup>[173]</sup> of water over temperature. Operating conditions: semi-batch;  $t_{\text{potentiostatic}} = 30$  min,  $t_{\text{galvanostatic}} = 40$  min,  $[\text{KHCO}_3] = 2$  M, pH = 10; standard GDE.

The temperature dependence of  $\text{CO}_2$  mass transport depends on both, solubility and diffusivity (see section 4.2.4.2, p. 41). At low temperatures it is governed by the insufficiently high diffusion coefficient of  $\text{CO}_2$ . With increasing temperature  $\text{CO}_2$  solubility decreases and starts to dominate the mass transport. However, at low temperatures the formate diffusion coefficient is also low and product mass transport limitation has to be considered as well. In order to investigate the influence of reactant and product diffusion, hydrogen *FE* was measured at different current densities while gradually lowering the  $\text{CO}_2$  or increasing the formate concentration. Results in figure 7.12 a) - c) demonstrate an optimum in  $\text{CO}_2$  mass transport at  $50^\circ\text{C}$ , presumably due to the opposing influence of  $\text{CO}_2$  solubility and diffusivity. At this point lowering the reactant concentration has the least negative impact compared to higher or lower temperatures. Besides  $\text{CO}_2$  mass transport, formate diffusion was also found to be insufficiently fast, especially at low temperatures (see figure 7.12 d) - f)). At  $20^\circ\text{C}$  addition of potassium formate to the electrolyte has a strong negative impact on mass transport, resulting in a steep increase in hydrogen formation. This effect is greatly reduced when heating up to  $50^\circ\text{C}$  and is not measurable any more at  $70^\circ\text{C}$ . In contrast to  $\text{CO}_2$  diffusion rates, solubility is not relevant (within the investigated concentration range), leading to a steady increase in product mass transport with increasing temperature. Note that reported *FEs* do not exactly match with those in figure 7.10 as they were obtained through fast stepwise galvanostatic measurements described in section 6.4.2, p. 82.

The obtained maximum in  $\text{CO}_2$  diffusion rates can be supported by calculating the maximum current density before mass transport limitation starts to set in. Equation 4.3.1, p. 43, assumes planar electrodes

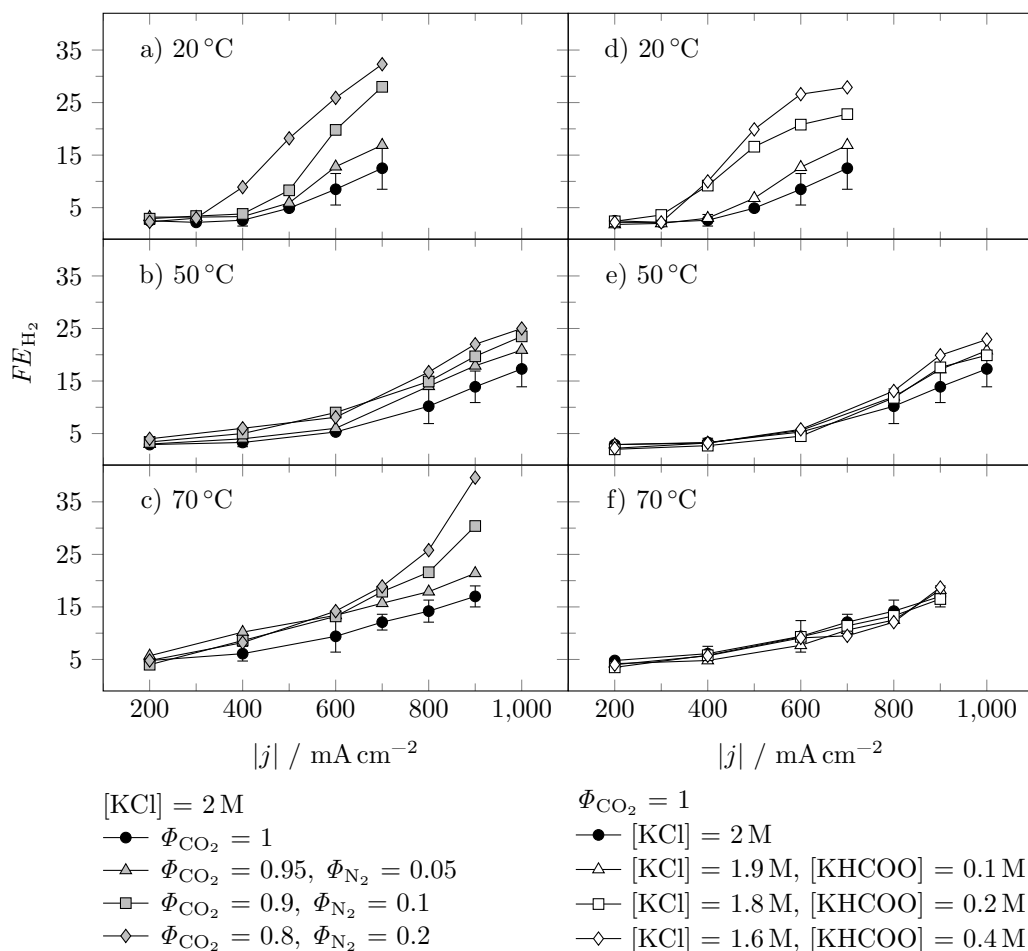


**Figure 7.12:** Hydrogen faradaic efficiency over current density as indicator for  $\text{CO}_2$  and formate transport limitation at different temperatures. a) - c) Gradually reduced  $\text{CO}_2$  feed concentration. d) - f) Gradually increased formate concentration. Operating conditions: semi-batch, fast hydrogen  $FE$  screening protocol; pH = 10; standard GDE.

but can be adapted to porous systems. In contrast to planar electrodes,  $\text{CO}_2$  diffusion pathways inside GDEs are significantly shorter with around  $2 \cdot 10^{-7} \text{ m}$  instead of  $5 \cdot 10^{-5} \text{ m}$ <sup>[111]</sup>. The diffusion length in the investigated GDE was estimated from experimental data and agglomerate size analysis (see figure 7.4, p. 111).<sup>[134]</sup> On the other hand, pore diffusion is around a factor of 10 slower than bulk diffusion.<sup>[134]</sup> The calculated values of table 7.8 show the same optimum as experimental data at a temperature of 50 °C and support the described opposite influences on  $\text{CO}_2$  mass transport very well. Note that the calculated values for the limiting current density in this case the current density at which HER starts to accelerate. They shall not be confused with the defined 80 % criteria of figure 7.10.

**Table 7.8:** Effect of temperature on the limiting current density. Values are calculated by using equation 4.3.1, p. 43. Values for solubility are obtained from <sup>[124, 129]</sup>, the ones for diffusion coefficients from <sup>[130, 131]</sup>. Effective pore diffusion coefficients are estimated to be  $D_{\text{eff}} = D/10$  at a diffusion length of  $l = 2 \cdot 10^{-7}$  m.<sup>[134]</sup>

$T / ^\circ\text{C}$	20	35	50	70
$D_{\text{eff}} \cdot 10^{10} / \text{m}^2 \text{s}^{-1}$	1.45	2.18	3.23	5.21
$S / \text{mol m}^{-3}$	25.04	17.63	13.17	7.47
$j_{\text{lim}} / \text{mA cm}^{-2}$	-342	-361	-400	-366

In contrast to short-term experiments, where the intrusion depth is relatively low, long-term experiments result in much longer product diffusion pathways. Monitoring the electrode wetting in continuous mode of operation over 24 h of time on stream in terms of measuring the  $C_{\text{DL}}$  illustrates the linear increase over time (see figure 7.14 c)). Note that the  $C_{\text{DL}}$  value is not directly proportional to the  $\text{CO}_2\text{RR}$  active area but with the total electrolyte covered one (ECSA). Thus, no conclusions can be drawn on the extension of reaction and flooded zone (see figure 4.18, p. 46).  $C_{\text{DL}}$  shows a linear increase over time on stream and reaches a value of  $19.5 \text{ mF cm}_{\text{geo}}^{-2}$  at  $t = 24$  h, compared to only  $2.7 \text{ mF cm}_{\text{geo}}^{-2}$  at 45 min in short-term operation.

Due to these large differences the influence of temperature was also tested at a moderate current density of  $-200 \text{ mA cm}^{-2}$  in continuous mode of operation within 24 h of time on stream. Results depicted in figure 7.13 again show an optimum temperature of  $50^\circ\text{C}$  with the most stable formate  $FE$  and lowest hydrogen production rate. At 1 h of time on stream product distribution matches the results of semi-batch operation with comparable hydrogen  $FE$  and a shift from formate to  $\text{CO}$  with higher temperatures (see figure 7.10). Lower and higher values than  $50^\circ\text{C}$  result in a strongly increasing hydrogen  $FE$  over time. Even though cathode potential is the least negative at  $70^\circ\text{C}$  (highest activity), the low formate selectivity results in a lower and faster declining  $ECE$  than at  $50^\circ\text{C}$ .

Since again  $50^\circ\text{C}$  was found to be the optimum temperature, the observed and calculated minimum in  $\text{CO}_2$  mass transport limitation can be assumed to become a decisive factor, even at low current densities, as electrolyte intrusion increases. However this could not be proven experimentally. On the other hand, other aspects were found to play a role as well, depending on the temperature.

Except for an initial phase where electrode activity rises and cathode potential becomes less negative due to an enlarging reaction zone (first 5 h), hydrogen  $FE$  and electrode potential are roughly reversed proportional. The more hydrogen needs to be produced for any reason, the more negative is the measured cathode potential due to the catalyst's higher overpotential for HER. This however, is only the case for a temperature range between  $20^\circ\text{C}$  to  $50^\circ\text{C}$ . At  $70^\circ\text{C}$  hydrogen  $FE$  rises continuously, while the cathode potential remains stable. This major difference suggests separate reasons for deactivation over time.

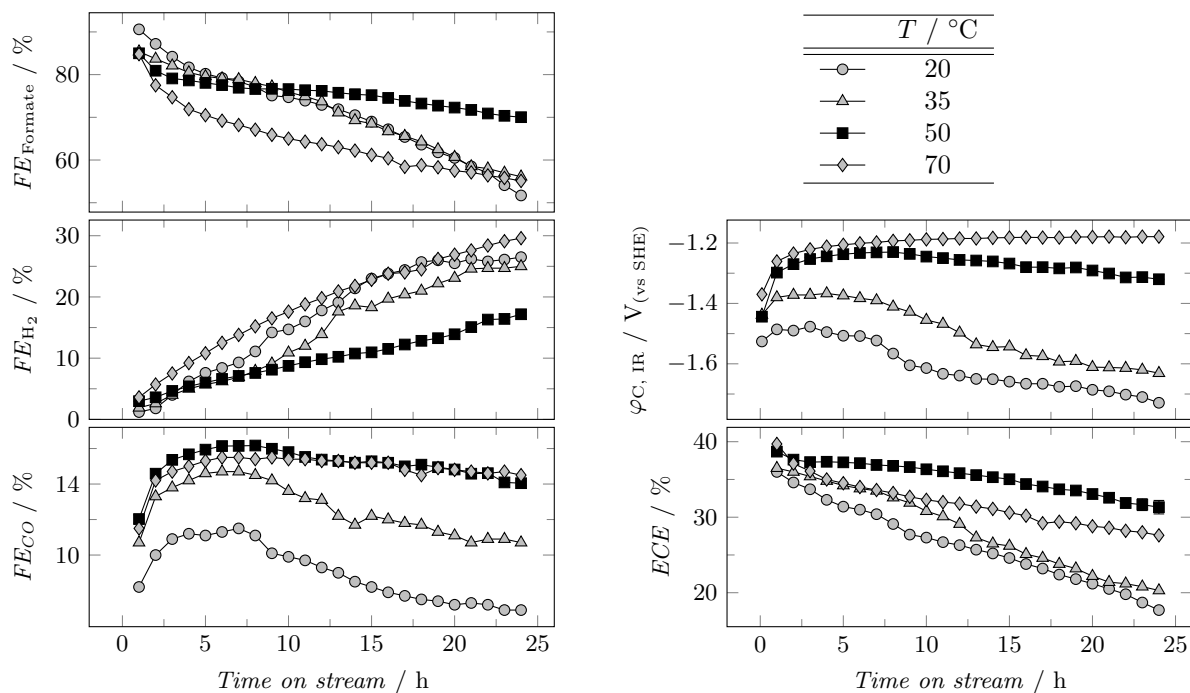


**Figure 7.13:** Long-term performance analysis for different temperatures.

Operating conditions: continuous;  $j = -200 \text{ mA cm}^{-2}$ ,  $[\text{KCl}] = 1 \text{ M}$ ,  $\text{pH} = 10$ ; standard GDE.

Whenever cathode potential and hydrogen  $FE$  correlate in such a reversed proportional manner ( $20^\circ\text{C}$  to  $50^\circ\text{C}$ ), mass transport limitation is assumed to be decisive. Due to the much stronger electrode wetting and consequently much longer diffusion pathway for formate into the bulk electrolyte, product mass transport becomes a limiting factor even at a moderate current density of  $-200 \text{ mA cm}^{-2}$ . A first indication for this hypothesis is the point at time on stream where hydrogen  $FE$  starts to deviate from the one at  $50^\circ\text{C}$ . For  $20^\circ\text{C}$  this is the case at about 5 h, while at  $35^\circ\text{C}$  hydrogen  $FE$  accelerates after 9 h. This correlates with the trend of increasing diffusion coefficients with higher temperatures.

Similar to the investigation of relevant types of mass transport during short-term operation, formate diffusion limitation during long-term operation was examined by gradually exchanging potassium chloride with potassium formate. Again, hydrogen  $FE$  is used as indicator for the degree of mass transport limitation (see figure 7.14). For a complete performance analysis see figure 9.9, p. 223 and figure 9.10, p. 224. At an elevated temperature of  $50^\circ\text{C}$ , the reaction is not intrinsically limited by product transport. An additional concentration of 0.1 M potassium formate corresponds to a 2.5-fold increase of the native bulk concentration (the one that is formed by the  $\text{CO}_2$  reduction reaction ( $\text{CO}_2\text{RR}$ ) itself, corresponding to around 0.04 M) but yielded no measurable difference in hydrogen  $FE$ . A roughly ten times larger concentration than the native one is necessary to observe an impeded formate mass transport. At lower temperatures e.g. at  $20^\circ\text{C}$  diffusion rates are reduced and local formate concentrations increased. Mass

transport limitation already sets in at an additional potassium formate concentration of 0.1 M. Also, hydrogen production accelerates significantly after a certain intrusion depth is reached.

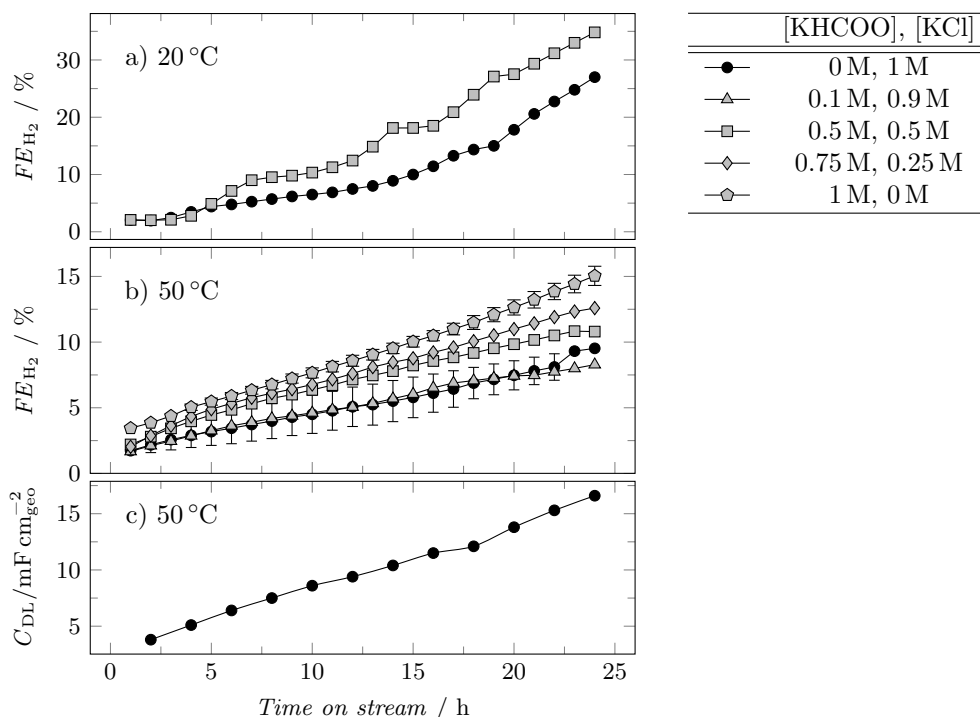


**Figure 7.14:** a + b) Course of hydrogen faradaic efficiency over time on stream for different feed formate concentrations and temperatures. c) Course of double layer capacitance over time on stream at 50 °C and pure KCl electrolyte. Operating conditions: continuous;  $j = -200 \text{ mA cm}^{-2}$ ,  $\text{pH} = 10$ ; standard GDE.

At a temperature of 70 °C the typical  $FE_{\text{H}_2} - \phi_{\text{C, IR}}$  correlation does not apply any more. That hints to changes to the active component, lowering the overpotential for HER. In order to get an idea of the tin catalysts oxidation state, CV measurements were performed between  $-1.26 \text{ V}$  (vs. SHE) to  $1.14 \text{ V}$  (vs. SHE) starting in anodic direction. Charge analysis of the tin oxidation peak then gives a relative measure for the amount of metallic tin present. Figure 7.15 shows the obtained cyclic voltammograms. The charge passed during tin oxidation at around  $-0.5 \text{ V}$  (vs. SHE) was found to be  $1.9 \text{ mC}$ ,  $2.1 \text{ mC}$ ,  $15.5 \pm 0.3 \text{ mC}$  and  $28 \text{ mC}$  at 20 °C, 35 °C, 50 °C and 70 °C, respectively. Accordingly, during electrolysis tin oxide is reduced to a much greater extent at 50 °C and 70 °C than at lower temperatures. Under strongly reducing reaction conditions tin oxide is only stable due to kinetic hindrance,<sup>[81]</sup> which seems to be possible to overcome at these temperatures. The reduced metallic tin is known to be moderately active for HER,<sup>[58, 80]</sup> explaining the observed increase in hydrogen production without cathode potential becoming more negative.

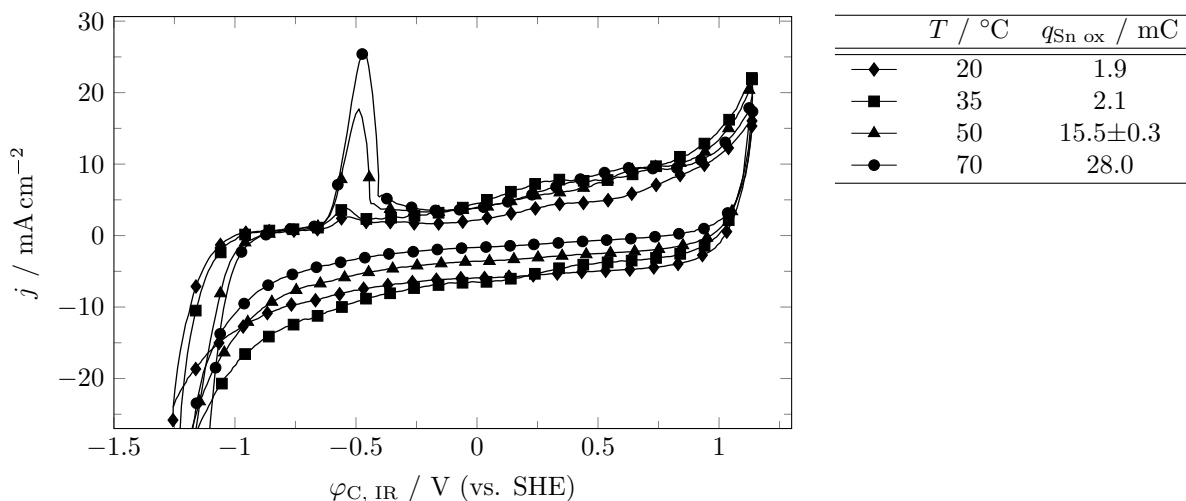


**Figure 7.15:** Cyclic voltammograms and resulting tin oxidation charge (area of the oxidative peak between  $-0.65 \text{ V (vs. SHE)}$  and  $-0.4 \text{ V (vs. SHE)}$ ) obtained after 24 h of galvanostatic electrolysis at  $-200 \text{ mA cm}^{-2}$  for different temperatures, given in figure 7.13.

### 7.3.2 Effects of the electrolyte

The electrolyte is one of the most important parameters in an electrolysis cell. This includes the type of solvent, as well as type and concentration of the conductive salt. Both can influence selectivity, activity and energy efficiency. The present work is restricted to water as solvent and focuses exclusively on the conductive salts.

#### 7.3.2.1 On the type of cation

The influence of the cation is already well reported in literature, with a clear trend in activity in the order  $\text{Li}^+ < \text{Na}^+ < \text{K}^+ < \text{Rb}^+ < \text{Cs}^+$  (see section 4.2.4.1, p. 37). However, cation related effects have been reported for current densities between  $-1 \text{ mA cm}^{-2}$  to  $-80 \text{ mA cm}^{-2}$ , which are much lower than the herein reported ones. Hence, activity and selectivity for different alkali metal cations were analyzed using a standard GDE. Polarization curves in figure 7.16 confirm the trend from literature. Activity rises in the order  $\text{Na}^+ < \text{K}^+ < \text{Rb}^+ < \text{Cs}^+$  both for chloride salts, as well as for hydroxides or bicarbonates (not shown). An explicit explanation for this observation cannot be given nor can any of the effects described in section 4.2.4.1, p. 37, be ruled out. Lithium is also in line with literature regarding the much lower activity using  $\text{Li}^+$  compared to  $\text{Na}^+$  but the underlying effect is unique. When exposed to aqueous  $\text{CO}_2$ , lithium salts form a moderately soluble carbonate ( $S_{\text{Li}_2\text{CO}_3, 35^\circ\text{C}} = 12 \text{ g L}^{-1}$ )<sup>[174]</sup>, which precipitates inside the pores and completely blocks the electrode. This is evidenced by the missing tin oxide reduction peak at around  $\varphi_{\text{C, IR}} = -0.6 \text{ V (vs. SHE)}$ , stating that there is no contact between catalyst and electrolyte, as well as by the measured  $C_{\text{DL}}$  of only  $0.2 \text{ mF cm}_{\text{geo}}^{-2}$  (see table 7.9).

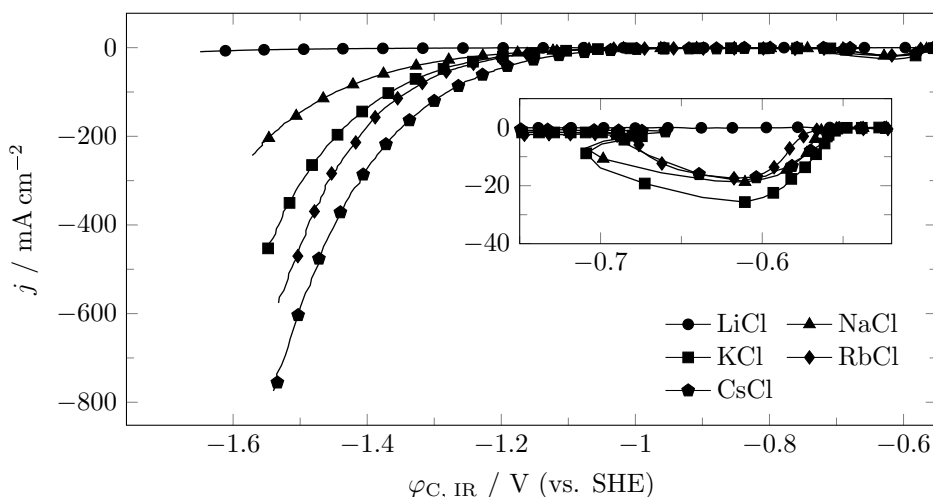


**Figure 7.16:** Polarization curves obtained from different metal chloride based electrolytes. Operating conditions: semi-batch;  $T = 35^\circ\text{C}$ ,  $[\text{MCl}] = 2\text{ M}$ ,  $\text{pH} = 10$ ; standard GDE.

The same trend was obtained during galvanostatic electrolysis with the cathode potential becoming less negative for larger cations. Regarding the *FEs* at a moderate current density, lithium shows an extreme hydrogen production rate, caused by pore blocking and the resulting inaccessibility of active sites. All other cations show only insignificant differences in selectivity. This changes for a highly mass transport limited current density of  $-700\text{ mA cm}^{-2}$ . The use of sodium leads to a nearly 4-fold increase in hydrogen evolution compared to potassium. Since the wetting behavior in terms of  $C_{\text{DL}}$  does only change within the error limits, hydrogen evolution cannot be attributed to mass transport limitation. Instead, the sluggish reaction kinetics at the sodium covered solid-liquid interface requires a high absolute value of cathode potential, which also induces HER.

**Table 7.9:** Faradaic efficiencies, compensated cathode potential and energetic cathode efficiency for different alkali metal chlorides at a moderate and high current density. Double layer capacitance was recorded after potentiostatic preconditioning in the activity/wetting sequence described in table 6.4, p. 80. Specific conductivity was measured at  $35^\circ\text{C}$ .

Operating conditions: semi-batch,  $t = 45\text{ min}$ ,  $T = 35^\circ\text{C}$ ,  $[\text{MCl}] = 2\text{ M}$ ,  $\text{pH} = 10$ ; standard GDE.

Cation	$j$ / $\text{mA cm}^{-2}$	$FE / \%$			$\varphi_{\text{C, IR}}$ / V (vs. SHE)	$ECE$ / %	$C_{\text{DL}}$ / $\text{mF cm}_{\text{geo}}^{-2}$	$\kappa$ / $\text{mS cm}^{-1}$
		$\text{H}_2$	$\text{CO}$	Formate				
$\text{Li}^+$		76	3	21	-2.86	4	0.2	108
$\text{Na}^+$	-200	2	4	94	-1.50	36	1.8	135
$\text{K}^+$		2	6	93	-1.34	40	2.2	192
$\text{Rb}^+$		3	6	90	-1.30	40	2.3	200
$\text{Na}^+$	-700	15	5	80	-1.78	26		
$\text{K}^+$		4	6	89	-1.66	31		



The choice of conductive salt does not only influence the electrode's activity and selectivity, it also determines ohmic overvoltages through electrolyte and membrane. Since for the used electrolysis cell the membrane's cross-sectional area is much larger ( $A_M \approx 12 \text{ cm}^2$ ) than the one of the GDE ( $A_{\text{GDE}} = 1 \text{ cm}^2$ ), measuring the total cell voltage does not result comparable values. In order to obtain a cell voltage that also applies to larger, industrial, cells, the ratio  $A_{\text{GDE}}/A_M$  needs to be equal to one. Hence, the cell voltage is calculated by determining and adding up the individual contributions according to equation 7.3.2. Equilibrium potentials, as well as activation and concentration overpotentials are included in the measured  $IR$  compensated electrode potentials  $\varphi_{\text{C, IR}}$  and  $\varphi_{\text{A, IR}}$ . Ohmic overvoltages cannot be measured due to the ratio  $A_{\text{GDE}}/A_M \neq 1$  and have to be calculated for both electrolytes and the membrane. This calculation is done with the electrical resistivity  $\rho_r = 1/\kappa$  ( $\kappa$ : electrical conductivity), cathode-anode distance  $l$  and current density  $j$ , according to equation 7.3.3. The electrode membrane distance of is assumed to be 3 mm, with a membrane thickness of 183  $\mu\text{m}$ . Note that electronic ohmic resistances inside the electrode's or outer electrical contacts have been neglected as they do not depend on the choice of electrolyte.

$$V_{\text{cell}} = \varphi_{\text{C, IR}} + \varphi_{\text{A, IR}} + V_{\Omega} \quad (7.3.1)$$

$$= \varphi_{\text{C, IR}} + \varphi_{\text{A, IR}} + V_{\text{el, C}} + V_{\text{el, A}} + V_M \quad (7.3.2)$$

$$V_x = IR_x = \rho_{r, x} \cdot l \cdot j = \frac{1}{\kappa_x} \cdot l \cdot j \quad (7.3.3)$$

**Table 7.10:** Contributions of electrode potentials, electrolyte and membrane resistance ( $IR$  drop) to the total cell voltage  $V_{\text{cell}}$  for sodium and potassium containing electrolytes.  
Cathode: standard gas diffusion electrode. Anode: nickel mesh.  $j = -200 \text{ mA cm}^{-2}$ ,  $T = 50^\circ\text{C}$ ,  $[\text{MCl}] = [\text{MOH}] = 2 \text{ M}$ . a) Assumed electrode membrane distance: 3 mm; specific conductivity is taken from table 7.9. b) Calculated from <sup>[175]</sup> for a membrane thickness of 183  $\mu\text{m}$ .

Cation	Membrane	$ \varphi_{\text{C, IR}} $	$\varphi_{\text{A, IR}}$	$IR_{\text{el, C}}^{\text{a)}$	$IR_{\text{el, A}}^{\text{a)}$	$IR_M^{\text{b)}$	$V_{\text{cell}}$
		/V (vs SHE)		/V			/V
Na <sup>+</sup>	Nafion N117	1.50	0.69	0.429	0.214	0.267	3.10
K <sup>+</sup>	"	1.34	0.64	0.316	0.188	0.349	2.83
Na <sup>+</sup>	KESD	1.50	0.69	0.429	0.214	0.313	3.15
K <sup>+</sup>	"	1.34	0.64	0.316	0.188	0.256	2.74

Table 7.10 shows that using potassium containing electrolytes lowers almost all losses contributing to the total cell voltage, clearly making potassium the better choice. The largest benefit arises from the cathode potential whose absolute value is lowered by 160 mV. Also, the electrolyte's ionic

conductivity increases significantly when using potassium salts. The only negative impact may arise from the membrane resistance, where the ranking of potassium vs. sodium depends on the membrane used. The so far used Nafion 117 membrane shows a higher resistance for potassium than for sodium, while for a KESD (polyethylene [polystyrenesulfonic acid-co-divinylbenzene]) membrane this ranking is reversed.<sup>[175]</sup> Based on the total cell voltage, the molar energy consumption can be calculated by equation 7.3.4. Results for sodium and potassium salts with different membranes are listed in Table 7.11.

$$E_m = \frac{P \cdot t}{n \cdot FE_{\text{Formate}}} = \frac{V_{\text{cell}} \cdot I \cdot t}{n \cdot FE_{\text{Formate}}} = \frac{V_{\text{cell}} \cdot z \cdot F}{FE_{\text{Formate}}} \quad (7.3.4)$$

**Table 7.11:** Comparison of molar energy consumption  $E_m$  and the resulting savings in electricity rate, as well as material costs for sodium and potassium salts.  $V_{\text{cell}}$  is taken from table 7.10.  $FE_{\text{Formate}} = 80\%$ . Electricity rate:  $0.07 \text{ € kWh}^{-1}$ .<sup>[176]</sup> Material prices taken from Alibaba.com.<sup>[151]</sup>

Cation	Membrane	$V_{\text{cell}}$ / V	$E_m$ / kW h mol <sup>-1</sup>	$\Delta E_m$	$\Delta \text{El. rate}$	Price MCl / € mol <sup>-1</sup>	Price MOH
Na <sup>+</sup>	Nafion 117	3.10	0.208	-	-	0.007	0.014
K <sup>+</sup>	"	2.83	0.190	-0.018	-0.0013	0.041	0.030
Na <sup>+</sup>	KESD	3.15	0.211	-	-	0.007	0.014
K <sup>+</sup>	"	2.74	0.184	-0.027	-0.0019	0.041	0.030

For the potassium containing electrolyte an electricity rate saving of just 0.0013 €/mol to 0.0019 €/mol is achieved. This is in strong contrast to the much higher material costs for potassium salts compared to the sodium form. From these short-term operation results it is obvious that the use of potassium is only economically reasonable if potassium formate is the desired product or if the cation can be recycled completely as it is possible by coupling CO<sub>2</sub>EL with BPED (see section 7.8.1, p. 171).

However, long-term operation shows a strong deactivation when using sodium instead of potassium containing electrolytes at a concentration of 1 M, as depicted in figure 7.17. The first point of measurement matches the results obtained in semi-batch mode (see table 7.9) with a slightly higher formate  $FE$  for sodium salts due to a selectivity shift away from CO with more negative potentials. Formate  $FE$ , however, already drops within the first two hours of time on stream below the one of potassium salts with a strong increase in hydrogen production rate. This observation may arise from the lower solubility of sodium bicarbonate (1.1 M, at 20 °C)<sup>[177]</sup>, compared to the potassium salt (3.3 M, at 20 °C),<sup>[178]</sup> which can lead to a local supersaturation and salt precipitation inside the GDE. This assumption is strengthened by comparison of different concentrations of sodium chloride used. When working under high amounts of sodium ions present cathode potentials collapses after 8 h of time on stream due to limited ion mass

transport out of the electrode ( $\text{NaHCOO}$ ,  $\text{NaHCO}_3$ ) followed by local supersaturation. Using only 0.1 M sodium chloride results in a much more stable cathode potential. However, at such low concentration hydrogen  $FE$  is strongly increased right from the beginning of electrolysis. A possible explanation would be a low reactant stabilization and/or increased surface proton availability due to the low amount of sodium cations available (see section 4.2.4.1, p. 37).

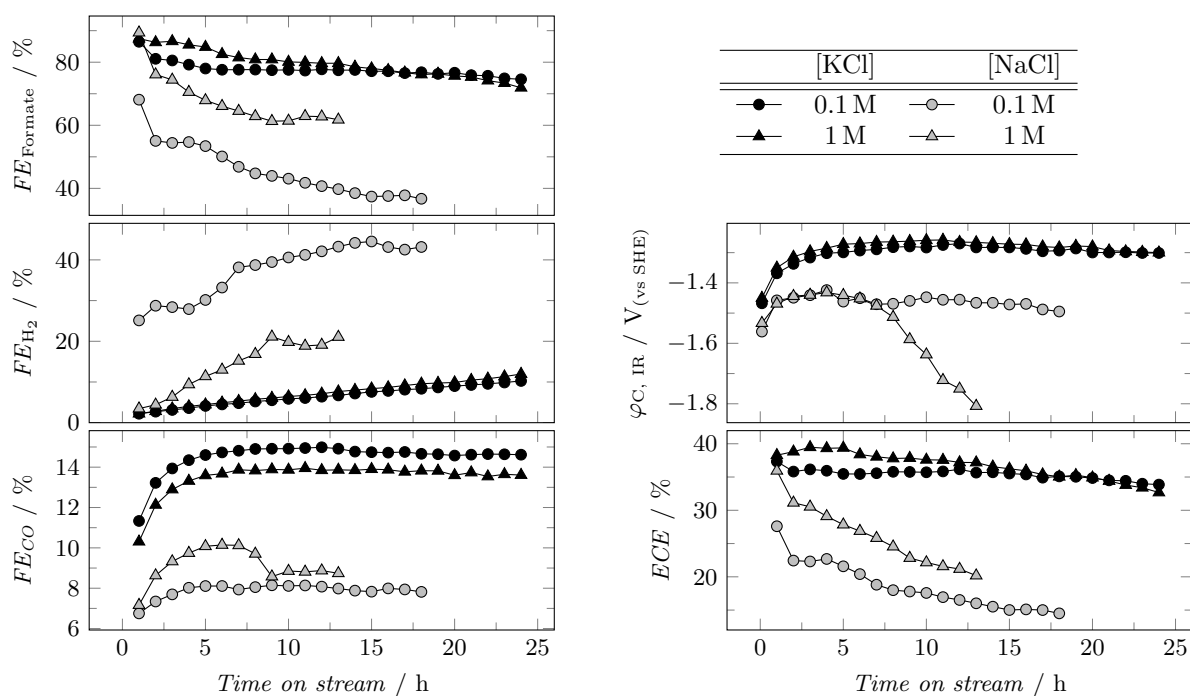


**Figure 7.17:** Long-term performance analysis of potassium and sodium chloride based electrolytes at different concentrations.

Operating conditions: continuous;  $j = -200 \text{ mA cm}^{-2}$ ,  $T = 50^\circ\text{C}$ ,  $\text{pH} = 10$ ; standard GDE.

Sodium based electrolytes would bring the benefit of much lower material costs in case that formate is the final product. However, this would require a stabilization of the electrode's performance. It is assumed that the strong and ongoing electrode wetting with time, resulting in long diffusion pathways for solvated products, is the major cause of observed deactivation. Consequently, a desired performance stabilization would require a fixed electrode wetting, which is difficult with the investigated homogeneous single-layer GDE design. Also, the range of possible electrolyte concentration is still limited to low values due to bicarbonate precipitation. For a non-stabilized electrode wetting the use of potassium based electrolytes is necessary. Hence, for alkaline  $\text{CO}_2\text{RR}$ , metal hydroxide consumption during electrolysis must be taken into account not only in terms of a techno-economic analysis but also in terms of a possible recycling to design a suitable process concept.

## 7.3.2.2 On the type of anion

Different anions are reported to significantly influence activity and selectivity in CO<sub>2</sub>RR. However, the reported findings strongly depend on the used electrode system and were as well investigated for the herein presented GDE. Polarization curves were recorded for typically used anions as well as for the product formate itself (see figure 7.18). Except for the acidic bisulfate anion and in contrast to literature, no difference within single or within double charged alkaline anions was found. Different halides (Cl<sup>-</sup>, Br<sup>-</sup> and I<sup>-</sup>) also did not show any difference. This is surprising as literature states a significant influence of halide anions improving CO<sub>2</sub>RR rates in the order of F<sup>-</sup> < Cl<sup>-</sup> < Br<sup>-</sup> < I<sup>-</sup>.<sup>[115–118]</sup> However, these findings were all observed on copper and zinc based electrodes. Anions need to adsorb directly on the metal surface, forming the inner Helmholtz plane (IHP), in order to affect charge transfer reactions. This adsorption is not possible for any kind of anion-electrode couple as described in more detail in section 4.1.1, p. 14. Assuming a tin oxide electrode with surface carbonates,<sup>[83]</sup> chemical intuition suggests a strong electrode-water interaction. On the other hand, anion-electrode interaction is expected to be much lower. This would lead to a positive total Gibb's free energy for anion adsorption and may be a reason for the non-existing halide dependence observed herein.

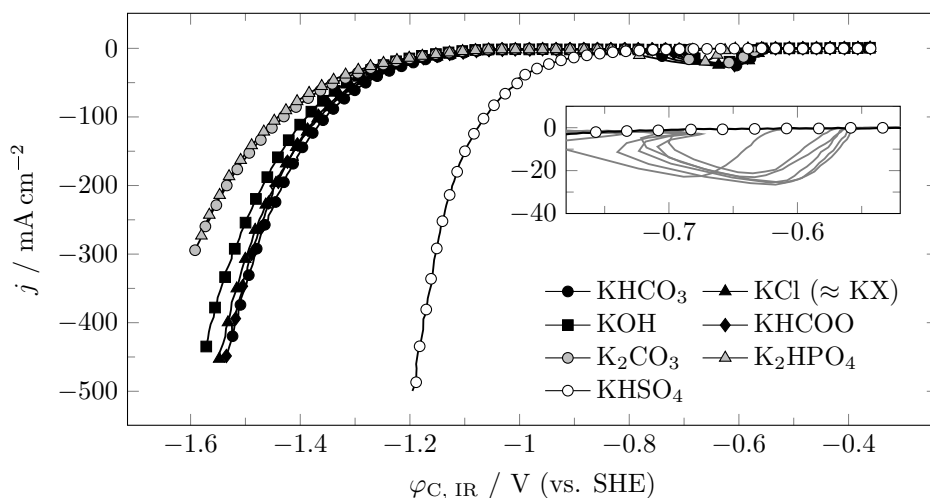


**Figure 7.18:** Polarization curves for different anions of the electrolyte. KX = KBr or KI. Operating conditions: semi-batch;  $T = 35^\circ\text{C}$ ,  $[\text{KA}] = 2\text{ M}$ ,  $\text{pH} = \text{native}$ ; standard GDE.

A slightly lower activity is observable for double charged anions compared to single charged ones. This difference may result from specific adsorptions within the Helmholtz plane due to the double charge but literature evidence is rare due to superposition with anion dependent CO<sub>2</sub> availability.<sup>[71]</sup> Bisulfate is the only strongly acidic anion used ( $\text{pH} = 0.9$ ). As expected, the polarization curve varies significantly from the alkaline electrolytes. This is mostly for two reasons. First, proton concentration is much higher than CO<sub>2</sub> concentration, shifting the onset for HER according to Nernst's equation to less

negative potentials. Second, acidic conditions facilitate the reduction of tin oxide to metallic tin during preconditioning,<sup>[81]</sup> which is known to be active for HER.<sup>[58]</sup>

At a current density of  $-200 \text{ mA cm}^{-2}$  the prevailing hydrogen selectivity when using potassium bisulfate was confirmed by GC analysis. Product distribution of all other mentioned alkaline anions showed no variation greater than the standard deviation. Exceptions were found for potassium bicarbonate with native pH for certain temperatures or formate salts within long-term operation. These exceptions are discussed in the following sections but they do not result from intrinsic effects on the charge transfer reaction.

### 7.3.2.3 pH dependency

Regarding literature results obtained in H-type cells proton concentration is known to have an influence on the electrode's performance (see section 4.2.4.1, p. 37). For alkaline pH, this applies mainly to  $\text{CO}_2$  availability at the active site, which drops with increasing pH due to the equilibrium shift towards bicarbonates/carbonates. However, results of such cells that run at a very low current density are barely comparable to flow cells using GDEs due to differences in the local electrolyte composition. It has been shown that a limited mass transfer of hydroxide ions away from the active surface results in a much higher local pH compared to the bulk electrolyte.<sup>[111]</sup> Burdyny and Smith predicted the local pH inside a GDE at a current density of  $-200 \text{ mA cm}^{-2}$  to differ by only one pH unit (13 to 14), regardless of the bulk pH between 7 and 13.<sup>[111]</sup> Since the hydroxide mass transport depends on factors like porosity, tortuosity, pore sizes and intrusion depth, the used GDE was investigated for any influence of the pH within a range of 7 to 14 and at different current densities ( $-200 \text{ mA cm}^{-2}$  and  $-700 \text{ mA cm}^{-2}$ ).

In contrast to mentioned literature from H-type cells, cathode potentials and *FEs* listed in table 7.12 show no significant difference or trend at neither current density. According to Nernst and the discussion given in section 4.2.2, p. 29, there should at least be a difference in the cathode potential since the equilibrium potential of the  $\text{CO}_2/\text{HCOO}^-$  couple becomes more negative with  $-0.0592/2 \text{ V}$  per pH. Since the calculation of the *ECE* involves this equilibrium potential, results for the *ECE* show a clear trend with higher pH being favorable. However, this is solely based on the calculation of the equilibrium potential. The actual power consumption ( $P = V \cdot I$ ) is not influenced.

**Table 7.12:** Faradaic efficiencies, compensated cathode potentials, equilibrium potentials and respective overpotentials, as well as energetic cathode efficiencies for different pH values at a moderate and high current density.

The equilibrium cathode potential was calculated with CO<sub>2</sub> as reactant following Nernst's equation, eq. 4.2.1, p. 29, according to the chemical equations (CEq 4.17) and (CEq 4.18).

Operating conditions: semi-batch;  $t = 45$  min,  $T = 35$  °C,  $[KCl] = 2$  M; standard GDE.

$pH$	$j$ / mA cm <sup>-2</sup>	$FE / \%$			$\varphi_{C, IR}$	$\varphi^0$	$\eta_{C, IR}$	$ECE$
		H <sub>2</sub>	CO	Formate	/ V (vs. SHE)		/ V	/ %
7		2	6	92	-1.34	-0.49	-0.87	33
10	-200	2 ± 1	6 ± 1	92 ± 2	-1.35 ± 0.02	-0.57	-0.83 ± 0.02	39 ± 1
12		2	6	92	-1.33	-0.63	-0.71	44
14		2	6	92	-1.31	-0.69	-0.63	49
7		5	6	89	-1.62	-0.49	-1.18	27
10	-700	6 ± 3	5 ± 1	88 ± 4	-1.55 ± 0.05	-0.57	-0.99 ± 0.05	33 ± 2
12		9	6	84	-1.61	-0.63	-0.99	33
14		7	6	87	-1.50	-0.69	-0.82	40

Hence, the results strengthen the hypothesis that the local pH differs only insignificantly for different bulk pH values. In literature it is often mentioned that too high pH values are disadvantageous for CO<sub>2</sub>RR since less CO<sub>2</sub> is available. Physically dissolved CO<sub>2</sub> in alkaline media can either be electrochemically reduced or react with hydroxide ions to form inactive bicarbonate/carbonates, according to the following chemical equation (CEq).



In order to make a quantitative statement of how much CO<sub>2</sub> is reduced and how much is lost into the bicarbonate/carbonate equilibrium, reaction rates of both reactions were calculated. The rate of reduction (at -700 mA cm<sup>-2</sup>) is given by Faraday's law according to equation 7.3.5, while the one of the hydroxylation to bicarbonate is estimated from literature values for a pH of 13 (equation 7.3.6). The rate constant  $k_1$ <sup>[179]</sup> and CO<sub>2</sub> solubility<sup>[130]</sup> are given at 35 °C. The volume of electrolyte inside the GDE  $V_{f, el, GDE}$  was estimated assuming an electrolyte intrusion depth of 70 μm (see SEM/XES analysis, appendix figure 9.8, p. 223). AB is assumed to show a porosity of  $\varphi_{p, AB} = 0.7$ <sup>[141]</sup> and a volume fraction of  $\Phi_{AB} = 0.65$ .

$$v_{\text{reduction}} = \frac{n}{t} = \frac{|I|}{z \cdot F} \cdot F E_{\text{Formate} + \text{CO}} = \frac{0.7 \text{ A}}{2 \cdot 96485 \text{ A s mol}^{-1}} \cdot 0.93 = 3.6 \cdot 10^{-6} \text{ mol s}^{-1} \quad (7.3.5)$$

$$v_{\text{hydroxylation}} = \frac{n}{t} = k_1 \cdot c_{\text{CO}_2} \cdot c_{\text{OH}^-} \cdot V_{\text{f, el, GDE}} \quad (7.3.6)$$

$$\begin{aligned} V_{\text{f, el, GDE}} &= A_{\text{GDE geo}} \cdot l_{\text{intr.}} \cdot \varphi_{\text{p, AB}} \cdot \Phi_{\text{AB}} \quad (7.3.7) \\ &= 1 \cdot 10^{-4} \text{ m}^2 \cdot 7 \cdot 10^{-5} \text{ m} \cdot 0.7 \cdot 0.65 = 3.2 \cdot 10^{-6} \text{ L} \end{aligned}$$

$$\begin{aligned} v_{\text{hydroxylation}} &= \frac{n}{t} = k_1 \cdot c_{\text{CO}_2} \cdot c_{\text{OH}^-} \cdot V_{\text{f, el, GDE}} \\ &= 2.45 \cdot 10^4 \text{ s}^{-1} \cdot 1.76 \cdot 10^{-2} \text{ mol L}^{-1} \cdot 0.1 \text{ mol L}^{-1} \cdot 3.2 \cdot 10^{-6} \text{ L} = 1.4 \cdot 10^{-4} \text{ mol s}^{-1} \end{aligned}$$

The results show that the reaction of  $\text{CO}_2$  with hydroxide ions proceeds around two orders of magnitude faster than the electrochemical reduction at  $-700 \text{ mA cm}^{-2}$ . This is in good accordance with the analysis of the formate/bicarbonate ratio within potassium chloride electrolytes after electrolysis. HPLC measurements showed a roughly 1:1 ratio between formate and bicarbonate. Hence, hydroxide ions that are formed during  $\text{CO}_2\text{RR}$  react quickly with another  $\text{CO}_2$  molecule. Previously, in figure 7.18, it was shown that there is no difference in activity when using 1 M potassium chloride or potassium hydroxide as bulk electrolyte, which should not be the case if the reaction of  $\text{CO}_2$  with hydroxide ions proceeds faster than the reduction reaction. However, this can again be explained by a limited hydroxide ion mass transfer within the GDE's porous structure. Upon reacting with  $\text{CO}_2$  hydroxide ions are consumed, which again lowers the local pH and reduces the rate of further bicarbonate formation.

## 7.3.2.4 Concentration effects

Increasing the electrolytes ion concentration is a common way to increase the energy efficiency ( $EE$ ). It is thereby important to distinguish causes for improved performance into reaction and ohmic resistance related ones. Increased salt concentrations lead to a higher conductivity and thus lower ohmic overpotentials. Due to this known fact the following results focus on reaction related improvements.

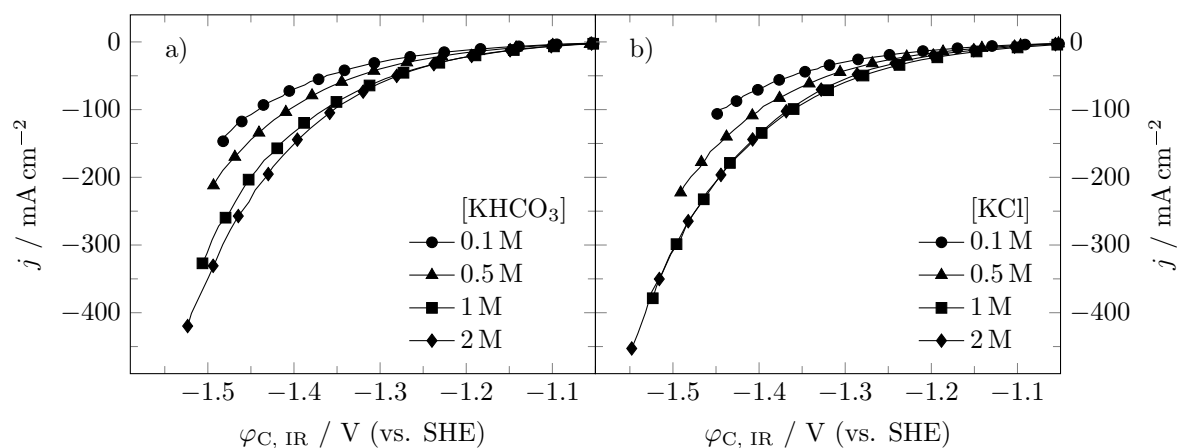


**Figure 7.19:** Polarization curves for different concentrations of a) the pH and  $\text{CO}_2$  buffering salt potassium bicarbonate and b) the non-buffering salt potassium chloride. Operating conditions: semi-batch;  $T = 35^\circ\text{C}$ , native pH; standard GDE.

$IR$ -compensated polarization curves were recorded for the pH and  $\text{CO}_2$  buffer system potassium bicarbonate, as well as for the non-buffering salt potassium chloride. Results depicted in figure 7.19 show the same trend for both kinds of salt with higher concentrations giving a slight raise to the absolute value of current density. This improvement falls below the standard deviation at a concentration above 1 M. The fact that this trend is also observed for the non-buffered potassium chloride based electrolyte suggests that  $\text{CO}_2$  availability is not significantly influenced by the presence of potassium bicarbonate and strengthens the hypothesis in the previous section that the local reaction environment is governed by the limited mass transport of hydroxide ions and does not differ as much as the bulk electrolyte. The more important effect seems to be related to the increasing amount of cations present. Potassium ions help to decrease the number of adsorbed protons and to stabilize active species. However, the influence of increased salt concentrations on product distribution is below the error of measurement for galvanostatic electrolysis at a moderate current density of  $-200 \text{ mA cm}^{-2}$  and shows no clear trend at a high current density of  $j = -700 \text{ mA cm}^{-2}$  (see table 9.5, p. 224).

The previous discussion only considered effects of short-term operation. Also, ohmic resistances cannot be completely separated from cathodic charge transfer. According to the equivalent circuit model of porous electrodes, described in section 4.3.3, p. 50, electrolyte and carbon matrix conductivity, as



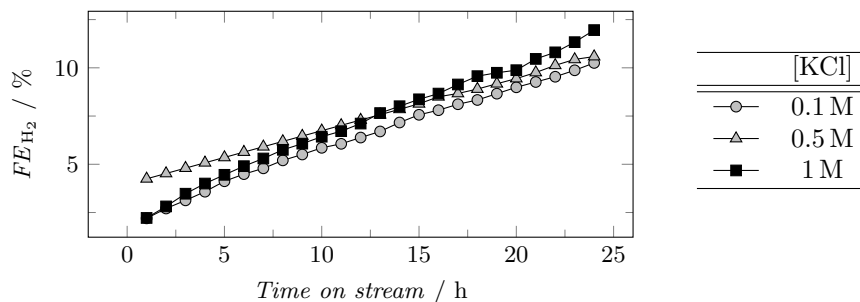


**Figure 7.20:** Course of hydrogen faradaic efficiency over time on stream for different potassium chloride concentrations.

Operating conditions: continuous;  $j = -200 \text{ mA cm}^{-2}$ ,  $T = 50 \text{ }^\circ\text{C}$ ,  $\text{pH} = 10$ ; standard GDE.

well as different charge transfer resistances determine the location and type of reduction reaction. This effect, if noticeable, is related to large intrusion depths and thus was investigated during long-term operation. Figure 7.20 shows the course of hydrogen  $FE$  for electrolyte concentrations between 0.1 M to 1 M (see appendix figure 9.11, p. 225, for the complete performance analysis) but presents no considerable difference. Conductivity of the carbon matrix was roughly analyzed and showed a value four to five orders of magnitude higher than the electrolyte ( $\kappa_{\text{matrix}, 20 \text{ }^\circ\text{C}} = 100 \text{ S cm}^{-1}$  to  $250 \text{ S cm}^{-1}$ ,  $\kappa_{\text{electrolyte}, 50 \text{ }^\circ\text{C}} = 20 \text{ mS cm}^{-1}$  to  $200 \text{ mS cm}^{-1}$ ).

From the equivalent circuit model a steeper increase in hydrogen  $FE$  for low concentrated electrolytes is expected due to the higher resistance. In a completely flooded electrode, electron pathway 2 (see 4.3.3, p. 50) becomes more favorable the lower the electrolyte's conductivity is. However, given results show no difference within the investigated concentration range. This could be due to small differences in local salt concentration, independent of the bulk phase. However, it could also be that the models assumption of a completely flooded pore system is wrong and that a scenario described in figure 4.18 b), p. 46, is present.

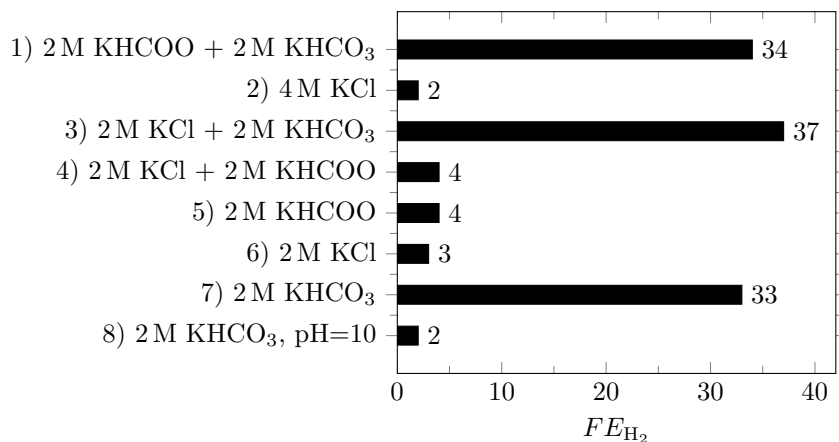


**Figure 7.21:** Hydrogen faradaic efficiency for different electrolytes at high concentrations. If not stated otherwise the pH was not adjusted.

Operating conditions: semi-batch;  $j = -200 \text{ mA cm}^{-2}$ ,  $t = 45 \text{ min}$ ,  $T = 50 \text{ }^\circ\text{C}$ ; standard GDE.

At a moderate current density of  $j = -200 \text{ mA cm}^{-2}$  product analysis of the so far discussed electrolytes showed no measurable difference. This, however, changes for certain salts when even higher concentrations than 2 M are employed. In section 7.8.1, p. 171, a potential coupling CO<sub>2</sub>EL with BPED will be introduced, which requires to operate electrolysis in a mixture of formate and bicarbonate ([potassium bicarbonate]  $\approx$  [KHCOO]). Such a 1:1 mixture with a total concentration of 4 M results in a massive increase in hydrogen *FE* to about 34 %. To investigate the causes of this collapse in performance different components were exchanged, with figure 7.21 illustrating the vast differences.

The sheer amount of contained ions cannot be responsible as 4 M potassium chloride solution (run 2) still yields the typical hydrogen *FE* of 2 %. A first suggestion was that the high concentration of formate leads to massive product diffusion limitation. This, however, was refuted by run 3 to 5. Replacing formate with chloride does not improve the performance. Instead, formate can even be used at 2 M either pure or in a mixture with 2 M chloride, resulting in just a little increase in hydrogen *FE*. Surprisingly, the real cause was found to be the high concentrated bicarbonate salt (run 7). Note that some of the previously shown results, like the catalyst screening or the temperature dependency, were obtained in 2 M potassium bicarbonate electrolyte without any such fail in performance. The difference to the herein reported electrolyte is its pH. While previously pH was adjusted to 10, it was left native for the here presented electrolyte (pH = 8.3). When adjusting the pH to 10 the typical performance was recovered (run 8). A first apparent explanation for this difference would be the different pH itself. This, however, is refuted by the discussion in the previous section (7.3.2.3) where the pH was scanned between 7 and 14 with no significant influence. Further investigation revealed that when lowering the temperature from 50 °C to 20 °C and using pure bicarbonate as electrolyte, hydrogen *FE* was again below 5 % (see figure 7.22). This observation eliminates solubility related causes like salt precipitation. Also, effects related to a slow diffusion of products can therefore be ruled out.

A possible explanation was found to be bicarbonate decomposition forming CO<sub>2</sub> and hydroxide ions during electrolysis.<sup>[76]</sup> When bubbles of gaseous CO<sub>2</sub> are formed inside electrolyte wetted regions of the GDE, active areas might be cut off by interrupting the ionic connection to the bulk phase. Bicarbonate decomposition rates were measured at different temperatures by adding fresh potassium bicarbonate with either native (8.3) or adjusted pH (10) to an used but intact GDE. Nitrogen was passed on the gas side with no potential applied and CO<sub>2</sub> content in the gas outlet stream was measured. The obtained CO<sub>2</sub> volume flow rates and hydrogen *FE* during electrolysis under identical conditions are represented in figure 7.22. At a pH of 10, potassium bicarbonate decomposition proceeds at a much lower and temperature independent rate, while at a native pH of 8.3 measured CO<sub>2</sub> flow rate strongly increases with temperature. These findings are in good correlation with the respectively obtained hydrogen *FE*.

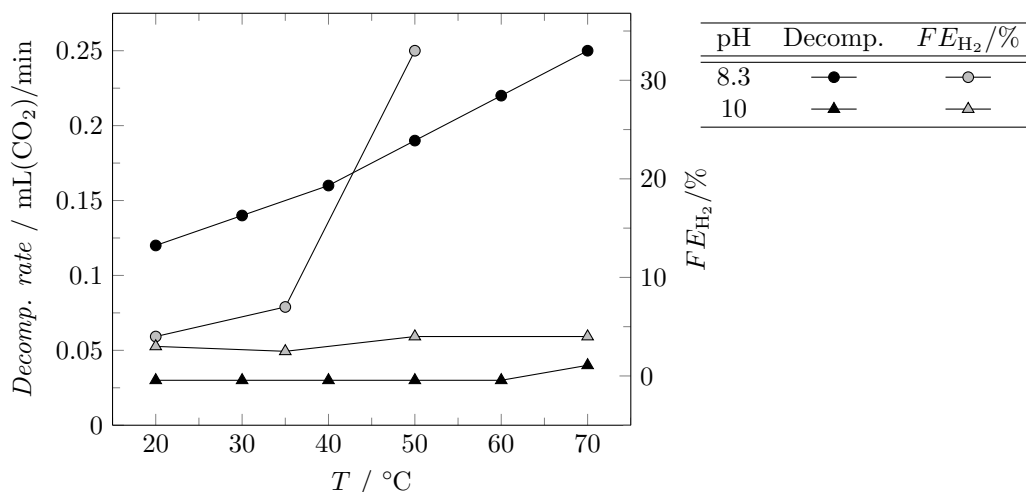


**Figure 7.22:** Volumetric  $\text{CO}_2$  flow resulting from potassium bicarbonate decomposition at different temperatures and pH values in comparison to the hydrogen faradaic efficiency obtained at the respective conditions.  $[\text{KHCO}_3] = 2 \text{ M}$ . Operating conditions for hydrogen analysis: semi-batch;  $t = 45 \text{ min}$ ,  $j = -200 \text{ mA cm}^{-2}$ ; standard GDE.

### 7.3.3 Requirements for reactant and electrolyte purity

Ideally, the source of  $\text{CO}_2$  emission contains  $\text{CO}_2$  in high purity so that it can be used directly. Any necessary gas purification adds a considerable amount of power demand to the  $\text{CO}_2\text{EL}$  system. Thus, it is essential to investigate the influence of impurities and lowered  $\text{CO}_2$  volume fraction on the  $\text{CO}_2\text{RR}$ . Furthermore, establishing an economically feasible process requires knowledge about the necessary electrolyte quality, meaning solvent and salt purity. Both represent important cost factors essential to be considered.

#### 7.3.3.1 Gas feed purity

First, the influence of a strongly lowered  $\text{CO}_2$  feed volume fraction was investigated for a moderate current density of  $-200 \text{ mA cm}^{-2}$ . The cathode potential recorded during 45 min of galvanostatic electrolysis is depicted in figure 7.23 a). For  $\text{CO}_2$  feed volume fractions of 80 vol-% and 90 vol-% cathode potential shows a course comparable to pure  $\text{CO}_2$  with a negligible shift to more negative values. At a fraction of 70 vol-% the typical course of potential shifts to more negative values and even shows a deactivation at  $\Phi_{\text{CO}_2} = 60 \text{ vol}\%$ . The reason for this differing course was found by analyzing the  $\text{CO}_2$  volume fraction in the outlet gas stream (equal to the bulk gas phase at the GDE) (see figure 7.23 b)). With increasing feed dilution the outlet  $\text{CO}_2$  volume fraction decreases more strongly with time. An increased hydrogen production rate further decreases the  $\text{CO}_2$  volume fraction, creating a negative feedback loop. Hydrogen originates from  $\text{CO}_2$  mass transport limitation induced by the lowered  $\text{CO}_2$  volume

fraction and corresponding lower concentration of solved  $\text{CO}_2$  in the electrolyte. The increasing amount of hydrogen then further dilutes the  $\text{CO}_2$ , which in turn further lowers the  $\text{CO}_2$  mass transport and boosts hydrogen production (see hydrogen  $FE$  in table 7.13).

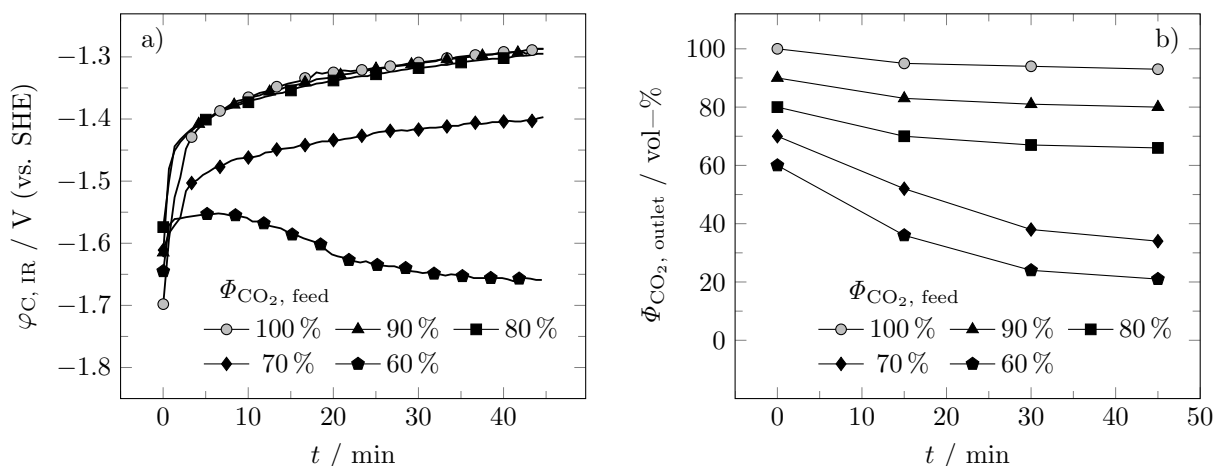


**Figure 7.23:** a) Cathode potential and b)  $\text{CO}_2$  volume fraction in the outlet gas stream, both over time at different  $\text{CO}_2$  feed volume fractions.

Operating conditions: semi-batch;  $j = -200 \text{ mA cm}^{-2}$ ,  $T = 50^\circ\text{C}$ ,  $[\text{KCl}] = 2 \text{ M}$ ,  $\text{pH} = 10$ ; standard GDE.

After about 45 min  $\text{CO}_2$  volume fraction reached a relatively stable value.  $FE$ s listed in table 7.13 are measured at that time. Just as indicated by the cathode potential, there is no measurable difference in the  $FE$ s for feed  $\text{CO}_2$  volume fractions between 100 vol-% and 80 vol-%. At  $\Phi_{\text{CO}_2, \text{feed}} = 70 \text{ vol}\%$ , performance starts to significantly drop due to the described negative feedback loop. Hydrogen  $FE$  starts to increase, resulting in an actual  $\text{CO}_2$  volume fraction of only 34 vol-% or less. Consequently, the required minimum  $\text{CO}_2$  purity is 80 vol-%. Note that the obtained hydrogen  $FE$  at  $\Phi_{\text{CO}_2, \text{output}} = 21 \text{ vol}\%$ ,  $j = -200 \text{ mA cm}^{-2}$  roughly corresponds to the one obtained at  $j = -1000 \text{ mA cm}^{-2}$  with pure feed (see table 7.13). This indicates that the lowered  $\text{CO}_2$  volume fraction and solved  $\text{CO}_2$  concentration according to Henry's law is the only decisive effect.

**Table 7.13:** Faradaic efficiencies and compensated cathode potentials for reduced feed CO<sub>2</sub> volume fractions. Values are obtained at  $t = 45$  min instead of being averaged over time to correlate the results with the stabilized CO<sub>2</sub> outlet gas volume fraction, given in figure 7.23. Operating conditions: semi-batch;  $j = -200 \text{ mA cm}^{-2}$ ,  $T = 50 \text{ }^\circ\text{C}$ ,  $[\text{KCl}] = 2 \text{ M}$ ,  $\text{pH} = 10$ ; standard GDE.

$j$ / $\text{mA cm}^{-2}$	$\Phi_{\text{CO}_2} / \%$		$FE_{t=45 \text{ min}} / \%$			$\varphi_{\text{C, IR}, t=45 \text{ min}}$ / V (vs. SHE)
	Feed	Outlet $t=45 \text{ min}$	H <sub>2</sub>	CO	Formate	
-200	100	93	3	11	87	-1.29
	90	80	3	10	88	-1.29
	80	66	4	9	88	-1.30
	70	34	12	8	82	-1.40
	60	21	25	6	71	-1.52
-1000	100	89	23	7	71	-1.71

Depending on the source of CO<sub>2</sub>, reactive substances may also be contained in the feed. Oxygen is a typical example for such a substance. Whenever oxygen is fed to the cathode oxygen reduction reaction (ORR) can occur. Its equilibrium potential is much more positive than the one of CO<sub>2</sub>RR ( $\varphi_{\text{ORR}, \text{pH}=10}^0 = +0.64 \text{ V (vs. SHE)}$ ,  $\varphi_{\text{CO}_2\text{RR}}^0 = -0.558 \text{ V (vs. SHE)}$ ) and when using oxygen evolution reaction (OER) as counter reaction the equilibrium cell voltage reduces to 0 V. Besides this large difference in thermodynamics tin oxide is also a known catalyst for ORR, meaning a moderate overpotential.<sup>[180]</sup> Polarization curves with CO<sub>2</sub>, nitrogen and synthetic air fed to the cathode were recorded, shown in figure 7.24. As expected a much more positive onset potential was found for ORR than for CO<sub>2</sub>RR ( $\varphi_{\text{onset, ORR}} = 0 \text{ V (vs. SHE)}$ ,  $\varphi_{\text{onset, CO}_2\text{RR}} = -1.05 \text{ V (vs. SHE)}$ ). Consequently, when oxygen is present in the CO<sub>2</sub> feed it is selectively reduced. ORR does not produce any gaseous products which would further dilute the CO<sub>2</sub> feed or could damage the GDE's structure. The reaction, however, consumes electric energy and thus lowers the cells  $EE$ . Other consequences are not expected. Nevertheless oxygen content should stay below 1%. The polarization curve obtained in pure nitrogen atmosphere was recorded to demonstrate that oxygen is the only component of synthetic air contributing to the observed reductive current.

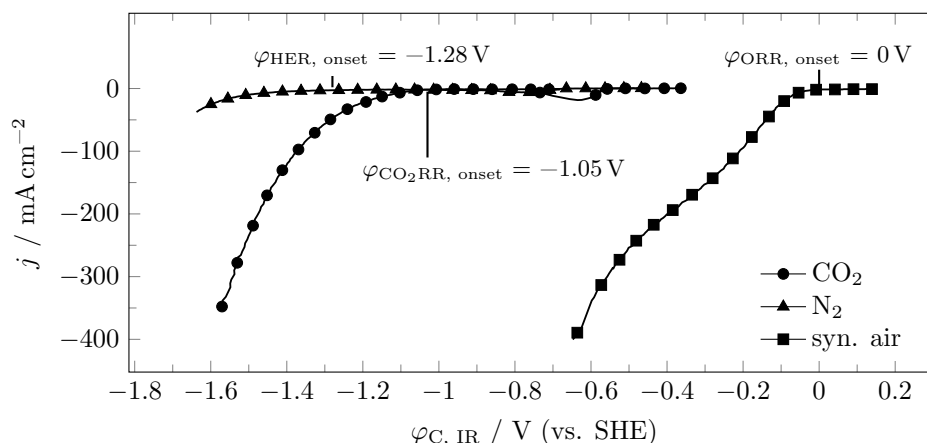


**Figure 7.24:** Comparison of polarization curves of CO<sub>2</sub>, nitrogen or synthetic air feed. Operating conditions: semi-batch;  $T = 50^\circ\text{C}$ ,  $[\text{KCl}] = 2\text{ M}$ ,  $\text{pH} = 10$ ; standard GDE.

### 7.3.3.2 Electrolyte purity

For many fields in electrochemistry, electrolyte purity is of utmost importance. Also for CO<sub>2</sub>RR it is known that the electrocatalytic properties of copper deteriorate due to a deposition of heavy metals.<sup>[39]</sup> Especially iron is often contained as impurity in electrolytes, which would represent a serious cost factor if high purity salts are necessary. In order to check for this requirement and to investigate possible contributions to deactivation in long-term operation, the influence of salt and solvent purity was investigated. Three different grades of potassium chloride and potassium hydroxide, as well as three different grades of solvent purity were investigated. In case of iron impurities hydrogen *FE* has to be considered. As described in more detail in section 4.2.3.2, p. 34, an increase in hydrogen *FE* can be expected when HER active heavy metals like iron are in-situ electrodeposited on the cathode. In contrast to the in literature reported copper based system, hydrogen evolution was found to be independent of the iron concentration (see figure 7.25). Differences in the *FE* are within the error of measurement despite having a considerable amount of iron in the electrolyte. During 24 h of time on stream 107 g of solved potassium chloride were pumped through the cell, containing 214 mg and 21 mg of iron for European Pharmacopoeia (fr. Pharmacopoeia Europaea) (ph. Eur.) and American Chemical Society (ACS) grade purity, respectively. Results are to be compared with the highest purity grade (4N5) including a total of < 10 mg of iron. Also, CV measurements after electrolysis revealed no additional peaks which might be attributed to Fe/Fe<sup>+</sup> redox processes. Same applies to different solvent grades with deionized (DI), double-distilled (DD) or HPLC grade water showing no considerable difference in hydrogen *FE* (see appendix figure 9.13, p. 226 for the complete performance analysis). Hence, an expected deposition of HER active heavy metals does either not occur or does not cause deactivation. Even though a trend in electrode potential with more negative potentials at higher iron content might be seen in the complete performance analysis (see

appendix figure 9.12, p. 225) differences are within the error of measurement. Accordingly, the observed increase in hydrogen  $FE$  over time has to originate from other effects. Note that even though electrode performance is not influenced by heavy metal impurities (in the investigated concentration range), they may negatively influence the membrane's ion transport requiring further cost analysis.<sup>[181]</sup>

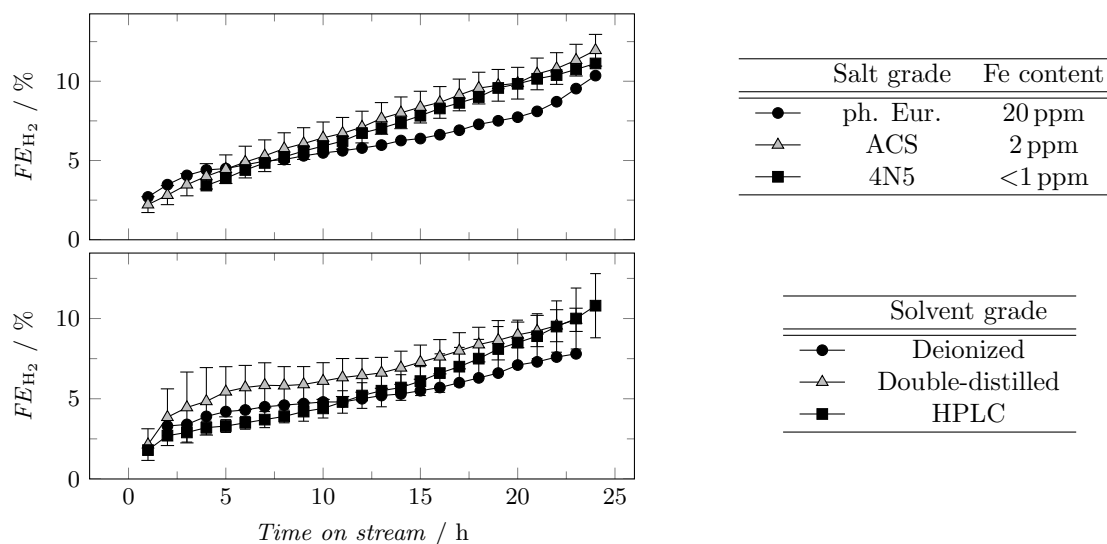


**Figure 7.25:** Course of hydrogen faradaic efficiency over time on stream for different salt and solvent grades. HPLC grade water was used as solvent for the investigation of salt purity. American Chemical Society grade salts and double-distilled water were usually used to prepare electrolytes described in the present work (displayed with open marks). Operating conditions: continuous;  $j = -200 \text{ mA cm}^{-2}$ ,  $T = 50 \text{ }^\circ\text{C}$ ,  $[\text{KCl}] = 1 \text{ M}$ ,  $\text{pH} = 10$ ; standard GDE.





## 7.4 Further optimization of the electrode's matrix

In section 4.3, p. 43, multiple parameters were described to determine the GDE's activity, selectivity and long-term stability. Among these parameters type of carbon black, ratio of meso- and macropores, as well as content and chemical nature of the binder are the most important ones. Unlike a variety of other carbon blacks, AB has already been reported to possess a beneficial meso- to macropore ratio, while showing an immense hydrophobicity that prevents flooding at high degrees of polarization.<sup>[138, 141]</sup> Hence, AB was chosen as carbon support for all measurements within this section. Here, GDE preparation parameters and variations in the binding agent were investigated.

### 7.4.1 Influence of preparation parameters

During electrode preparation, multiple parameters were being investigated for their effect on the GDE's performance. Pressing power and time were varied to influence the compression of macro-agglomerates. Pressure range was limited by the used press and the requirement of obtaining a mechanical stable electrode. Temperature and time of the heating step was varied to create differences regarding the PTFE distribution. However, non of the parameters listed below had an effect on product distribution or activity beyond the corresponding error of measurement at a current density of  $j = -1000 \text{ mA cm}^{-2}$ .

- Pressing power:  $p = 8.5 \text{ kN cm}^{-2}$  to  $19.8 \text{ kN cm}^{-2}$ .
- Pressing time:  $t = 3 \text{ min}$  to  $60 \text{ min}$ .
- Temperature of heat treatment:  $T = 340 \text{ }^\circ\text{C}$  to  $400 \text{ }^\circ\text{C}$ .
- Time of heat treatment:  $t = 10 \text{ min}$  to  $92 \text{ min}$ .

### 7.4.2 Fine tuning the electrode's hydrophobicity

Keeping in mind that for elevated temperatures product diffusion contributes to mass transport limitation in a rather small manner, electrode hydrophobicity was lowered to allow for an easier intrusion of the electrolyte. Although this would impede product transport even more, a larger ECSA can result in a lower local current density and thus helps to reduce the necessary cathode potential and to prevent  $\text{CO}_2$  depletion. This, however, implies that only the reaction zone, illustrated in figure 4.18, p. 46, is enlarged with macropores remaining open for  $\text{CO}_2$  supply. First, the electrode's hydrophobicity was adjusted by using different mixtures of Nafion and PTFE as binder. The results in figure 7.26 show a clear optimum at a Nafion content of 43 wt-%, while capacitance increases in a linear way with rising Nafion content. At a current density of  $-1000 \text{ mA cm}^{-2}$  formate selectivity could be raised from 71 % to 81 % by suppression

of the HER. As envisaged, electrode wetting is enlarged, which lowers the local current density. This, in turn, reduces the amount of  $\text{CO}_2$  required per active site and thus reduces  $\text{CO}_2$  mass transport limitation. Consequently, hydrogen  $FE$  decreases. At the same time, the electrode potential necessary to achieve a current density of  $-1000 \text{ mA cm}^{-2}$  decreases, mainly for two reasons. First, the mentioned local current density decreases, which, according to the Butler-Volmer equation (equation 4.1.22, p. 23), lowers the necessary electrode potential. Second, less hydrogen needs to be produced. As hydrogen can only be produced at a high overpotential using tin oxide based catalysts contribution of the HER overpotential is reduced. A certain fraction of PTFE, however, is necessary to prevent macropores from flooding, which seems to prevail at Nafion percentages higher than 43 wt-% again impeding  $\text{CO}_2$  transport.

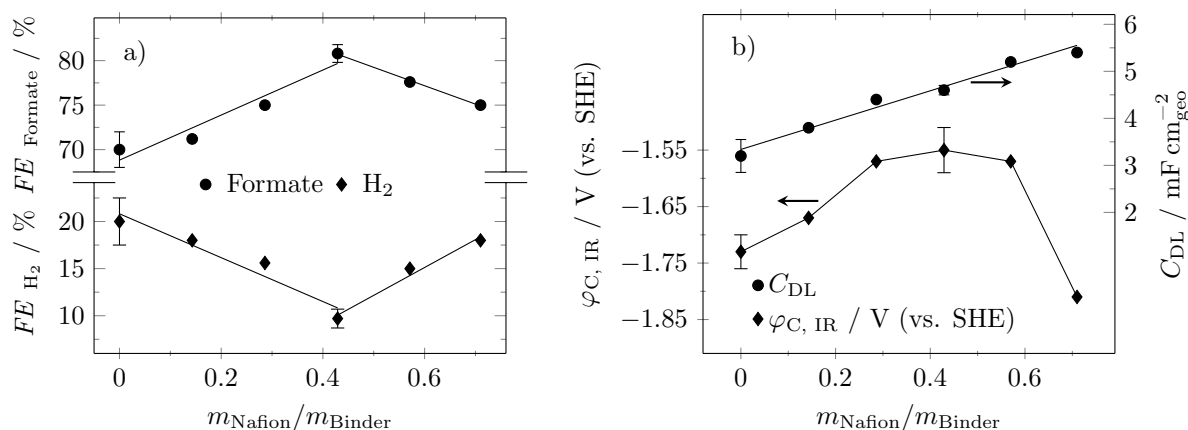


**Figure 7.26:** Performance of the GDE for different contents of Nafion and PTFE in the electrode's binder.  
 a) Faradaic efficiencies of formate and hydrogen.  $\text{CO}$  selectivity is not shown but adds the sum of all products up to  $(100 \pm 2) \%$ .  
 b) Cathode potential at the end of galvanostatic electrolysis and measured double layer capacitance.  
 Operating conditions during selectivity analysis:  $j = -1000 \text{ mA cm}^{-2}$ ,  $t = 45 \text{ min}$ .  
 Double layer capacitance is obtained after potentiostatic electrolysis in the activity-wetting sequence (see table 6.4, p. 80).  
 General operating conditions: semi-batch;  $T = 50^\circ\text{C}$ ,  $[\text{KCl}] = 2 \text{ M}$ ,  $\text{pH} = 10$ ;  $\sigma_{\text{Sn}} = 1 \text{ mg cm}^{-2}_{\text{geo}}$ , binder:AB ratio = 35:65.

The given results were obtained at a very high current density of  $-1000 \text{ mA cm}^{-2}$ . However, for the sake of a longer lifetime, smaller current densities are recommendable. Figure 7.27 shows how the beneficial effect of Nafion/PTFE mixtures on selectivity and activity depends on the current density. Surprisingly, it weakens with falling current densities and vanishes at  $j = -200 \text{ mA cm}^{-2}$ . While the hydrogen  $FE$  is already low for pure PTFE bound electrodes and thus hard to further suppress, the effect on cathode potential was expected to be more noticeable as more catalyst should be accessible due to the increased wettability. A reason for this missing influence of Nafion content on electrode potential was found by measuring the  $C_{\text{DL}}$  after galvanostatic electrolysis at  $-200 \text{ mA cm}^{-2}$  and  $-1000 \text{ mA cm}^{-2}$ .

Assuming that PTFE and Nafion do not change the specific capacitance of the carbon and tin oxide catalyst,  $C_{DL}$  values can be directly compared. At  $-200 \text{ mA cm}^{-2}$  obtained values differ only within the typical standard deviation of  $\pm 0.3 \text{ mF cm}_{\text{geo}}^{-2}$ . At  $-1000 \text{ mA cm}^{-2}$ , on the other hand, a significant difference was found ( $C_{DL, \text{PTFE}} = 3.2 \text{ mF cm}_{\text{geo}}^{-2}$ ;  $C_{DL, \text{Nafion/PTFE}} = 4.6 \text{ mF cm}_{\text{geo}}^{-2}$ ). Consequently, it seems that the differences in the GDE's wetting behavior, as illustrated in figure 7.26, are only significant at high degrees of polarization.

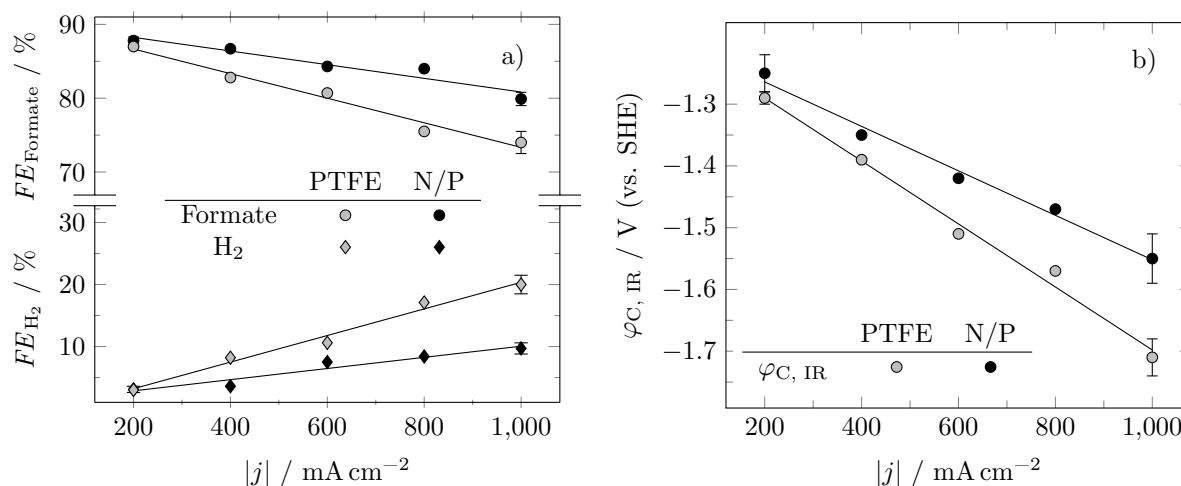


**Figure 7.27:** Performance comparison between GDE's bound with pure PTFE and an optimum Nafion/PTFE mixture (N/P) of  $m_{\text{Nafion}}/m_{\text{Binder}} = 0.43$  at different current densities.

a) Faradaic efficiencies for formate and hydrogen over current density. CO selectivity is not shown but adds the sum of all products up to  $(100 \pm 1)$  %.

b) Cathode potential over current density.

Operating conditions: semi-batch;  $t = 45 \text{ min}$ ,  $T = 50^\circ\text{C}$ ,  $[\text{KCl}] = 2 \text{ M}$ ,  $\text{pH} = 10$ ;  $\sigma_{\text{Sn}} = 1 \text{ mg cm}_{\text{geo}}^{-2}$ , binder:AB ratio = 35:65.

Since Nafion powder is about a factor of 50 more expensive than PTFE, a cheaper alternative for enhancing the electrode wetting without changing the carbon support was investigated. Electrowetting does not only depend on hydrophobicity of the solid electrode but also on the electrolyte's surface tension. Addition of a surfactant to the electrolyte lowers its surface tension and allows for an easier intrusion. TritonX was used for this purpose with concentrations of 1 mM, 5 mM and 10 mM, which led to a measured  $C_{DL}$  of 4.3, 5.1 and 5.5  $\text{mF cm}_{\text{geo}}^{-2}$ , respectively. A comparison of formate and hydrogen  $FE$ s for PTFE bound GDEs with such modified electrolyte and a Nafion/PTFE bound GDE ( $m_{\text{Nafion}}/m_{\text{Binder}} = 0.43$ ) without additional surfactant is given in figure 7.28. While Nafion addition results in an optimum at a  $C_{DL}$  of 4.6  $\text{mF cm}_{\text{geo}}^{-2}$ , TritonX addition worsened the performance in a roughly linear manner. Although the direct comparison of  $C_{DL}$  values might not be too accurate in this case (TritonX adsorption on the electrode may alter the specific capacitance), the completely diverging trend in hydrogen selectivity suggests a different type of wetting behavior. One possible explanation is that due to the large difference in polarity, Nafion and PTFE particles are not mixed homogeneously. This still results in highly hy-

drophobic CO<sub>2</sub> transport pores formed by PTFE and regions of lower hydrophobicity formed by Nafion particles. Consequently, electrode wetting is increased in terms of more carbon agglomerates being wetted while CO<sub>2</sub> transport pores remain open. In contrast to this selective wetting, lowering the electrolytes surface tension results in an easier penetration of both macro- and mesopores. This unselective wetting also floods CO<sub>2</sub> transport pores, further deteriorating reactant availability.

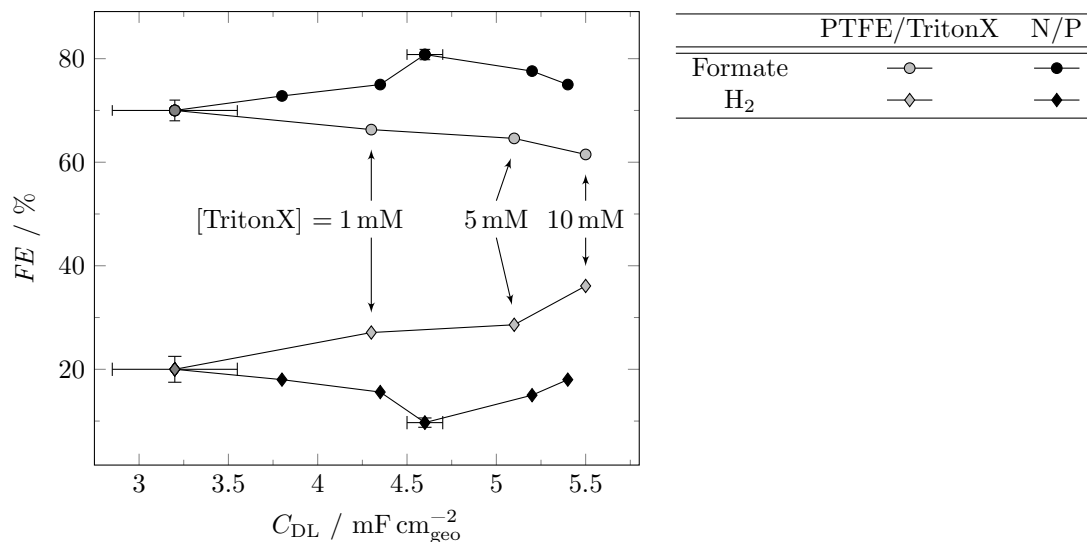


**Figure 7.28:** Formate and hydrogen faradaic efficiencies over the double layer capacitance obtained from PTFE bound GDEs with different concentrations of surfactant (TritonX) added to the electrolyte, compared to Nafion/PTFE bound GDEs ( $m_{\text{Nafion}}/m_{\text{Binder}} = 0.43$ ) (N/P) without additional surfactant. CO selectivity is not shown but adds the sum of all products up to  $(100 \pm 3)\%$ . Operating conditions: semi-batch;  $j = -1000 \text{ mA cm}^{-2}$ ,  $t = 45 \text{ min}$ ,  $T = 50^\circ\text{C}$ ,  $[\text{KCl}] = 2 \text{ M}$ ,  $\text{pH} = 10$ ;  $\sigma_{\text{Sn}} = 1 \text{ mg cm}_{\text{geo}}^{-2}$ , binder:AB ratio = 35:65.

## 7.5 Merging single parameter optimizations

Finally, the most successful single parameter optimizations were merged with regard to maximizing the limiting current density. Three different aspects were therefore considered.

- Optimum temperature of 50 °C.
- Optimum GDE composition with 15 wt-% Nafion, 20 wt-% PTFE and 65 wt-% AB, as well as an increased electrode loading of 2 mg cm<sub>geo</sub><sup>-2</sup>.
- Optimum electrolyte composition containing 2 M cesium chloride at pH = 10.

Results given in figure 7.29 show a massive increase in the limiting current density starting at  $-1000 \text{ mA cm}^{-2}$  for a standard GDE with optimized electrolysis temperature. Changing the standard GDE composition from  $\sigma_{\text{Sn}} = 1 \text{ mg cm}_{\text{geo}}^{-2}$ , 35 wt-% PTFE and 65 wt-% AB to an optimized one with  $\sigma_{\text{Sn}} = 2 \text{ mg cm}_{\text{geo}}^{-2}$ , 15 wt-% Nafion, 20 wt-% PTFE ( $m_{\text{Nafion}}/m_{\text{Binder}} = 0.43$ ) and 65 wt-% AB shifts the maximum current density to  $-1200 \text{ mA cm}^{-2}$ . Finally, exchanging potassium with cesium cations allows for a maximum of  $-1500 \text{ mA cm}^{-2}$ . When compared to literature the enormous potential of these kind of GDE under optimized reaction conditions is obvious. To date (August 2019) and to the best of the authors knowledge, the highest current densities achieved for CO<sub>2</sub> reduction to formate under ambient pressure were around  $-400 \text{ mA cm}^{-2}$  to  $-500 \text{ mA cm}^{-2}$ ,<sup>[19, 67]</sup> which means a roughly three- to four-fold increase with comparable formate *FE*. However, it is important to mention that these results are average values with a lifetime of only 45 min and further research is necessary to stabilize this performance over longer time on stream.

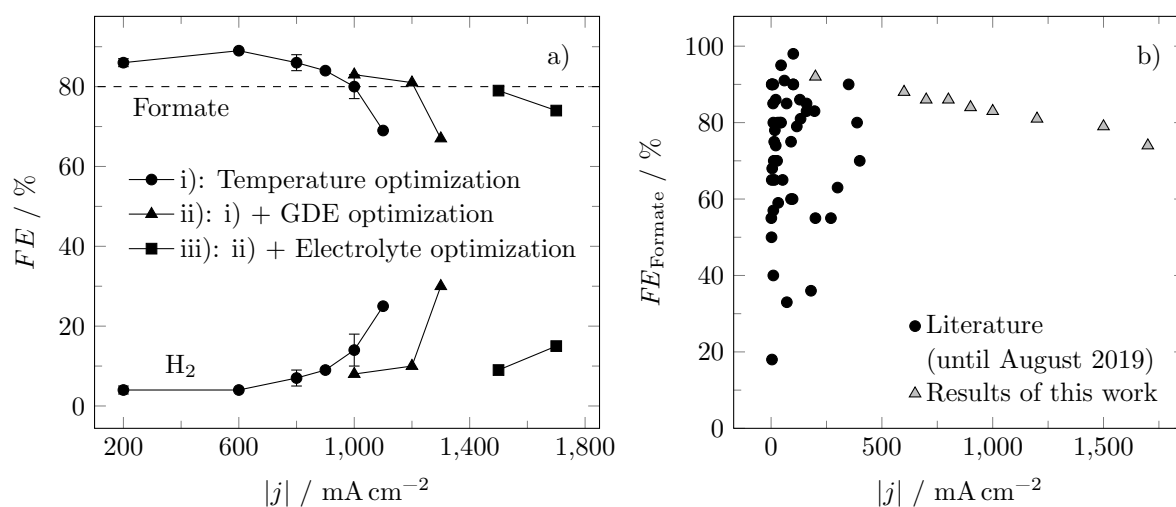


**Figure 7.29:** Limiting current densities for different optimizations, compared with the state of the art.

a) Formate and hydrogen faradaic efficiency over current density.

i) Optimum temperature of  $50\text{ }^\circ\text{C}$ ;  $[\text{KCl}] = 2\text{ M}$ ,  $\text{pH} = 10$ ; standard GDE.

ii)  $T = 50\text{ }^\circ\text{C}$  and the optimized GDE composition with  $\sigma_{\text{Sn}} = 2\text{ mg cm}_{\text{geo}}^{-2}$ , Nafion/PTFE mixture as binder of  $m_{\text{Nafion}}/m_{\text{Binder}} = 0.43$ ;  $[\text{KCl}] = 2\text{ M}$ ,  $\text{pH} = 10$ .

iii)  $T = 50\text{ }^\circ\text{C}$ , optimized GDE composition and the optimized electrolyte of  $[\text{CsCl}] = 2\text{ M}$ ,  $\text{pH} = 10$ .

b) Comparison of state of the art results for ambient pressure  $\text{CO}_2$  reduction reaction to formate with results of the present work.

## 7.6 Temporal behavior

Considering CO<sub>2</sub>EL as an industrial application implies certain requirements for the system's temporal behavior. Size of the electrolyzer, effort and price for replacement mainly determine the necessary electrode lifetime. Also, when CO<sub>2</sub>EL is supposed to be operated as energy storage system to cover fluctuations in the power grid it needs to exhibit a high flexibility. OER on solid metal catalysts in general is a very stable reaction.<sup>[182]</sup> Consequently, investigation of the CO<sub>2</sub>EL systems temporal behavior will focus solely on the cathode side.

### 7.6.1 Long-term stability

Based on the previously discussed optimizations, long-term operation in continuous mode was further investigated with regard to maximizing the GDE's lifetime. The lifetime of a GDE was defined as time on stream when hydrogen *FE* reached 20 % or when a sudden sharp increase in said *FE* was observed resulting from a breakthrough of electrolyte thereby contacting the stainless steel current collector.

Results of the following investigations refer to an optimum temperature of 50 °C and 1 M potassium chloride solution as catholyte. The starting point for maximizing time on stream with results being depicted in figure 7.30 was the standard electrode with a tin loading of 1 mg cm<sub>geo</sub><sup>-2</sup>, pure PTFE as binder and an area related mass of  $m/A = 55 \text{ mg cm}_{\text{geo}}^{-2}$  (corresponds to an electrode thickness of around 800 μm). Here, a GDE lifetime of around 24 h was obtained.

As described in more detail in section 7.4.2, selectively increasing the hydrophilicity of the GDE results in a lower local current density and can help to reduce mass transport limitation related hydrogen evolution. However, it was also shown that for short-term operation in semi-batch mode at a low current density of  $-200 \text{ mA cm}^{-2}$  PTFE or Nafion/PTFE bound GDEs do not show any significant difference in performance. On the other hand, during long-term operation shown in figure 7.30 the Nafion/PTFE bound GDE does show a significantly less steep increase in hydrogen *FE* over time on stream compared to the PTFE bound GDE. Consequently the GDE's lifetime is extended from 24 h to 48 h. A proven explanation of this extension in lifetime cannot be given but a relation to the altered wetting behavior when using the Nafion/PTFE mixture as binder seems reasonable. However, besides the positive effect on hydrogen *FE* and hence the GDE's lifetime CO production increases as well. Due to the larger ECSA more catalysts is available, which shifts the electrode potential to less negative values. This in turn results

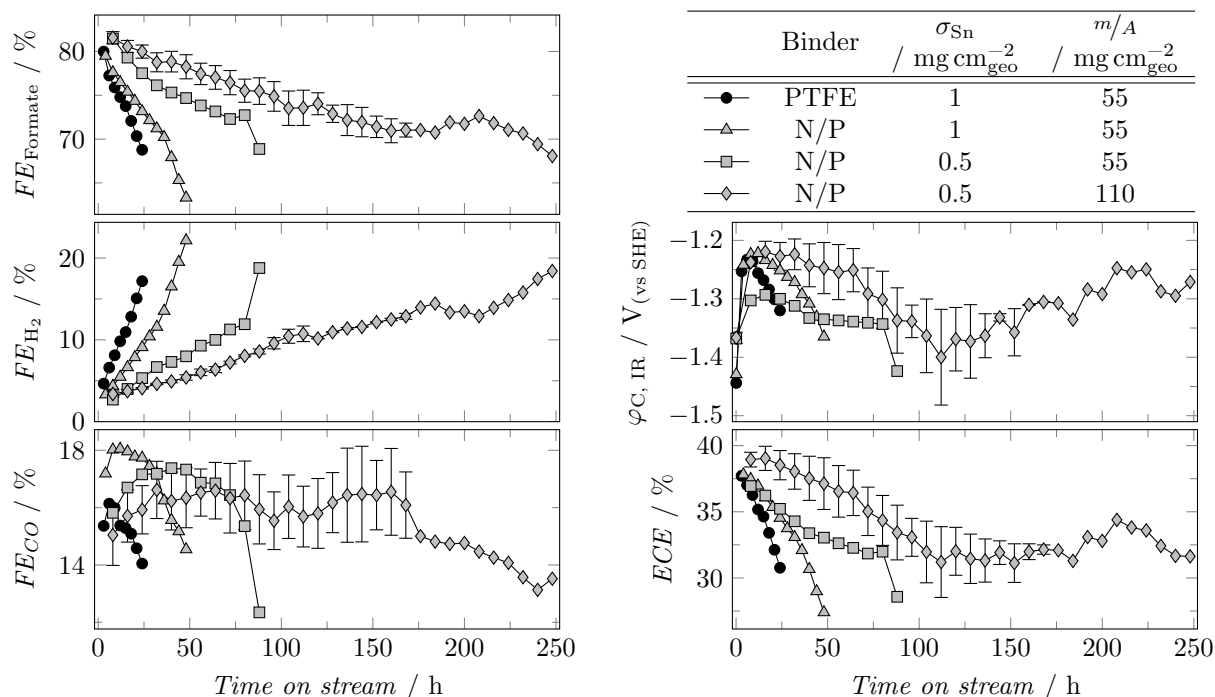


**Figure 7.30:** Long-term performance analysis for different electrode compositions.

Operating conditions: continuous;  $j = -200 \text{ mA cm}^{-2}$ ,  $T = 50 \text{ }^\circ\text{C}$ ,  $[\text{KCl}] = 1 \text{ M}$ ,  $\text{pH} = 10$ ; N/P: Nafion/PTFE mixture of  $m_{\text{Nafion}}/m_{\text{Binder}} = 0.43$ , binder:AB ratio = 35:65.

in a shift in  $\text{CO}_2\text{RR}$  products from formate to CO due to the potentiostatic character of tin oxide. The  $ECE$  is therefore barely increased.

Keeping the less negative cathode potential in mind the electrode's tin loading was lowered to counteract the increased CO  $FE$  by lowering the GDE's activity (see section 7.2.3, p. 111). As envisaged, the Nafion/PTFE bound GDE loaded with only  $0.5 \text{ mg cm}_{\text{geo}}^{-2}$  of tin shows a lower CO production rate with formate evolution being favored. Surprisingly, not only the formate:CO ratio was enhanced but hydrogen evolution has also been further suppressed. It is assumed that this suppression arises from the lowered CO production rate which leads to a lower dilution of the  $\text{CO}_2$  feed. Also, the lowered coverage of AB with tin oxide probably results in a slightly higher hydrophobicity that prevents flooding. With this electrode composition lifetime is extended to 80 h. At this point a breakthrough of electrolyte occurred, visible by the steep rise in hydrogen  $FE$  and drop in  $ECE$ .

Since monitoring the electrode's wetting in terms of measuring the  $C_{\text{DL}}$  has its limitations like large measurement errors due to mechanical degradation or long open circuit potential (OCP) breaks, the suggested linear increase in electrolyte intrusion was checked by doubling the electrode's thickness. Assuming a linearly increasing intrusion, the time for breakthrough is expected at around 160 h of time on stream. However, hydrogen evolution of such electrode (Nafion/PTFE mixture as binder of  $m_{\text{Nafion}}/m_{\text{Binder}} = 0.43$ ,  $\sigma = 0.5 \text{ mg cm}_{\text{geo}}^{-2}$  and  $m/A = 110 \text{ mg cm}_{\text{geo}}^{-2}$ ) shows no sharp increase that could



be associated with a breakthrough. Instead, a lifetime of at least 250 h was achieved. This result questions the assumed linear wetting behavior and gives rise to the hope on a stabilization of the electrolyte front by reaching an equilibrium state between hydrophobicity and capillary forces. Interestingly, within this run some kind of self-recovery is observed starting at around 110 h. Simultaneously to the cathode potential starting to become less negative, mechanical degeneration of the GDE started and small fragments were found in the electrolyte. By removal of probably completely flooded layers of the electrode formate diffusion is facilitated and concentration overpotential decreases. The mechanical degradation is confirmed by visual observation and by cross section SEM and XES analysis of a PTFE bound GDE with  $m/A = 110 \text{ mg cm}_{\text{geo}}^{-2}$  after 48 h of time on stream (see figure 7.31). Potassium distribution, originating from residual electrolyte, shows the GDE's wetted part undergoing alteration during electrolysis. A clear delamination is visible almost over the whole active area, which leads to the observed fragmentation. Thus, this pseudo regeneration comes with an irreversible electrode destruction and is of very limited potential. Also, the suspected stabilization seems to be realized only with large intrusion depth which requires very thick electrodes ( $\approx 1.6 \text{ mm}$ ). This is disadvantageous due to increased energy consumption mainly for two reasons. First, prolonged formate diffusion pathways raise the concentration overpotential, shifting selectivity towards hydrogen. Second, ohmic resistances throughout the GDE are increased. Hence, a stabilization of the electrolyte front closer to the bulk liquid phase as well as a mechanical enforcement of the GDE's matrix are necessary, requiring further research.

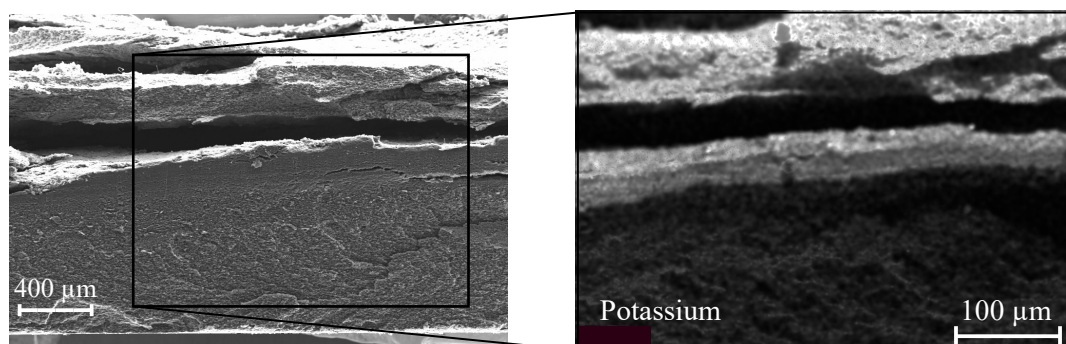


**Figure 7.31:** Scanning electron microscopy cross-sectional imaging with elemental analysis of a gas diffusion electrode after 48 h of time on stream.

Operating conditions: continuous;  $j = -200 \text{ mA cm}^{-2}$ ,  $T = 50 \text{ }^\circ\text{C}$ ,  $[\text{KCl}] = 1 \text{ M}$ ,  $\text{pH} = 10$ ; Standard GDE composition with doubled mass to area ratio,  $m/A = 110 \text{ mg cm}_{\text{geo}}^{-2}$ .

In section 7.3.1 it was shown that the oxidic tin species is, at least partially, reduced to its metallic state during operation, which contributes to the increasing hydrogen production. Consequently, an attempt to periodically recover the oxidic species was performed by applying a low oxidizing potential of  $\varphi_{\text{C, IR}} = +0.64 \text{ V}$  (vs. SHE). An anodic current of around  $+500 \text{ } \mu\text{A}$  was thereby observed. Analyzing the tin oxidation charge within CV measurements prior to and directly after recovery confirmed that

around 64 % of the metallic species was re-oxidized ( $q_{\text{Sn ox, before recovery}} = 10.4 \text{ mC}$  and  $q_{\text{Sn ox, after recovery}} = 3.7 \text{ mC}$ , see appendix figure 9.14, p. 227). This recovering routine was first started after 24 h of electrolysis and then repeated every 10 h. Results depicted in figure 7.32 show that formate selectivity is partially recovered, while cathode potential continuous to become more negative. This behavior can be explained by the different overlaying effects contributing to deactivation. Catalyst deactivation indeed seems to be reduced by this oxidative treatment. A periodically increasing formate selectivity is achieved by retarding HER while CO FE remains roughly constant. However, electrode wetting continues to increase which gives rise to the formate diffusion overpotential.

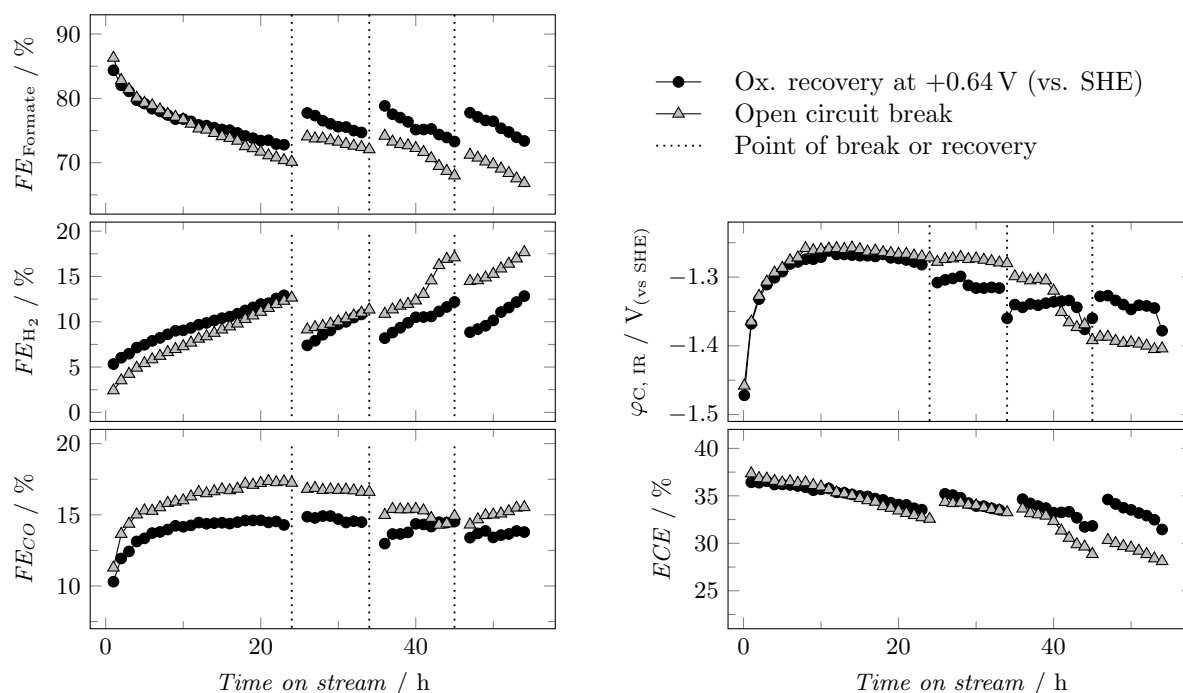


**Figure 7.32:** Performance recovery by 30 min of oxidative polarization at 0.64 V (vs. SHE) compared to an open circuit break. Operating conditions: continuous;  $j = -200 \text{ mA cm}^{-2}$ ,  $T = 50 \text{ }^\circ\text{C}$ ,  $[\text{KCl}] = 1 \text{ M}$ ,  $\text{pH} = 10$ ; standard GDE.

Interestingly, formate selectivity was also partially restored by an identically timed open circuit break, even though it seems less effective than an oxidative current. It could be assumed that, instead of the catalysts oxidation state, the retreating electrolyte when turning off the driving force for electro-wetting might be the real cause. However, investigation of the GDE's transient behavior, discussed in the next section, will show that electrolyte withdrawal and consecutive re-wetting is on a much shorter time scale. It might also be possible that metallic tin is oxidized by still adsorbed oxygenated surface species. This fact and the observed better performance under oxidative recovery hints to a similar contribution of tin oxide reduction and electrode flooding to deactivation.

Another approach to stabilize the catalyst's performance under highly reductive conditions would be to apply a catalyst that is active for CO<sub>2</sub>RR when in its reduced state. Pander et al.<sup>[80]</sup> reported lead as such material, even though results are not completely consistent with other literature.<sup>[183, 184]</sup> Due to the strong interdependence of catalyst oxidation state and reaction conditions, lead oxide was tested for its stability during long-term operation. Performance evaluation based on figure 7.33 reveals that the anticipated effect of a less pronounced shift to hydrogen formation is missing. Instead, HER is favored over the tin based GDE for both investigated temperatures despite the shift from oxidic to metallic state for tin. Due to these disappointing results investigation of the lead based catalyst was discontinued.

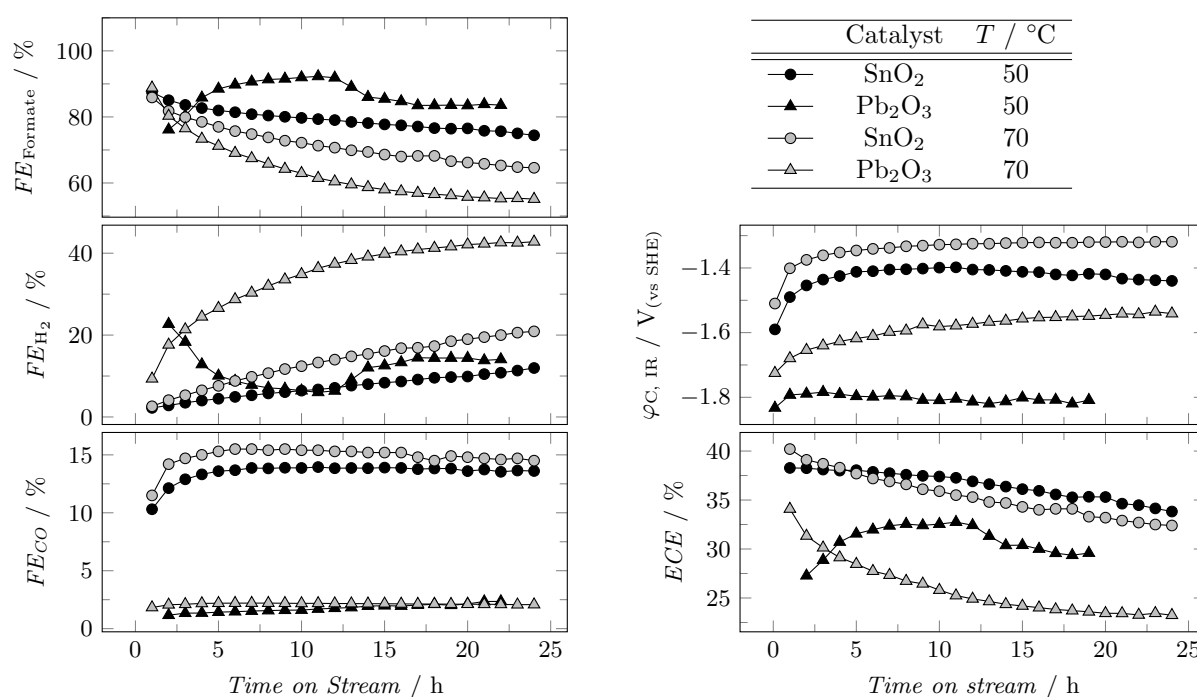


**Figure 7.33:** Long-term performance analysis for lead or tin loaded GDEs.

Operating conditions: continuous;  $j = -200 \text{ mA cm}^{-2}$ ,  $[\text{KCl}] = 1 \text{ M}$ ,  $\text{pH} = 10$ ;  $\sigma_{\text{Me}} = 1 \text{ mg cm}_{\text{geo}}^{-2}$ , standard GDE matrix.

Finally, long-term stability was investigated at higher absolute values of current density. For comparison, the standard GDE composition was tested first, with results given in figure 7.34. Obviously, cathode potential starts to drop much sooner and steeper with increasing current density. This results in a much stronger driving force for electrowetting and consequent electrode flooding. At a current density of  $-400 \text{ mA cm}^{-2}$  electrolyte breakthrough occurs already after 14 h of time on stream. At this point solely water is reduced at the stainless steel current collector. The idea arises that due to this potential induced flooding, electrode loading should be adapted to the targeted current density. Thus, tin loading was raised to  $\sigma_{\text{Sn}} = 2.5 \text{ mg cm}_{\text{geo}}^{-2}$  and operated at  $j = -300 \text{ mA cm}^{-2}$ . Even though with such an electrode cathode potential is a lot less negative, performance degradation occurs at the same rate. It has to be kept

in mind that when increasing the tin loading the electrode's matrix becomes more hydrophilic as more tin oxide is present at the surface. Hence, even though the driving force for electrowetting is lowered with an increased tin loading and corresponding less negative cathode potential, the electrode's matrix can be wetted more easily. An indication for the onset of formate mass transport limitation is the time on stream were the cathode potential starts to become more negative. There seems to be no significant difference between a loading of  $\sigma_{\text{Sn}} = 1 \text{ mg cm}_{\text{geo}}^{-2}$  and  $\sigma_{\text{Sn}} = 2.5 \text{ mg cm}_{\text{geo}}^{-2}$ . Thus, both described effects, the lowered driving force for electrowetting and the GDE's lowered hydrophobicity, seem to cancel each other out.

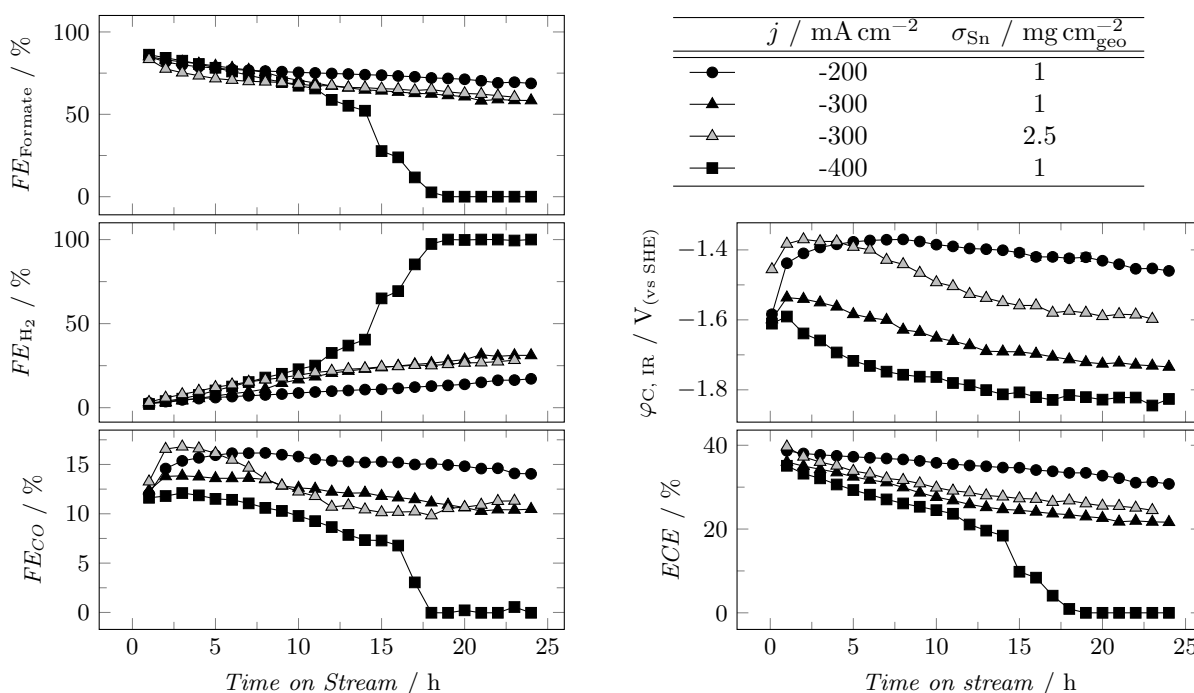


**Figure 7.34:** Long-term performance analysis at different current densities using the standard gas diffusion electrode, compared to an increased tin loading. Operating conditions: continuous;  $T = 50 \text{ }^\circ\text{C}$ ,  $[\text{KCl}] = 1 \text{ M}$ ,  $\text{pH} = 10$ ; standard GDE matrix.

## 7.6.2 Transient behavior

Storing electricity in the form of chemical energy for time-shifted recovery can be a way to smoothen the fluctuating supply of renewable energies. Depending on the type of application and implementation in the power grid such an energy storage system needs to cope well with temporal changes. As an extreme case the used GDE was investigated for its behavior towards step changes of the power input meaning a sudden shut-down and/or start-up with a constant current.

First, the necessity for preconditioning of a fresh GDE was investigated. A fresh GDE is barely in contact with electrolyte due to its extreme hydrophobicity. When directly applying the full current, local

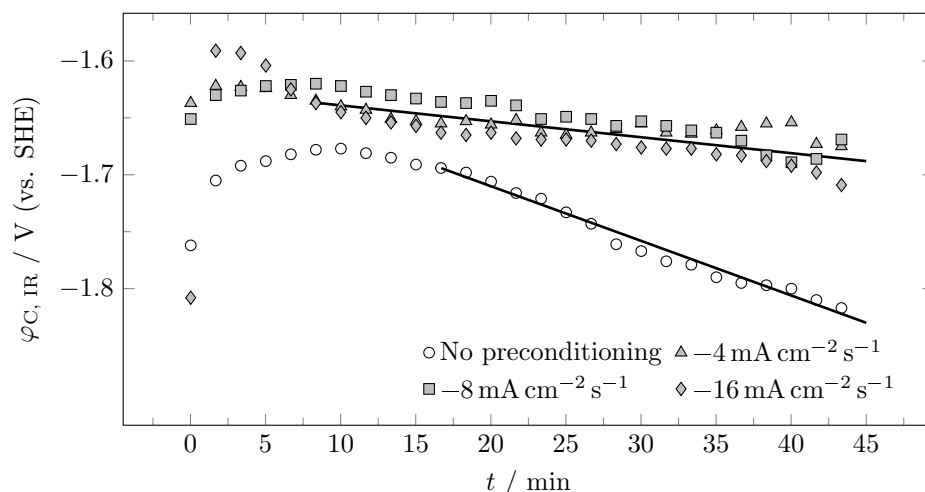


**Figure 7.35:** Course of cathode potential during galvanostatic electrolysis. The electrode was either not preconditioned or ramped up by a linear galvanodynamic scan with different scan rates. Operating conditions: semi-batch;  $j = -1000 \text{ mA cm}^{-2}$ ,  $T = 50^\circ\text{C}$ ,  $[\text{KCl}] = 2 \text{ M}$ ,  $\text{pH} = 10$ ; standard GDE.

current density ( $j_{\text{local}} = I/\text{ECSA}$ ) is significantly larger than  $\text{CO}_2$  transport allows. This would result in an excessive hydrogen production, which might harm the electrode's structure. A first discussion of this effect was already given in section 7.1.1, p. 99, when improving reproducibility. Figure 7.35 now shows the course of cathode potential obtained during galvanostatic electrolysis at  $j = -1000 \text{ mA cm}^{-2}$  with and without galvanodynamic preconditioning. Regardless of the current density scan rate, within a range of  $-4 \text{ mA cm}^{-2} \text{ s}^{-1}$  to  $-16 \text{ mA cm}^{-2} \text{ s}^{-1}$  electrode preconditioning has a positive effect on both activity and stability. Maximum activity is raised in terms of the absolute value of cathode potential being lowered by 55 mV to 90 mV from 1.679 V (vs. SHE) to around 1.585 V (vs. SHE) to 1.623 V (vs. SHE). Stability is enhanced with average cathode potential becoming more negative at only  $-1.4 \text{ mV min}^{-1}$  with preconditioning, while the one without preconditioning declines at  $-4.8 \text{ mV min}^{-1}$ . Note that these observations were made at a high current density of  $-1000 \text{ mA cm}^{-2}$ . For a moderate current density of  $-200 \text{ mA cm}^{-2}$ , as used during long-term operation, preconditioning had no considerable effect.

Second, the electrode's off/on behavior was investigated at moderate current density. The constant current supply was periodically turned off for 30 min and gradually raised back to  $-200 \text{ mA cm}^{-2}$ . Note that the electrode loading was lowered to  $0.5 \text{ mg cm}_{\text{geo}}^{-2}$  to reduce the influence of electrode deactivation discussed for figure 7.8, p. 115. Cathode potential recorded during active time on stream is depicted in figure 7.36. Every shut down results in some kind of deactivation. When turning the current back on, the necessary cathode potential is significantly more negative than when it was turned off. Each period of operation shows a similar course as the first one, at least within the first 20 h. This temporary reduction in activity is assumed to be related to the electrode's wetting behavior. Turning off the power supply also removes the driving force for electrowetting. At this point the electrolyte retreats partially,

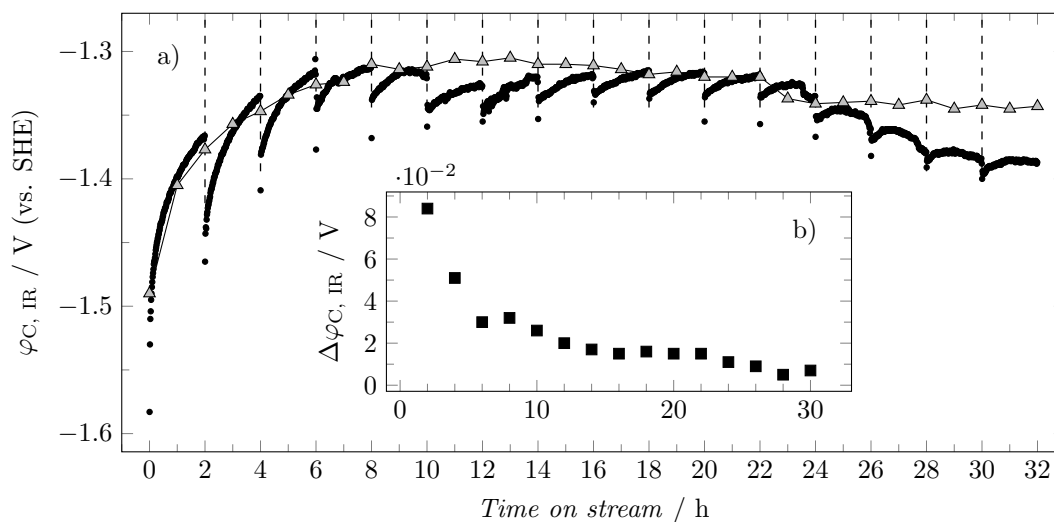


**Figure 7.36:** a) Course of cathode potential with active time on stream. Circles: every 2 h the current supply was turned off for 30 min (dotted lines) and powered up again with a current density scan rate of  $-10 \text{ mA cm}^{-2} \text{ s}^{-1}$  (not shown here). Triangles: course for non-interrupted operation. b) Drop in cathode potential ( $\Delta\varphi_{C, IR}$ ) during the respective break. Operating conditions: continuous;  $j = -200 \text{ mA cm}^{-2}$ ,  $T = 50 \text{ }^\circ\text{C}$ ,  $[\text{KCl}] = 1 \text{ M}$ ,  $\text{pH} = 10$ ;  $\sigma_{\text{Sn}} = 0.5 \text{ mg cm}_{\text{geo}}^{-2}$ , standard GDE matrix.

lowering the ECSA and making a re-wetting necessary. With ongoing electrolysis the drop in cathode potential during down time ( $\Delta\varphi_{C, IR}$ ) becomes less pronounced, which hints to a partial irreversibility of the wetting process.

Comparing this type of operation with the non-interrupted one shows that soon after restarting cathode potential re-aligns with the one of the non-interrupted run. The attempt to counteract the continuous progression in electrode wetting by frequently turning off the power supply and allowing the electrolyte to retreat was therefore not successful. The reduced ECSA lowers the electrolyte's activity and thus requires a more negative potential after restarting. Hence, the driving force for electrowetting is increased at this point and re-wetting occurs rather fast.

Such need for re-wetting the electrode results in a reduction of  $EE$  by a higher cell voltage and should therefore be avoided. An attempt to maintain the reaction zone during off-time was undertaken by applying a small standby current (SB). This way, electrode polarization can be kept up at a slightly lower value while having just a small power input. Figure 7.37 shows the effect of standby currents of different values compared to an OCP break for 30 min. Within the varied range of standby current no considerable difference is observed and a current density of  $-1 \text{ mA cm}^{-2}$  (achieved with  $\varphi_{C, IR} = -0.96 \text{ V}$  (vs. SHE)) is enough to maintain the electrode's activity.

In order to check if the degree of retreat of the electrolyte shows a relevant time dependency, OCP break was varied between 5 min and 2 h. Results in figure 7.38 show that there is no consistent trend in the drop of cathode potential during down time. Electrolyte withdrawal seems to be quite fast since 5 min

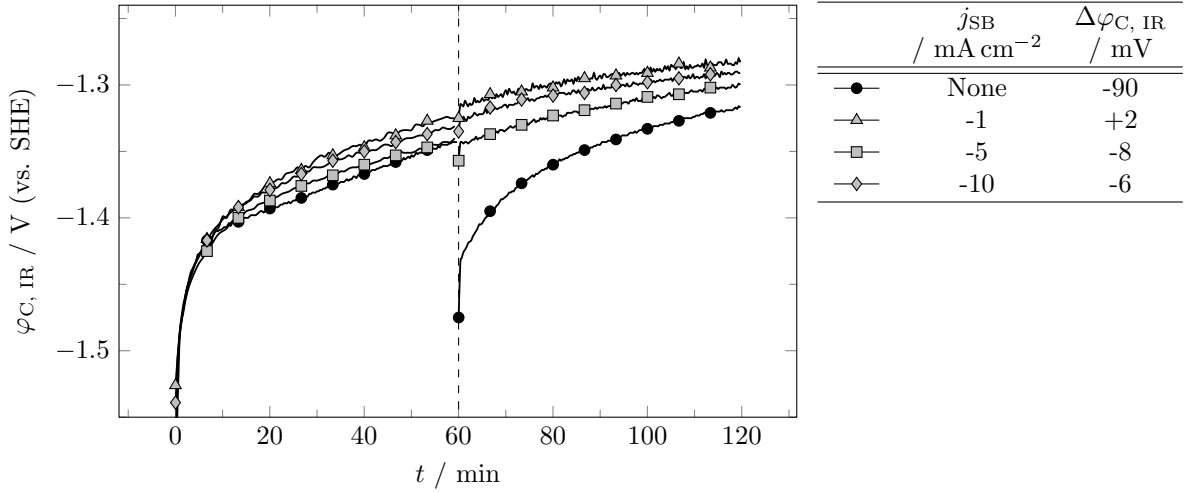


**Figure 7.37:** Course of cathode potential for interrupted electrolysis with either an open circuit break or a standby current being applied for 30 min.  $\Delta\varphi_{C, IR}$  gives the drop in potential during interruption. Operating conditions: semi-batch;  $j = -200 \text{ mA cm}^{-2}$ ,  $T = 35 \text{ }^\circ\text{C}$ ,  $[\text{KCl}] = 2 \text{ M}$ ,  $\text{pH} = 10$ ; standard GDE.

of down time are not short enough to see a significant difference. The observed deactivation, setting in at a rather early point ( $t \approx 120 \text{ min}$ ) when compared with results of figure 7.13, p. 123, is attributed to the fact that here the results were obtained at moderate temperature in semi-batch mode with accumulation of formate, thus showing severe product mass transport limitation. Note that this time a slightly stronger drop in cathode potential of  $-15 \text{ mV}$  was observed with a standby current of  $-1 \text{ mA cm}^{-2}$ , in contrast to  $+2 \text{ mV}$  in figure 7.37. Hence, results can be expected to show a measurement error of around  $\pm 10 \text{ mV}$ .

Consequently, applying a small standby current is recommendable to maintain the electrode's activity and maximize energetic efficiency. However, applying this current also consumes electric power which results in a break-even point after a certain period of down time. After this time, more energy has been consumed by the standby current than it would have been by the required re-wetting during the next on-time. To calculate this break-even point, electrical energy consumed during standby operation and that being saved during subsequent electrolysis are equated.

$$E_{SB} = E_{\Delta\varphi_{C, IR}} \quad (7.6.1)$$

$$V_{\text{cell, SB}} \cdot I_{SB} \cdot t_{SB} = I_{GSE} \cdot \int_0^{t_{\text{align}}} \Delta\varphi_{C, IR} \quad (7.6.2)$$

With  $I_{GSE}$  being the current density that is applied during on-time.  $t_{\text{align}} = 60 \text{ min}$  corresponds to the time period necessary for the cathode potential to re-align with the one of the standby current (see figure 7.39).  $\Delta\varphi_{C, IR}$  represents the difference in cathode potential after the open circuit and after the standby current break. Its integral is represented in figure 7.39 by the hatched area. While the saved

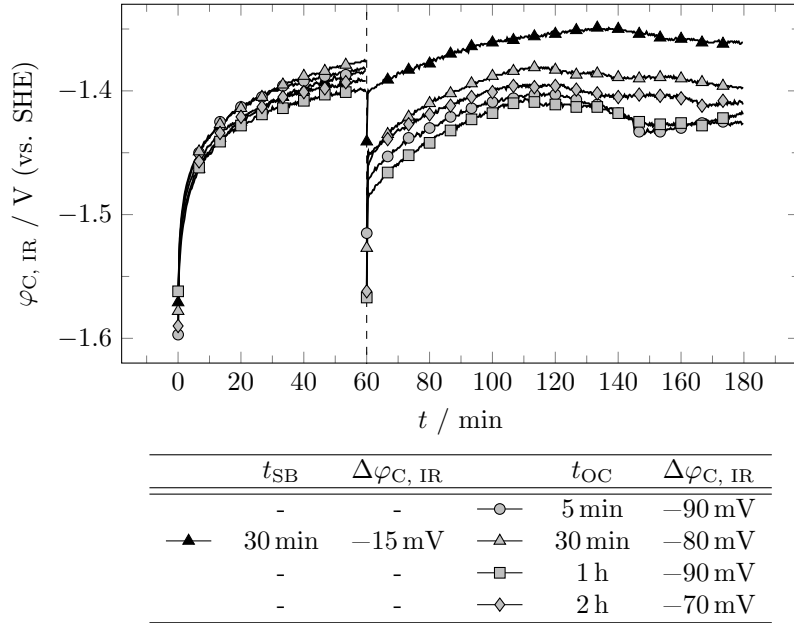


**Figure 7.38:** Course of cathode potential and resulting drop during the break  $\Delta\varphi_{C, IR}$  for interrupted electrolysis with either  $-1 \text{ mA cm}^{-2}$  being applied as standby current or with an open circuit (OC) break for different periods of time. Operating conditions: semi-batch;  $j = -200 \text{ mA cm}^{-2}$ ,  $T = 35 \text{ }^\circ\text{C}$ ,  $[\text{KCl}] = 2 \text{ M}$ ,  $\text{pH} = 10$ ; standard GDE.

electrical energy  $E_{\Delta\varphi_{C, IR}}$  results exclusively from effects at the cathode side, energy consumption during standby operation  $E_{SB}$  is related to the whole cell. Therefore, the anode potential at  $j = -1 \text{ mA cm}^{-2}$  was measured and added to obtain the whole cell voltage  $V_{\text{cell}, SB}$ . Remaining voltage drop contributions, as discussed in section 7.3.2.1, p. 125, sum up to around 10 mV and were added as well. Rearranging equation 7.6.2 and applying experimental data results in the break-even point of standby time of:

$$t_{SB} = \left| \frac{I_{GSE} \cdot \int_0^{t_{\text{align}}} \Delta\varphi_{C, IR}}{I_{SB} \cdot V_{\text{cell}, SB}} \right| \quad (7.6.3)$$

$$= \left| \frac{0.2 \text{ A} \cdot 25.2 \text{ V s}}{0.001 \text{ A} \cdot (-1.46 \text{ V})} \right| \approx 1 \text{ h} \quad (7.6.4)$$

Up to 1 h of down time applying a standby current results in an increased  $EE$  compared to an open circuit interrupted electrolysis. These calculations, however, correspond to a chosen initial time of electrolysis of 60 min and are expected to vary with time on stream. More precisely, the break-even point is expected to be reached sooner when interruptions occur at a later time of operation. Returning to figure 7.36, b) shows that the drop in cathode potential during open circuit break becomes smaller with time on stream. Energy savings  $E_{\Delta\varphi_{C, IR}}$  during the next on-time consequently becomes less pronounced, while the standby operations power consumption  $E_{SB}$  remains the same.



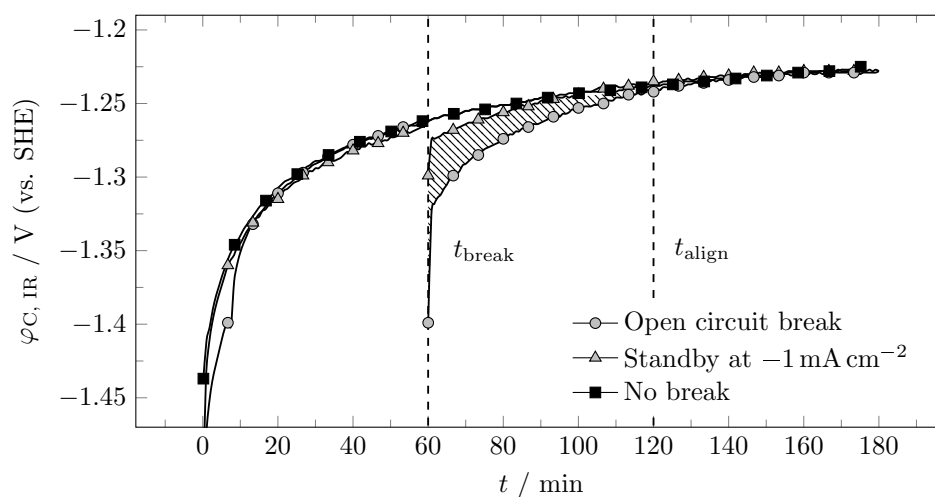


**Figure 7.39:** Course of cathode potential for interrupted electrolysis with either an open circuit break or a standby current of  $-1 \text{ mA cm}^{-2}$  being applied for 30 min. For comparison a non-interrupted run is also shown.

Operating conditions: semi-batch;  $j = -200 \text{ mA cm}^{-2}$ ,  $T = 50 \text{ }^\circ\text{C}$ ,  $[\text{KCl}] = 2 \text{ M}$ ,  $\text{pH} = 10$ ; standard GDE.



## 7.7 Scale-up

A fundamental aspect for industrialization of any reaction is the ability to scale up the process without significant loss in performance. This includes not only the electrode or electrolyzer itself but also catalyst synthesis and electrode preparation. The following sections deal with all four of these aspects.

### 7.7.1 Scale-up of the catalyst synthesis

First, tin oxide deposition was scaled up in a geometrical manner with a factor of three by simply using a larger reaction vessel. Precipitation was performed in a 2 L round-bottomed flask with 1.5 L of carbon black suspension under magnetic stirring. Results in table 7.14 show a significant loss of performance, which was most likely caused by an insufficient stirring power during synthesis. The less homogeneous heat and material distribution may lead to a lower metal dispersion with increased diffusion pathways and higher local current densities. Consequently, magnetic stirring was substituted by a larger anchor stirrer to effectively mix the carbon black suspension. With this adjustment, typical catalyst performance of a standard 500 mL synthesis batch regarding *FEs* and cathode potential was achieved.

**Table 7.14:** Faradaic efficiencies, compensated cathode potentials and energetic cathode efficiencies with their standard deviation/error within and between differently sized and stirred catalyst synthesis batches at high current density.  
Operating conditions: semi-batch;  $j = -1000 \text{ mA cm}^{-2}$ ,  $t = 45 \text{ min}$ ,  $T = 50^\circ\text{C}$ ,  $[\text{KCl}] = 2 \text{ M}$ ,  $\text{pH} = 10$ ; standard GDE.

$V_{\text{f, solvent}}$ / L	$V_{\text{f, vessel}}$ / L	Stirring	<i>FE</i> / %			$\varphi_{\text{C, IR}}$ / V (vs. SHE)	Runs
			H <sub>2</sub>	CO	Formate		
0.5	1	Magnetic	15.9 ± 5.6	7.5 ± 0.5	75.4 ± 4.4	-1.60 ± 0.04	3
1.5	2	Magnetic	27.3 ± 4.2	6.6 ± 0.6	66.7 ± 4.2	-1.76 ± 0.04	2
1.5	2	Anchor	16.7	6.6	76.7	-1.63	1

### 7.7.2 Scale-up of the electrode preparation

Up-scaling the preparation of GDEs was done by the project partner German Aerospace Center, Stuttgart, Germany (DLR). In contrast to the herein used pressing technique in cylindrical masks, the goal for industrial applications is to use rollers for a potentially continuous preparation. Their results show that the addition of a fine nickel mesh as backbone is necessary to achieve sufficient mechanical stability. The tin oxide loaded carbon black/PTFE mixture is rolled onto this mesh followed by a thermal treatment step at 340 °C, resulting in a stable and flexible GDE. The used metal mesh can simultaneously act as

current collector but must not come in contact with the electrolyte to avoid massive hydrogen evolution. However, it was found that using the so far described fine PTFE powder ( $\bar{d}_p = 4 \mu\text{m}$ )<sup>[160]</sup> is not suitable for up-scaling in terms of mechanical stability. Instead a much coarser powder had to be used ( $\bar{d}_p = 520 \mu\text{m}$ )<sup>[160]</sup>. The influence of these different sized powders on long-term performance at moderate current density was investigated with results depicted in figure 7.40.

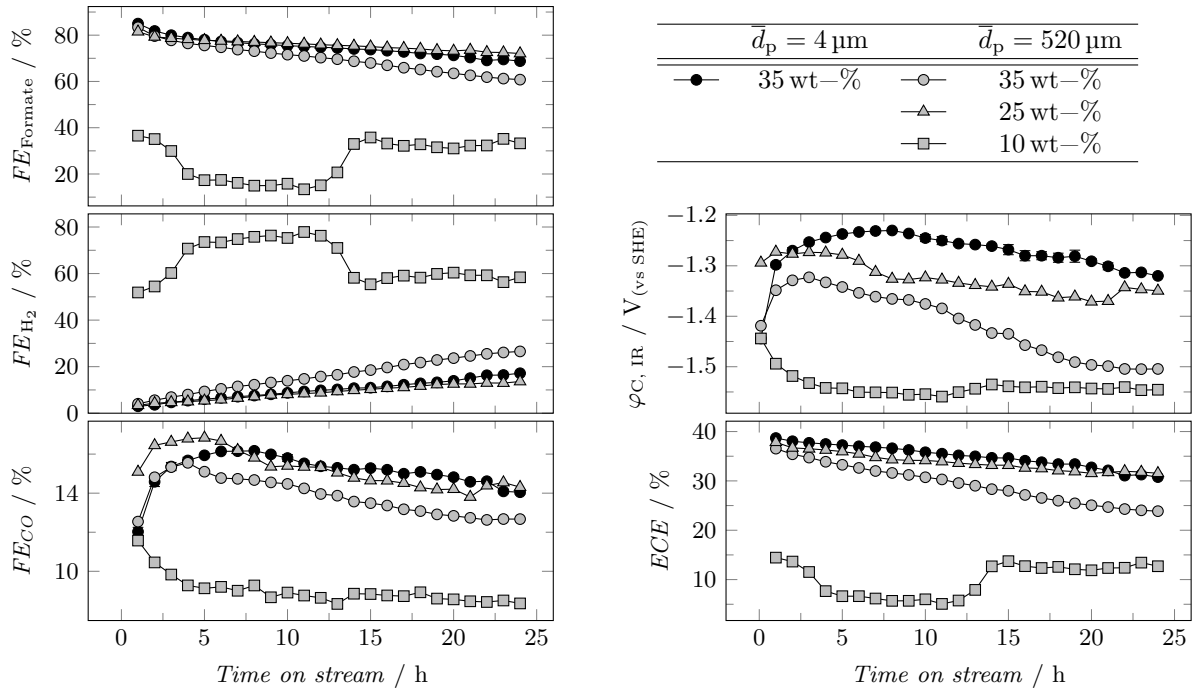


**Figure 7.40:** Long-term performance analysis for gas diffusion electrodes prepared from differently sized PTFE powders of various matrix shares. Operating conditions: continuous;  $j = -200 \text{ mA cm}^{-2}$ ,  $T = 50 \text{ }^\circ\text{C}$ ,  $[\text{KCl}] = 1 \text{ M}$ ,  $\text{pH} = 10$ ;  $\sigma_{\text{Sn}} = 1 \text{ mg cm}_{\text{geo}}^{-2}$ .

A first comparison between the fine and coarse powdered PTFE with a 35 wt-% matrix share shows a higher hydrogen production rate for the coarse one. It is expected that the less homogeneous distribution of gas and electrolyte filled pores (due to the larger PTFE particle size) is decisive for this observation. However, also local hydrophobicity is probably influenced and a much more detailed investigation of pore size distribution and wetting behavior would be required to make certain statements.

Consequently, adjustments of the electrode's composition were made by reducing the amount of coarse PTFE. Results in figure 7.40 show a maximum in *ECE* at 25 wt-%. The performance with such a composition roughly matches the one obtained with 35 wt-% of the fine PTFE. Hence, the fine PTFE powder can be replaced by the coarse one, at least for moderate current densities, by simply adjusting its mass share.

Using the fine powdered PTFE a relatively high amount of PTFE (>25 wt-%) is necessary to achieve sufficient mechanical stability.<sup>[138]</sup> With the coarse powder, on the other hand, GDE s with as little as

10 wt-% PTFE have been successfully by both preparation methods. The accordingly higher amount of carbon black can be beneficial because it allows for a higher total porosity and more active sites per geometrical electrode area. Also, conductivity is increased with higher shares of conductive carbon material.<sup>[138]</sup> However, with only 10 wt-% of PTFE it seems like no significant reaction zone (co-existing open and filled pores) is formed since hydrogen *FE* is starting at around 50 % and further rising. It can be assumed that the electrode's hydrophobicity is too low and that flooding occurs. Also, macropores are mainly formed during the thermal treatment in the GDE preparation process by melting the PTFE particles. With only 10 % PTFE, macropores are probably not formed in sufficient quantity and CO<sub>2</sub> mass transport is impeded.

### 7.7.3 Scale-up of the electrochemical cell

Finally, the electrochemical cell was scaled up in two steps from an active geometrical electrode area of 1 cm<sup>2</sup> to 10 cm<sup>2</sup> to 70 cm<sup>2</sup>. Within the first step, the fundamental design was not changed as visualized in figure 6.2 and 6.3, p. 72 and 73. This kind of cell allows visual observation during electrolysis by its transparent and spacious body to identify any problems. Such could be internal or external leakages, bubble trapping or mechanical degradation of the GDE.

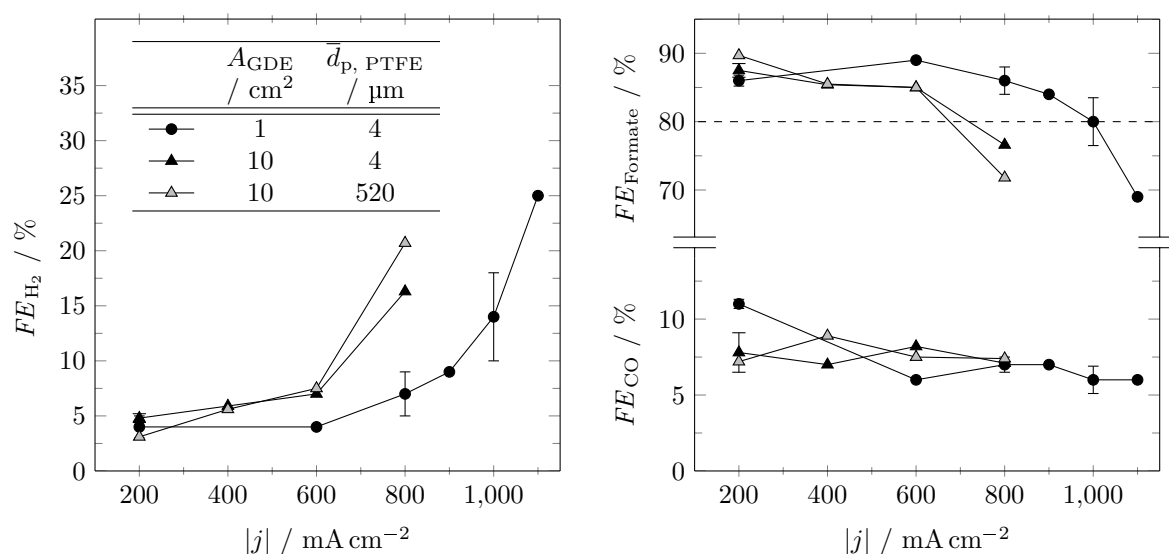


**Figure 7.41:** Faradaic efficiencies of the three main products over current density for standard 1 cm<sup>2</sup> and 10 cm<sup>2</sup> gas diffusion electrodes of different matrix compositions.

The legend applies to both figures.

Operating conditions: semi-batch;  $t = 45$  min,  $T = 50$  °C,  $[\text{KCl}] = 2$  M,  $\text{pH} = 10$ ;  $\sigma_{\text{Sn}} = 1$  mg cm<sup>-2</sup><sub>geo</sub>, PTFE:AB ratio = 35:65.

Comparing *FEs* of the three main products for the 1 cm<sup>2</sup> and 10 cm<sup>2</sup> GDE with a 4 μm PTFE shows a significant reduction in limiting current density from  $-1000$  mA cm<sup>-2</sup> to  $-700$  mA cm<sup>-2</sup>. Product dis-

tribution shifts from formate to hydrogen while CO does not vary notable. A first explanation for this worsened performance was that the mechanical stability is not high enough. Attempts to measure the product distribution at a current density of  $-1000 \text{ mA cm}^{-2}$  were not even possible as electrodes completely broke after a few minutes. However, suggested replacement of the fine PTFE powder through the coarse one with adapted share does not improve the performance even though stable electrodes are obtained. The difference between both cells could be caused by a limited heat transfer. After electrolysis at high absolute values of current density ( $|j| > 600 \text{ mA cm}^{-2}$ ) partly molten acrylonitrile butadiene styrene (ABS) based components (CO<sub>2</sub> flow distributor and supporting mask, see figure 6.3, p. 73) were found only in the  $10 \text{ cm}^2$  cell, even though both cells contain such parts. The indicated higher thermal stress in the  $10 \text{ cm}^2$  cell is probably caused by the higher absolute value of current and slight differences in the electric contacting (size and contact pressure of the spring connection, as well as mesh size of the current collector). This results in a significantly higher temperature inside the GDE, compared to the temperature controlled bulk electrolyte, and in an increased CO<sub>2</sub> mass transport limitation by the lowered CO<sub>2</sub> solubility.

In order to quantify different contributions to the total cell voltage, individual losses were separated and identified. A silver wire pseudo reference electrode (R) was placed in the catholyte chamber 5 mm from the membrane (M). Cathode and anode potential were measured by recording voltages against that pseudo reference. After electrolysis the used wire was calibrated against the Hg/HgO (1 M KOH) reference electrode in the respective catholyte at operating temperature. Voltages between cathode (C) and membrane or anode (A) and membrane are referred to as CM and AM, respectively. Except for reaction related voltage drops ( $\varphi_{C, IR}$  and  $\varphi_{A, IR}$ ), voltage losses divide into electronic and ionic ohmic losses for both half-cells. Voltage drops from electronic resistances ( $V_{CM, \Omega, e}$  and  $V_{AM, \Omega, e}$ ) are caused by a finite conductivity through outer circuit, electrode connection and the electrode itself. Voltage drops from ionic resistances ( $V_{CM, \Omega, i}$ ,  $V_{AM, \Omega, i}$  and  $V_{M, \Omega, i}$ ) result from the limited ionic conductivity of the electrolytes and membrane. The total cell voltage can be expressed as follows:

$$V_{\text{cell}} = V_{\text{CM}} + V_{\text{AM}} + V_{\text{M}, \Omega, i} \quad (7.7.1)$$

$$= \underbrace{\varphi_{C, IR} + V_{\text{CM}, \Omega, e} + V_{\text{CM}, \Omega, i}}_{V_{\text{CM}}} + \underbrace{\varphi_{A, IR} + V_{\text{AM}, \Omega, e} + V_{\text{AM}, \Omega, i}}_{V_{\text{AM}}} + V_{\text{M}, \Omega, i} \quad (7.7.2)$$

All seven contributions of equation 7.7.2 were measured as described in the following paragraphs with results given in figures 7.42 and 7.43.

Reaction related losses ( $\varphi_{C, IR}$  and  $\varphi_{A, IR}$ ) were measured by recording *IR* compensated voltages of both half-cells and converting them to the standard hydrogen electrode (SHE) scale. In order to separate both half-cells a reference electrode is necessary which can be placed either inside the catholyte or inside the anolyte. The exact position influences the measured ionic voltage losses and needs to be considered. In the described cell spatial conditions only allowed the insertion into the catholyte compartment. However, voltage drop contributions of each half-cell would then be measured from cathode to reference (CR) and from anode to reference (AR) instead of cathode to membrane and anode to membrane. This difference can be calculated by knowing the voltage drop inside the membrane ( $V_{M, \Omega, i}$ ) and within the electrolyte between reference and membrane ( $V_{RM, \Omega, i}$ ).  $V_{M, \Omega, i}$  can be calculated from literature values,<sup>[175]</sup> while  $V_{RM, \Omega, i}$  is determined by measuring the electrolytes specific conductivity  $\kappa_{RM}$  and knowing the RM distance  $l_{RM}$ , as well as the areal cross section  $A_{RM}$ .  $V_{CM}$  and  $V_{AM}$  can then be expressed as:

$$V_{CM} = V_{CR} + V_{RM, \Omega, i} \quad (7.7.3)$$

$$= V_{CR} + \left( \frac{1}{\kappa_{RM}} \cdot \frac{l_{RM}}{A_{RM}} \cdot I \right) \quad (7.7.4)$$

$$V_{AM} = V_{AR} - V_{RM, \Omega, i} - V_{M, \Omega, i} \quad (7.7.5)$$

$$= V_{AR} - \left( \frac{1}{\kappa_{RM}} \cdot \frac{l_{RM}}{A_{RM}} \cdot I \right) - \left( \frac{1}{\kappa_M} \cdot \frac{l_M}{A_M} \cdot I \right) \quad (7.7.6)$$

$V_{CR}$  and  $V_{AR}$  were both measured by recording uncompensated voltages between cathode and reference, as well as between anode and reference. Ohmic losses are then given by:

$$V_{CM, \Omega, i+e} = V_{CM} - \varphi_{C, IR} \quad (7.7.7)$$

$$V_{AM, \Omega, i+e} = V_{AM} - \varphi_{A, IR} \quad (7.7.8)$$

and can further be separated into ionic and electronic voltage losses:

$$V_{CM, \Omega, i+e} = V_{CM, \Omega, e} + V_{CM, \Omega, i} \quad (7.7.9)$$

$$V_{AM, \Omega, i+e} = V_{AM, \Omega, e} + V_{AM, \Omega, i} \quad (7.7.10)$$

$V_{AM, \Omega, e}$  is accessible by measuring the resistance between outer contact (OC) and the center of the anode (further referred to as electrical connection (EC)) and calculating the voltage loss according to Ohm's law.

$$V_{AM, \Omega, e} = R_{EC, A} \cdot I \quad (7.7.11)$$

The anode's last remaining contribution,  $V_{AM, \Omega, i}$ , is then obtained by rearranging equation 7.7.10. Note that this contribution cannot be estimated from the electrolyte's specific conductivity, since evolving gas bubbles decrease the ion conducting cross section area by an unknown degree.

While  $V_{AM, \Omega, e}$  is easily accessible, determining  $V_{CM, \Omega, e}$  cannot be measured directly. Electronic conductivity between outer circuit and reaction zone inside the GDE is not constant and depends on factors like the degree of wetting or the local temperature. Hence, the ionic voltage loss between cathode and membrane needed to be calculated. It was determined from measured electrolyte conductivity and the known reactor geometry. The latter divides into two parts with different cross section areas  $A_{CM, 1}$  and  $A_{CM, 2}$ , as well as different lengths  $l_{CM, 1}$  and  $l_{CM, 2}$  (see figure 6.3, p. 73).  $V_{CM, \Omega, i}$  can be calculated by:

$$V_{CM, \Omega, i} = \left[ \left( \frac{1}{\kappa_{CM}} \cdot \frac{l_{CM, 1}}{A_{CM, 1}} \right) + \left( \frac{1}{\kappa_{CM}} \cdot \frac{l_{CM, 2}}{A_{CM, 2}} \right) \right] \cdot I \quad (7.7.12)$$

Input parameters are  $\kappa_{CM} = 0.3 \text{ S cm}^{-1}$ ,  $l_{CM, 1} = 0.9 \text{ cm}$ ,  $l_{CM, 2} = 1.0 \text{ cm}$ ,  $A_{CM, 1} = 14 \text{ cm}^2$  and  $A_{CM, 2} = 40 \text{ cm}^2$ . Electronic voltage losses are then calculated by rearranging equation 7.7.9.

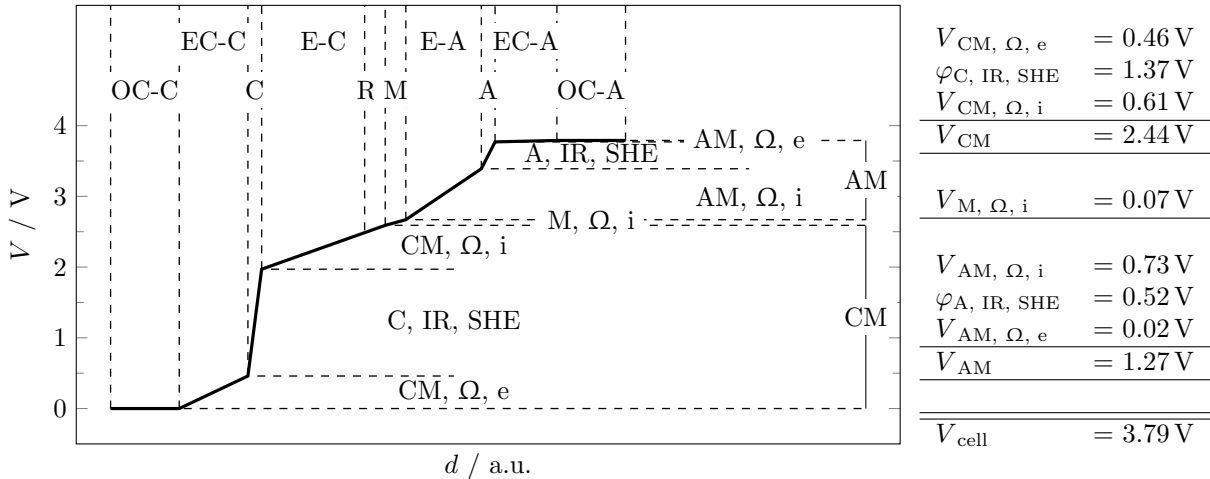


**Figure 7.42:** Visualization and listing of voltage drop contributions at  $j = 200 \text{ mA cm}^{-2}$  between both outer circuit connections.  $\Delta V$  values are shown to scale,  $\Delta d$  are arbitrary. Abbreviations: C: cathode (GDE - wetted part); A: anode; R: reference; OC: outer circuit; EC: electrical connection; E: electrolyte; M: membrane; CM: voltage drop between cathode and membrane; AM: voltage drop between anode and membrane. Indices:  $\Omega, e$ : electrical ohmic resistance;  $\Omega, i$ : ionic ohmic resistance.

Operating conditions: semi-batch;  $t = 45 \text{ min}$ ,  $T = 50 \text{ }^\circ\text{C}$ ,  $[\text{KCl}]_C = 2 \text{ M}$ ,  $\text{pH} = 10$ ,  $[\text{KOH}]_A = 5 \text{ M}$ ; standard GDE,  $A = 10 \text{ cm}^2$ .



Figure 7.42 visualizes and lists all measured and calculated voltage drops at a current density of  $200 \text{ mA cm}^{-2}$ . Obviously the cathode side contributes in greater manner for both ohmic and non-ohmic losses, even though it has to be kept in mind that the latter depends on the used reference electrode. A significant portion of ohmic resistance was found to arise from the GDE's electronic connection. Due to the stacked structure of current collector, GDL and GDE, multiple contact resistances have to be overcome. Since the current collector is not integrated into the GDE it is important to ensure a close and uniform contact. Here, the addition of a second current collector between the first one and the gas diffusion layer (GDL) with a much smaller mesh size already decreased the whole cell voltage from  $4.7 \text{ V}$  to  $3.8 \text{ V}$ . However, even when ohmic resistances are minimized, the  $\text{CO}_2\text{RR}$  potential still represents the largest contribution. In this case  $\varphi_{\text{C, IR}}$  accounts to around 40 % of the whole cell voltage with 19 % being related to activation and concentration overpotential ( $\eta_{\text{act. + conc.}} = 0.71 \text{ V}$ ).

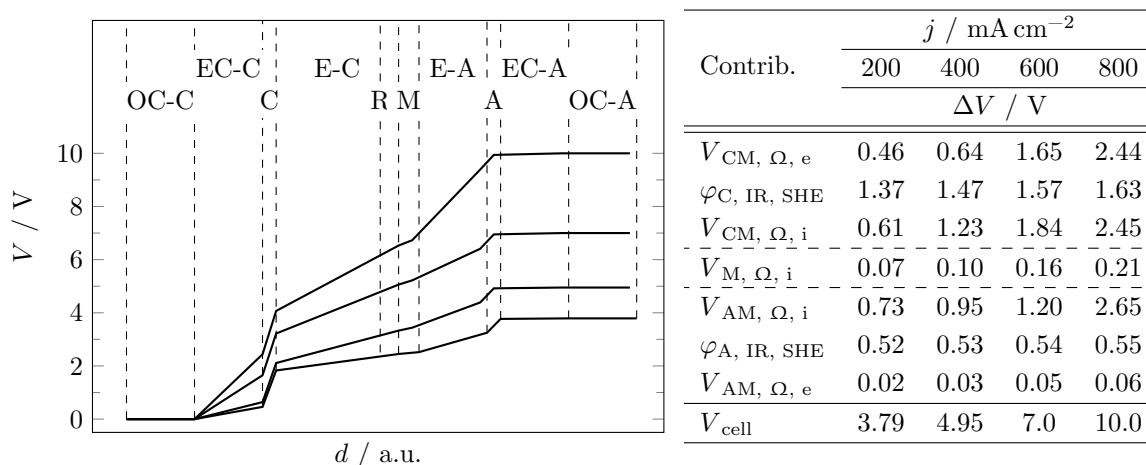


**Figure 7.43:** Visualization and listing of voltage drop contributions at different current densities between both outer circuit connections.  $\Delta V$  values are shown to scale,  $\Delta d$  are arbitrary. Abbreviations: C: cathode (GDE - wetted part); A: anode; R: reference; OC: outer circuit; EC: electrical connection; E: electrolyte; M: membrane; CR: voltage drop between cathode and reference; AR: voltage drop between anode and reference. Indices:  $\Omega, e$ : electronic ohmic resistance;  $\Omega, i$ : ionic ohmic resistance.

Operating conditions: semi-batch;  $t = 45 \text{ min}$ ,  $T = 50 \text{ }^\circ\text{C}$ ,  $[\text{KCl}]_{\text{C}} = 2 \text{ M}$ ,  $\text{pH} = 10$ ,  $[\text{KOH}]_{\text{A}} = 5 \text{ M}$ ; standard GDE,  $A = 10 \text{ cm}^2$ .

The same differentiation was done for higher current densities shown in figure 7.43. At a current density of  $800 \text{ mA cm}^{-2}$  ohmic losses increased to a total of  $7.82 \text{ V}$ . Especially the cathode's electronic and anode's ionic resistances ( $V_{\text{CM}, \Omega, e}$  and  $V_{\text{AM}, \Omega, i}$ ) strongly depend on current density and rise in a non-linear manner as it would be expected for ohmic resistances. The large voltage drop through the cathode's electrical connection arise from the mentioned multiple contact resistances and a related strong heat development. Thermal stress was apparent for current densities  $> 600 \text{ mA cm}^{-2}$  at which ABS based accessory parts in close contact to the GDE began to melt. Anionic electrolyte resistance, on the other hand, increases exponentially due to the excessive formation of oxygen bubbles. Even though the nickel

mesh was placed directly on the membrane, a heterogeneous gas-liquid phase with reduced conductance forms in between.

Consequently, attempts to reduce these described effects were undertaken. Apart from changing the cell geometry, bubble size can be reduced by adding a surfactant to the electrolyte. By reducing the solvents surface tension smaller oxygen bubbles are formed, which can escape more easily through the metal mesh.<sup>[182]</sup> The addition of 1 mM to 10 mM Triton X indeed reduced the ionic resistance by around 0.1 V at  $200 \text{ mA cm}^{-2}$ . Note that this gain in activity is not included in the listings of figure 7.42 and 7.43, resulting in a total cell voltage of 3.69 V.

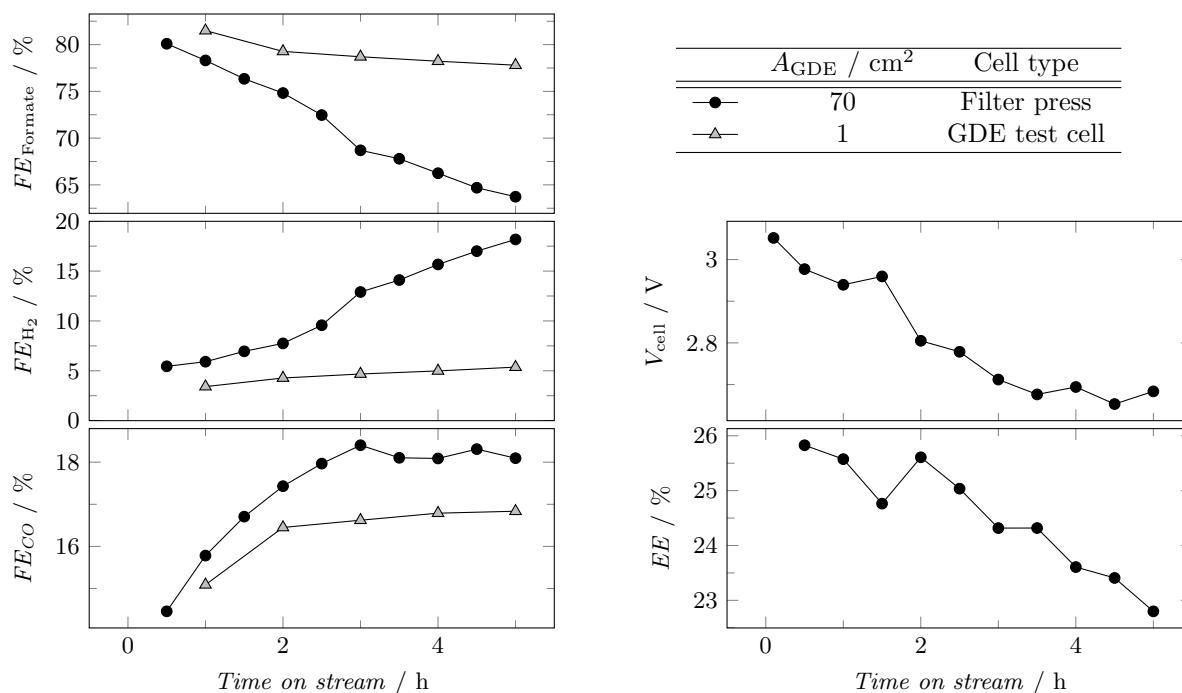


**Figure 7.44:** Performance analysis for the  $70 \text{ cm}^2$  filter press type cell in comparison to the  $1 \text{ cm}^2$  standard GDE test cell. An energetic efficiency cannot be given for the smaller cell due to the differently sized cathode, membrane and anode within that cell.

Operating conditions: continuous;  $j = 200 \text{ mA cm}^{-2}$ ,  $T = 50 \text{ }^\circ\text{C}$ ,  $[\text{KCl}]_{\text{C}} = 2 \text{ M}$ ,  $\text{pH} = 10$ ,  $[\text{KOH}]_{\text{A}} = 5 \text{ M}$ ;  $\sigma_{\text{Sn}} = 1 \text{ mg cm}_{\text{geo}}^{-2}$ ,  $\text{PTFE}_{520 \mu\text{m}}:\text{AB}$  ratio = 35:65.

Significantly reducing all three of the mentioned critical voltage drops required a totally new electrolyzer design. A filter press type flow cell with an even larger active electrode area of  $70 \text{ cm}^2$ , shown in figure 6.4, p. 74, was therefore developed. Key changes were an integration of the current collector into the GDE's matrix, significant reduction of the cathode membrane distance and a direct contact between membrane and anode mesh. Current collector integration was done by directly rolling the carbon/PTFE mixture on a nickel mesh. Thus, contact resistances were minimized and the uniformity of current distribution is assumed to be improved. Reducing the cathode membrane distance to 4 mm was achieved by 3D printing a flow field with external tubing connections. The anode nickel mesh was integrated into a

silicon sealing and pressed directly against the membrane. This allows no notable space between anode and membrane where gas bubbles can be trapped. This 70 cm<sup>2</sup> cell was operated in continuous mode of operation at a current density of 200 mA cm<sup>-2</sup> and a total current of 14 A. Results are depicted in figure 7.44 and compared to the 1 cm<sup>2</sup> standard GDE test cell.

Obviously, initial product distribution is comparable for both cells but starts to drift apart already after 2 h. Within the scaled-up cell a strong shift from formate to hydrogen over time is observed. Multiple reasons for that are conceivable. First, solvent evaporation and re-condensation on the GDE's backside lead to the formation of water droplets. These droplets require a certain mass in order to be removed by gravity and the passing gas flow. When sticking to the electrode they block the efficient CO<sub>2</sub> transport towards the active surface. Second, a wetting gradient may be forming along the cell height. Due to increasing differences in hydrostatic pressure electrolyte intrusion can differ quite significantly for regions at the top or bottom of the GDE. Last, the efficiency of heat transfer could not be determined. Hence, it cannot be ruled out that local depletion of CO<sub>2</sub> by the reduced solubility at higher temperatures occurs. Quantification of these mentioned aspects requires further investigation.

Note that the absolute cell voltage (non-compensated) and real *EE* are shown here instead of the usually used cathode potential and *ECE*. Both values can only be given for the 70 cm<sup>2</sup> cell as the other cells do not comprise equally sized membrane and electrodes. Larger geometrical cross section areas of membrane and anode, compared to the cathode, would mean lower ion and current densities through membrane and anode, thus resulting in a lower voltage drop than in an industrial electrolyzer. Excluding all ohmic resistances results in a theoretical minimum cell voltage of 1.89 V. Hence, the obtained range in voltage of 3.05 V to 2.68 V already represents a remarkable value compared to literature.<sup>[76, 78, 185, 186]</sup>



## 7.8 Process concepts

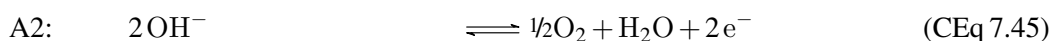
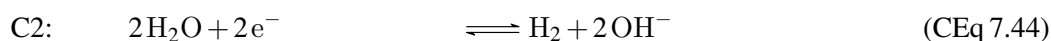
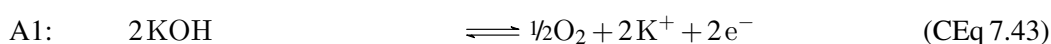
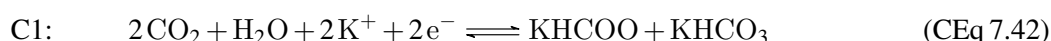
Finally, some fundamental disadvantages of the so far investigated CO<sub>2</sub>EL system were tackled. Alkaline CO<sub>2</sub>RR has some indisputable advantages discussed in section 4.4.1, p. 53. However, it comes with the formation of formate instead of formic acid which is crucial for some applications.<sup>[11]</sup> Also, hydroxide is consumed and bicarbonate formed in near stoichiometric amounts contaminating the final product. Downstream processing of the obtained mixture by bipolar membrane electro dialysis (BPED) might be a way to get pure formic acid while maintaining the benefits of alkaline CO<sub>2</sub>EL.

Another disadvantage of the investigated system is related to the deployed counter reaction at the anode. So far OER is used, which requires a high energy input but only yields a product of low market value. Replacing this anode reaction with selective alcohol oxidation can help to reduce the power consumption and to yield another valuable product.

### 7.8.1 Coupling carbon dioxide electrolysis with bipolar membrane electro dialysis

As mentioned, BPED can be used to tackle the main disadvantages of alkaline CO<sub>2</sub>RR. It is used to regenerate consumed hydroxide ions and to protonate formate and bicarbonate ions (see section 4.4.2, p. 54). The latter is converted to unstable carbonic acid, which can then be separated by removing free CO<sub>2</sub> from the product stream.

Such a downstream processing can be coupled with electrolysis to close loops according to an overall process proposed in figure 7.45. Substantial for this overall process is that electrolysis is performed in a recycled product mixture containing potassium formate and bicarbonate in similar amounts. It is important to maintain a high ionic conductivity throughout both cells. Hence, material flows have to be adjusted in a way that just a small salt portion is produced or consumed compared to the total salt load. Electrolysis and dialysis are terminated by the following reactions.



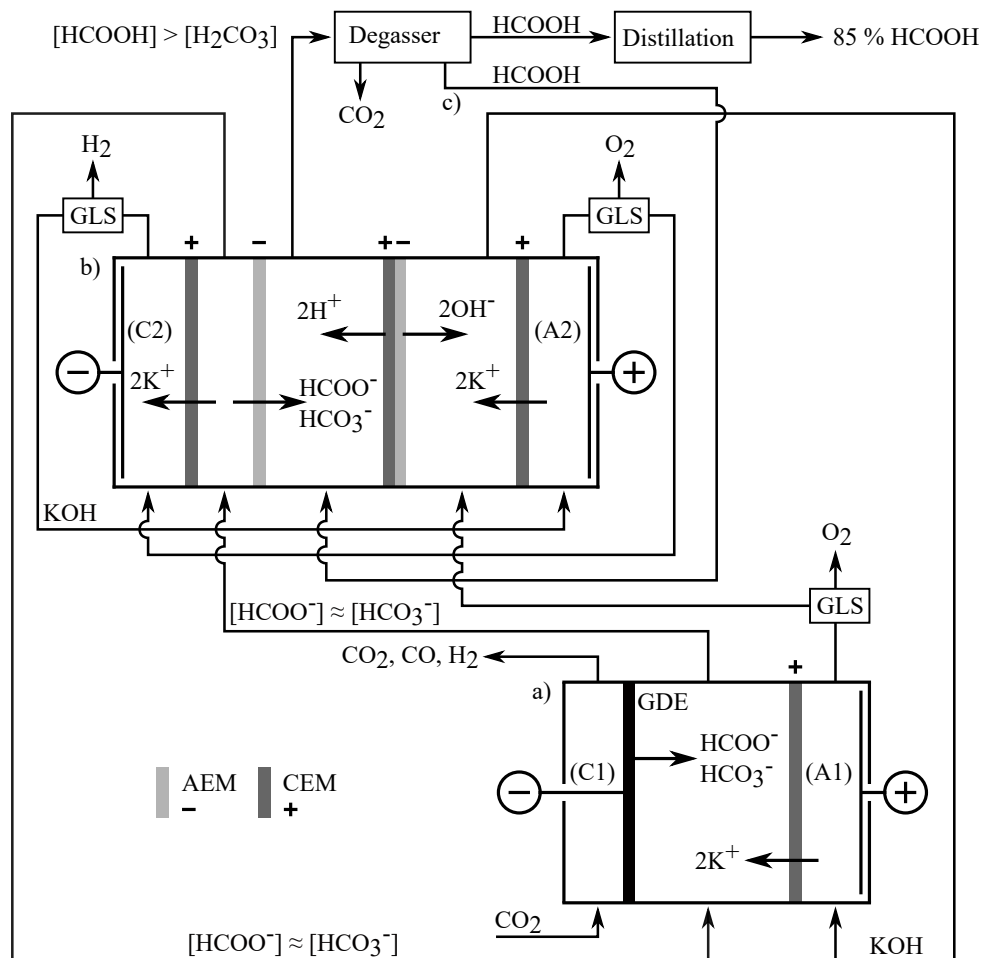
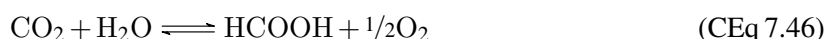


**Figure 7.45:** Potential coupling of alkaline CO<sub>2</sub> electrolysis (a) with bipolar membrane electrodiolysis (b). Overall, water and CO<sub>2</sub> are converted into formic acid and oxygen. GLS: gas-liquid separator. Reactions C1, C2, A1 and A2 are given in the text.

Comparing the overall substance input and output results in a total reaction equation of:



An important feature of the BPED cell is that it can be used to increase the concentration of formic acid prior to distillation by recirculating a certain portion of the product stream (see figure 7.45 c). As already mentioned in section 4.4.2, p. 54, distillation consumes a vast amount of energy when low concentrated ( $\approx 1$  M) solutions of formic acid have to be processed. At such low concentrations the costs for distillation can easily exceed the market value of the final product (85 wt-% formic acid). It is therefore crucial to increase the concentration, e.g. by BPED. Of course such a process consumes energy as well and the total energy input for downstream processing has to be calculated. Based on calculations of the project partner Plinke GmbH, KBR, energy consumption of the distillation step depending on the formic acid input concentration (equals the output concentration of the BPED cell) can be given.<sup>[150]</sup>

The corresponding energy consumption of the BPED cell is known from literature.<sup>[147]</sup> Both individual contributions, as well as the total energy costs are given in table 7.15. Comparing the total energy costs depending on the BPED's formic acid output concentration and assuming a market value of 600 € t<sub>FA</sub><sup>-1</sup><sup>[151]</sup> it becomes obvious that a concentration of at least 6 M is necessary. From literature it is known that BPED can yield such high concentrations with acceptable diffusion losses.<sup>[147]</sup>

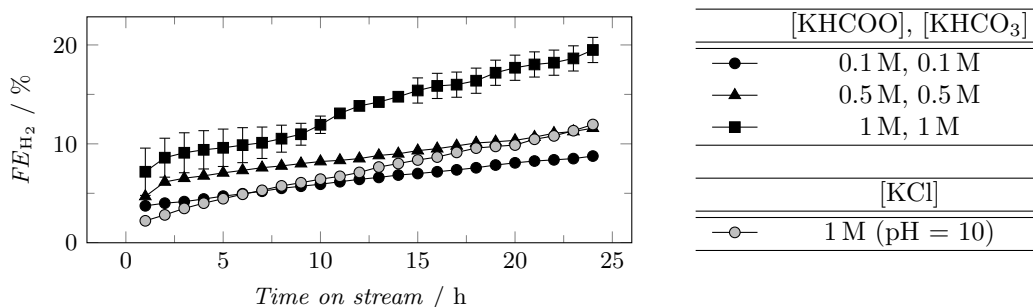
**Table 7.15:** Individual and total energy consumptions and costs per tonne of 85 wt-% formic acid with bipolar membrane electro dialysis and distillation as post-electrolysis process. Energy costs for heating and cooling were estimated to be 0.055 € kWh<sup>-1</sup> and 0.01 € kWh<sup>-1</sup>, respectively.<sup>[150]</sup> Electricity rate is estimated to be 0.07 € kWh<sup>-1</sup>.<sup>[176]</sup> a) Formic acid output concentration obtained by bipolar membrane electro dialysis.

c <sub>FA</sub> <sup>a)</sup> / M	Distillation <sup>[150]</sup>					BPED <sup>[147]</sup>		Total
	E/m <sub>FA</sub> / kW h t <sup>-1</sup>		Cost/m <sub>FA</sub> / € t <sub>FA</sub> <sup>-1</sup>			E/m <sub>FA</sub>	El.rate/m <sub>FA</sub>	Cost/m <sub>FA</sub>
	Heating	Cooling	Heating	Cooling	Total	/ kW h t <sup>-1</sup>	/ € t <sub>FA</sub> <sup>-1</sup>	/ € t <sub>FA</sub> <sup>-1</sup>
1.1	22785	20853	1253	209	1462	325	21	1483
1.5	16622	15225	914	152	1066	449	29	1095
2.2	11949	10941	657	109	767	675	42	809
3.4	8295	7592	456	76	532	1090	65	597
4.6	6458	5912	355	59	414	1543	88	502
5.8	5376	4914	296	49	345	2040	111	456
7.1	4662	4263	256	43	299	2637	136	435
9.6	3801	3486	209	35	244	3994	183	427

### 7.8.1.1 Operating carbon dioxide electrolysis in the recycled product mixture

The requirement of operating CO<sub>2</sub>EL in a recycled product solution results from the fact that no separation method other than degassing should be applied to yield pure aqueous formic acid. This, however, represents a challenge for electrolysis. Highly concentrated mixtures of formate and bicarbonate have already been described to severely decrease the cathode's performance in semi-batch mode (see figure 7.21 and 7.22, p. 135). Also, during long-term operation high formate concentrations lead to a product mass transport limitation (see figure 7.14, p. 124). Long-term stability in formate/bicarbonate mixtures was therefore analyzed to identify the maximum possible total concentration used as electrolyte feed.

Figure 7.46 shows a severe increase in hydrogen production when operating in a total salt concentration of 2 M instead of 1 M (see appendix figure 9.15, p. 228, for the complete analysis). In order to further investigate the underlying causes, operating conditions and composition of the highest concentrated electrolyte were modified. Hydrogen FE analysis over time is depicted in figure 7.47 (see appendix



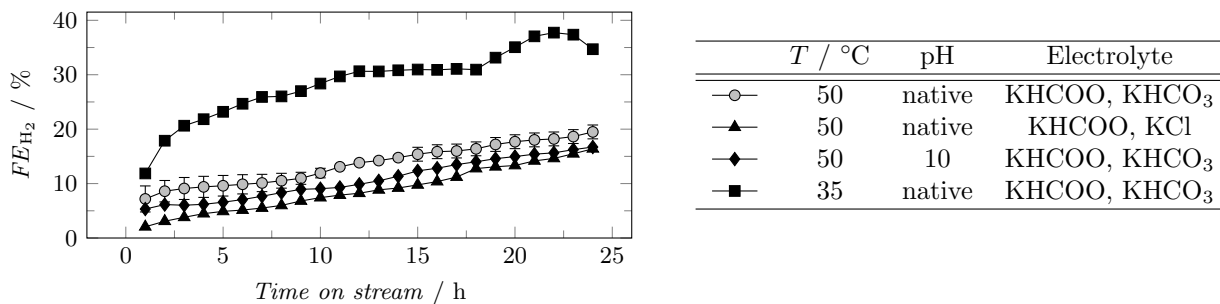
**Figure 7.46:** Course of hydrogen faradaic efficiency over time on stream for formate/bicarbonate 1:1 mixtures of different concentrations. The standard electrolyte [KCl] = 1 M is shown for comparison. Operating conditions: continuous;  $j = -200 \text{ mA cm}^{-2}$ ,  $T = 50 \text{ }^\circ\text{C}$ , native pH; standard GDE.

figure 9.16, p. 229, for the complete analysis). The most obvious explanation would be a high product diffusion limitation. However, this cannot be the only contribution, since exchanging potassium bicarbonate with potassium chloride significantly improves the performance. Hydrogen *FE* is also lowered when increasing the native pH of that formate/bicarbonate mixture from around 8.5 to pH = 10. Both observations are in accordance with the semi-batch measurements of figure 7.21, p. 135. Accordingly, the same reason may apply for long-term operation. Bicarbonate decomposition is increased at lower pH values, potentially leading to a partial loss of active surface area by gas formation. In contrast to results of figure 7.21, decreasing the temperature to 35 °C yielded a much worse performance with high hydrogen *FE*. Here the different modes of operation come into play. During long-term operation the liquid electrolyte penetrates deeper into the electrode. The resulting much longer diffusion pathways require high product diffusion coefficients, which are lowered with decreasing temperatures. Hence, product diffusion limitation prevails and hydrogen evolution rises.

These findings, however, make it challenging to improve electrolysis. Increasing the pH will lead to an increasingly favored transfer of hydroxide or bicarbonate ions through the BPED's anion exchange membrane (AEM) due to their enlarged number. Also, besides the lowered electrolyte conductivity during electrolysis, lower total salt concentrations will be shown to increase formic acid diffusion rates out of the corresponding compartment. Both effects strongly decrease the efficiency of the dialysis cell.

In the next section it will be shown that operating the BPED with a formate/bicarbonate mixture of 2 M in total concentration is crucial. However, this would mean a significant loss in performance during electrolysis, at least for the standard GDE. Hence, the so far best performing electrode composition (reduced tin loading of  $0.5 \text{ mg cm}_{\text{geo}}^{-2}$  and a Nafion/PTFE/AB (15/20/65 wt-%) matrix) was applied to this electrolyte. Long-term stability analysis depicted in figure 7.48 shows an unexpected result. While the standard GDE exhibits a continuous deactivation, the optimized GDE starts with a worse performance but improves significantly within the first 24 h. After this period, deactivation sets in also with this





**Figure 7.47:** Course of hydrogen faradaic efficiency over time on stream for different electrolyte mixtures (1:1) with varied operating conditions. Operating conditions: continuous;  $j = -200 \text{ mA cm}^{-2}$ , total salt concentration = 2 M; standard GDE.

electrode. Considering the large standard deviation and interpreting results in a negative way, hydrogen  $FE$  is barely below the self-defined 20 % criterion (see section 7.6.1, p. 149). Reasons for the observed strange behavior were not further investigated due to the negative findings obtained when evaluating the BPED process itself.

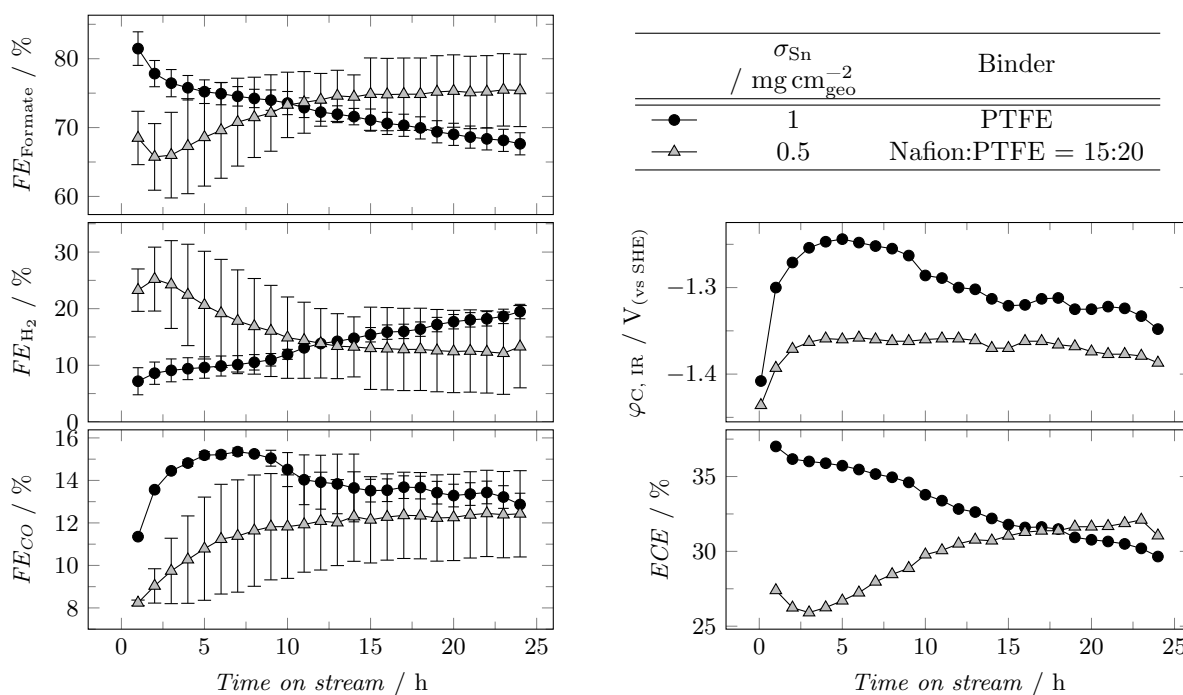


**Figure 7.48:** Long-term performance analysis of a standard and optimized gas diffusion electrode in a 1:1 potassium formate/bicarbonate mixture with a total concentration of 2 M. Operating conditions: continuous;  $j = -200 \text{ mA cm}^{-2}$ ,  $T = 50 ^\circ\text{C}$ , native pH.

### 7.8.1.2 Bipolar membrane electrodialysis

In order to investigate the potential use of BPED for post-electrolysis protonation of formed formate/bicarbonate salts and for hydroxide regeneration, a dialysis cell with five compartments was fabricated.

Figure 7.49 shows its schematic design with compartment 1 and 5 (C1, C5) housing the terminal nickel mesh electrodes for water splitting. Aqueous potassium hydroxide solution (1 M) was cycled through both these compartments. Within the final process aqueous solutions of potassium formate/bicarbonate, formic acid and potassium hydroxide are fed to compartment 2, 3 and 4 (C2, C3 and C4), respectively. Formate and bicarbonate anions are transferred through the AEM from C2 to C3 and are subsequently protonated, while potassium ions move through the cation exchange membranes (CEMs) from C2 to C1 and from C5 to C4. Hydroxide ions produced within the bipolar membrane (BPM) then lead to the formation of potassium hydroxide in C4.

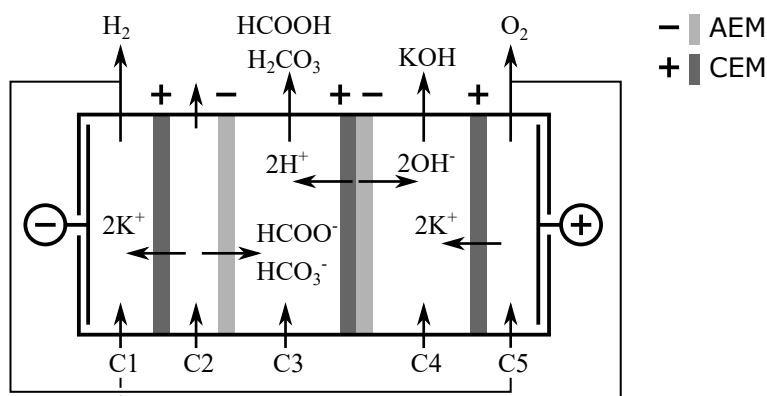


**Figure 7.49:** Three compartment configuration of bipolar membrane electrodesalination for formic acid/carbonic acid and potassium hydroxide production. Water splitting is used as terminal reduction and oxidation. Figure adapted from Jamie-Ferrer et al.<sup>[148]</sup>

First of all, the dialysis cell was checked for external and/or internal leakages. External leakages have not been found in terms of visual inspection. Possible internal leakages were examined by applying an indicator solution (1 M KCl) to one compartment, while the others were fed with pure water. HPLC analysis of those pure water containing compartments revealed no measurable crossover or leakages ( $\text{Cl}^-$  detection limit  $\approx 1$  mM).

Next, the general functionality was proven by feeding solutions of potassium chloride into compartment C2, C3 and C4 and measuring the change of pH in C3 and C4. From Faraday's law theoretical pH values can be calculated according to:

$$C3 : pH = -\log\left(\frac{I}{z \cdot F \cdot \dot{V}}\right) \quad (7.8.1)$$

$$C4 : pH = 14 - \log\left(\frac{I}{z \cdot F \cdot \dot{V}}\right) \quad (7.8.2)$$

These equations assume complete dissociation of the produced hydrochloric acid and potassium hydroxide, activity coefficients equal to 1 and a water splitting efficiency of the BPM of 100%<sup>[187]</sup>.

Feeding the electrolytes in compartment C3 and C4 at a volumetric flow rate of  $10 \text{ mL min}^{-1}$  and applying a current of 2 A results in theoretical pH values of 0.9 and 13.1 in compartment C3 and C4, respectively. Measured pH values ranged from 1.5 to 2 in compartment C3 and from 12.1 to 12.7 in compartment C4, proofing the general functionality of the developed BPED cell. The differences between calculated and measured pH values probably arise from the assumptions in equation 7.8.1 and 7.8.2.

Ideally, the cell should give large formic acid and potassium hydroxide concentrations, while supplying a comparably low concentrated formate/bicarbonate mixture. Low formate/bicarbonate input concentrations are required to operate  $\text{CO}_2\text{RR}$  efficiently. High formic acid and potassium hydroxide concentrations, on the other hand, are important for efficient distillation and OER, respectively. According to the discussion in section 7.8.1, p.171, a 6 M formic acid solution should be obtained to minimize the overall energy consumption of post-electrolysis processing (BPED and distillation). Hence, investigations were commenced with a 6 M formic acid input.

Feeding a 2 M formate/bicarbonate (1:1) solution to compartment C2 and a 6 M formic acid solution to compartment C3 and measuring the formate/formic acid concentration in the respective output, however, showed that instead of being increased, formic acid concentration in compartment C3 decreased. The main problem seems that, after protonation, undissociated formic acid at such high concentrations diffuses through the cation exchange and bipolar membrane enclosing compartment C3. Due to unreliable results of HPLC analysis for small changes in concentration at high absolute concentration values, the loss of formic acid in compartment C3 could not be quantified with sufficient accuracy. Instead, the amount of formic acid diffusing into compartment C2 and C4 was measured with potassium chloride as input solution in both of these compartments. Results of formic acid crossover are summarized in table 7.16. Within compartment C1 and C5 no formate was found as undissociated formic acid, diffusing out of C3, gets deprotonated in C2 and C4 due to the therein existing high pH and is kept from reaching C1 and C5 by the respective CEM.

Similar to equation 7.8.1 the theoretical change in acid concentration in compartment C3 can be calculated. Adjusting the electrolyte's volumetric flow rate to  $10 \text{ mL min}^{-1}$  and applying a total current of 2 A results in a maximum change in concentration of:

$$\Delta c = \frac{I}{z \cdot F \cdot \dot{V}} = \frac{2 \text{ A}}{1 \cdot 96485 \text{ A s mol}^{-1} \cdot 1.67 \cdot 10^{-4} \text{ L s}^{-1}} = 124 \text{ mM} \quad (7.8.3)$$

Considering that potassium formate and bicarbonate are fed in a 1:1 ratio and that they are of similar size and polarity then gives a theoretical change in formic acid concentration of  $\Delta c_{\text{FA}} = 62 \text{ mM}$ . Hence, formic acid crossover from compartment C3 into C2 is already larger than what would be transferred into the other direction (run 1). In other words, formic acid is not concentrated in compartment C3 but

**Table 7.16:** Summary of set input electrolytes and measured changes in concentration in compartments C2 and C4 related to the unintentional diffusion of formic acid out of compartment C3.  
 F/B: potassium formate and bicarbonate 1:1 mixture. Theoretical concentration increase in C3:  $\Delta c_{\text{FA}} = +62 \text{ mM}$ .  
 Operating conditions:  $j = 50 \text{ mA cm}^{-2}$ ,  $\dot{V} = 10 \text{ mL min}^{-1}$ .

Run	$T / ^\circ\text{C}$	Input			$\Delta c_{\text{FA}}$ output / mM			$V_{\text{cell}} / \text{V}$
		C2	C3	C4	C2	C3	C4	
1	r.t.	1 M KCl	6 M FA	1 M KCl	+70	$-140 \pm 10$	$+70 \pm 10$	5.2
2	r.t.	2 M KCl	6 M FA	1 M KCl	+22	$-92 \pm 10$	$+70 \pm 10$	5.0
3	r.t.	2 M F/B	6 M FA	5 M KOH	n.d.	n.d.	+78	7.0
4	0	2 M F/B	6 M FA	5 M KOH	n.d.	n.d.	+71	8.0
5	-6	2 M F/B	6 M FA	5 M KOH	n.d.	n.d.	+62	10.0
6	r.t.	2 M F/B	1 M FA	5 M KOH	n.d.	n.d.	+27	7.2
7	r.t.	2 M F/B	0.5 M FA	5 M KOH	n.d.	n.d.	+19	8.6

lost from it. Increasing the salt load in compartment C2 significantly reduced this crossover (run 2) but losses still account to around 35 % (of  $\Delta c_{\text{FA}}$ ). An even higher input concentration is not reasonable as this would cause severe problems during electrolysis. When it comes to the diffusion of formic acid from compartment C3 into C4, increasing the salt load from 1 M to 8 M potassium hydroxide in C4 (not shown) did not lower the cross-over rate. Losses of  $(70 \pm 10) \text{ mM}$  into compartment C4 were found, which sums up the total loss of formic acid from C3 to  $(92 \pm 10) \text{ mM}$  to  $(140 \pm 10) \text{ mM}$ .

An option to reduce diffusion is of course lowering the temperature. However, even the lowest possible temperature, just above the electrolytes melting point, did not reduce the losses to a satisfying extend (run 3-5). Also, this option comes with a significant increase in ohmic losses (see cell voltages in table 7.16) and hence decreasing  $EE$ .

With the used membranes a formic acid input concentration of 6 M is definitely too high and specifications for an economically reasonable energy input in distillation cannot be fulfilled. Even with an input concentration of as little as 0.5 M to 1 M, losses into compartment C4 were still found to be in a range of 30 % to 45 %. Voltage losses increased as well due to the lowered conductivity in compartment C3.

Results presented in this section significantly differ from what was expected from literature.<sup>[147]</sup> However, it has to be stressed that literature also states a strong influence of the used AEM and BPM through which formic acid diffusion occurs.<sup>[147]</sup> Within the present work only membranes from Fumat-ech BWT GmbH, FAB-PK-130 (AEM) and FBM-PK (BPM) were available. Hence, other commercial membranes should be tested or developed with regard to minimizing the formic acid crossover.

### 7.8.2 Coupling carbon dioxide reduction with selective alcohol oxidation

So far, exclusively OER was used as counter reaction to CO<sub>2</sub> reduction. This oxidation reaction, however, suffers from a comparatively high standard potential but mostly from a product of moderate value. Here, selective alcohol oxidation can be used to minimize power consumption, while simultaneously producing other valuable products.<sup>[154, 155]</sup> Selective oxidation of methanol can result formate/formic acid, representing a comproportionation when coupled with CO<sub>2</sub>RR. Hence, the energetic efficiency can be doubled by using methanol oxidation reaction (MOR) as counter reaction.

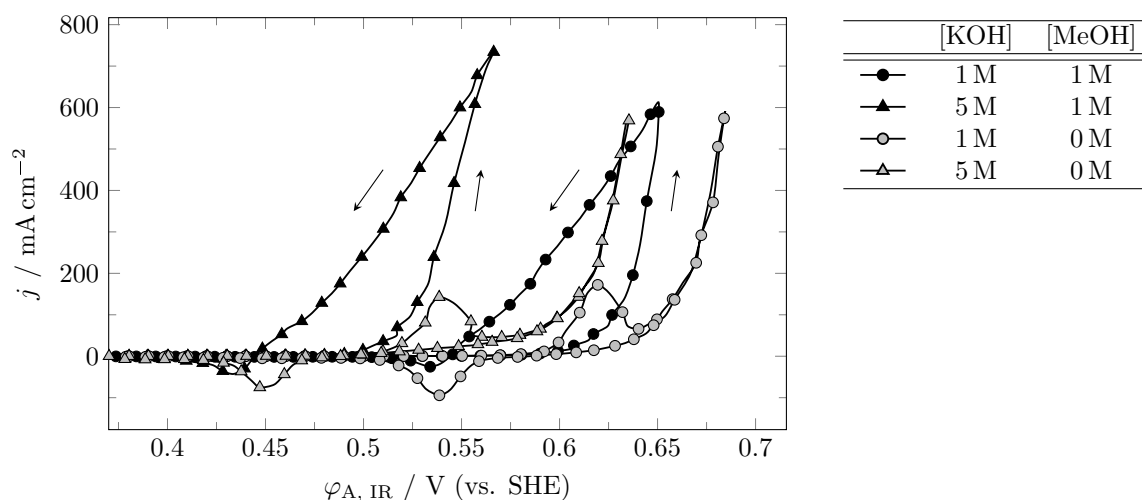


**Figure 7.50:** Cyclic voltammograms of a fine nickel mesh in electrolytes with 1 M and 5 M potassium hydroxide with or without 1 M methanol added. Operating conditions:  $T = 50\text{ }^{\circ}\text{C}$ ,  $d\phi_{A, IR}/dt = 50\text{ mV s}^{-1}$ .

The anodic conversion of methanol using transition metal catalysts like nickel, cobalt, iron and copper was investigated (see appendix figure 9.17, p. 229). Within the mentioned metals, nickel showed the highest activity and the following results will be restricted to this element. Analyzing polarization curves in figure 7.50 results in onset potentials of  $\phi_{\text{OER}} = 0.6\text{ V (vs. SHE)}$  and  $\phi_{\text{MOR}} = 0.57\text{ V (vs. SHE)}$  for an electrolyte concentration of  $[\text{KOH}] = 1\text{ M}$ , as well as of  $\phi_{\text{OER}} = 0.53\text{ V (vs. SHE)}$  and  $\phi_{\text{MOR}} = 0.47\text{ V (vs. SHE)}$  for an electrolyte concentration of  $[\text{KOH}] = 5\text{ M}$  (all determined from the forward scan). This rather disappointingly small difference between MOR and OER is unexpected when looking at the respective equilibrium potentials of  $\phi_{\text{OER}}^0 = 0.43\text{ V (vs. SHE)}$  and  $\phi_{\text{MOR}}^0 = -0.87\text{ V (vs. SHE)}$  ( $\text{pH} = 14$ ). Naturally, there are catalysts known with much higher MOR activity, e.g. platinum or palladium based ones.<sup>[156, 188]</sup> However, these metals tend to completely oxidize the reactant to CO<sub>2</sub> which makes no sense within this preparative approach. Also, the nickel catalyst shows a strong hysteresis when turning into reductive direction, which is related to the conversion of nickel into nickel(II) hydroxide.<sup>[189]</sup> This oxidic species appears to be more active for MOR, resulting in extrapolated onset potentials of

$\phi_{\text{MOR, 1M KOH}} = 0.52 \text{ V}$  (vs. SHE) and  $\phi_{\text{MOR, 5M KOH}} = 0.43 \text{ V}$  (vs. SHE). Onset potentials for OER are not influenced. The differences related to KOH concentration variation are as expected according to Nernst's equation.

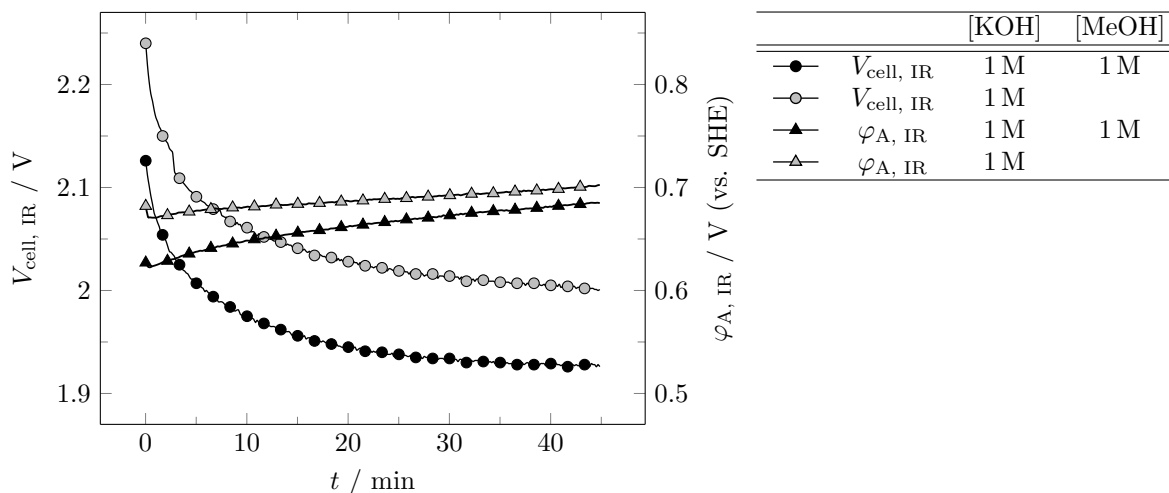


**Figure 7.51:** Course of cell voltage for coupled  $\text{CO}_2$  reduction and methanol oxidation reaction, as well as anode potential during galvanostatic electrolysis. Operating conditions: semi-batch;  $j = 200 \text{ mA cm}^{-2}$ ,  $T = 50^\circ\text{C}$ ,  $[\text{KCl}]_{\text{C}} = 2 \text{ M}$ ,  $\text{pH} = 10$ ; nickel mesh anode, standard GDE cathode.

*FEs* of the possible MOR products formaldehyde, formate and  $\text{CO}_2$ , as well as oxygen from OER were analyzed during galvanostatic operation. Results in table 7.17 show that MOR at the applied nickel-based electrocatalyst yields formate at a *FE* of 86 % with formaldehyde,  $\text{CO}_2$  and oxygen as minor side products. CO was not detected. *IR* compensated anode potentials and cell voltages were recorded in electrolytes containing 1 M potassium hydroxide either with or without additional methanol (1 M) (see figure 7.51). Both curves show opposing developments. While the anode potential rises over time, the whole cell voltage drops. This can be explained by the distinct activation phase of the cathode (standard GDE) as it was already shown in figure 7.7, p. 113. Anode potential increases with time since hydroxide ions in the batch wise added electrolyte are consumed, rising the equilibrium potential according to Nernst's equation. In a continuous process this deactivation is supposed to vanish.

The *IR* compensated cell voltage of  $\text{CO}_2\text{RR}$  and OER results in a value of 2.0 V while the  $\text{CO}_2\text{RR}/\text{MOR}$  couple is only 70 mV lower with a total of 1.93 V. Considering that the addition of methanol lowers the electrolytes conductivity by about  $20 \text{ mS cm}^{-1}$ , the non-compensated cell voltage of a flow cell is expected to be roughly the same for both couples. Hence, the only remaining benefit of using MOR instead of OER as oxidation reaction is the material issue.

The total oxidation to  $\text{CO}_2$ , which is typically the main product in AOR of direct alcohol fuel cells, is widely suppressed with the used nickel catalyst. Instead the partial oxidation to formate yields the

**Table 7.17:** Faradaic efficiencies and compensated anode potentials of methanol oxidation and oxygen evolution reaction during galvanostatic electrolysis on a nickel mesh.R/R\*: H or C<sub>n</sub>H<sub>2n+1</sub>.Operating conditions: semi-batch;  $j = 200 \text{ mA cm}^{-2}$ ,  $T = 50 \text{ }^\circ\text{C}$ .

Electrolyte	<i>FE</i> / %				$\varphi_{A, IR}$ / V (vs. SHE)
	RCOR*	RCOO <sup>-</sup>	CO <sub>2</sub>	O <sub>2</sub>	
- , 1 M KOH	0	0	0	100	0.77 - 0.84
1 M MeOH, 1 M KOH	5	86	2	7	0.67 - 0.74
1 M MeOH, 5 M KOH	6	86	3	5	0.59 - 0.64
1 M EtOH, 1 M KOH	3	74	11	12	0.65 - 0.70
1 M n-PrOH, 1 M KOH	3	80	6	11	0.64 - 0.69
1 M i-PrOH, 1 M KOH	70	-	10	20	0.64 - 0.69

highest *FE* independently of the used potassium hydroxide concentration. Due to its low stability in aqueous media formaldehyde is obtained only in small quantities. Also, water oxidation is a rather minor side reaction, as expected from the cyclic voltammograms in figure 7.50. Besides methanol, ethanol, n-propanol and i-propanol were as well investigated for their product distribution (see table 7.17). Very similar *FEs* were obtained for ethanol and n-propanol with the respective carboxylic acid anion as the main product. In general a slightly higher total oxidation rate when compared to methanol is observed, which might be attributed to differences in the adsorption of intermediates at the anode. Also, the parasitic OER is slightly increased. In contrast to these primary alcohols, oxidation of i-propanol yields acetone in large quantities. It can be suggested that the oxidation mechanism comprises a carbonic acid as intermediate, which cannot form from a secondary alcohol. Hence, the oxidation of acetone to CO needs to proceed via a four electron transfer, which is presumably slower than the two electron transfer when oxidizing an aldehyde to the respective carbonic acid.





# 8 | Conclusion and Outlook

## 8.1 Conclusion

Within the present work an energy efficient electrolysis process for the conversion of CO<sub>2</sub> to formate has been developed and demonstrated. This includes investigations on the composition of the electrocatalyst and the used gas diffusion electrode (GDE), important reaction conditions like temperature and electrolyte, as well as the cell design. Electrode composition and reaction parameters were tuned for the process to operate at maximum current density or with longest possible time on stream. Low energetic cathode efficiencies (*ECEs*) and limiting current densities typically arise for similar reasons like mass transport limitations, moderately active and/or deactivating electrocatalysts or due to unsuitable electrolytes. Hence, pushing the limiting current density to maximum values usually also benefits the *ECE*.

Nano-scaled metal oxide and palladium based electrocatalysts supported on carbon black were prepared and evaluated for their *ECE*. Both were chosen due to their great performance and integrability into the carbon support, previously demonstrated in a preceding project<sup>[19]</sup> and reported in literature<sup>[103]</sup>. An efficiency ranking was found in the order of: SnO<sub>x</sub> > PbO<sub>x</sub> > InO<sub>x</sub>. Even though tin oxide is neither the most selective nor the most active species it exhibits solid values for both. It remains the element of choice with its wide availability, cheap production costs and low toxicity.<sup>[190, 191]</sup> Two palladium based electrocatalysts were investigated as well. Despite exhibiting a much lower onset potential, their lack of selectivity (especially at higher absolute values of current density) results in a comparable or even lower *ECE* than the much cheaper tin based one.

The optimum tin oxide loading depends on the striven time of operation. During short-term operation 7.5 mg cm<sub>geo</sub><sup>-2</sup> of tin showed a maximum activity. In general, within a range of 0.25 mg cm<sub>geo</sub><sup>-2</sup> to 10 mg cm<sub>geo</sub><sup>-2</sup>, higher loadings result in an initially increased activity but deactivation effects intensify as well. A final explanation for this behavior is still missing even though several aspects could be excluded.

During long-term operation, the potentiostatic character of tin oxide and observed deactivation effects lead to an optimum tin loading of  $0.5 \text{ mg cm}_{\text{geo}}^{-2}$ .

Significant progress in the GDE's performance was achieved by fine tuning its local hydrophilicity. Replacing 43 % of the PTFE binder with a Nafion powder greatly reduced the absolute value of overpotential by as much as 160 mV at a current density of  $-1000 \text{ mA cm}^{-2}$ . Analysis of the double layer capacitance obtained with different methods for increasing the degree of wetting suggests a unique wetting behavior as cause for the improved performance. It is assumed that the addition of Nafion increases the share of wetted carbon agglomerates, while hydrophobic  $\text{CO}_2$  transport pores remain open. Hence, the local current density is lowered, mitigating mass transport related issues.

Despite being often overlooked in literature, temperature plays an important role to consider. Its influence on reaction kinetics, mass transport, catalyst deactivation and resulting long-term stability is enormous. Few present studies, focusing on a systematical temperature variation, suggest quite low values between  $0^\circ\text{C}$  and  $35^\circ\text{C}$  to promote the solubility of  $\text{CO}_2$ .<sup>[17, 26, 112, 128]</sup> However, this conclusion was found to be too short-sighted. Reaction kinetics and diffusivity are greatly accelerated by higher temperature values, which leads to an optimum at  $50^\circ\text{C}$ . Detailed investigations on reactant and product mass transport supported by a simple model revealed the underlying causes.

In conclusion, the observed optimum arises from three different aspects. Most importantly, the  $\text{CO}_2$  mass transport rate itself exhibits a maximum at  $50^\circ\text{C}$ . At lower temperatures diffusivity of  $\text{CO}_2$  is insufficient while at higher temperatures the  $\text{CO}_2$  solubility is too low. Second, at lower temperature values product mass transport becomes essential. Due to the decreasing diffusion coefficients, formate is not removed from the GDE fast enough. This effect becomes especially important at long-term operation where higher electrolyte intrusion depths are observed. Last, the reduction rate of tin oxide to less active metallic tin rises exponentially with increasing temperature. Here, a periodic oxidative polarization helps to regenerate the active oxide species and to recover selectivity.

Effects of the chosen electrolytes were less pronounced, except for different cations and highly concentrated formate/bicarbonate mixtures. While the variation of alkali metal cations showed an increasing activity with ion size, various types of anions (only alkaline ones), bulk pH (7 to 14) and the salt concentration of potassium chloride or potassium bicarbonate electrolytes (0.1 M to 2 M at pH = 10) do barely show any difference neither for activity nor for selectivity. It is assumed that a high discrepancy between local and bulk electrolyte composition is responsible for this observation. High current densities and impeded mass transfer cause high local salt concentrations, independent of changes in the bulk phase. Hence, the focus of choosing a suitable electrolyte can be set on other properties like conductivity or material costs. An exception was found for highly concentrated solutions of potassium formate/bicarbonate

mixtures ( $c_{\text{total}} \geq 2\text{ M}$ ) with native pH, which result in a collapse of performance. The respective causes were found to be a severe product mass transport limitation and, presumably, bicarbonate decomposition inside the GDE.

In conclusion, optimum reaction conditions include a temperature of  $50\text{ }^\circ\text{C}$  and an electrolyte composition of  $[\text{CsCl}] = 2\text{ M}$  at  $\text{pH} = 10$ . Combining these conditions with the mentioned Nafion/poly-(tetrafluoroethylene) (PTFE) bound GDE bearing a slightly increased tin loading of  $2\text{ mg cm}_{\text{geo}}^{-2}$  allows for a current density of  $-1500\text{ mA cm}^{-2}$  at 79 % formate faradaic efficiency (*FE*). Comparing this result with literature clarifies the tremendous potential of said electrodes. On the other hand, lowering the electrode loading to  $0.5\text{ mg cm}_{\text{geo}}^{-2}$  and doubling the electrode's thickness allows for a time on stream of at least 250 h at  $-200\text{ mA cm}^{-2}$ .

However, even though the lifetime was greatly extended, used GDEs still suffer from gradual deactivation due to ongoing electrolyte intrusion. Other than that, multiple effects that can contribute to electrode deactivation were described in the present work. Concluding the ones that have been shown to probably contribute, the ones that have been shown to improbably contribute and such that are still uncertain to contribute can be listed as follows:

Probable effects:

- Formate diffusion limitation at low temperatures ( $20\text{ }^\circ\text{C}$ ) and high intrusion depths of the electrolyte. Figure 7.14, p. 124.
- Formate diffusion limitation at  $50\text{ }^\circ\text{C}$  and elevated product concentrations ( $>0.5\text{ M}$ ). Figure 7.14, p. 124.
- Catalyst reduction to metallic tin. Figure 7.15, p. 125.
- Mechanical degradation of the GDE's matrix. Figure 7.31, p. 151.

Improbable effects:

- Intrinsic formate diffusion limitation at elevated temperatures ( $>50\text{ }^\circ\text{C}$ ) up to  $400\text{ }\mu\text{m}$  of intrusion depth. Figure 7.14, p. 124.
- Increase in hydrogen *FE* by electrodeposition of HER active heavy metals like iron. Figure 7.25, p. 141.
- Increase in hydrogen *FE* due to the lower conductivity of electrolyte filled pores compared to the GDE's matrix according to the equivalent circuit model of porous electrodes (see section 4.3.3, p, 50). Figure 7.20, p. 135.

Uncertain effects:

- Formate diffusion limitation at elevated temperatures ( $50\text{ }^\circ\text{C}$ ) and intrusion depth larger than  $400\text{ }\mu\text{m}$ .
- Severeness of  $\text{CO}_2$  mass transport limitation.
- Catalyst alteration other than reduction including leaching or agglomeration.
- Extend and temporal development of the GDE's flooded zone and its effect on mass transport limitations and  $\text{CO}_2\text{RR}$  active surface area. Figure 4.18, p. 46.

An optimized filter press type electrolysis cell with enlarged geometrical electrode area of  $70\text{ cm}^2$  was developed. From a first geometrical scale-up from  $1\text{ cm}^2$  to  $10\text{ cm}^2$  of active cathode area different voltage loss contributions were identified and tackled within the final design. First, integrating the current collector into the GDE's matrix allows for an efficient electrical contacting between outer circuit and cathode. Second, minimized ionic resistances for both cathode and anode side were ensured by reducing the electrode-electrode distance to around 4 mm. Last, integrating the anode mesh into a thin silicon sealing reduced the oxygen bubble trapping between anode and membrane. With these modifications, and applying optimal reaction conditions, a cell voltage of just 2.7 V to 3.0 V and formate *FE* of 80 % to 64 % at 14 A ( $200\text{ mA cm}^{-2}$ ) was achieved.

Finally, a potential coupling of alkaline  $\text{CO}_2$  electrolysis ( $\text{CO}_2\text{EL}$ ) with downstream bipolar membrane electrodialysis (BPED) was investigated on a fundamental basis. Its purpose is to protonate obtained formate/bicarbonates and to regenerate consumed hydroxide salts. After demonstrating the general functionality it was shown that only low formic acid concentrations of around 1 M can be obtained. Attempts to further concentrate the product to a range where distillation can be performed on an economically feasible basis failed. The main issue is that for formic acid concentrations higher than 1 M losses by cross-membrane diffusion become larger than the actual production rate.

Selective alcohol oxidation reaction (AOR) was also investigated on a proof-of-concept basis, showing a large potential. Using moderately active catalysts towards the total oxidation of light alcohols allowed for a *FE* of up to 86 % towards the respective carboxylic acid anion. Hence, when coupled with  $\text{CO}_2$  reduction reaction ( $\text{CO}_2\text{RR}$ ), methanol oxidation reaction (MOR) can double the energy efficiency (*EE*) of the  $\text{CO}_2\text{EL}$  process by doubling the *FE* towards formate.

## 8.2 Outlook

The presented kind of GDE showed great potential overcoming hurdles on the way to industrialization of CO<sub>2</sub>RR. Its capability to work efficiently at high current densities is its major benefit. Reported results are not limited to the production of formate but may also be transferred to other CO<sub>2</sub> reduction reactions. Exchanging the tin oxide catalyst with silver or copper based ones, for example, paves the way for CO, methane or alcohol synthesis. Immobilized molecular catalysts, which activate water instead of CO<sub>2</sub> and work via a hydride transfer mechanism are also conceivable for integration.

However, some fundamental issues originating from alkaline reaction conditions prevail, namely near stoichiometric bicarbonate formation and stoichiometric hydroxide consumption. Even though BPED was demonstrated to produce formic/carbonic acid and recover potassium hydroxide, it is limited to moderate formic acid concentrations. An alternative would be to operate CO<sub>2</sub>EL in acidic environment. The formic acid cross-over issue, however, prevails in a similar manner. Due to its much lower equilibrium voltage formic acid re-oxidation is greatly favored over water oxidation when diffusion to the anode is possible. Hence, some of the product is lost anyhow. For both solutions future research needs to focus on the development of membranes with low formic acid cross-over.

The developed 70 cm<sup>2</sup> filter press type electrolysis cell already showed a remarkable performance regarding its cell voltage. However, long-term stability was found to be significantly lower than for the 1 cm<sup>2</sup> cell. To investigate and solve this issue needs be one of the next steps. Also, despite being designed with the ultimate goal to create a stackable cell, a final demonstration of an electrolysis stack remains open. The developed design being operated at 200 mA cm<sup>-2</sup>, scaled-up to 110 cm<sup>2</sup> and stacking fifteen cells of around 3 V cell voltage and 80 % formate *FE*, would give a 1 kW electrolyzer with a potassium formate output of 414 g h<sup>-1</sup>.



# Bibliography

- (1) Le Quéré, C. *Earth Syst. Sci. Data* **2018**, *10*, 2141–2194, DOI: 10.5194/essd-10-2141-2018.
- (2) United Nations Kyoto Protocol to the United Nations Framework Convention on Climate Change., Japan, 1998.
- (3) Blunden, J.; Arndt, D. S. *Bull. Am. Meteorol. Soc.* **2019**, *100*, Si–S306, DOI: 10.1175/2019BAMS.
- (4) Hansen, J.; Sato, M.; Ruedy, R.; Lo, K.; Lea, D. W.; Medina-Elizade, M. *Proc. Natl. Acad. Sci. USA* **2006**, *103*, 14288–14293, DOI: 10.1073/pnas.0606291103.
- (5) REN21 Renewables 2019 Global Status Report., Paris, 2019, [www.ren21.net](http://www.ren21.net).
- (6) Bienen, F.; Kopljar, D.; Löwe, A.; Abmann, P.; Stoll, M.; Rößner, P.; Wagner, N.; Friedrich, A.; Klemm, E. *Chem. Ing. Tech.* **2019**, *91*, 872–882, DOI: 10.1002/cite.201800212.
- (7) Martín, A. J.; Larrazábal, G. O.; Pérez-Ramírez, J. *Green Chem.* **2015**, *17*, 5114–5130, DOI: 10.1039/C5GC01893E.
- (8) Scialdone, O.; Galia, A.; Lo Nero, G.; Proietto, F.; Sabatino, S.; Schiavo, B. *Electrochim. Acta* **2016**, *119*, 332–341, DOI: 10.1016/j.electacta.2016.02.079.
- (9) Yishai, O.; Lindner, S. N.; La Gonzalez de Cruz, J.; Tenenboim, H.; Bar-Even, A. *Curr. Opin. Chem. Biol.* **2016**, *35*, 1–9, DOI: 10.1016/j.cbpa.2016.07.005.
- (10) Cotton, C. A.; Claassens, N. J.; Benito-Vaquerizo, S.; Bar-Even, A. *Curr. Opin. Biotechnol.* **2019**, *62*, 168–180, DOI: 10.1016/j.copbio.2019.10.002.
- (11) Claassens, N. J.; Cotton, C. A. R.; Kopljar, D.; Bar-Even, A. *Nat. Catal.* **2019**, *2*, 437–447, DOI: 10.1038/s41929-019-0272-0.
- (12) Konishi, H.; Manabe, K. *Synlett* **2014**, *25*, 1971–1986, DOI: 10.1055/s-0033-1339136.
- (13) Leitner, W.; Brunner, H.; Brown, J. M. *J. Am. Chem. Soc.* **1993**, *115*, 152–159, DOI: 10.1021/ja00054a021.
- (14) Ostapowicz, T. G.; Schmitz, M.; Krystof, M.; Klankermayer, J.; Leitner, W. *Angew. Chem., Int. Ed. Engl.* **2013**, *52*, 12119–12123, DOI: 10.1002/anie.201304529.
- (15) Bulushev, D. A.; Zacharska, M.; Guo, Y.; Beloshapkin, S.; Simakov, A. *Catal. Commun.* **2017**, *92*, 86–89, DOI: 10.1016/j.catcom.2017.01.011.
- (16) Lee, H. J.; Kang, D.-C.; Pyen, S. H.; Shin, M.; Suh, Y.-W.; Han, H.; Shin, C.-H. *Appl. Catal., A* **2017**, *531*, 13–20, DOI: 10.1016/j.apcata.2016.11.032.
- (17) Du, D.; Lan, R.; Humphreys, J.; Tao, S. *J. Appl. Electrochem.* **2017**, *47*, 661–678, DOI: 10.1007/s10800-017-1078-x.

- (18) Lu, X.; Leung, D. Y. C.; Wang, H.; Leung, M. K. H.; Xuan, J. *ChemElectroChem* **2014**, *1*, 836–849, DOI: 10.1002/ce1c.201300206.
- (19) Kopljar, D.; Wagner, N.; Klemm, E. *Chem. Eng. Technol.* **2016**, *39*, 2042–2050, DOI: 10.1002/ceat.201600198.
- (20) Schmidt, V. M., *Elektrochemische Verfahrenstechnik: Grundlagen, Reaktionstechnik, Prozeßoptimierung*; Wiley–VCH Verlag GmbH & Co. KGaA: 2003, ISBN: 3527299580.
- (21) Bockris, J. O.; Reddy, A. K. N., *Modern Electrochemistry*; Plenum Press: New York, NY, 1970; Vol. 2, ISBN: 978-0-306-25002-6.
- (22) Bockris, J. O.; Reddy, A. K. N., *Modern Electrochemistry*; Plenum Press: New York, NY, 1970; Vol. 1, ISBN: 978-1-4615-7469-9.
- (23) Bard, A. J.; Faulkner, L. R., *Electrochemical methods: Fundamentals and applications*, 2. ed.; Wiley: Hoboken, NJ, 2001, ISBN: 9780471043720.
- (24) van der Merwe, J.; Uren, K.; van Schoor, G.; Bessarabov, D. *Int. J. Hydrogen Energy* **2014**, *39*, 14212–14221, DOI: 10.1016/j.ijhydene.2014.02.096.
- (25) Adams, R. N., *Electrochemistry at Solid Electrodes*; Marcel Dekker, INC.: New York, NY, 1969, ISBN: 9780824710057.
- (26) Endrodi, B.; Bencsik, G.; Darvas, F.; Jones, R.; Rajeshwar, K.; Janaky, C. *Prog. Energy Combust. Sci.* **2017**, *62*, 133–154, DOI: 10.1016/j.pecs.2017.05.005.
- (27) Wu, J.; Yuan, X.; Wang, H.; Blanco, M.; Martin, J.; Zhang, J. *Int. J. Hydrogen Energy* **2008**, *33*, 1735–1746, DOI: 10.1016/j.ijhydene.2008.01.013.
- (28) Hamann, C. H.; Vielstich, W., *Elektrochemie*, 4.; Wiley-VCH-Verlag GmbH & Co. KGaA: Weinheim, 2005, ISBN: 978-3-527-31068-5.
- (29) Prakash, G. S.; Viva, F. A.; Olah, G. A. *J. Power Sources* **2013**, *223*, 68–73, DOI: 10.1016/j.jpowsour.2012.09.036.
- (30) Faraday, M., *Experimental Researches in Electricity. Seventh Series*, 1834; Vol. 124, DOI: 10.1098/rstl.1834.0008.
- (31) Whipple, D. T.; Kenis, P. J. A. *J. Phys. Chem. Lett.* **2010**, *1*, 3451–3458, DOI: 10.1021/jz1012627.
- (32) Jhong, H.-R. M.; Ma, S.; Kenis, P. J. A. *Curr. Opin. Chem. Eng.* **2013**, *2*, 191–199, DOI: 10.1016/j.coche.2013.03.005.
- (33) Ma, S.; Sadakiyo, M.; Heima, M.; Luo, R.; Haasch, R. T.; Gold, J. I.; Yamauchi, M.; Kenis, P. J. A. *J. Am. Chem. Soc.* **2016**, *139*, 47–50, DOI: 10.1021/jacs.6b10740.
- (34) Reller, C.; Krause, R.; Volkova, E.; Schmid, B.; Neubauer, S.; Rucki, A.; Schuster, M.; Schmid, G. *Adv. Energy Mater.* **2017**, *7*, 1602114, DOI: 10.1002/aenm.201602114.
- (35) Sebastián, D.; Palella, A.; Baglio, V.; Spadaro, L.; Siracusano, S.; Negro, P.; Niccoli, F.; Aricò, A. S. *Electrochim. Acta* **2017**, *241*, 28–40, DOI: 10.1016/j.electacta.2017.04.119.
- (36) Lee, S.; Park, G.; Lee, J. *ACS Catal.* **2017**, *7*, 8594–8604, DOI: 10.1021/acscatal.7b02822.



- (37) Kuhl, K. P.; Cave, E. R.; Abram, D. N.; Jaramillo, T. F. *Energy Environ. Sci.* **2012**, *5*, 7050–7059, DOI: 10.1039/c2ee21234j.
- (38) König, M.; Vaes, J.; Klemm, E.; Pant, D. *iScience* **2019**, *19*, 135–160, DOI: 10.1016/j.isci.2019.07.014.
- (39) Hori, Y. In *Modern Aspects of Electrochemistry*; Vol. 42, pp 89–189, DOI: 10.1007/978-0-387-49489-0.
- (40) Reda, T.; Plugge, C. M.; Abram, N. J.; Hirst, J. *Proc. Natl. Acad. Sci. USA* **2008**, *105*, 10654–10658, DOI: 10.1073/pnas.0801290105.
- (41) Lee, S.; Ocon, J. D.; Son, Y.-i.; Lee, J. *J. Phys. Chem. C* **2015**, *119*, 4884–4890, DOI: 10.1021/jp512436w.
- (42) Wuttig, A.; Yoon, Y.; Ryu, J.; Surendranath, Y. *J. Am. Chem. Soc.* **2017**, *139*, 17109–17113, DOI: 10.1021/jacs.7b08345.
- (43) Alper, E.; Yuksel Orhan, O. *Petroleum* **2017**, *3*, 109–126, DOI: 10.1016/j.petlm.2016.11.003.
- (44) H. A. Schwarz and R. W. Dodson *J. Phys. Chem.* **1989**, *93*, 409–414, DOI: 10.1021/j100338a079.
- (45) Zhang, Q.; Xu, W.; Xu, J.; Liu, Y.; Zhang, J. *Catal. Today* **2018**, *318*, 15–22, DOI: 10.1016/j.cattod.2018.03.029.
- (46) Qiao, J.; Liu, Y.; Hong, F.; Zhang, J. *Chem. Soc. Rev.* **2014**, *43*, 631–675, DOI: 10.1039/c3cs60323g.
- (47) Zhu, D. D.; Liu, J. L.; Qiao, S. Z. *Adv. Mater.* **2016**, *28*, 3423–3452, DOI: 10.1002/adma.201504766.
- (48) Francke, R.; Schille, B.; Roemelt, M. *Chem. Rev.* **2018**, *118*, 4631–4701, DOI: 10.1021/acs.chemrev.7b00459.
- (49) Duan, X.; Xu, J.; Wei, Z.; Ma, J.; Guo, S.; Wang, S.; Liu, H.; Dou, S. *Adv. Mater.* **2017**, *29*, 1701784, DOI: 10.1002/adma.201701784.
- (50) Oloman, C.; Li, H. *ChemSusChem* **2008**, *1*, 385–391, DOI: 10.1002/cssc.200800015.
- (51) Whipple, D. T.; Finke, E. C.; Kenis, P. J. A. *Electrochem. Solid-State Lett.* **2010**, *13*, B109–B111, DOI: 10.1149/1.3456590.
- (52) Machunda, R. L.; Lee, J.; Lee, J. *Surf. Interface Anal.* **2010**, *42*, 564–567, DOI: 10.1002/sia.3245.
- (53) Agarwal, A. S.; Zhai, Y.; Hill, D.; Sridhar, N. *ChemSusChem* **2011**, *4*, 1301–1310, DOI: 10.1002/cssc.201100220.
- (54) Del Castillo, A.; Alvarez-Guerra, M.; Irabien, A. *AIChE J.* **2014**, *60*, 3557–3564, DOI: 10.1002/aic.14544.
- (55) Del Castillo, A.; Alvarez-Guerra, M.; Solla-Gullón, J.; Sáez, A.; Montiel, V.; Irabien, A. *J. CO<sub>2</sub> Util.* **2017**, *18*, 222–228, DOI: 10.1016/j.jcou.2017.01.021.
- (56) Albo, J.; Irabien, A. *J. Catal.* **2015**, *343*, 232–239, DOI: 10.1016/j.jcat.2015.11.014.

- (57) Alvarez-Guerra, M.; Quintanilla, S.; Irabien, A. *Chem. Eng. J.* **2012**, *207*, 278–284, DOI: 10.1016/j.cej.2012.06.099.
- (58) Chen, Y.; Kanan, M. W. *J. Am. Chem. Soc.* **2012**, *134*, 1986–1989, DOI: 10.1021/ja2108799.
- (59) Del Castillo, A.; Alvarez-Guerra, M.; Solla-Gullón, J.; Sáez, A.; Montiel, V.; Irabien, A. *Appl. Energy* **2015**, *157*, 165–173, DOI: 10.1016/j.apenergy.2015.08.012.
- (60) Furuya, N.; Yamazaki, T.; Shibata, M. *J. Electroanal. Chem.* **1997**, *431*, 39–41, DOI: 10.1016/S0022-0728(97)00159-9.
- (61) Irtem, E.; Andreu, T.; Parra, A.; Hernández-Alonso, M. D.; García-Rodríguez, S.; Riesco-García, J. M.; Penelas-Pérez, G.; Morante, J. R. *J. Mater. Chem. A* **2016**, *4*, 13582–13588, DOI: 10.1039/C6TA04432H.
- (62) Köleli, F.; Atilan, T.; Palamut, N.; Gizir, A. M.; Aydin, R.; Hamann, C. H. *J. Appl. Electrochem.* **2003**, *33*, 447–450, DOI: 10.1023/A:1024471513136.
- (63) Li, H.; Oloman, C. *J. Appl. Electrochem.* **2005**, *35*, 955–965, DOI: 10.1007/s10800-005-7173-4.
- (64) Li, H.; Oloman, C. *J. Appl. Electrochem.* **2006**, *36*, 1105–1115, DOI: 10.1007/s10800-006-9194-z.
- (65) Lv, W.; Zhou, J.; Bei, J.; Zhang, R.; Wang, L.; Xu, Q.; Wang, W. *Appl. Surf. Sci.* **2017**, *393*, 191–196, DOI: 10.1016/j.apsusc.2016.10.017.
- (66) Mahmood, M. N.; Masheder, D.; Harty, C. J. *J Appl Electrochem* **1987**, *17*, 1159–1170, DOI: 10.1007/BF01023599.
- (67) Sen, S.; Skinn, B.; Hall, T.; Inman, M.; Taylor, E. J.; Brushett, F. R. *MRS Adv.* **2017**, *2*, 451–458, DOI: 10.1557/adv.2016.652.
- (68) Wang, Q.; Dong, H.; Yu, H.; Yu, H. *J. Power Sources* **2015**, *279*, 1–5, DOI: 10.1016/j.jpowsour.2014.12.118.
- (69) Wang, Q.; Dong, H.; Yu, H. *J. Power Sources* **2014**, *271*, 278–284, DOI: 10.1016/j.jpowsour.2014.08.017.
- (70) Wang, Q.; Dong, H.; Yu, H. *RSC Adv.* **2014**, *4*, 59970–59976, DOI: 10.1039/C4RA10775F.
- (71) Wu, J.; Risalvato, F. G.; Ke, F.-S.; Pellechia, P. J.; Zhou, X.-D. *J. Electrochem. Soc.* **2012**, *159*, F353–F359, DOI: 10.1149/2.049207jes.
- (72) Wu, J.; Risalvato, F. G.; Ma, S.; Zhou, X.-D. *J. Mater. Chem. A* **2014**, *2*, 1647–1651, DOI: 10.1039/C3TA13544F.
- (73) Wu, J.; Sharma, P. P.; Harris, B. H.; Zhou, X.-D. *J. Power Sources* **2014**, *258*, 189–194, DOI: 10.1016/j.jpowsour.2014.02.014.
- (74) Zhang, S.; Kang, P.; Meyer, T. J. *J. Am. Chem. Soc.* **2014**, *136*, 1734–1737, DOI: 10.1021/ja4113885.
- (75) Zhao, C.; Wang, J.; Goodenough, J. B. *Electrochem. Commun.* **2016**, *65*, 9–13, DOI: 10.1016/j.elecom.2016.01.019.

- (76) Lee, W.; Kim, Y. E.; Youn, M. H.; Jeong, S. K.; Park, K. T. *Angew. Chem., Int. Ed. Engl.* **2018**, *57*, 6883–6887, DOI: 10.1002/anie.201803501.
- (77) Lei, T.; Zhang, X.; Jung, J.; Cai, Y.; Hou, X.; Zhang, Q.; Qiao, J. *Catal. Today* **2018**, *318*, 32–38, DOI: 10.1016/j.cattod.2017.10.003.
- (78) Li, H.; Oloman, C. *J. Appl. Electrochem.* **2007**, *37*, 1107–1117, DOI: 10.1007/s10800-007-9371-8.
- (79) Lu, X.; Leung, D. Y.; Wang, H.; Xuan, J. *Appl. Energy* **2017**, *194*, 549–559, DOI: 10.1016/j.apenergy.2016.05.091.
- (80) Pander, J. E.; Baruch, M. F.; Bocarsly, A. B. *ACS Catal.* **2016**, *6*, 7824–7833, DOI: 10.1021/acscatal.6b01879.
- (81) Dutta, A.; Kuzume, A.; Kaliginedi, V.; Rahaman, M.; Sinev, I.; Ahmadi, M.; Roldán Cuenya, B.; Vesztergom, S.; Broekmann, P. *Nano Energy* **2018**, *53*, 828–840, DOI: 10.1016/j.nanoen.2018.09.033.
- (82) Dutta, A.; Kuzume, A.; Rahaman, M.; Vesztergom, S.; Broekmann, P. *ACS Catal.* **2015**, *5*, 7498–7502, DOI: 10.1021/acscatal.5b02322.
- (83) Baruch, M. F.; Pander, J. E.; White, J. L.; Bocarsly, A. B. *ACS Catal.* **2015**, *5*, 3148–3156, DOI: 10.1021/acscatal.5b00402.
- (84) Alvarez-Guerra, M.; Del Castillo, A.; Irabien, A. *Chem. Eng. Res. Des.* **2014**, *92*, 692–701, DOI: 10.1016/j.cherd.2013.11.002.
- (85) Hwang, E.; Kim, H.; Park, H.; Lim, T.; Kim, Y.-T.; Ahn, S. H.; Kim, S.-K. *J. Nanosci. Nanotechnol.* **2017**, *17*, 7547–7555, DOI: 10.1166/jnn.2017.14823.
- (86) Lu, Q.; Rosen, J.; Jiao, F. *ChemCatChem* **2015**, *7*, 38–47, DOI: 10.1002/cctc.201402669.
- (87) Lupan, O.; Chow, L.; Chai, G.; Heinrich, H.; Park, S.; Schulte, A. *Phys. E* **2009**, *41*, 533–536, DOI: 10.1016/j.physe.2008.10.001.
- (88) Li, Y.; Qiao, J.; Zhang, X.; Lei, T.; Girma, A.; Liu, Y.; Zhang, J. *ChemElectroChem* **2016**, *3*, 1618–1628, DOI: 10.1002/celec.201600290.
- (89) Liu, Y.; Fan, M.; Zhang, X.; Zhang, Q.; Guay, D.; Qiao, J. *Electrochim. Acta* **2017**, *248*, 123–132, DOI: 10.1016/j.electacta.2017.07.140.
- (90) Won, D. H.; Choi, C. H.; Chung, J.; Chung, M. W.; Kim, E.-H.; Woo, S. I. *ChemSusChem* **2015**, *8*, 3092–3098, DOI: 10.1002/cssc.201500694.
- (91) Li, F.; Chen, L.; Knowles, G. P.; MacFarlane, D. R.; Zhang, J. *Angew. Chem., Int. Ed. Engl.* **2017**, *129*, 520–524, DOI: 10.1002/ange.201608279.
- (92) Gao, D.; Cai, F.; Wang, G.; Bao, X. *Curr. Opin. Green Sustainable Chem.* **2017**, *3*, 39–44, DOI: 10.1016/j.cogsc.2016.10.004.
- (93) Wang, H.; Rogach, A. L. *Chem. Mater.* **2014**, *26*, 123–133, DOI: 10.1021/cm4018248.
- (94) Dou, X.; Sabba, D.; Mathews, N.; Wong, L. H.; Lam, Y. M.; Mhaisalkar, S. *Chem. Mater.* **2011**, *23*, 3938–3945, DOI: 10.1021/cm201366z.

- (95) Li, Z.; Zhou, Y.; Yu, T.; Liu, J.; Zou, Z. *CrystEngComm* **2012**, *14*, 6462, DOI: 10.1039/c2ce25954k.
- (96) Anawati; Frankel, G. S.; Agarwal, A.; Sridhar, N. *Electrochim. Acta* **2014**, *133*, 188–196, DOI: 10.1016/j.electacta.2014.04.057.
- (97) Lee, S.; Ju, H.; Machunda, R.; Uhm, S.; Lee, J. K.; Lee, H. J.; Lee, J. *J. Mater. Chem. A* **2015**, *3*, 3029–3034, DOI: 10.1039/C4TA03893B.
- (98) Hori, Y.; Konishi, H.; Futamura, T.; Murata, A.; Koga, O.; Sakurai, H.; Oguma, K. *Electrochim. Acta* **2005**, *50*, 5354–5369, DOI: 10.1016/j.electacta.2005.03.015.
- (99) Chaplin, R.; Wragg, A. A. *J. Appl. Electrochem.* **2003**, *33*, 1107–1123, DOI: 10.1023/B:JACH.0000004018.57792.b8.
- (100) Feaster, J. T.; Shi, C.; Cave, E. R.; Hatsukade, T.; Abram, D. N.; Kuhl, K. P.; Hahn, C.; Norskov, J. K.; Jaramillo, T. F. *ACS Catal.* **2017**, *7*, 4822–4827, DOI: 10.1021/acscatal.7b00687.
- (101) Cui, C.; Han, J.; Zhu, X.; Liu, X.; Wang, H.; Mei, D.; Ge, Q. *J. Catal.* **2016**, *343*, 257–265, DOI: 10.1016/j.jcat.2015.12.001.
- (102) Gattrell, M.; Gupta, N.; Co, A. *J. Electroanal. Chem.* **2006**, *594*, 1–19, DOI: 10.1016/j.jelechem.2006.05.013.
- (103) Min, X.; Kanan, M. W. *J. Am. Chem. Soc.* **2015**, *137*, 4701–4708, DOI: 10.1021/ja511890h.
- (104) Thorson, M. R.; Siil, K. I.; Kenis, P. J. A. *J. Electrochem. Soc.* **2012**, *160*, F69–F74, DOI: 10.1149/2.052301jes.
- (105) Frumkin, A. Z. *Phys. Chem., Abt. A* **1930**, *3*, 121–133, DOI: 10.1515/zpch-1933-16411.
- (106) Hori, Y.; Suzuki, S. *Bull. Chem. Soc. Jpn.* **1982**, *55*, 660–665, DOI: 10.1246/bcsj.55.660.
- (107) Kilic, M. S.; Bazant, M. Z.; Ajdari, A. *Phys. Rev. E* **2007**, *75*, 021502, DOI: 10.1103/PhysRevE.75.021502.
- (108) Singh, M. R.; Kwon, Y.; Lum, Y.; Ager, J. W.; Bell, A. T. *J. Am. Chem. Soc.* **2016**, *138*, 13006–13012, DOI: 10.1021/jacs.6b07612.
- (109) Ayemoba, O.; Cuesta, A. *ACS Appl. Mater. Interfaces* **2017**, *9*, 27377–27382, DOI: 10.1021/acsmi.7b07351.
- (110) Li, Y. C.; Lee, G.; Yuan, T.; Wang, Y.; Nam, D.-H.; Wang, Z.; García de Arquer, F. P.; Lum, Y.; Dinh, C.-T.; Voznyy, O.; Sargent, E. H. *ACS Energy Lett.* **2019**, *4*, 1427–1431, DOI: 10.1021/acsenerylett.9b00975.
- (111) Burdyny, T.; Smith, W. A. *Energy Environ. Sci.* **2019**, *12*, 1442–1453, DOI: 10.1039/C8EE03134G.
- (112) Kim, H.-Y.; Choi, I.; Ahn, S. H.; Hwang, S. J.; Yoo, S. J.; Han, J.; Kim, J.; Park, H.; Jang, J. H.; Kim, S.-K. *Int. J. Hydrogen Energy* **2014**, *39*, 16506–16512, DOI: 10.1016/j.ijhydene.2014.03.145.
- (113) Schouten, K. J. P.; Pérez Gallent, E.; Koper, M. T. *J. Electroanal. Chem.* **2014**, *716*, 53–57, DOI: 10.1016/j.jelechem.2013.08.033.

- (114) Varela, A. S.; Kroschel, M.; Reier, T.; Strasser, P. *Catal. Today* **2016**, *260*, 8–13, DOI: 10.1016/j.cattod.2015.06.009.
- (115) Gao, D.; Scholten, F.; Roldan Cuenya, B. *ACS Catal.* **2017**, *7*, 5112–5120, DOI: 10.1021/acscatal.7b01416.
- (116) Varela, A. S.; Ju, W.; Reier, T.; Strasser, P. *ACS Catal.* **2016**, *6*, 2136–2144, DOI: 10.1021/acscatal.5b02550.
- (117) Ogura, K.; Ferrell, J. R.; Cugini, A. V.; Smotkin, E. S.; Salazar-Villalpando, M. D. *Electrochim. Acta* **2010**, *56*, 381–386, DOI: 10.1016/j.electacta.2010.08.065.
- (118) Le Nguyen, D. T.; Jee, M. S.; Won, D. H.; Oh, H.-S.; Min, B. K.; Hwang, Y. J. *Catal. Commun.* **2018**, *114*, 109–113, DOI: 10.1016/j.catcom.2018.06.020.
- (119) Hong, S.; Lee, S.; Kim, S.; Lee, J. K.; Lee, J. *Catal. Today* **2017**, *295*, 82–88, DOI: 10.1016/j.cattod.2017.05.063.
- (120) Verma, S.; Lu, X.; Ma, S.; Masel, R. I.; Kenis, P. J. A. *Phys. Chem. Chem. Phys.* **2016**, *18*, 7075–7084, DOI: 10.1039/c5cp05665a.
- (121) Gurudayal, G.; Bullock, J.; Srankó, D. F.; Towle, C. M.; Lum, Y.; Hettick, M.; Scott, M. C.; Javey, A.; Ager, J. *Energy Environ. Sci.* **2017**, *10*, 2222–2230, DOI: 10.1039/C7EE01764B.
- (122) Ma, L.; Fan, S.; Zhen, D.; Wu, X.; Liu, S.; Lin, J.; Huang, S.; Chen, W.; He, G. *Ind. Eng. Chem. Res.* **2017**, *56*, 10242–10250, DOI: 10.1021/acs.iecr.7b00819.
- (123) Zhong, H.; Fujii, K.; Nakamo, Y. *J. Electrochem. Soc.* **2017**, *164*, 923–927, DOI: 10.1149/2.0601709jes.
- (124) Duan, Z.; Sun, R. *Chem. Geol.* **2003**, *193*, 257–271, DOI: 10.1016/S0009-2541(02)00263-2.
- (125) Cadogan, S. P.; Hallett, J. P.; Maitland, G. C.; Trusler, J. P. M. *J. Chem. Eng. Data* **2014**, *60*, 181–184, DOI: 10.1021/je5009203.
- (126) Carmo, M.; Fritz, D. L.; Mergel, J.; Stolten, D. *Int. J. Hydrogen Energy* **2013**, *38*, 4901–4934, DOI: 10.1016/j.ijhydene.2013.01.151.
- (127) Azuma, M. *J. Electrochem. Soc.* **1990**, *137*, 1772–1778, DOI: 10.1149/1.2086796.
- (128) Dufek, E. J.; Lister, T. E.; McIlwain, M. E. *J. Appl. Electrochem.* **2011**, *41*, 623–631, DOI: 10.1007/s10800-011-0271-6.
- (129) Harned, H. S.; Raymond JR., D. *J. Am. Chem. Soc.* **1943**, *10*, 2030–2037, DOI: 10.1021/ja01250a059.
- (130) A. A. Unver and D. M. Himmelblau *J. Chem. Eng. Data* **1964**, *9*, 428–431, DOI: 10.1021/je60022a043.
- (131) A. Tamimi; Edward B. Rinker; and Orville C. Sandall *J. Chem. Eng. Data* **1994**, *39*, 330–332, DOI: 10.1021/je00014a031.
- (132) Cadogan, S. P.; Maitland, G. C.; Trusler, J. P. M. *J. Chem. Eng. Data* **2014**, *59*, 519–525, DOI: 10.1021/je401008s.

- (133) Hara, K.; Kudo, A.; Sakata, T. *J. Electroanal. Chem.* **1995**, *386*, 257–260, DOI: 10.1016/0022-0728(95)03917-6.
- (134) Löwe, A.; Rieg, C.; Hierlemann, T.; Salas, N.; Kopljar, D.; Wagner, N.; Klemm, E. *ChemElectroChem* **2019**, *6*, 4497–4506, DOI: 10.1002/ce1c.201900872.
- (135) Kraysberg, A.; Ein-Eli, Y. *Energy Fuels* **2014**, *28*, 7303–7330, DOI: 10.1021/ef501977k.
- (136) Bidault, F.; Brett, D.; Middleton, P. H.; Brandon, N. P. *J. Power Sources* **2009**, *187*, 39–48, DOI: 10.1016/j.jpowsour.2008.10.106.
- (137) Pinnow, S.; Chavan, N.; Turek, T. *J. Appl. Electrochem.* **2011**, *41*, 1053–1064, DOI: 10.1007/s10800-011-0311-2.
- (138) D. Kopljar, unpublished dissertation, Stuttgart: University of Stuttgart.
- (139) K. Tomantschger, K. V., Kordesch *J. Power Sources* **1989**, *25*, 195–214, DOI: 10.1016/0378-7753(89)80004-7.
- (140) Singh, M.; Vander Wal, R. *C* **2019**, *5*, 1–12, DOI: 10.3390/c5010002.
- (141) Wang, X. L.; Zhang, H. M.; Zhang, J. L.; Xu, H. F.; Tian, Z. Q.; Chen, J.; Zhong, H. X.; Liang, Y. M.; Yi, B. L. *Electrochim. Acta* **2006**, *51*, 4909–4915, DOI: 10.1016/j.electacta.2006.01.048.
- (142) Lundblad, A.; Björnbom, P. *J. Electrochem. Soc.* **1994**, *141*, 1503–1508, DOI: 10.1149/1.2054953.
- (143) Pander, J. E.; Ren, D.; Yeo, B. S. *Catal. Sci. Technol.* **2017**, *7*, 5820–5832, DOI: 10.1039/C7CY01785E.
- (144) Yu, L.; Akolkar, R. *J. Electroanal. Chem.* **2017**, *792*, 61–65, DOI: 10.1016/j.jelechem.2017.03.037.
- (145) Kubannek, F.; Turek, T.; Krewer, U. *Chem. Ing. Tech.* **2019**, *91*, 720–733, DOI: 10.1002/cite.201800181.
- (146) McCrory, C. C. L.; Jung, S.; Peters, J. C.; Jaramillo, T. F. *J. Am. Chem. Soc.* **2013**, *135*, 16977–16987, DOI: 10.1021/ja407115p.
- (147) Ferrer, J. J.; Laborie, S.; Durand, G.; Rakib, M. *J. Membr. Sci.* **2006**, *280*, 509–516, DOI: 10.1016/j.memsci.2006.02.012.
- (148) J. S. Jaime-Ferrer; E. Couallier; Ph. Viers; G. Durand; M. Rakib *J. Membr. Sci.* **2008**, *325*, 528–536, DOI: 10.1016/j.memsci.2008.07.059.
- (149) Jaime-Ferrer, J. S.; Couallier, E.; Viers, P.; Rakib, M. *J. Membr. Sci.* **2009**, *328*, 75–80, DOI: 10.1016/j.memsci.2008.10.058.
- (150) Kevin Schnabel, Plinke GmbH, KBR: 02.06.2020.
- (151) Alibaba.com, 20.08.2019, www.alibaba.com.
- (152) Lister, T. E.; Dufek, E. J. *Energy Fuels* **2013**, *27*, 4244–4249, DOI: 10.1021/ef302033j.
- (153) Liu, Y.; Shu, C.; Fang, Y.; Chen, Y.; Liu, Y. *J. Power Sources* **2017**, *361*, 160–169, DOI: 10.1016/j.jpowsour.2017.06.062.

- (154) Pagliaro, M. V.; Bellini, M.; Bevilacqua, M.; Filippi, J.; Folliero, M. G.; Marchionni, A.; Miller, H. A.; Oberhauser, W.; Caporali, S.; Innocenti, M.; Vizza, F. *RSC Adv.* **2017**, *7*, 13971–13978, DOI: 10.1039/C7RA00044H.
- (155) Chen, Y. X.; Lavacchi, A.; Miller, H. A.; Bevilacqua, M.; Filippi, J.; Innocenti, M.; Marchionni, A.; Oberhauser, W.; Wang, L.; Vizza, F. *Nat. Commun.* **2014**, *5*, 4036, DOI: 10.1038/ncomms5036.
- (156) Liu, J.; Ye, J.; Xu, C.; Jiang, S. P.; Tong, Y. *J. Power Sources* **2008**, *177*, 67–70, DOI: 10.1016/j.jpowsour.2007.11.015.
- (157) Drogui, P.; Elmaleh, S.; Rumeau, M.; Bernard, C.; Rambaud, A. *J. Appl. Electrochem.* **2001**, *31*, 877–882, DOI: 10.1023/A:1017588221369.
- (158) Song, K. C.; Kang, Y. *Mater. Lett.* **2000**, *42*, 283–289, DOI: 10.1016/S0167-577X(99)00199-8.
- (159) Nguyen, H., master thesis, University of Stuttgart, 2018.
- (160) 3M corp., 2020, [www.3m.com](http://www.3m.com).
- (161) Tinkerforge GmbH, 18.05.2020, [www.tinkerforge.com](http://www.tinkerforge.com).
- (162) Bronkhorst High-Tech B.V. *Instruction manual* **2019**, 1–39.
- (163) Inan, A. Experimentelle Untersuchungen zur technischen Machbarkeit der elektrochemischen CO<sub>2</sub>-Reduktion., Dissertation, Stuttgart: University of Stuttgart, 2019.
- (164) Gao, D.; Zhou, H.; Cai, F.; Wang, J.; Wang, G.; Bao, X. *ACS Catal.* **2018**, *8*, 1510–1519, DOI: 10.1021/acscatal.7b03612.
- (165) Zhang, R.; Lv, W.; Lei, L. *Appl. Surf. Sci.* **2015**, *356*, 24–29, DOI: 10.1016/j.apsusc.2015.08.006.
- (166) Adegoke, K. A.; Radhakrishnan, S. G.; Gray, C. L.; Sowa, B.; Morais, C.; Rayess, P.; Rohwer, E. R.; Comminges, C.; Kokoh, K. B.; Roduner, E. *Sustainable Energy & Fuels* **2020**, *4*, 4030–4038, DOI: 10.1039/D0SE00623H.
- (167) Gao, D.; Zhou, H.; Cai, F.; Wang, D.; Hu, Y.; Jiang, B.; Cai, W.-B.; Chen, X.; Si, R.; Yang, F.; Miao, S.; Wang, J.; Wang, G.; Bao, X. *Nano Res.* **2017**, *10*, 2181–2191, DOI: 10.1007/s12274-017-1514-6.
- (168) Rahaman, M.; Dutta, A.; Broekmann, P. *ChemSusChem* **2017**, *10*, 1733–1741, DOI: 10.1002/cssc.201601778.
- (169) Zhou, F.; Li, H.; Fournier, M.; Macfarlane, D. *ChemSusChem* **2017**, *10*, 1509–1516, DOI: 10.1002/cssc.201601870.
- (170) Rajendra Prasad, K.; Miura, N. *Electrochem. Commun.* **2004**, *6*, 849–852, DOI: 10.1016/j.elecom.2004.06.009.
- (171) Osaka, T.; Liu, X.; Nojima, M. *J. Power Sources* **1998**, *74*, 122–128, DOI: 10.1016/S0378-7753(98)00043-3.
- (172) Kestin, J.; Sokolov, M.; Wakeham, W. A. *J. Phys. Chem. Ref. Data* **1978**, *7*, 941–948, DOI: 10.1063/1.555581.

- (173) Vargaftik, N. B.; Volkov, B. N.; Voljak, L. D. *J. Phys. Chem. Ref. Data* **1983**, *12*, 817–820, DOI: 10.1063/1.555688.
- (174) Caley, E. R.; Elving, P. J. In *Inorganic Synthesis*, Booth, H. S., Ed.; McGraw-Hill, Inc.: 1939; Vol. 1, pp 1–2, ISBN: 9780470131602.
- (175) Koter, S.; Piotrowski, P.; Kerres, J. *J. Membr. Sci.* **1999**, *153*, 83–90, DOI: 10.1016/S0376-7388(98)00242-7.
- (176) statista.de, 09.08.2019, [www.statista.de](http://www.statista.de).
- (177) IFA - Gestis Stoffdatenbank, 12.10.2019, [gestis.itrust.de](http://gestis.itrust.de).
- (178) IFA - Gestis Stoffdatenbank, 12.10.2019, [gestis.itrust.de](http://gestis.itrust.de).
- (179) Kucka, L.; Kenig, E. Y.; Górak, A. *Ind. Eng. Chem. Res.* **2002**, *41*, 5952–5957, DOI: 10.1021/ie020452f.
- (180) Wang, B. *J. Power Sources* **2005**, *152*, 1–15, DOI: 10.1016/j.jpowsour.2005.05.098.
- (181) Sun, S.; Shao, Z.; Yu, H.; Li, G.; Yi, B. *J. Power Sources* **2014**, *267*, 515–520, DOI: 10.1016/j.jpowsour.2014.05.117.
- (182) Zeng, K.; Zhang, D. *Prog. Energy Combust. Sci.* **2010**, *36*, 307–326, DOI: 10.1016/j.pecs.2009.11.002.
- (183) Blom, M. J.; Smulders, V.; van Swaaij, W. P.; Kersten, S. R.; Mul, G. *Appl. Catal., B* **2019**, *268*, 118420, DOI: 10.1016/j.apcatb.2019.118420.
- (184) Lee, C. H.; Kanan, M. W. *ACS Catal.* **2015**, *5*, 465–469, DOI: 10.1021/cs5017672.
- (185) Díaz-Sainz, G.; Alvarez-Guerra, M.; Solla-Gullón, J.; García-Cruz, L.; Montiel, V.; Irabien, A. *J. CO<sub>2</sub> Util.* **2019**, *34*, 12–19, DOI: 10.1016/j.jcou.2019.05.035.
- (186) Yang, H.; Kaczur, J. J.; Sajjad, S. D.; Masel, R. I. *J. CO<sub>2</sub> Util.* **2017**, *20*, 208–217, DOI: 10.1016/j.jcou.2017.04.011.
- (187) Fumatech BWT GmbH, 2019, [www.fumatech.com](http://www.fumatech.com).
- (188) Zhou, L.; Zhao, Z. L.; Zhang, L. Y.; An, H. M.; Li, C. M. *ChemistrySelect* **2017**, *2*, 6317–6322, DOI: 10.1002/slct.201701379.
- (189) Abdel Rahim, M. A.; Abdel Hameed, R. M.; Khalil, M. W. *J. Power Sources* **2004**, *134*, 160–169, DOI: 10.1016/j.jpowsour.2004.02.034.
- (190) Sabin, A. E.; Bleiwas, D. I.; Peterson, U. S. *Nat. Resour. Forum* **1986**, *10*, 165–203, DOI: 10.1111/j.1477-8947.1986.tb00090.x.
- (191) De Groot, A.; Feron, V.; Til, H. *Food Chem. Toxicol.* **1973**, *11*, 19–30, DOI: 10.1016/0015-6264(73)90058-8.
- (192) NIST, <https://webbook.nist.gov/>.







# List of Figures

4.1	Schematic illustration of an electrolysis cell. . . . .	14
4.2	Illustration of different electrical double layer models and respective course of electric potential on a negatively polarized electrode. . . . .	16
4.3	Electrode arrangement and points of measurement in a three electrode configuration. . .	17
4.4	Contributions of activation, concentration and ohmic overpotential to the electrode potential as function of current density. . . . .	19
4.5	Randle's equivalent circuit with idealized course of voltage and current after current interruption. . . . .	20
4.6	Gibb's free energy for the transition of an electron from a negatively polarized electrode to a charge carrier in the electrolyte. . . . .	21
4.7	The dependence of current density on overpotential according to Butler-Volmer. . . . .	23
4.8	Schematic illustration of multiple cells being stacked in a filter press. . . . .	26
4.9	Schematic illustration of an electrolysis cell converting CO <sub>2</sub> and potassium hydroxide into the respective formate/bicarbonate salt mixture and oxygen. . . . .	28
4.10	Pourbaix diagram for hydrogen evolution and various CO <sub>2</sub> reduction reaction products. .	30
4.11	Pourbaix diagram for CO <sub>2</sub> reduction to formic acid/formate and oxygen evolution reaction. .	31
4.12	Summary of faradaic efficiencies to formate, energetic cathode efficiencies and energy efficiencies reported in literature over the respective current density. . . . .	32
4.13	Pourbaix diagram of tin. . . . .	33
4.14	Mechanisms of different CO <sub>2</sub> reduction reaction pathways. . . . .	36
4.15	Influence of temperature on the CO <sub>2</sub> solubility in 2 M aqueous sodium chloride solution and on the CO <sub>2</sub> diffusion coefficient in water. . . . .	42
4.16	Chemical structure of poly-(tetrafluoroethylene) and Nafion. . . . .	44
4.17	Schematic illustration of different types of gas diffusion electrodes. . . . .	45
4.18	Schematic representation of the used homogeneous single-layer gas diffusion electrodes with different scenarios for electrode wetting. . . . .	46

4.19	Idealized electrocapillary curve with surface tension as function of the electrode potential.	48
4.20	Equivalent circuit model of porous electrodes, illustrating different pathways for electricity from outer circuit into the bulk electrolyte. . . . .	52
4.21	Three and two compartment configuration of bipolar membrane electro dialysis for formic acid and potassium hydroxide production from potassium formate. . . . .	55
4.22	Pourbaix diagram of different oxidation reactions with resulting equilibrium cell voltages when coupled with CO <sub>2</sub> reduction reaction to formic acid/formate. . . . .	57
6.1	Piping and instrumentation diagram of the whole setup installed for the present work. . .	69
6.2	Exploded view of the developed 1 cm <sup>2</sup> standard gas diffusion electrode test cell. . . . .	72
6.3	Exploded view of the developed 10 cm <sup>2</sup> first stage scale-up cell. . . . .	73
6.4	Detail and exploded view of the developed 70 cm <sup>2</sup> second stage scale-up cell. . . . .	74
6.5	Current density profile during fast hydrogen selectivity screening. . . . .	84
6.6	Exploded view of the developed bipolar membrane electro dialysis cell. . . . .	91
6.7	Piping and instrumentation diagram of the setup used to investigate the protonation of formate/bicarbonate mixtures in the bipolar membrane electro dialysis cell. . . . .	92
6.8	Exploded view of the cell used for investigating the selective alcohol oxidation. . . . .	94
6.9	Exploded view of the cell used for coupling CO <sub>2</sub> reduction reaction and alcohol oxidation reaction. . . . .	94
7.1	Polarization curves of the standard gas diffusion electrode prepared from different batches of catalyst synthesis. . . . .	102
7.2	Polarization curves for different metals/metal oxides, supported on acetylene black. . . .	106
7.3	Polarization curves for two palladium based gas diffusion electrodes with different loadings on a pre-oxidized Vulcan XC 72 support, compared to the standard gas diffusion electrode. . . . .	108
7.4	Scanning and transmission electron microscopy images of tin oxide loaded acetylene black.	111
7.5	Course of current density during potentiostatic preconditioning for different electrode loadings and polarization curves obtained immediately after potentiostatic preconditioning.	112
7.6	Double layer capacitance of gas diffusion electrodes with electrode loadings between 0.5 mg cm <sub>geo</sub> <sup>-2</sup> to 10 mg cm <sub>geo</sub> <sup>-2</sup> after potentiostatic preconditioning and time dependent double layer capacitance for a loading of 10 mg cm <sub>geo</sub> <sup>-2</sup> . . . . .	113
7.7	Course of cathode potential over time and average hydrogen faradaic efficiency at a current density of -200 mA cm <sup>-2</sup> for different electrode loadings. . . . .	113

---

7.8	Long-term performance analysis for different electrode loadings. . . . .	115
7.9	Polarization curves obtained at different temperatures from a single electrode and course of current density as function of temperature. . . . .	118
7.10	Average faradaic efficiencies for the three main products over current density at different temperatures. . . . .	119
7.11	Double layer capacitance obtained after potentiostatic and galvanostatic electrolysis, compared to the relative viscosity and surface tension of water over temperature. . . . .	120
7.12	Hydrogen faradaic efficiency over current density as indicator for CO <sub>2</sub> and formate transport limitation at different temperatures. . . . .	121
7.13	Long-term performance analysis for different temperatures. . . . .	123
7.14	Course of hydrogen faradaic efficiency for different feed formate concentrations and temperatures, as well as course of double layer capacitance, both over time on stream. . . . .	124
7.15	Cyclic voltammograms and resulting tin oxidation charge obtained after 24 h of galvanostatic electrolysis at $-200 \text{ mA cm}^{-2}$ for different temperatures. . . . .	125
7.16	Polarization curves obtained from different metal chloride based electrolytes. . . . .	126
7.17	Long-term performance analysis of potassium and sodium chloride based electrolytes at different concentrations. . . . .	129
7.18	Polarization curves for different anions of the electrolyte. . . . .	130
7.19	Polarization curves for different concentrations of the pH and CO <sub>2</sub> buffering salt potassium bicarbonate and the non-buffering salt potassium chloride. . . . .	134
7.20	Course of hydrogen faradaic efficiency over time on stream for different potassium chloride concentrations. . . . .	135
7.21	Hydrogen faradaic efficiency for different electrolytes at high concentrations. . . . .	135
7.22	Volumetric CO <sub>2</sub> flow resulting from potassium bicarbonate decomposition at different temperatures and pH values in comparison to the hydrogen faradaic efficiency obtained at the respective conditions. . . . .	137
7.23	Cathode potential and CO <sub>2</sub> volume fraction in the outlet gas stream, both over time at different CO <sub>2</sub> feed volume fractions. . . . .	138
7.24	Comparison of polarization curves of CO <sub>2</sub> , nitrogen or synthetic air feed. . . . .	140
7.25	Course of hydrogen faradaic efficiency over time on stream for different salt and solvent grades. . . . .	141
7.26	Performance of the GDE for different contents of Nafion and PTFE in the electrode's binder. . . . .	144

7.27	Performance comparison between GDE's bound with pure PTFE and an optimum Nafion/PTFE mixture of $m_{\text{Nafion}}/m_{\text{Binder}} = 0.43$ at different current densities. . . . .	145
7.28	Formate and hydrogen faradaic efficiencies over the double layer capacitance obtained from PTFE bound GDEs with different concentrations of surfactant (TritonX) added to the electrolyte, compared to Nafion/PTFE bound GDEs without additional surfactant. . .	146
7.29	Limiting current densities for different optimizations, compared with the state of the art.	148
7.30	Long-term performance analysis for different electrode compositions. . . . .	150
7.31	Scanning electron microscopy cross-sectional imaging with elemental analysis of a gas diffusion electrode after 48 h of time on stream. . . . .	151
7.32	Performance recovery by 30 min of oxidative polarization compared to an open circuit break. . . . .	152
7.33	Long-term performance analysis for lead or tin loaded GDEs. . . . .	153
7.34	Long-term performance analysis at different current densities using the standard gas diffusion electrode, compared to an increased tin loading. . . . .	154
7.35	Course of cathode potential during galvanostatic electrolysis. The electrode was either not preconditioned or ramped up by a linear galvanodynamic scan with different scan rates.	155
7.36	Course of cathode potential with active time on stream during interrupted electrolysis. . .	156
7.37	Course of cathode potential for interrupted electrolysis with either an open circuit break or a standby current being applied for 30 min. . . . .	157
7.38	Course of cathode potential and resulting drop during the break for interrupted electrolysis with either $-1 \text{ mA cm}^{-2}$ being applied as standby current or with an open circuit break of different periods of time. . . . .	158
7.39	Course of cathode potential for interrupted electrolysis with either an open circuit break or a standby current of $-1 \text{ mA cm}^{-2}$ being applied for 30 min. . . . .	159
7.40	Long-term performance analysis for gas diffusion electrodes prepared from differently sized PTFE powders of various matrix shares. . . . .	162
7.41	Faradaic efficiencies of the three main products over current density for standard $1 \text{ cm}^2$ and $10 \text{ cm}^2$ gas diffusion electrodes of different matrix compositions. . . . .	163
7.42	Visualization and listing of voltage drop contributions at $j = 200 \text{ mA cm}^{-2}$ between both outer circuit connections. . . . .	166
7.43	Visualization and listing of voltage drop contributions at different current densities between both outer circuit connections. . . . .	167

---

7.44	Performance analysis for the 70 cm <sup>2</sup> filter press type cell in comparison to the 1 cm <sup>2</sup> standard GDE test cell. . . . .	168
7.45	Potential coupling of alkaline CO <sub>2</sub> electrolysis with bipolar membrane electro dialysis. . . . .	172
7.46	Course of hydrogen faradaic efficiency over time on stream for formate/bicarbonate 1:1 mixtures of different concentrations. . . . .	174
7.47	Course of hydrogen faradaic efficiency over time on stream for different electrolyte mixtures (1:1) with varied operating conditions. . . . .	175
7.48	Long-term performance analysis of a standard and optimized gas diffusion electrode in a 1:1 potassium formate/bicarbonate mixture with a total concentration of 2 M. . . . .	175
7.49	Three compartment configuration of bipolar membrane electro dialysis for formic acid/carbonic acid and potassium hydroxide production. . . . .	176
7.50	Cyclic voltammograms of a fine nickel mesh in electrolytes with 1 M and 5 M potassium hydroxide with or without 1 M methanol added. . . . .	179
7.51	Course of cell voltage for coupled CO <sub>2</sub> reduction and methanol oxidation reaction, as well as anode potential during galvanostatic electrolysis. . . . .	180
9.1	Illustration of issues occurring during potentiostatic preconditioning. . . . .	217
9.2	Conformity of consecutively recorded polarization curves. . . . .	218
9.3	Course of open circuit potential over time with two possible outcomes of subsequently measured non-faradaic cyclic voltammograms, depending on the time of open circuit. . . . .	219
9.4	Illustration of a typical double layer capacitance measurement. . . . .	219
9.5	X-ray diffractograms obtained from the unsupported but equally treated metal oxides. . . . .	220
9.6	Transmission electron microscopy images of both supported palladium catalysts. . . . .	221
9.7	Cyclic voltammograms obtained after 30 min of preconditioning at a certain cathode potential for a tin loading of 1 mg cm <sub>geo</sub> <sup>-2</sup> and 10 mg cm <sub>geo</sub> <sup>-2</sup> . . . . .	222
9.8	Cross section scanning electron microscopy/X-ray emission spectroscopy element mapping of a standard GDE after 45 min of operation. . . . .	223
9.9	Long-term performance analysis for different feed formate concentrations at 50 °C. . . . .	223
9.10	Long-term performance analysis for different feed formate concentrations at 20 °C. . . . .	224
9.11	Long-term performance analysis for different electrolyte concentrations. . . . .	225
9.12	Long-term performance analysis for different salt grades. . . . .	225
9.13	Long-term performance analysis for different solvent grades. . . . .	226
9.14	Cyclic voltammograms obtained before and after applying an oxidizing potential of 0.64 V (vs. SHE) for 30 min. . . . .	227

9.15 Long-term performance analysis for formate/bicarbonate 1:1 mixtures of different concentrations. . . . .	228
9.16 Long-term performance analysis for formate/bicarbonate 1:1 mixtures with varied operating conditions and electrolyte composition. . . . .	229
9.17 Cyclic voltammograms of different metals in electrolytes containing 1 M potassium hydroxide and 1 M methanol. . . . .	229



# List of Tables

1	List of abbreviations. . . . .	V
2	List of symbols. . . . .	VIII
3	List of indices. . . . .	X
4	List of constants. . . . .	XI
6.1	Overview of important characteristics for all three electrochemical cells developed within the present work. . . . .	71
6.2	Instrumental parameters of the conventional GC (7890A) and $\mu$ -GC (G3581A) used within the present work. . . . .	75
6.3	Instrumental parameters of the HPLC (1260 Infinity II) used within the present work for both offline and online analysis. . . . .	76
6.4	Overview of the experimental routine used for determining electrode activity and degree of wetting in semi-batch mode of operation. . . . .	80
6.5	Overview of the experimental routines used for determining product distribution, energetic efficiencies and degree of wetting in semi-batch or continuous mode of operation. . . . .	81
7.1	Faradaic efficiencies, compensated cathode potentials and energetic cathode efficiencies with their standard deviation within and between different batches of catalyst synthesis at moderate current density. . . . .	99
7.2	Faradaic efficiencies, compensated cathode potentials and energetic cathode efficiencies with their standard deviation for different adjustments in the measurement protocol at high current density. . . . .	101
7.3	Faradaic efficiencies, compensated cathode potentials and energetic cathode efficiencies with their standard deviation/error within and between different batches of catalyst synthesis at high current density. . . . .	101
7.4	Current densities obtained at certain compensated cathode potentials and respective standard deviation/error within and between different batches of catalyst synthesis. . . . .	103

7.5	Measured double layer capacitance and respective standard deviation/error within and between different batches of catalyst synthesis. . . . .	103
7.6	Faradaic efficiencies, compensated cathode potentials and energetic cathode efficiencies of different metal/metal oxide catalysts at different current densities. . . . .	107
7.7	Double layer capacitances, current densities, faradaic efficiencies and energetic cathode efficiencies obtained at certain overpotentials for palladium based catalysts in comparison to the standard gas diffusion electrode. . . . .	110
7.8	Effect of temperature on the limiting current density. . . . .	122
7.9	Faradaic efficiencies, compensated cathode potential and energetic cathode efficiency for different alkali metal chlorides at a moderate and highly mass transport limited current density of $-200 \text{ mA cm}^{-2}$ and $-700 \text{ mA cm}^{-2}$ . . . . .	126
7.10	Contributions of electrode potentials, electrolyte and membrane resistance ( <i>IR</i> drop) to the total cell voltage for sodium and potassium containing electrolytes. . . . .	127
7.11	Comparison of molar energy consumption and the resulting savings in electricity rate, as well as material costs for sodium and potassium salts. . . . .	128
7.12	Faradaic efficiencies, compensated cathode potentials, equilibrium potentials and respective overpotentials, as well as energetic cathode efficiencies for different pH values at a moderate and high current density. . . . .	132
7.13	Faradaic efficiencies and compensated cathode potentials for reduced feed $\text{CO}_2$ volume fractions. . . . .	139
7.14	Faradaic efficiencies, compensated cathode potentials and energetic cathode efficiencies with their standard deviation/error within and between differently sized and stirred catalyst synthesis batches at high current density. . . . .	161
7.15	Individual and total energy consumptions and costs per tonne of 85 wt-% formic acid with bipolar membrane electrodialysis and distillation as post-electrolysis process. . . .	173
7.16	Summary of set input electrolytes and measured changes in concentration in compartments C2 and C4 related to the unintentional diffusion of formic acid out of compartment C3. . . . .	178
7.17	Faradaic efficiencies and compensated anode potentials of methanol oxidation and oxygen evolution reaction during galvanostatic electrolysis on a nickel mesh. . . . .	181
9.1	List of salts, alcohols and solvents used for the preparation of electrolytes. . . . .	211
9.2	List of chemicals and materials used within the present work. . . . .	212
9.3	Thermodynamic data for reactants and products described within the present work. . . .	213

9.4	List of thermodynamic data and respective standard potentials vs the standard hydrogen electrode for different reactions described within the present work. . . . .	214
9.5	Faradaic efficiencies, compensated cathode potentials and energetic cathode efficiencies at different catholyte concentrations and current densities. . . . .	224



## 9 | Appendix

**Table 9.1:** List of salts, alcohols and solvents used for the preparation of electrolytes.

	<b>Chemical</b>	<b>Purity</b>	<b>Supplier</b>
		$\geq 99.5\%$ , Ph.Eur.	
	KCl	$\geq 99.5\%$ , ACS	Carl Roth
		$\geq 99.995\%$ , 4N5	
		$\geq 85\%$ , Ph.Eur.	
	KOH	$\geq 99.98\%$ , ACS	Carl Roth
		$\geq 99.98\%$ , 3N8	
Salts	KHCOO	$\geq 98\%$ , syn.	
	KHCO <sub>3</sub>	$\geq 99.5\%$ , p.a.	
	NaCl	$\geq 99.5\%$ , ACS	
	RbCl	$\geq 99.5\%$ , p.a.	
	CsCl	$\geq 99.999\%$ , p.a.	
	NaOH	$\geq 98\%$ , p.a.	Carl Roth
	K <sub>2</sub> CO <sub>3</sub>	$\geq 99\%$ , p.a.	
	K <sub>2</sub> HPO <sub>4</sub>	$\geq 98\%$	
	KHSO <sub>4</sub>	$\geq 99\%$ , p.a.	
	KBr	$\geq 99\%$ , p.a.	
	KI	$\geq 99.5\%$ , p.a.	
	Formic acid	$\geq 98\%$ , p.a., ACS	
Alcohols	Methanol	$\geq 99.5\%$ , p.a.	
	Ethanol	$\geq 99.5\%$ , p.a.	Fluka
	1-Propanol	$\geq 99.5\%$ , p.a.	
	i-Propanol	$\geq 99.5\%$ , p.a.	
Solvents		HPLC grade	Carl Roth
	Water	DI	In-house preparation
		DD	

**Table 9.2:** List of chemicals and materials used within the present work.

	<b>Chemical</b>	<b>Purity</b>	<b>Supplier</b>
Supports	acetylene black (100 % compressed)	$\geq 99\%$	Alfa Aesar
	Vulcan XC 72	-	Cabot
Binders	PTFE (TF 92070Z and TF 2053Z)	-	Dyneon
	Nafion	-	DuPont
Catalyst precursor	$\text{SnCl}_2 \cdot 2 \text{H}_2\text{O}$	$\geq 99.99\%$	Carl Roth
	$\text{SnCl}_4 \cdot 5 \text{H}_2\text{O}$	$\geq 98\%$	
	$\text{SnCl}_4$	$\geq 99.99\%$	Sigma Aldrich
	$\text{PbCl}_2$	$\geq 99\%$	Strem Chemicals
	$\text{InCl}_3$	$\geq 99.99\%$	Alfa Aesar
	$\text{Pd}(\text{NO}_3)_2 \cdot 2\text{H}_2\text{O}$	$\approx 40\%$ Pd	Sigma Aldrich
Synthesis auxiliaries	SDS	$\geq 99\%$	Sigma Aldrich
	Urea	$\geq 99.5\%$	Carl Roth
Gas diffusion media	Sigracet Graphite GDL 39AA	-	Ion Power
Gases	$\text{CO}_2$	4.5	Westfalen AG
	$\text{N}_2$	5.0	
	He	4.6	
	Ar	5.0	
Cell components	ABS cell accessory parts	-	Prusa Research
	Stainless steel current collector	-	
	Nickel mesh anode ( $d = 0.14 \text{ mm}$ , mesh = 0.5 mm)	$\geq 99.2\%$	Haver & Boecker
	Stainless steel mesh anode ( $d = 0.2 \text{ mm}$ , mesh = 0.5 mm)	$\geq 99.5\%$	Metallwaren-Riffert
	Copper mesh anode ( $d = 0.2 \text{ mm}$ , mesh = 0.63 mm)	$\geq 80\%$	Sigma Aldrich
HPLC eluent	Water	HPLC grade	Carl Roth
	$\text{H}_2\text{SO}_4$	$\geq 98\%$	Sigma Aldrich
Membranes	Nafion 117	-	DuPont
	FKB-PK-130	-	Fumatech BWT GmbH
	FAB-PK-130	-	
	FBM-PK	-	

## 9.1 Carbon dioxide reduction reaction - Standard potential calculation

For a general chemical equation (CEq) like:



the standard Gibb's free energy ( $\Delta_R G^\theta$ ) is given by:

$$\Delta_R G^\theta = \Delta_R H^\theta - T \Delta_R S^\theta \quad (9.1.1)$$

with the standard reaction enthalpy ( $\Delta_R H^\theta$ ) and the standard reaction entropy ( $\Delta_R S^\theta$ ), which again can be calculated from the sum of all standard formation enthalpies and standard entropies ( $\Delta_f H_i^\theta$  and  $S_i^\theta$ ) of the involved substances  $i$ . The stoichiometric factors  $v_i$  are thereby negative for reactants and positive for products.

$$\Delta_R H^\theta = \sum |v_i| \cdot \Delta_f H_i^\theta \quad (9.1.2)$$

$$\Delta_R S^\theta = \sum |v_i| \cdot S_i^\theta \quad (9.1.3)$$

**Table 9.3:** Thermodynamic data for reactants and products described within the present work.<sup>[192]</sup>

Substance	$\Delta_f H^\theta$	$S^\theta$
	/ kJ mol <sup>-1</sup>	/ J mol <sup>-1</sup> K
CH <sub>4</sub>	-74.6	188.7
Cl <sub>2</sub>	0	223.1
CO	-110.5	197.6
CO <sub>2</sub>	-393.5	213.8
H <sub>2</sub>	0	130.7
H <sub>2</sub> O	-285.8	69.9
HCl	-92.3	186.9
HCOOH	-425.0	131.0
O <sub>2</sub>	0	205.1
CH <sub>3</sub> OH	-238.4	127.2
C <sub>2</sub> H <sub>5</sub> OH	-276.0	160.0
C <sub>3</sub> H <sub>7</sub> OH	-303	193
CH <sub>3</sub> COOH	-484.00	158.00
C <sub>2</sub> H <sub>5</sub> COOH	-510	191

**Table 9.4:** List of thermodynamic data and respective standard potentials vs the standard hydrogen electrode for different reactions described within the present work.<sup>[192]</sup>

Reaction	$\Delta_R H^\theta$ / kJ mol <sup>-1</sup>	$\Delta_R S^\theta$ / J mol <sup>-1</sup> K	$\Delta_R G^\theta$ / kJ mol <sup>-1</sup>	$\phi^\theta$ / V (vs. SHE)
$\text{CO}_2 + 2\text{H}^+ + 2\text{e}^- \rightleftharpoons \text{HCOOH}$				
$\text{CO}_2 + \text{H}_2 \rightleftharpoons \text{HCOOH}$	-31.5	-82.8	-6.83	-0.166
$\text{CO}_2 + 2\text{H}^+ + 2\text{e}^- \rightleftharpoons \text{CO} + \text{H}_2\text{O}$				
$\text{CO}_2 + \text{H}_2 \rightleftharpoons \text{CO} + \text{H}_2\text{O}$	-2.8	53.7	-18.81	-0.104
$\text{CO}_2 + 8\text{H}^+ + 8\text{e}^- \rightleftharpoons \text{CH}_4 + 2\text{H}_2\text{O}$				
$\text{CO}_2 + 4\text{H}_2 \rightleftharpoons \text{CH}_4 + 2\text{H}_2\text{O}$	-252.7	114.7	-286.89	0.170
$\frac{1}{2}\text{O}_2 + 2\text{H}^+ + 2\text{e}^- \rightleftharpoons \text{H}_2\text{O}$				
$\frac{1}{2}\text{O}_2 + \text{H}_2 \rightleftharpoons \text{H}_2\text{O}$	285.8	163.3	237.12	1.229
$\text{HCOOH} + 4\text{H}^+ + 4\text{e}^- \rightleftharpoons \text{CH}_3\text{OH} + \text{H}_2\text{O}$				
$\text{HCOOH} + 2\text{H}_2 \rightleftharpoons \text{CH}_3\text{OH} + \text{H}_2\text{O}$	-99.2	-195.3	-41.00	0.106
$\text{CH}_3\text{COOH} + 4\text{H}^+ + 4\text{e}^- \rightleftharpoons \text{C}_2\text{H}_5\text{OH} + \text{H}_2\text{O}$				
$\text{CH}_3\text{COOH} + 2\text{H}_2 \rightleftharpoons \text{C}_2\text{H}_5\text{OH} + \text{H}_2\text{O}$	-77.8	-189.5	-21.33	0.055
$\text{C}_2\text{H}_5\text{COOH} + 4\text{H}^+ + 4\text{e}^- \rightleftharpoons \text{C}_3\text{H}_7\text{OH} + \text{H}_2\text{O}$				
$\text{C}_2\text{H}_5\text{COOH} + 2\text{H}_2 \rightleftharpoons \text{C}_3\text{H}_7\text{OH} + \text{H}_2\text{O}$	-78.8	-189.5	-22.33	0.058



## 9.2 Preparation methods - Additional derivations

### 9.2.1 Preparation of the supported catalyst

The total mass of precursor  $m_{\text{prec}}$  added for loading the carbon black with the metal Me can be calculated by:

$$m_{\text{prec}} = m_{\text{prec, GDE}} \cdot \frac{V_{\text{f, solvent}}}{V_{\text{f, el, GDE}}} \quad (9.2.1)$$

$$= \frac{n_{\text{prec, GDE}}}{M_{\text{prec}}} \cdot V_{\text{f, solvent}} \cdot \frac{c_{\text{prec}}}{n_{\text{prec, GDE}}} \quad (9.2.2)$$

$$= c_{\text{prec}} \cdot M_{\text{prec}} \cdot V_{\text{f, solvent}} \quad (9.2.3)$$

The amount of carbon black per GDE was set to  $38 \text{ mg cm}_{\text{geo}}^{-2}$  for historical reasons. Under the condition that  $n_{\text{prec}} = n_{\text{Me}}$ , the mass of carbon black per synthesis batch is given by:

$$m_{\text{CB}} = 38 \text{ mg cm}_{\text{geo}}^{-2} \cdot A_{\text{geo}} \cdot \frac{V_{\text{f, solvent}}}{V_{\text{f, el, GDE}}} \quad (9.2.4)$$

$$= 38 \text{ mg cm}_{\text{geo}}^{-2} \cdot A_{\text{geo}} \cdot V_{\text{f, solvent}} \cdot \frac{c_{\text{prec}}}{n_{\text{prec, GDE}}} \quad (9.2.5)$$

$$= 38 \text{ mg cm}_{\text{geo}}^{-2} \cdot A_{\text{geo}} \cdot V_{\text{f, solvent}} \cdot \frac{c_{\text{prec}}}{n_{\text{Me, GDE}}} \quad (9.2.6)$$

$$= 38 \text{ mg cm}_{\text{geo}}^{-2} \cdot A_{\text{geo}} \cdot V_{\text{f, solvent}} \cdot c_{\text{prec}} \cdot \frac{M_{\text{Me}}}{m_{\text{Me, GDE}}} \quad (9.2.7)$$

$$= 38 \text{ mg cm}_{\text{geo}}^{-2} \cdot A_{\text{geo}} \cdot V_{\text{f, solvent}} \cdot c_{\text{prec}} \cdot \frac{M_{\text{Me}}}{\sigma_{\text{Me, GDE}} \cdot A_{\text{geo}}} \quad (9.2.8)$$

$$= \frac{38 \text{ mg cm}_{\text{geo}}^{-2} \cdot V_{\text{f, solvent}} \cdot c_{\text{prec}} \cdot M_{\text{Me}}}{\sigma_{\text{Me}}} \quad (9.2.9)$$

The mass of urea added for precipitation is simply given by:

$$m_{\text{urea}} = n_{\text{urea}} \cdot M_{\text{urea}} \quad (9.2.10)$$

$$= c_{\text{urea}} \cdot V_{\text{f, solvent}} \cdot M_{\text{urea}} \quad (9.2.11)$$

### 9.2.2 Preparation of gas diffusion electrodes

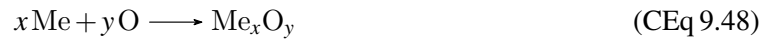
The mass of catalyst loaded carbon black used for a single GDE can be calculated by the sum of carbon black and the deposited catalyst. Note that, even though loading refers to the mass of catalyst in its metallic state, a metal oxide is present, whose mass has to be considered as follows:

$$m_{\text{Me}_x\text{O}_y+\text{CB}} = m_{\text{CB}} + m_{\text{Me}_x\text{O}_y} \quad (9.2.12)$$

$$= A_{\text{geo}} \cdot 38 \text{ mg cm}_{\text{geo}}^{-2} + m_{\text{Me}_x\text{O}_y} \quad (9.2.13)$$

$$= A_{\text{geo}} \cdot 38 \text{ mg cm}_{\text{geo}}^{-2} + n_{\text{Me}_x\text{O}_y} \cdot M_{\text{Me}_x\text{O}_y} \quad (9.2.14)$$

with the general expression:



$n_{\text{Me}_x\text{O}_y}$  is connected to  $n_{\text{Me}}$  by:

$$\frac{1}{V_x} n_{\text{Me}} = n_{\text{Me}_x\text{O}_y} \quad (9.2.15)$$

which leads to:

$$m_{\text{Me}_x\text{O}_y+\text{CB}} = A_{\text{geo}} \cdot 38 \text{ mg cm}_{\text{geo}}^{-2} + \frac{1}{V_x} \cdot n_{\text{Me}} \cdot M_{\text{Me}_x\text{O}_y} \quad (9.2.16)$$

$$= A_{\text{geo}} \cdot 38 \text{ mg cm}_{\text{geo}}^{-2} + \frac{1}{V_x} \cdot \frac{m_{\text{Me}}}{M_{\text{Me}}} \cdot M_{\text{Me}_x\text{O}_y} \quad (9.2.17)$$

$$(9.2.18)$$

substituting  $m_{\text{Me}}$  with the metal loading  $\sigma_{\text{Me}}$  finally results in:

$$m_{\text{Me}_x\text{O}_y+\text{CB}} = A_{\text{geo}} \cdot 38 \text{ mg cm}_{\text{geo}}^{-2} + \frac{1}{V_x} \cdot \frac{\sigma_{\text{Me}} \cdot A_{\text{geo}}}{M_{\text{Me}}} \cdot M_{\text{Me}_x\text{O}_y} \quad (9.2.19)$$

### 9.3 Electroanalytical methods - Supporting explanations

The first two elements of the activity-wetting analysis sequence are potentiostatic preconditioning steps. They are necessary to achieve a defined and sufficient wetting of the GDE for further electrochemical analysis. Without this preconditioning step, no significant current is measured in low potential ranges (e.g. LSV or CV measurements), as the highly hydrophobic GDE does not allow for a sufficient degree of wetting. Empirically, values of  $-1.66$  V (vs. SHE) and  $-1.36$  V (vs. SHE) were found to be a good compromise for most conditions. The first step (2 min at  $-1.66$  V (vs. SHE)) is necessary to quickly seal the GDE and stop the crossover of  $\text{CO}_2$  gas into the catholyte chamber. Such bubbling through would cause fluctuations in the electrochemical active surface area (ECSA) and result in a low reproducibility. The second step is performed immediately after the first one and is necessary to achieve a decent degree of wetting. For this second step (30 min at  $-1.36$  V (vs. SHE)) two basic problems can occur. First, if for any reason high currents are reached during this phase a deactivation can set in, e.g. by mechanical degradation or for catalyst related reasons. Second, the other extreme meaning very low current densities causes an insufficient sealing of the electrode against leaking  $\text{CO}_2$ . Hence, bubbles form in front of the electrode, periodically changing the geometrical active area. If the set potential is too high, deactivation occurs for highly active reaction conditions. Setting the potential too low will result the described

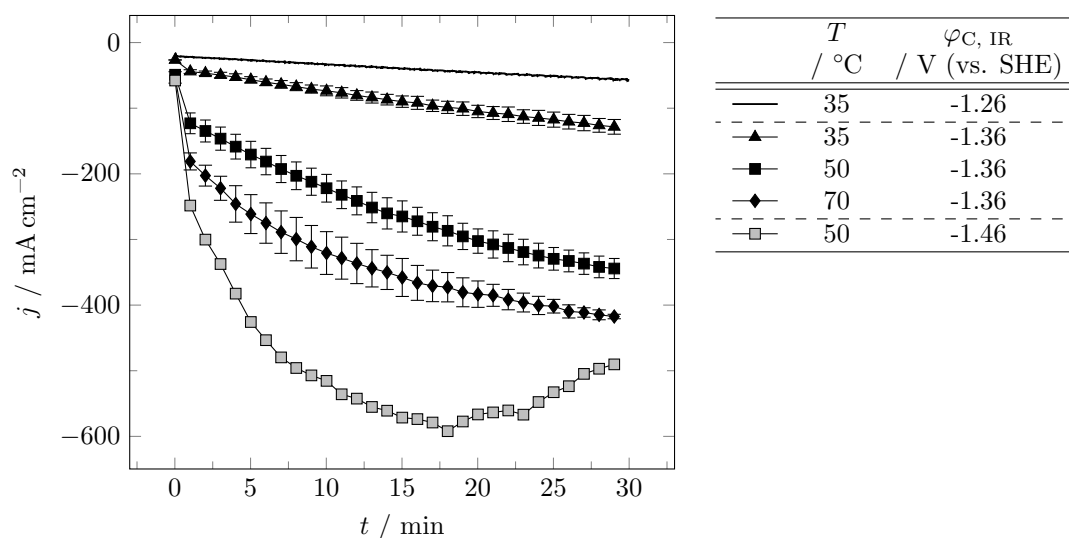


**Figure 9.1:** Illustration of issues occurring during potentiostatic preconditioning. Low temperatures and moderate cathode potentials (no marks) result in very low current densities which cannot keep the electrode sealed. This allows for  $\text{CO}_2$  crossover into the catholyte chamber, periodically changing the surface area. Elevated temperatures and higher cathode potentials (open squares), on the other hand, result in too high current densities at which a deactivation is observed.

Operating conditions: semi-batch;  $[\text{KHCO}_3] = 2$  M,  $\text{pH} = 10$ ; standard GDE.

bubbling-through for moderately active conditions. Figure 9.1 shows the measured current density over time during the second preconditioning step at different conditions.

Polarization curves in terms of linear sweep voltammetry (LSVs) were recorded within the activity-wetting analysis sequence and for evaluating the influence of temperature. For the latter, multiple scans are performed successively. The legitimate question arises whether these LSV scans distort subsequent measurements. Evaluation of four consecutive scans performed at identical reaction conditions shows that this question can be negated. A slight decrease in activity is observed but is supposed to arise from retrieving electrolyte during periods of no or little potential being applied.

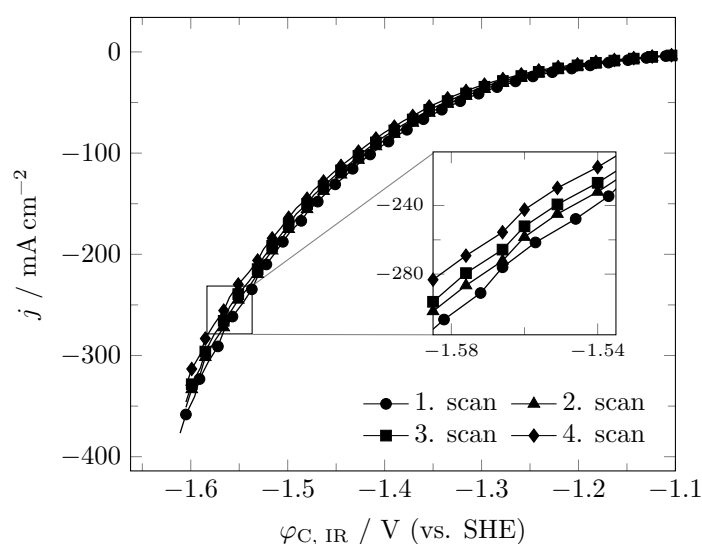


**Figure 9.2:** Conformity of consecutively recorded polarization curves.  
Operating conditions: semi-batch;  $T = 35\text{ }^{\circ}\text{C}$ ,  $[\text{KHCO}_3] = 2\text{ M}$ ,  $\text{pH} = 10$ ; standard GDE.

In order to record undisturbed non-faradaic cyclic voltammograms to assess the double layer capacitance ( $C_{\text{DL}}$ ), the absolute value of open circuit potential (OCP) has to decline to at least 400 mV (vs. SHE) beforehand. When the time of OCP between LSV and the non-faradaic cyclic voltammetry (CV) measurements is chosen to be little (scenario a) in figure 9.3 non-faradaic cyclic voltammograms will show a non-parallel behavior, which is essential for determining the  $C_{\text{DL}}$ . Only after reaching the said absolute value of OCP (scenario b) in figure 9.3) obtained curves will be evaluable. This observation is of pure empirical nature and, until now, the underlying cause cannot be given.

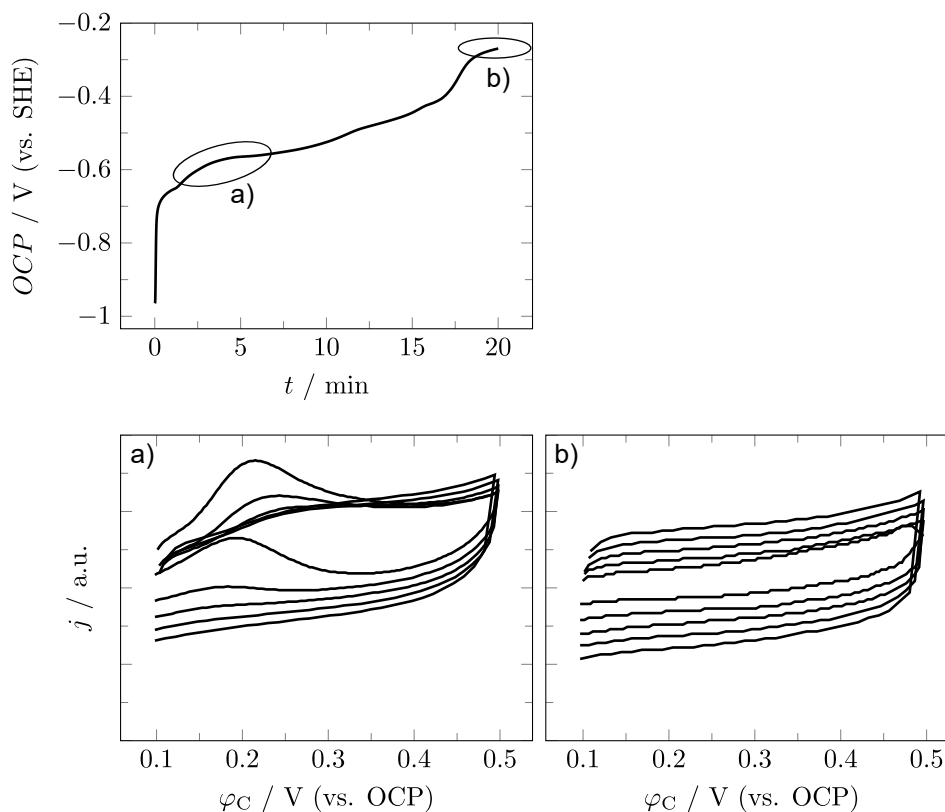


**Figure 9.3:** Course of open circuit potential over time with two possible outcomes of subsequently measured non-faradaic cyclic voltammograms, depending on the time of open circuit.

An illustration of a typical  $C_{DL}$  measurement is given in figure 9.4. The used range in potential allows recording undisturbed double layer charging currents, visible by parallel, nearly horizontal lines. Plotting the current density obtained at  $\varphi_C = 0.3$  V (vs. OCP) over the respective scan rate gives the shown linear regression line. Its slope is the  $C_{DL}$ .

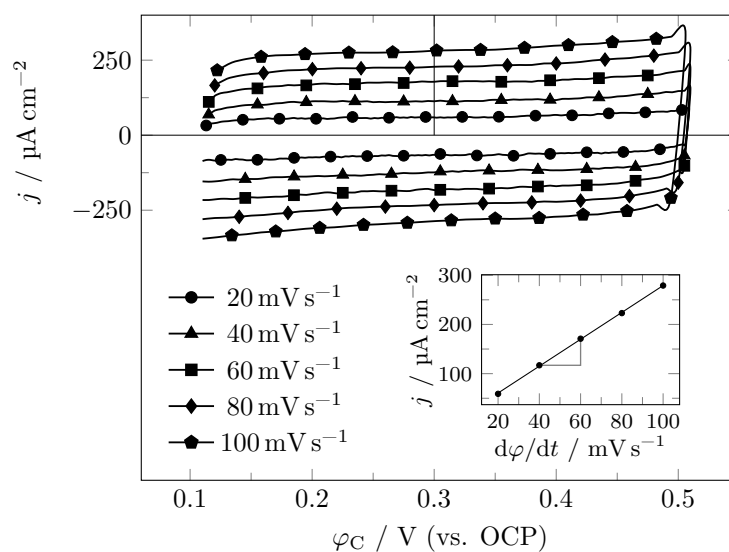


**Figure 9.4:** Illustration of a typical double layer capacitance measurement.

## 9.4 Investigations on the catalyst

### 9.4.1 Type of catalyst

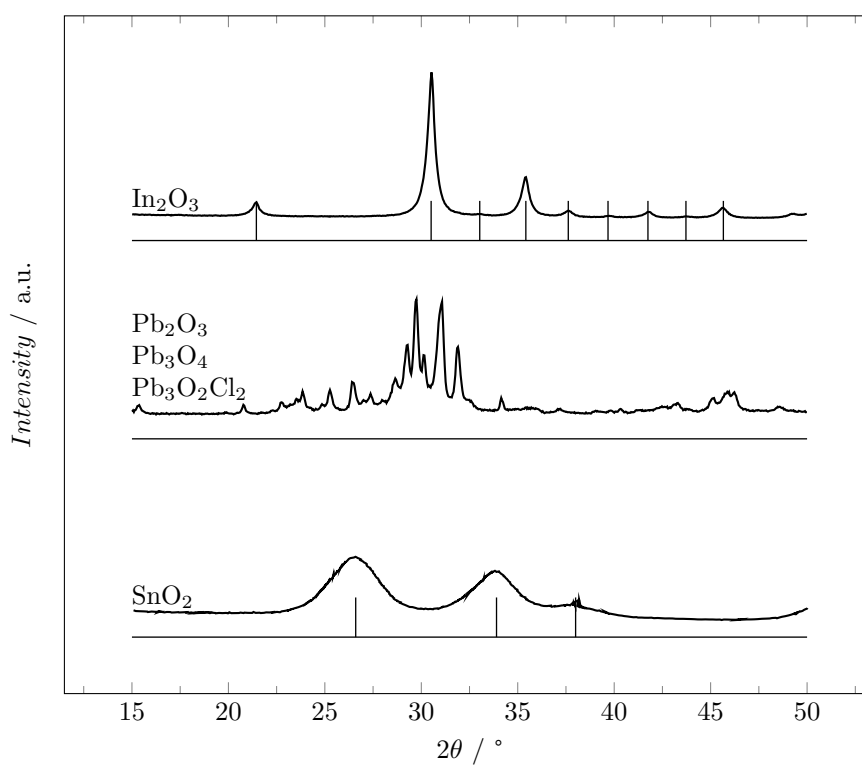


**Figure 9.5:** X-ray diffractograms obtained from the unsupported but equally treated metal oxides.

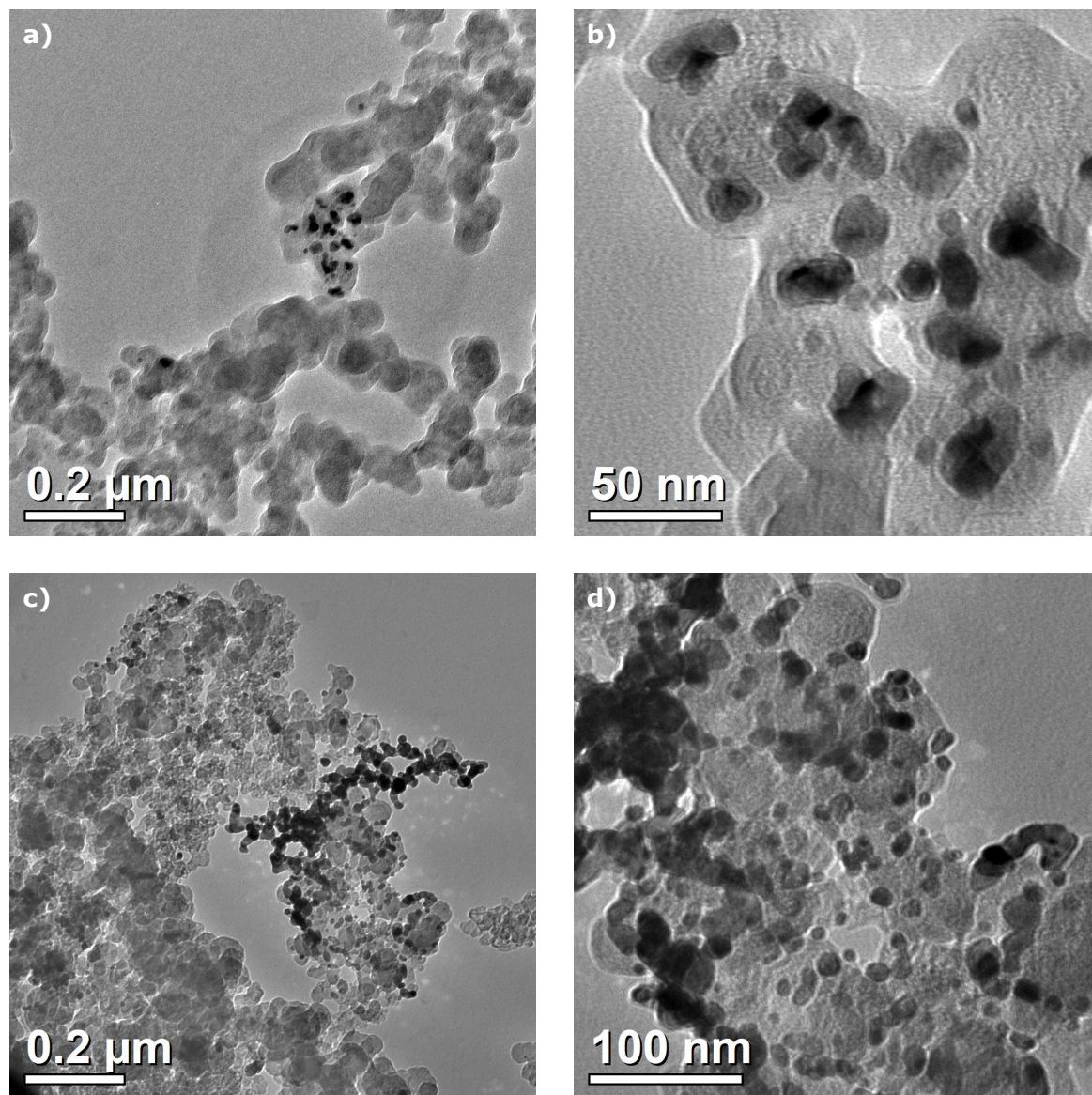


**Figure 9.6:** Transmission electron microscopy images of both supported palladium catalysts.  
a) + b) 0.5Pd/VX<sub>ox</sub>; c) + d) 3.3Pd/VX<sub>ox</sub>.

## 9.4.2 Tin oxide loading - Estimations on the quantity of metallic tin

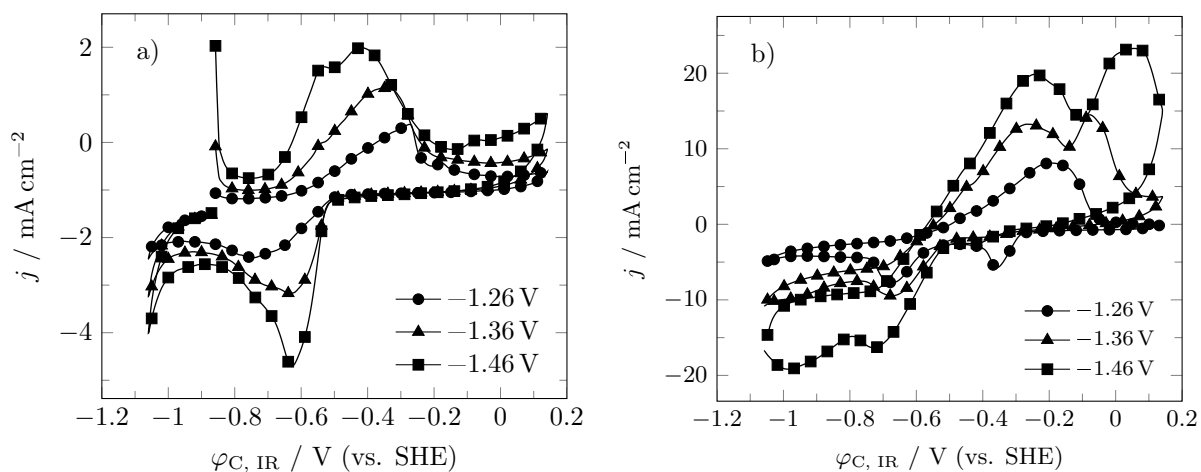


**Figure 9.7:** Cyclic voltammograms obtained after 30 min of preconditioning at a certain cathode potential for a tin loading of a) 1 mg cm<sup>-2</sup><sub>geo</sub> and b) 10 mg cm<sup>-2</sup><sub>geo</sub>.



## 9.5 Investigations on process conditions

### 9.5.1 The effect of temperature

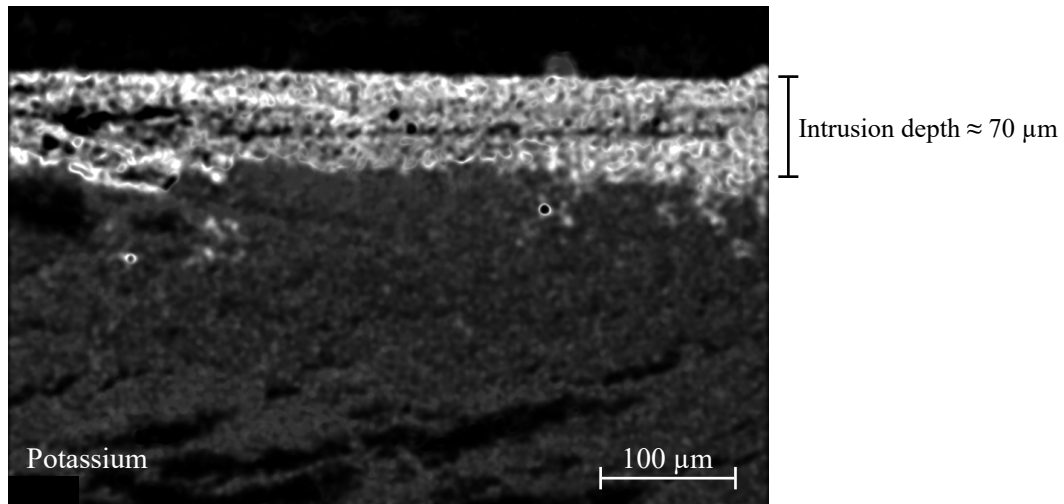


**Figure 9.8:** Cross section scanning electron microscopy/X-ray emission spectroscopy element mapping of a standard GDE after 45 min of operation. Operating conditions: semi-batch;  $j = -200 \text{ mA cm}^{-2}$ ,  $T = 35 \text{ }^\circ\text{C}$ ,  $[\text{KHCO}_3] = 2 \text{ M}$ ,  $\text{pH} = 10$ .

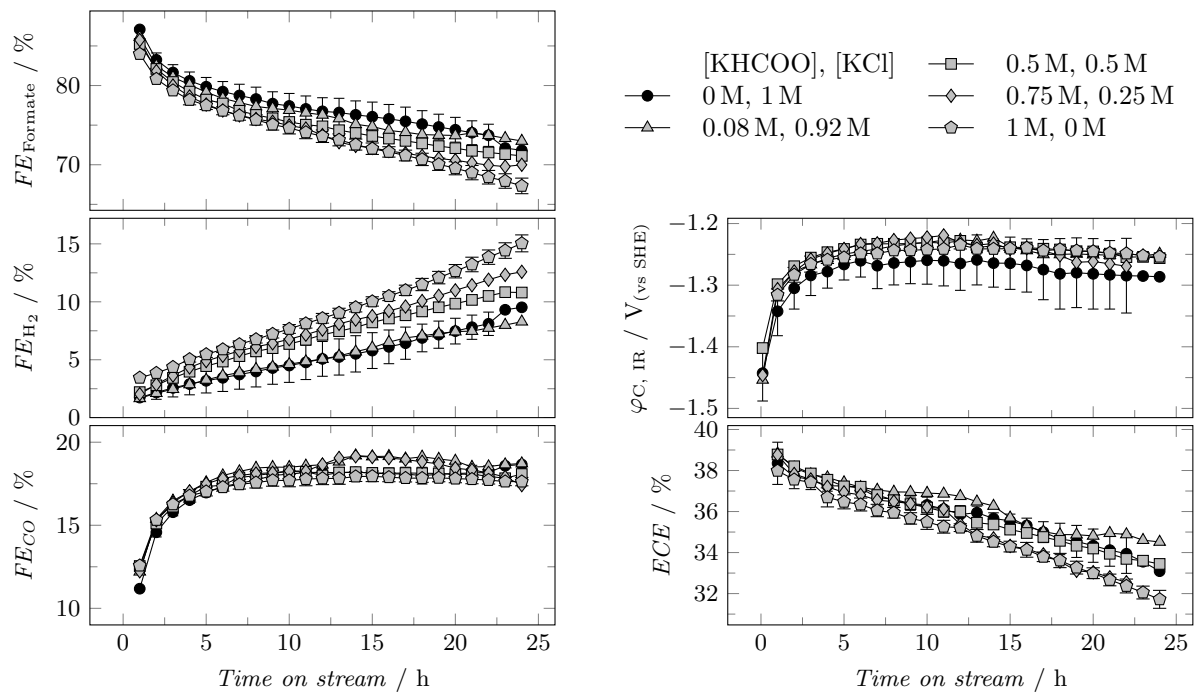


**Figure 9.9:** Long-term performance analysis for different feed formate concentrations at  $50 \text{ }^\circ\text{C}$ . Operating conditions: continuous;  $j = -200 \text{ mA cm}^{-2}$ ,  $\text{pH} = 10$ ; Standard GDE.

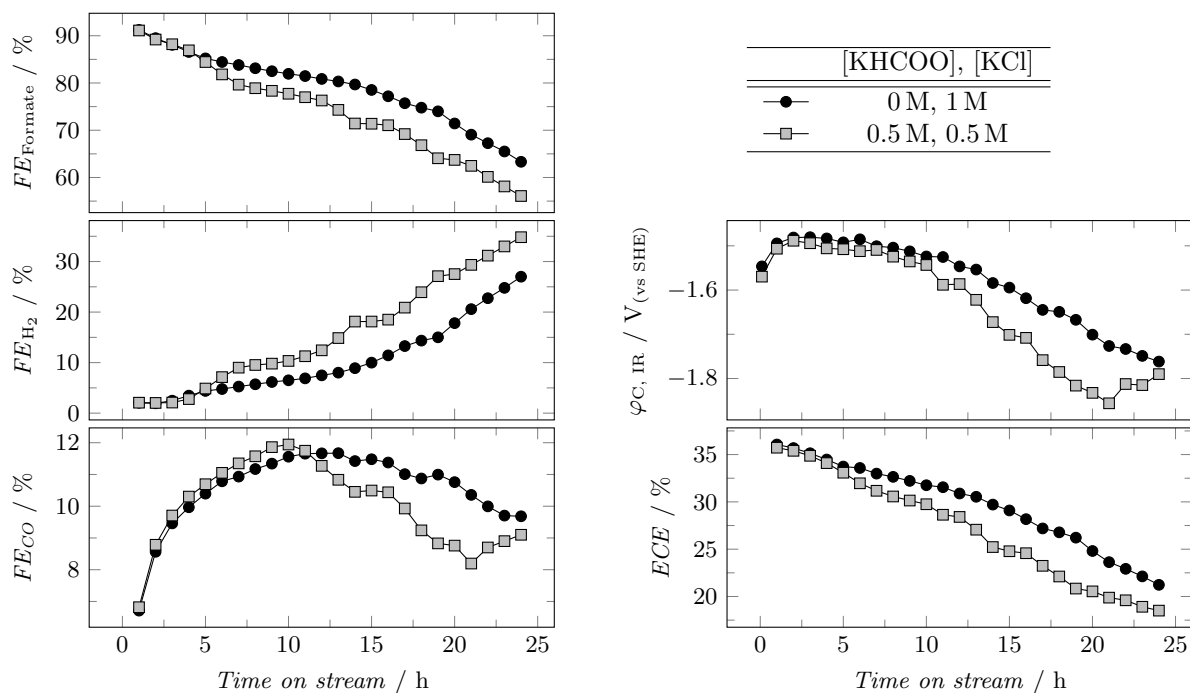


**Figure 9.10:** Long-term performance analysis for different feed formate concentrations at 20 °C. Operating conditions: continuous;  $j = -200 \text{ mA cm}^{-2}$ , pH = 10; Standard GDE.

## 9.5.2 Concentration effects

**Table 9.5:** Faradaic efficiencies, compensated cathode potentials and energetic cathode efficiencies at different catholyte concentrations and current densities.

Operating conditions: semi-batch;  $t = 40 \text{ min}$ ,  $T = 35 \text{ °C}$ , KCl; standard GDE.

$c$ / M	$j$ / $\text{mA cm}^{-2}$	$FE / \%$			$\varphi_{\text{C, IR}}$ / V (vs. SHE)	$ECE$ / %
		H <sub>2</sub>	CO	Formate		
0.1	200	2	6	93	-1.32	37
0.5		2	6	92	-1.34	35
1		2	5	93	-1.33	36
2		2	6	93	-1.33	36
0.1	700	5	7	88	-1.62	32
0.5		9	6	86	-1.64	30
1		4	6	88	-1.62	32
2		5	6	87	-1.65	29

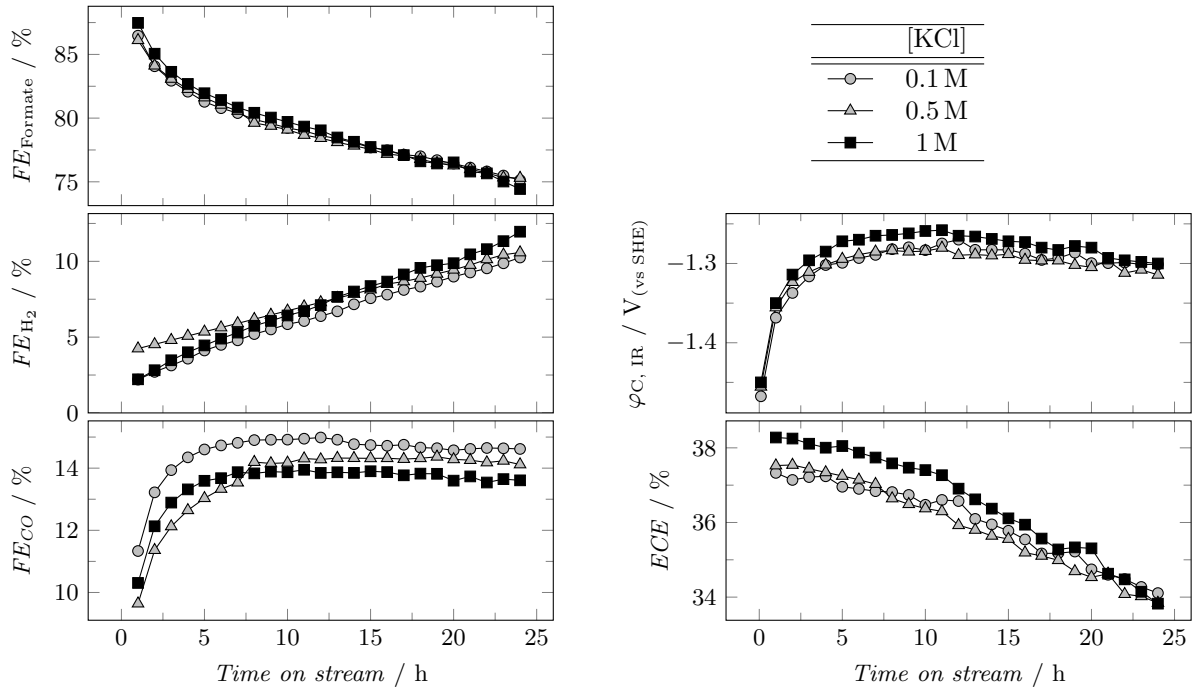


**Figure 9.11:** Long-term performance analysis for different electrolyte concentrations. Operating conditions: continuous;  $j = -200 \text{ mA cm}^{-2}$ ,  $T = 50 \text{ }^\circ\text{C}$ ,  $\text{pH} = 10$ ; Standard GDE.

### 9.5.3 Electrolyte purity

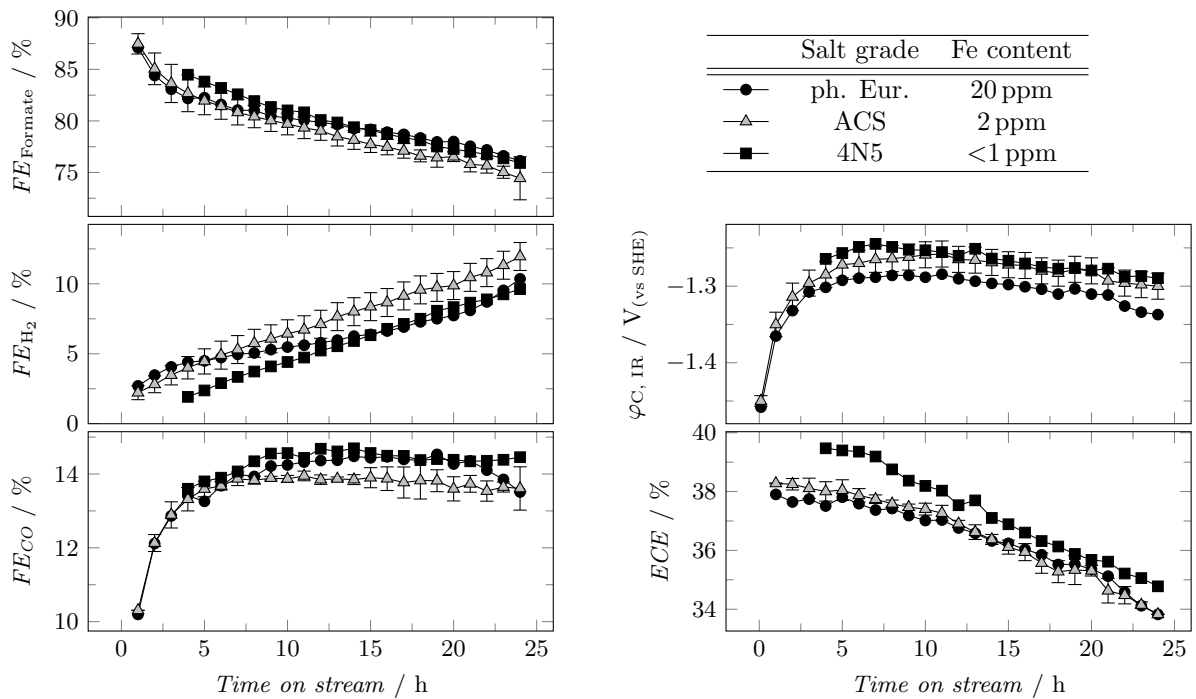


**Figure 9.12:** Long-term performance analysis for different salt grades. HPLC grade water was used as solvent. Operating conditions: continuous;  $j = -200 \text{ mA cm}^{-2}$ ,  $T = 50 \text{ }^\circ\text{C}$ ,  $[\text{KCl}] = 1 \text{ M}$ ,  $\text{pH} = 10$ ; Standard GDE.

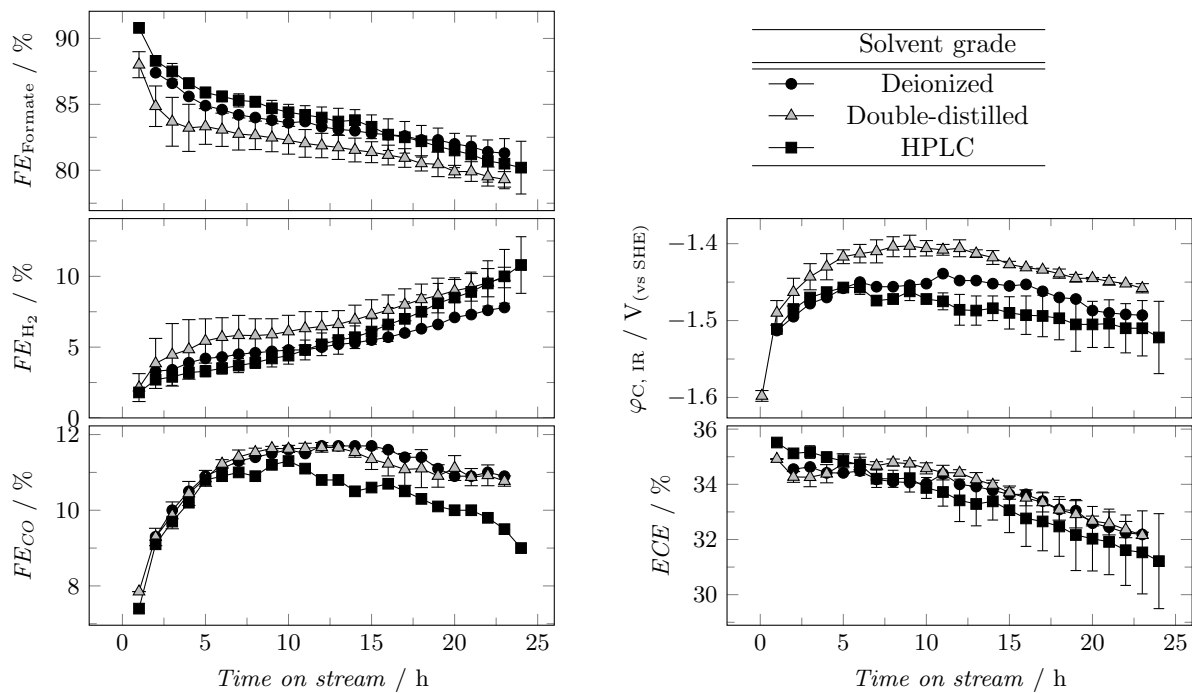


**Figure 9.13:** Long-term performance analysis for different solvent grades.  
Operating conditions: Continuous;  $j = -200 \text{ mA cm}^{-2}$ ,  $T = 50 \text{ }^\circ\text{C}$ ,  $[\text{KCl}] = 1 \text{ M}$ ,  $\text{pH} = 10$ ; Standard GDE.

## 9.6 Temporal behavior - Long-term stability

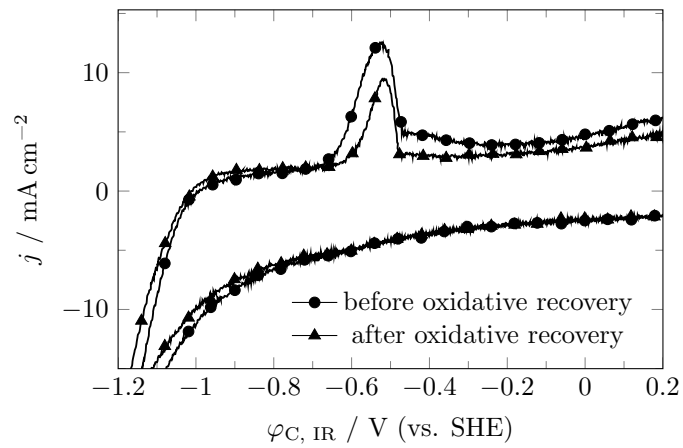


**Figure 9.14:** Cyclic voltammograms obtained before and after applying an oxidizing potential of 0.64 V (vs. SHE) for 30 min.

## 9.7 Process concepts

### 9.7.1 Operating carbon dioxide electrolysis in the recycled product mixture

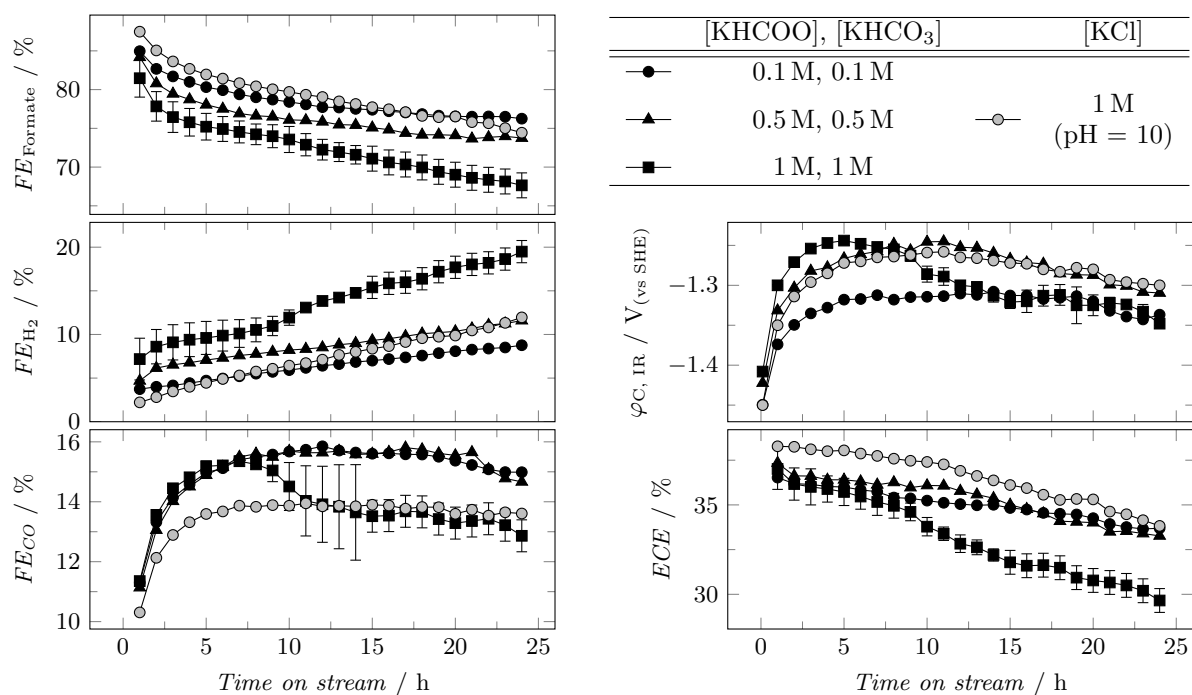


**Figure 9.15:** Long-term performance analysis for formate/bicarbonate 1:1 mixtures of different concentrations. The standard electrolyte [KCl] = 1 M is shown for comparison. Operating conditions: continuous;  $j = -200 \text{ mA cm}^{-2}$ ,  $T = 50 \text{ }^\circ\text{C}$ , native pH; Standard GDE.

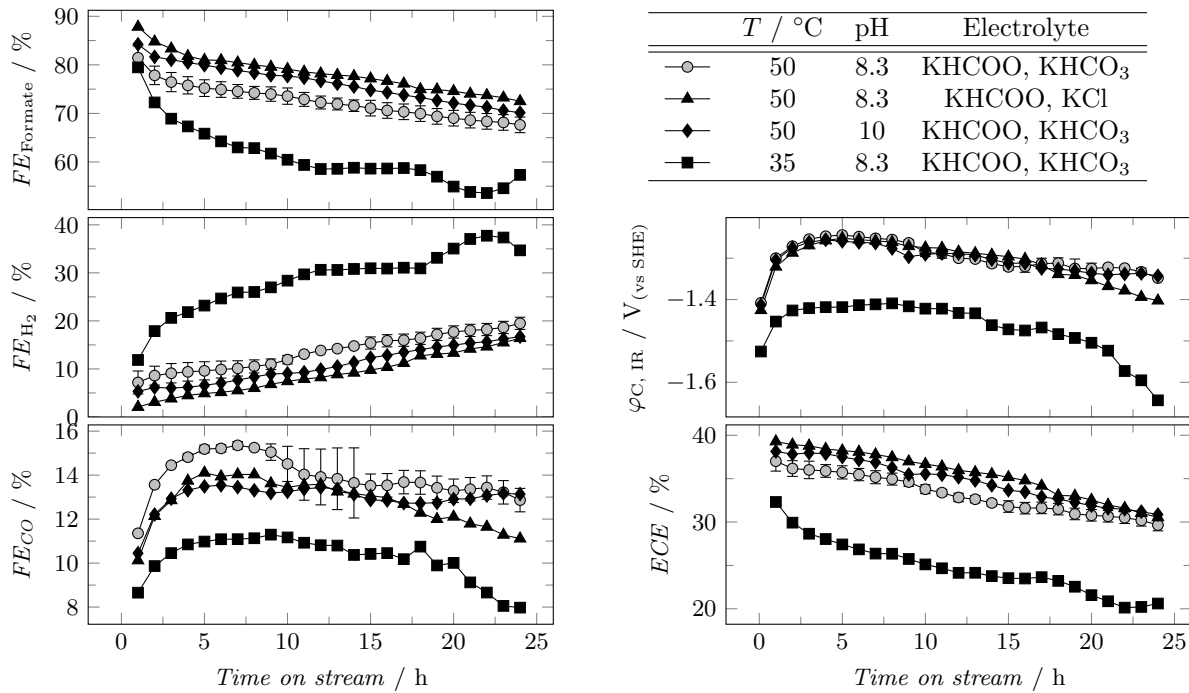


**Figure 9.16:** Long-term performance analysis for formate/bicarbonate 1:1 mixtures with varied operating conditions and electrolyte composition.

Operating conditions: continuous;  $j = -200 \text{ mA cm}^{-2}$ , total salt concentration = 2 M; standard GDE.

## 9.7.2 Coupling carbon dioxide reduction with selective alcohol oxidation

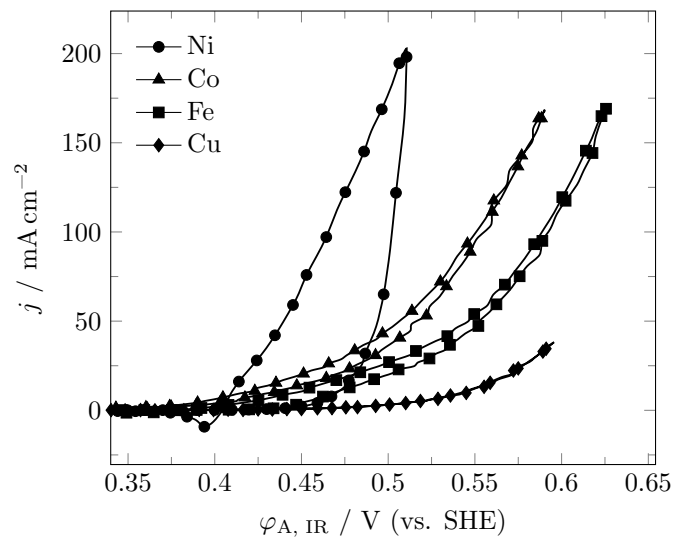


**Figure 9.17:** Cyclic voltammograms of different metals in electrolytes containing 1 M potassium hydroxide and 1 M methanol.

Operating conditions:  $T = 50 ^\circ\text{C}$ ,  $d\phi_{A, IR}/dt = 50 \text{ mV s}^{-1}$ .